Estimation of Arterial Diameter Using Bioimpedance Spectroscopy on a Human Wrist Phantom

Yang Yu

A thesis submitted to

Auckland University of Technology

in fulfilment of the requirements for the degree of

Doctor of Philosophy (PhD.)

Institute of Biomedical Technologies

School of Engineering, Computer and Mathematical Sciences

Faculty of Design and Creative Technologies

Supervisors:

Prof. Andrew Lowe and

Dr. Gautam Anand

August 2022

ABSTRACT

Background: Blood pressure measurement (BPM) is a well-known clinical method to monitor cardiovascular function, and it is also a reliable predictor of death and cardiovascular disease. Since the beginning of this century, a type of cuff-less continuous BPM has been investigated based on the strong relationship between pulse wave propagation (i.e., pulse wave velocity, pulse transit time, and pulse arrival time) and blood pressure (BP). A comprehensive review was undertaken to explore the limitations of the existing pulse wave propagation method (PWPM), including the techniques, mathematical models, and clinical protocols. It was found that the lack of absolute arterial diameter information in previous studies might limit the performance of existing PWPM because the arterial diameter change has been proved to be one significant factor in BP change from both theoretical and experimental perspectives.

Hemodynamic monitoring is concerned with the dynamic blood flow within the human circulatory system. Bio-impedance measurement (BIM) can sense the physical and electrochemical processes in human tissues and hence can monitor various physiological variations. In the context of ambulatory hemodynamic monitoring, there has been interest in portable BIM for both diagnostic and research purposes by placing the electrodes on human extremities, such as the wrist. The radial artery is a common location to detect pulsatile blood due to the thin surrounding tissue layers, which has been used for pulse wave propagation determination. When a pulse wave arrives, the amount of blood inside the artery increases and the measured impedance decreases because of the higher conductivity of the blood. Therefore, BIM at the wrist is a promising technique to estimate the arterial diameter, offering an improvement in PWPM for cuffless BPM in the future.

Objectives: The main objective of this research is to improve the accuracy of arterial diameter estimation from bio-impedance signals by reaching a consensus between observed impedance values (from computational simulation and phantom experiments) and mathematical modelling. This thesis focuses on the effects of different electrode configurations on current density and electric field (E-field) distribution within the wrist, aiming to achieve a reasonably uniform E-field distribution such that the cross-sectional area changes of the blood can be estimated more accurately.

Method: Finite element analysis was performed on a 3D human wrist segment containing fat, muscle, and a blood-filled radial artery. Then, the skin layer, bones and a contralateral

blood-filled ulnar artery were stepwise added, helping to understand the dielectric response of multi-tissues and blood flow in the β-dispersion band (from 1 kHz to 100 MHz), the current distribution throughout the wrist, and the optimisation of electrode configurations for arterial pulse sensing.

Two wrist phantoms were fabricated to verify the simulation results from both one-artery model and two-arteries models. Each wrist phantom contained two components: (1) the surrounding tissue simulant was fabricated by mixing 20 wt.% gelatine power with 0.017 M sodium chloride (NaCl) solution, (2) the conductive blood was simulated using 0.08 M NaCl solution. The blood-filled artery was constricted by a commercial desktop injection pump, and the impedance change was synchronously measured using the multi-frequency impedance analyser.

Main results: The simulation results indicated the promising abilities of band electrode method to generate a more uniform current distribution than the traditional spot electrode approach. Both simulation and phantom experimental results demonstrated that a longer spacing between current-carrying (CC) electrodes with shorter spacing between pick-up (PU) electrodes in the middle region can sense a more uniform E-field, engendering a more accurate arterial diameter estimation. For the one-artery model, the arterial diameter could be accurately estimated with an average percent error of less than 1% in both simulation and phantom experiments. For two synchronously pulsatile arteries, the band electrode configuration exhibited a significantly higher accuracy in sensing overall blood volume change throughout the measured region.

Conclusion: In summary, this thesis contributes to the accurate quantification of arterial diameter-dependent impedance variance by investigating the effect of electrode configuration. A promising band electrode configuration was developed for more accurate arterial diameter estimation from the numerical simulation and tissue phantom perspectives. More accurate arterial diameter estimation via BIM could further improve the performance of existing PWPM and cuffless BPM in the future.

TABLE OF CONTENTS

ATTESTATION OF AUTHORSHIP

I, Yang Yu, hereby declare that this submission is my own work and that, to the best of my knowledge and belief, it contains no material previously published or written by another person (except where explicitly defined in the acknowledgements), nor material which to a substantial extent has been submitted for the award of any other degree or diploma of a university or other institution of higher learning.

Signature:

Date: 08/08/2022

ACKNOWLEDGMENTS

It is my pleasure to thank everyone who supported and assisted me during my PhD study.

First of all, I would like to express my heartfelt gratitude to my primary supervisor Prof. Andrew Lowe, for his insightful guidance and illuminating instructions throughout my PhD research. Furthermore, I would like to extend my sincere gratitude to my secondary supervisor Dr. Gautam Anand, for all of his valuable suggestions and continuous assistance on my PhD project. In the past three and half years, my supervisors have been my mentor, friend, and listener, all of these and more. This thesis would not have been possible without their consistent support and guidance.

Additionally, I would show my appreciation to thank everyone in the Institute of Biomedical Technologies, Auckland University of Technology, for their kind assistance and friendly collaboration both in academic and daily life.

Lastly but most importantly, I would like to say thank you to my family. It is difficult to express in words how grateful I am for the selfless dedication of my father Dongsheng Yu and my mother Qiuling Xia. It is their infinite love and support that enable me to go through hard times and pursue a better life. I would also like to thank my adorable dog Tony for maintaining my optimistic attitude to life.

LIST OF SYMBOLS AND ABBREVIATIONS UNITS

Symbols

Symbol	Quantity
A	Cross-sectional area
C	Capacitance
D/d	Diameter
E	Young's modulus
f	Ordinary frequency
g	Gravitational acceleration
h	Thickness
H	Height
I	Current
J	Current density
L/l	Length
P/p	Blood pressure
R	Resistance
S	Sensitivity
t	Time
U	Voltage
V	Volume
Z	Impedance
ρ	Density
σ	Conductivity
ω	Angular frequency
ε_r	Relative permittivity

Abbreviations

2D	Two-dimensional
3D	Three-dimensional
A-mode	Amplitude Mode (of ultrasound imaging)
AC	Alternating Current
AKF	Adaptive Kalman Filter
ANN	Artificial Neural Network
ANSI/AAMI/ISO	American National Standards Institute, the Association for the Advancement of Medical Instrumentation, International Organization for Standardization
APG	Acceleration Plethysmograph
B-mode	Brightness Mode (of ultrasound imaging)
BCG	Ballistocardiogram
BHS	British Hypertension Society
BIDMC	Boston's Beth Israel Deaconess Medical Centre
BIM	Bio-impedance Measurement
BP	Blood Pressure
BPM	Blood Pressure Measurement
BSN	Body Sensor Network
CC	Current Carrying
CNN	Conventional Neural Network
DBP	Diastolic Blood Pressure
DC	Direct Current
E-field	Electric Field
ECG	Electrocardiogram
ESH	European Society of Hypertension
FDA	Food and Drug Administration
FEA	Finite Element Analysis

GA	Genetic Algorithm
HR	Heart Rate
ICU	Intensive Care Unit
IEEE	Institute of Electrical and Electronics Engineers
IPG	Impedance Plethysmography
M-mode	Motion Mode (of ultrasound imaging)
MAD or MAE	Mean Absolute Difference/Error
MARS	Multi-adaptive Regression Spline
MBP	Mean Blood Pressure
MIMIC	Multiparameter Intelligent Monitoring in Intensive Care
MIV	Mean Impact Value
ML	Machine Learning
MLE	Maximum-likelihood Estimation
NaCl	Sodium Chloride
PAT	Pulse Arrival Time
PCB	Printed Circuit Board
PCG	Phonocardiogram
PE	Percent Error
PEP	Pre-ejection Period
PETG	Polyethylene Terephthalate Glycol
PIR	Photoplethysmogram Intensity Ratio
PLA	Polylactic Acid
PP	Pulse Pressure
PPG	Photoplethysmography
PTT	Pulse Transit Time
PTTV	Variability of Pulse Transit Time
PU	Pick Up

PWPM	Pulse Wave Propagation Method
PWV	Pulse Wave Velocity
RBC	Red Blood Cell
RBPM	Reference Blood Pressure Measurement
RC	Resistor-Capacitor
RE	Relative Error
RMSE	Root Mean Square Error
RMSEs	Root-mean-squared-errors
RR	Respiratory Rate
SBP	Systolic Blood Pressure
SCG	Seismocardiogram
SD	Standard Deviation
SNS	Sympathetic Nervous System
SpO_2	Oxygen Saturation
SVR	Support Vector Regression
VPPT	Variation of Pulse Transit Time

LIST OF FIGURES

LIST OF TABLES

CHAPTER 1. INTRODUCTION

1.1 The importance of blood pressure measurement

The morbidity and mortality of cardiovascular disease are the highest in the current disease spectrum worldwide. Globally, it was reported that approximately 12.8% of deaths and 4.4% of disability-adjusted life years were caused by abnormal blood pressure. Moreover, the leading cause of the worldwide burden of disease is high blood pressure (hypertension) [1]. Hypertension management is always a formidable task, from accurate measurement to effective treatment [2]. The American Heart Association classifies blood pressure (BP) and corresponding diagnosis in four categories according to the systolic blood pressure (SBP) and diastolic blood pressure (DBP) levels: normal, elevated, stage 1 hypertension, and stage 2 hypertension [3], as summarised in Table 1. The blood pressure measurement (BPM) is a well-known clinical method to monitor cardiovascular function, and it is also a strong predictor of death and cardiovascular disease [4]. The history of BPM can be dated back to the end of the 18th century [5]. During these decades, many advancements in concept and technology of BPM have allowed us to diagnose abnormal blood pressure and predict cardiovascular pathologies effectively. However, the research on sphygmomanometers does not stop there. New techniques with more portability (e.g., ambulatory devices) and acceptable accuracy have gradually become standardised and gained consensus.

Table 1. Classification of blood pressure.

BP level classification	**SBP (mmHg)**		**DBP (mmHg)**
Normal	<120	and	<80
Elevated	120-129	and	<80
Stage 1 hypertension	130-139	or	80-89
Stage 2 hypertension	≥140	or	≥90

1.2 Conventional blood pressure measurement

1.2.1 Category of blood pressure monitors on sale

The techniques of BPM can be divided into two categories: Direct (invasive) and indirect (non-invasive). Non-invasive BPM can be further classified into cuff-based and cuff-less BPMs, as shown in Figure 1.

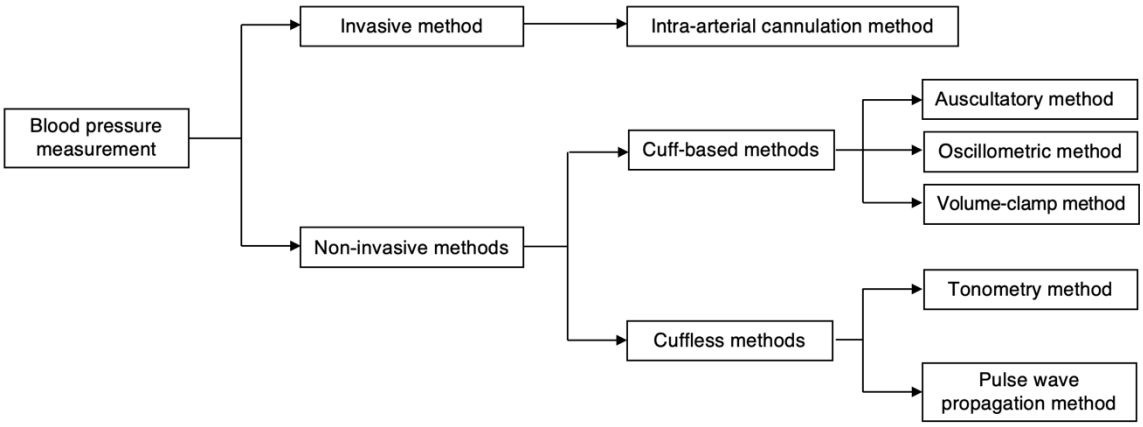

Figure 1. Categories of blood pressure measurement.

The invasive (intra-arterial) cannulation method can provide the most accurate beat-to-beat blood pressure values, which is regarded as the gold standard in BPM. As the name suggests, this method requires an invasive catheter to contact blood flow directly, and the pressure transducer converts the mechanical signal created by the real-time blood pressure into an electrical signal. Finally, the electrical signal is transmitted and displayed as a pulse waveform to the physicians [6]. Even though the invasive method can reflect real-time intravascular pressure accurately and reliably, its high cost, professional operational requirements and potential harm to patients limit the scope of application. It is especially unsuitable for home-based monitoring. Therefore, it is generally employed in the Intensive Care Unit (ICU) settings [7].

Sphygmomanometer, as known as the blood pressure monitor or blood pressure gauge, is a classic cuff-based BPM, which based on principles of auscultation or oscillometry. The conventional manual sphygmomanometer includes three components: an inflatable cuff, a stethoscope and a measuring unit (aneroid gauge or mercury manometer). The working principle involves the cuff inflated around the artery (arms or legs) to occlude the blood flow. As the cuff is slowly deflated, the SBP is detected when the first Korotkoff sound is first heard and the DBP is traditionally recorded at which the fourth Korotkoff sound is just barely audible by well-trained personnel with the stethoscope [8]. However, the fifth Korotkoff sound (i.e., silence) has been recently used as the mark of DBP, as this has been felt to be more reproducible [9]. This traditional manual sphygmomanometer is still used in some clinical situations due to being sufficiently accurate, less costly and non-invasive. However, the requirement of experienced personnel to operate the sphygmomanometer limits its use in the home setting [10].

Similar to the auscultation method, oscillometry was discovered over 100 years ago [11], which also applied an inflatable cuff wrapping around the arm or wrist of subjects. Instead

of recording Korotkoff sounds, oscillometry has a built-in pressure sensor to detect pressure oscillations in the cuff while the cuff is gradually deflated [12]. The mean blood pressure (MBP) is obtained at the maximum amplitude variations of oscillation, and then SBP and DBP are approximately estimated from MBP and the oscillation envelope. The automatic oscillometry method is the commonest sphygmomanometer for home-based conditions due to its more convenient operation. A recent study extended oscillometric principles to a smartphone to detect variable amplitude blood volume oscillations from a pressure sensor [13].

The cuff structure was re-designed innovatively as a watch band and incorporated with a smartwatch for wearable BPM [14]. However, oscillometry might fail to estimate BP values accurately in several specific conditions. For example, the detected amplitudes of pulse oscillation may be weak for subjects with arterial fibrillation, obesity and atherosclerosis. Moreover, SBP and DBP are estimated by empirical coefficients, which might be unreliable for some individuals [15]. An inherent drawback of auscultation and oscillometry sphygmomanometers is that they cannot measure BP changes beat-to-beat. In other words, the measured BP values are not continuous.

Finapres® NOVA technology [16] is an automated system for continuous BPM using servo-plethysmo-manometry, which employs volume clamp principles at the fingers [17]. The precision of Finapres was verified about the same order of magnitude as that of oscillometry devices by Pace and East in 1991 [18]. Moreover, comparisons between Finapres and other conventional sphygmomanometers have been carried out at the end of the last century. Even though Finapres can obtain nearly beat-to-beat BP values, its unstable accuracy limits the capability to substitute for the invasive method [19]. Compared with the auscultation device, the agreement was especially good for SBP but not DBP [16, 17]. One problem was the reduction of accuracy related to time (drift) [22]. Further, the measurement is easily influenced by physical and physiological factors [23], such as patients administered cold pressor [24] and pregnant women [25].

Tonometry (vascular unloading method) is a technique for non-invasive continuous BPM without a cuff. The principle is that a probe flattens or applanates the artery to press it against the bone, requiring measurement in superficial vessels close to the bone, such as radial, temporal arteries, and dorsal pedis [26]. The applied pressure is maintained at a level to counteract the circumferential tension of the target artery wall [12]. However, its accuracy is inconsistent between different research, and it always requires calibration

with a cuff-based measurement due to the difficulty of application [27]. Three main operating conditions could cause incorrect results: (1) if the applied pressure is too small or too high, BP cannot be measured; (2) the tonometer should be placed above the centre of the artery; a tiny displacement could reduce the accuracy; (3) the results are also susceptible to movement artefacts.

Belani and his colleagues described a novel non-invasive device Vasotrac (Medwave, Arden Hills, MN) based on the Tonometry method [28] [29]. Its working principle is to detect the zero-load state of the radial artery at the wrist by generating compression and decompression frequently, and the BP parameters and waveform can be displayed every 12 to 15 beats. Different from oscillometry, the Vasotrac directly compresses the radial artery in a cyclical fashion and determines the pressure at which maximum energy transfer occurs, isolating the transversal component of the pressure pulse. Moreover, it can avoid compression injuries caused by the cuff because it does not apply circumferential pressure around the arms.

1.2.2 Status of blood pressure measurement on the market

As of now, several prestigious organizations have developed clinical validation protocols for BPM devices, such as the "ANSI/AAMI/ISO 81060-2:2013" by American National Standards Institute, the Association for the Advancement of Medical Instrumentation [30], the BHS Protocol by British Hypertension Society [31], the ESH International Protocol by the European Society of Hypertension [32], and the IEEE standard for Wearable, Cuffless Blood Pressure Measuring Devices by the Institute of Electrical and Electronics Engineers [33]. Such standards specify consistent approaches throughout the clinical investigation, from validation to statistical analysis [34]. Even though they have similarities in the main concept and procedure, their methodology details are different. Due to the oversight of regulatory requirements and non-uniform standards for BPM devices, the actual performance of devices on sale may not be like what manufacturers advertised.

The brachial cuff-based sphygmomanometer is a widely-used BPM in the home setting, but it was reported that over 30% of them are inaccurate [35]. According to a comprehensive meta-analysis [36], cuff-based BPM is likely to underestimate SBP and overestimate DBP compared with the intra-arterial brachial method. As a result, the variable accuracy of current cuff-based BPM might influence the correct classification of BP. The worse fact is that over 85% of cuff-based BPM devices have not published

evidence on accuracy performance in the current market [37]. It is questioned that manufacturers made false claims about their validation of BPM devices [38]. If clinicians and customers are unaware of this issue, an incorrect diagnosis or wrong treatment decision might be made [39]. As a result, patients would lose the best practice of clinic care and weaken the efficacy of cardiovascular disease prevention [40].

1.3 Blood pressure estimation using pulse wave propagation

In recent years, cuffless BPM based on the strong relationship between pulse wave propagation information and the changes in BP has been investigated and developed. This is referred to as the pulse wave propagation method (PWPM) in this thesis. Specifically, the time components of pulse wave propagation information comprise pulse transit time (PTT), pulse arrival time (PAT) and pulse wave velocity (PWV). PTT was early determined by Weltman et al. in 1964 [41] by using the electrocardiogram (ECG) complex and a downstream pulse signal. PTT can be defined as the time taken for the blood pulse wave to travel from a proximal site to a distal site along the arterial tree. PAT is defined as the time interval between the R-peak of ECG signal and a characteristic point of the photoplethysmography (PPG) wave, which is equal to the sum of PTT and pre-ejection period (PEP). It is worth noting that PEP is not related to the blood pulse propagation; it consists of electromechanical delay and the time of isovolumic contraction [42]. However, several papers confound PTT and PAT, which might become misleading terminology.

PWV is a gold standard for arterial stiffness assessment in clinical practice [43]. It can be defined as the velocity of a pulse wave propagating through two different arterial sites and can be calculated by a distance divided by the transit time.

$$PWV = \frac{Distance}{PTT} \qquad \textit{Equation 1}$$

As early as 1922, the PWV (in cm/s) was used as an index of distensibility [44], giving a basic relationship with BP change (ΔP in dyne/cm^2) and blood volume change (ΔV)/ cross-sectional area change (ΔA):

$$PWV = \sqrt{\frac{V\Delta P}{\rho\Delta V}} = \sqrt{\frac{A\Delta P}{\rho\Delta \mathrm{A}}} \qquad \textit{Equation 2}$$

where V is the initial volume, A is the initial cross-sectional area, and ρ is the density of blood. Expressing ΔP in mm/Hg and PWV in m/s, then substituting ρ=1.055, the above equation becomes:

$$PWV = 0.357\sqrt{\frac{V\Delta P}{\Delta V}} = 0.357\sqrt{\frac{A\Delta P}{\Delta \mathrm{A}}} \qquad \textit{Equation 3}$$

Later in 1963, PWV was also expressed by the elasticity of arteries in the well-known Moens-Korteweg formula by assuming the artery as an elastic tube [45]:

$$PWV = \sqrt{\frac{Eh}{\rho d}} \qquad \textit{Equation 4}$$

where h is the thickness, E is Young's modulus of the arterial wall, d is the inner arterial diameter, and ρ is the density of blood.

The arterial wall comprises three main structures: elastin, collagen and cells (endothelial cells, fibroblasts and smooth muscle cells), and their proportions are varied between different arteries [46]. Generally, the elastic properties of vessel walls depend on the proportion of elastin and collagen. Collagen can provide mechanical integrity and strength; elastin is much more flexible. Arterial walls will expand during systole and contract during diastole with blood flow passing by, and the dynamic elastic modulus of central arteries increases exponentially with increasing BP [47]:

$$E = E_0 e^{\gamma P} \qquad \textit{Equation 5}$$

where E_0 is the elastic modulus at zero pressure, P is the mean BP (mmHg), and γ is the subject-dependent coefficient ranging from 0.016 to 0.018 ($mmHg^{-1}$). This equation was an empiric formula obtained from vivo experiments of dogs' aortas and omitted other factors such as ageing and viscosity of walls. Combining Equation 1, Equation 4, and Equation 5, a relationship between BP and PWV/PTT is then given by:

$$PWV = \frac{Distance}{PTT} = \sqrt{\frac{hE_0 e^{\gamma P}}{\rho d}} \qquad \textit{Equation 6}$$

Equation 3 and Equation 6 drove research in the area of PWPM. First, a research group found the changes in PWV reliably followed the changes in BP through theoretical analysis and experiments on subjects [48]. Specifically, a linear relationship was found

between PAT and MBP, and a non-linear decrease of PTT with increasing BP was measured in anaesthetized dogs [49]. The possibility and potential clinical application for humans were indicated in the following years [50], [51], including suitability for cardiopulmonary exercise conditions [52]. Therefore, more and more researchers have tried to estimate BP via PTT/PAT/PWV since early 2000s. Strictly speaking, the BP values are "calculated" instead of "measured". Several research groups have achieved moderate accuracy based on these principles so far, although performance is still questioned [53]. Figure 2 shows four common steps of the development process of PWPM: 1) measure waveforms located at two different sites along the arterial tree; 2) determine PTT/PAT/PWV from waveforms; 3) estimate BP values from PTT/PAT/PWV by mathematical models; 4) clinical investigation with critical protocols to validate the proposed system.

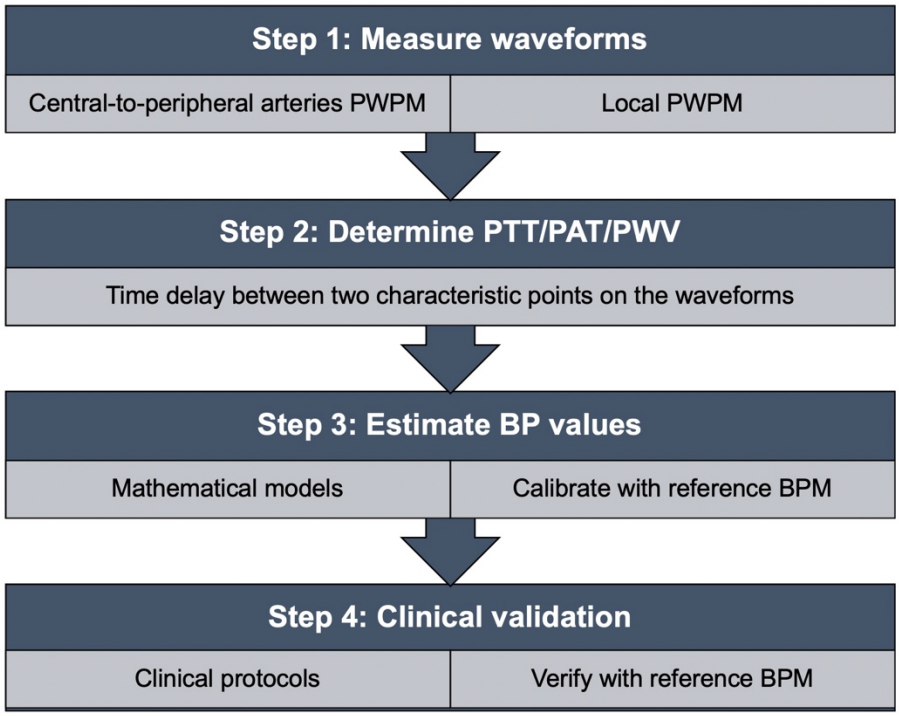

Figure 2. Four common steps of the development process of PWPM.

1.4 Arterial blood volume measurement

1.4.1 Ultrasound imaging

Ultrasound imaging is a diagnostic technique to construct a real-time image of internal body structures and measure some characteristics such as distances and velocities. Ultrasound is composed of sound waves with a typical frequency range from 2 MHz to

10 MHz for clinical purposes, which are significantly higher than the upper limit of human hearing. Frequency is determined by the sound source rather than the medium [54]. The main principle of ultrasound imaging can be briefly described as follows: ultrasound pulses are emitted into target tissues using a probe (i.e., transducer), then ultrasound pulses echo off tissues with different reflection properties (i.e., acoustic impedance) and return to the probe, which are then used to record and display the information as an image. Several types of ultrasound images can be formed with different information, such as Amplitude mode (A-mode), Brightness mode (B-mode), Motion mode (M-mode), Doppler mode and etc. [55].

Ultrasound imaging has been applied to measure arterial diameter change by a number of studies. The first investigation was described by Arndt et al. in 1968 [56], who detected the position of the arterial walls using an amplitude threshold in A-mode. It is straightforward but time-consuming to measure arterial diameters manually with calipers in M-mode or B-mode images [57]. Therefore, several previous studies [57]–[61] developed semi-automatic or automatic arterial wall detection algorithms/systems for M-mode and B-mode images processing to estimate both the distension and the absolute arterial diameter. However, these algorithms also suffered from the limited ultrasound image resolution. Furthermore, ultrasound equipment is expensive, and requires the significant skill of the operator to avoid the effects of artefacts.

1.4.2 Photoplethysmography

Photoplethysmography (PPG) is a non-invasive optical technology to track arterial blood volume change based on the principle of pulse oximetry. An optical sensor emits light to the skin and measures the intensity of light which is reflected back or transmitted through the skin [62], [63]. The amplitude of PPG signals depends on the amount of blood rushing into the peripheral vascular bed, the optical absorption of blood, skin pigmentation, ambient light and the wavelength (e.g., infrared and green) used to illuminate the blood [64]. The early application of PPG by Hertzman et al. to record the change in blood content of nasal septum [65], fingers and toes [66] dates back to 1937, and to the cutaneous blood pulse in 1946 [67]. Nowadays, PPG sensors are widely applied in wrist-worn smart devices to detect users' heart rates during daily physical activities [68]. Additionally, there has been much interest in extracting more valuable health-related information from the PPG signal in addition to heart rate estimation and pulse oximetry readings. It was reported that the second derivative wave of the PPG signal could help

researchers and clinicians to evaluate various cardiovascular-related diseases such as atherosclerosis and arterial stiffness [69]. Recently, the advancements in signal processing techniques have opened up new horizons for cuffless continuous BPM using multi-features from PPG signals with machine learning and artificial intelligence [70]–[72].

1.4.3 Bio-impedance measurement as a tool for hemodynamic monitoring

Hemodynamic monitoring concerns the dynamic blood flow within the human circulatory system. The definition of hemodynamic monitoring could range from micro-circulation and mitochondrial function monitoring to heart rate (HR) and blood pressure measurement [73]. The past few decades have witnessed vast development of technologies for hemodynamic monitoring. Measurement technology has gradually shifted from very invasive to less-invasive and non-invasive technologies [74]–[76]. The usage scenario has expanded from the clinical environment [77] to daily mobile monitoring [78].

In the context of ambulatory hemodynamic monitoring, there has been a booming interest in portable bio-impedance measurement (BIM) for both research and diagnostic purposes, which applies the electrodes on limbs such as the forearm near the wrist. It conforms to the current trend of wearable devices for health monitoring, easily put on and assessed. Bio-impedance is an exogenic bioelectric response instead of relying on endogenic bioelectric signals. BIM can sense the physical and electrochemical processes in human tissues and hence can monitor various physiological variations [79].

The radial artery near the wrist has been a typical position to detect pulsatile blood due to the thin surrounding tissue layers. For example, Tonometry is a widely used technique to measure arterial BP from the radial artery [80]. For BIM, it was indicated that the signals measured at radial and ulnar arteries exhibited better signal qualities than tibial and carotid arteries [81]. Thus, wearable BIM on the wrist has been popular because of its capability to detect the blood volume change caused by heart pulsation [82]. When a pulse wave arrives, the amount of blood inside the artery increases and the measured impedance decreases due to the higher electrical conductivity of the blood. Besides the blood volume changes, it has been widely reported and discussed that the velocity-dependent blood conductivity change is also an importance source of impedance changes, specifically, the orientation of red blood cells (RBC), which can trace back to 1968 [83]. For instant, the conductivity of flowing blood could change with the shape of velocity profile (i.e.,

accelerating and decelerating flow) [84]. In recent years, several studies have been carried out to endeavour to quantify and remove the influences of RBC orientation using mathematical modelling from measured signals to improve the accuracy of arterial diameter estimation [85], [86].

Figure 3 illustrates the overall principle of the common BIM using four-spot electrodes aligned on the human wrist. Two outer electrodes named current-carrying (CC) electrodes are connected with an alternating current power supply and inject a tiny alternating current (I) into nether tissues from the skin. Two inner electrodes named pick-up (PU) electrodes measure the voltage (U) over a certain distance. The overall measured magnitude impedance ($Z_{overall}$) is equal to:

$$Z_{overall} = \frac{U}{I} \qquad \textit{Equation 7}$$

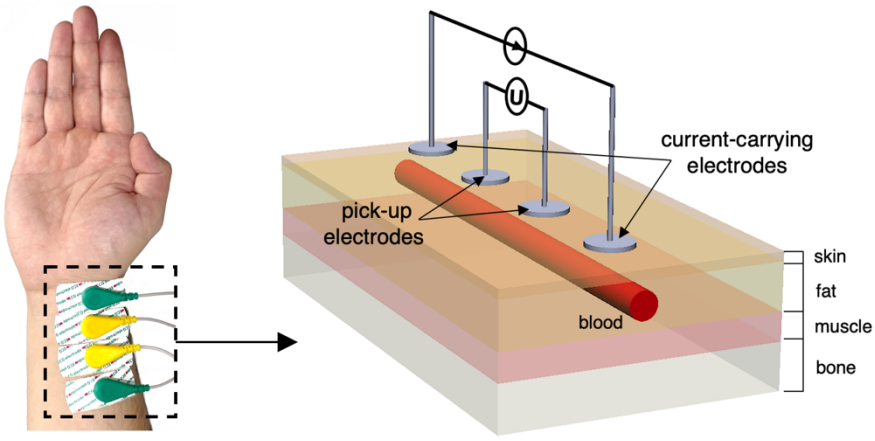

Figure 3. Overview of 4-spot electrodes BIM on the human wrist and the equivalent schematic.

1.5 Motivations

According to Equation 3, BP change is a function of both PWV and the blood volume/ cross-sectional area change radio (i.e., $\Delta V/V$ or $\Delta A/A$). Furthermore, Equation 6 demonstrates that the inner arterial diameter shows a positive relationship with BP. More specifically, Sugawara et al. [87] measured carotid arterial pressure and diameter change simultaneously, observing a linear relationship between the carotid arterial pressure–diameter. Even though PPG amplitude could kind of reflect arterial diameter-related information, BIM signal is more likely to be used for absolute arterial diameter estimation. These drove the motivation of this research, aiming to accurately estimate the

arterial diameter (change) from impedance variance on the wrist. We believe the absolute arterial diameter information would further improve the performance of PWPM and cuffless BPM in the future.

The sensitivity of the measured bio-impedance signal generally depends on the electrode configuration. Several works have investigated various placements of electrodes to acquire clearer bio-impedance waveforms [88]–[92]. Nevertheless, it might lack an understanding in whether the acquired waveforms can accurately represent the responses of target tissues and pulsatile blood from a mathematical perspective, which may limit our representation of hemodynamic parameters from bio-impedance signals. Different from previous arterial diameter estimation methods [86], [93], this research mainly focuses on the impacts of varied electrode configurations on current density and electric field (E-field) distribution throughout the wrist. The objective is to achieve a reasonably uniform E-field distribution such that the cross-sectional area changes of the blood can be estimated more accurately.

1.6 Thesis synopsis

The thesis is composed of seven chapters. Following this chapter, which forms the introduction, Chapter 2 systematically reviews previous research, highlighting the techniques and mathematical models for BP estimation via pulse wave propagation. Moreover, the relative performance of eligible studies was compared to explore the advantages and disadvantages of current development in PWPM. The research objectives are indicated with several revealed research gaps.

Chapter 3 proposes mathematical modelling to analyse the individual and overall contribution of tissues and pulsatile blood under BIM, aiming to accurately quantify the arterial diameter-dependent impedance variance and thereby estimate the arterial diameter.

Chapter 4 initially substantiates the proposed mathematical modelling through finite element analysis (FEA) of the static simplified human wrist segment, which included two tissue domains (fat and muscle) and one blood-filled radial artery. This simulation primarily focused on analysing various electrode configurations, including different shapes, materials and spacings. This simulation helped in understanding the dielectric response of fat, muscle and blood flow in the β-dispersion band (from 1 kHz to

100 MHz), the current distribution throughout the wrist region, and the optimisation of electrode configurations for arterial pulse sensing.

Chapter 5 extended the initial wrist model to more realistic geometries by adding other tissue domains, including the outer skin layer, centre bones, and the adjacent ulnar artery. Additionally, the linear geometry was restructured as a cylindrical model. The updated wrist models were simulated stepwise to observe the contribution of multi-tissues and whether the estimated arterial diameter change still maintains high accuracy when the wrist model becomes more complex.

In Chapter 6, two different experimental phantom models were fabricated to simulate the human forearm near the wrist for further verification of simulation results, including the *one-artery model* and *two-arteries model*. The wrist phantoms contained two components: gelatine-based surrounding tissue simulant and sodium chloride (NaCl) solution. A desktop injection pump was applied to change the blood simulant volume inside the artery. Meanwhile, the impedance signal was measured by the multi-frequency impedance analyser.

Chapter 7 summarises the academic contribution of this thesis and discusses the potential for future work with an emphasis on advancing cuffless BPM by measuring changes in arterial diameter using impedance.

Some aspects of the work presented in this thesis have been published as journal articles in SENSORS [94] and Physiological Measurement [79] before the thesis submission. These publications are:

- *Y. Yu, G. Anand, A. Lowe, H. Zhang, and A. Kalra, 'Towards Estimating Arterial Diameter Using Bioimpedance Spectroscopy: A Computational Simulation and Tissue Phantom Analysis', Sensors, vol. 22, no. 13, p. 4736, Jun. 2022, doi: 10.3390/s22134736.*
- *G. Anand, Y. Yu, A. Lowe, and A. Kalra, 'Bioimpedance analysis as a tool for hemodynamic monitoring: overview, methods and challenges', Physiol. Meas., vol. 42, no. 3, p. 03TR01, Mar. 2021, doi: 10.1088/1361-6579/abe80e.*

CHAPTER 2. LITERATURE REVIEW

2.1 Introduction

This chapter presents a review of previous studies mainly relevant to PWPM and BIM for hemodynamic monitoring. A systematic search was performed for literature published between November 2018 and April 2022. Figure 4 shows the process and the eligibility criteria at each stage in this search. Literature (e.g., articles, books, websites and patents) was searched from the Google Scholar database using the keywords ‘non-invasive blood pressure measurement’, ‘non-invasive blood pressure estimation’, ‘pulse wave velocity’, ‘pulse transit time’, ‘pulse arrival time’ and ‘bio-impedance measurement’. Supplementary papers were further traced from their reference lists in the process. All articles were restricted to the English language and were published in academic journals and conferences. All quoted resources were collected and managed by Zotero software (6.0.4), which can reduce citation errors and avoid duplicate papers.

The literature mainly concerned the following themes:

1) **Techniques to determine pulse wave propagation**: studies were eligible if they described a system/device for BP estimation by detecting pulse wave propagation, revealing different advantages and disadvantages of types of techniques.
2) **Bio-impedance measurement**: focused on the investigation of BIM for hemodynamic monitoring (including but not limited to PWPM), highlighting current physical application and the potential approaches by using computational simulation.
3) **Mathematical models**: included typical algorithms of BP estimation via pulse wave propagation, aiming to analyse the limitation of current models and explore the promising components that could be added to improve the accuracy of BP estimation.
4) **Clinical protocols**: summarized the clinical validation process of previous studies in detail, providing a better understanding of the current limitations and promising improvements for future investigation.

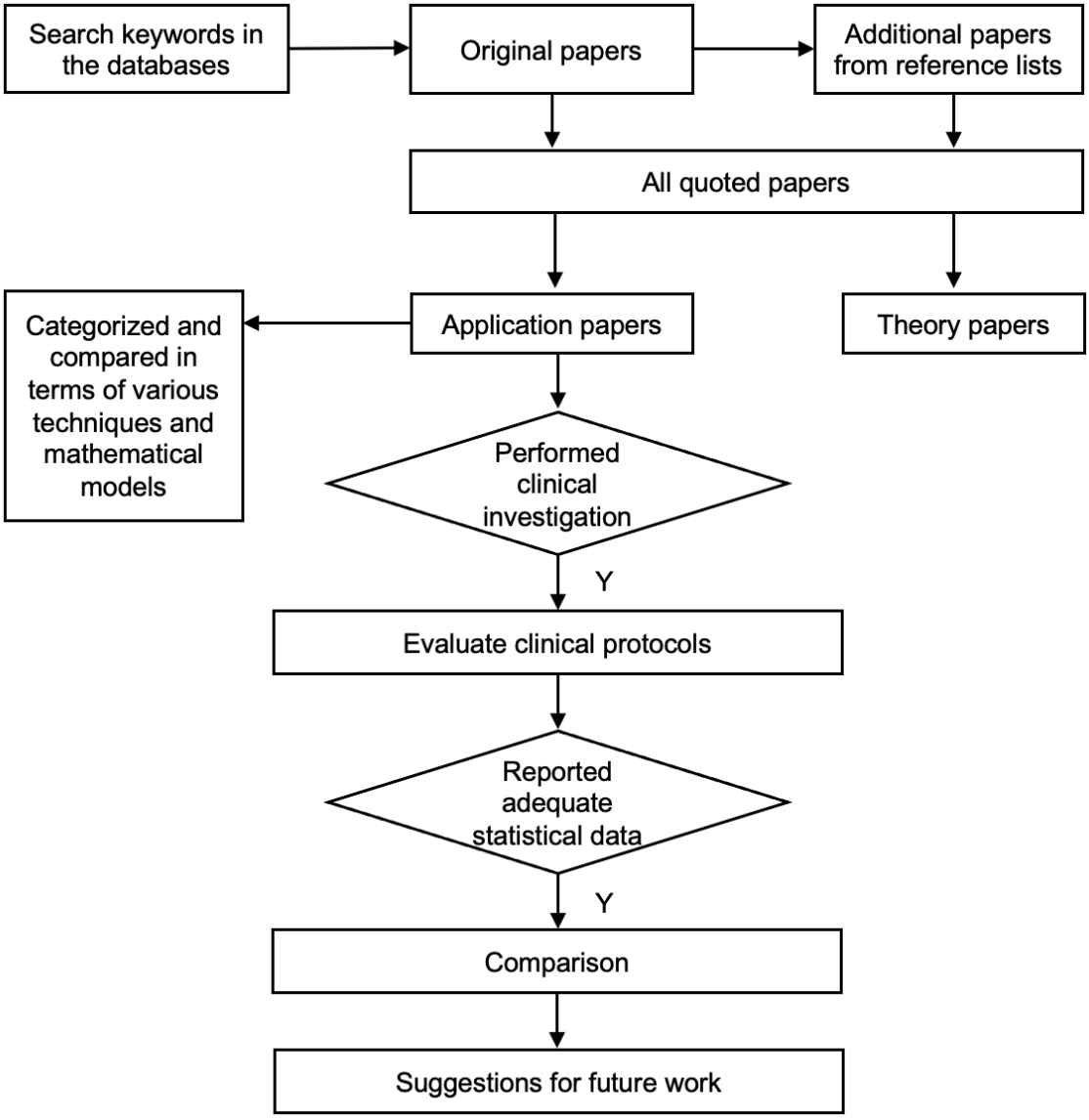

Figure 4. The process and the eligibility criteria at each stage in this literature review

2.2 Techniques to determine pulse wave propagation

2.2.1 Central-to-peripheral arteries methods

2.2.1.1 ECG-PPG system

The pulse wave propagation from the central artery to a peripheral artery is obtained by calculating the time delay between two related waveforms along the arterial tree. This kind of method is named "central-to-peripheral arteries PWPM" in this thesis. The electrocardiogram to photoplethysmography (ECG-PPG) method is the most typical system in the clinical setting to detect pulse wave propagation by calculating the time delay between a proximal ECG waveform (e.g., the thorax) and a distal PPG waveform

(e.g., finger, wrist, ear, and toe). The ECG and PPG signals need to be acquired synchronously with reference BP values. It is worth noting that the time interval here is PAT, containing irrelevant PEP besides the requisite PTT. Several earlier papers appear to confuse this terminology. It has been evidenced that the relationship is not reliable enough for PAT to be used as a surrogate marker of SBP, although it may be useful in assessing BP variability. DBP and MBP could not be estimated from PAT without correcting for PEP. In other words, PAT should not be used as a marker of purely vascular function [95].

Figure 5 illustrates three common characteristic points on the PPG waveform. They are applied by different research groups as follows:

- **R-peak of ECG to the peak of PPG** [96]–[102];
- **R-peak of ECG to the foot point of PPG** [98], [103]–[105];
- **R-peak of ECG to the middle point of PPG**, this point was consistently named as onset point, which was determined by the steepest slope of rising edge (peak of derivative PPG signal) [23], [52], [106]–[116].

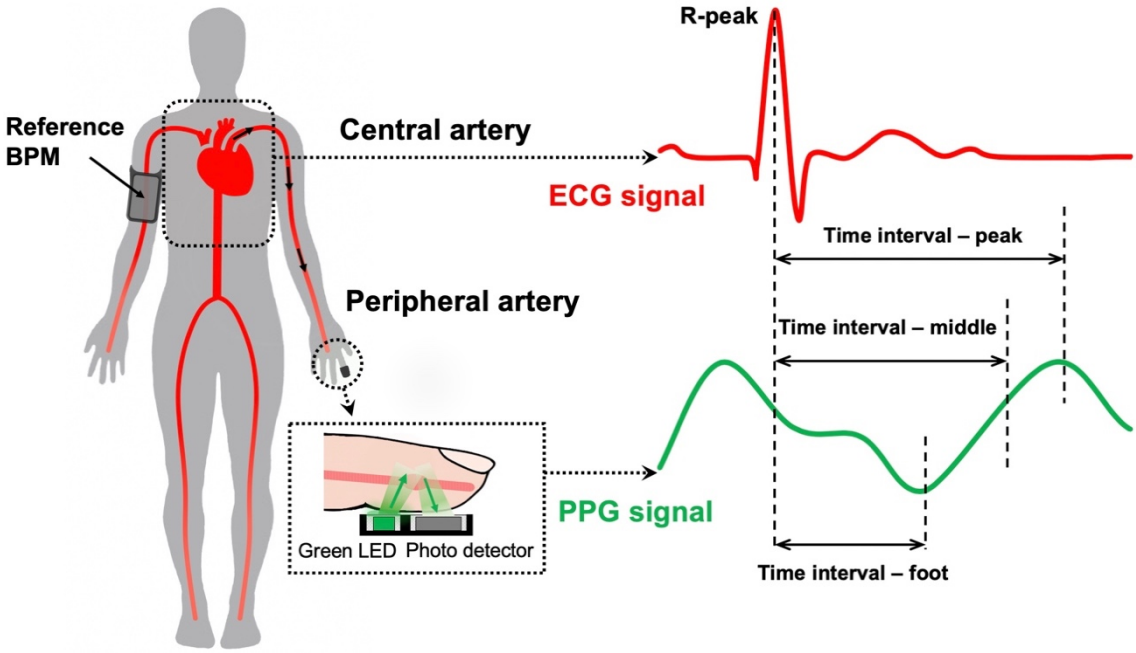

Figure 5. Common characteristic points of the ECG-PPG system.

One issue that limits the accuracy of the ECG-PPG system might be the inconsistent characteristic points on waveforms. One study suggested that using R-peak to the next relative minimum point of the PPG signal was a more appropriate method [42], contrasting with another study that claimed the estimated BP using PPG-peak had a higher correlation and lower errors [98]. Moreover, one study reported using the maximum point

in the first derivative of the PPG wave as the characteristic point performed better than other approaches [117]. The uncertainty of determining the most suitable characteristic points between different studies may reflect the subject-dependent relationship between pulse wave propagation and BP.

With the development of smart wireless devices, researchers attempted to extend the ECG-PPG system to wearable sensors for portable monitoring during daily activities. An earlier work integrated the ECG electrodes into a chair and the PPG sensors into the computer mouse for long-time computer users [118]. Another work combined ECG and PPG sensors into a "smart vest" [113]. The portability of the ECG-PPG system was improved further by being designed as an ear-worn device [119]. Additionally, smart phones were used to wirelessly communicate with wearable sensors (e.g., chest belt and wrist band) in Body Sensor Network (BSN) systems for BP monitoring [120]–[122]. Nowadays, the high performance of mobile devices could provide effective data processing and convenient communication with other devices and cloud services, which provides a new opportunity for daily BPM. Recently, an intelligent application embedded medical-grade ECG and PPG sensors into a smartwatch. In this way, PTT can be accurately calculated when users place one finger on the sensors, and then the device will feedback the BP information [123]. However, the manufacturer claimed that the measurement results are for reference only.

The studies introduced above almost all acquired the PPG waveform from the fingers. However, a recent study investigated thirty-two subjects and found that the PAT determined from the R-peak of ECG to the foot point of toe-PPG showed a better standard Pearson correlation with the reference SBP than the conventional "superior marker" finger-PPG signal. Recently, Chandrasekhar and his colleagues [124] noticed that the contact pressure of PPG sensor could induce substantial amplitude and shape variations in the PPG waveform, causing a wrong determination of time-based pulse wave propagation information.

ViSi Mobile System (SoteraWireless®, Inc, US) is a commercially available continuous surveillance monitoring for multiple healthcare parameters [125] which has been cleared for marketing by the Food and Drug Administration (FDA). This device estimates continuous BP via PAT measured between chest ECG and the Oxygen saturation (SpO_2) thumb sensor, requiring an initial calibration of PAT for an individual patient using conventional cuff-based BPM. It has been validated that the mean difference between

ViSi Mobile System and a conventional automated cuff oscillometric BPM was 4 mmHg for both SBP and DBP [126].

In 2021, a research team developed a MATLAB toolbox named PulseLab, covering all necessary steps for BP estimation using pulse wave PWV-based models via raw ECG and PPG signals [127]. This toolbox includes a user-friendly graphical user interface that offers visualization for the step-by-step processing of measured signals, which is available online [128].

2.2.1.2 Substitutions for ECG and PPG

In order to eliminate the potential errors caused by PEP and questionable characteristic points, several studies applied other techniques and different measuring sites. The following techniques provide more optional measurements and have potential advantages over the ECG-PPG system.

a. Ballistocardiogram (BCG) was used as an alternative proximal timing reference in deriving PTT. A customized weighing scale could measure BCG signals by detecting the reaction forces of the whole body to the cardiac ejection of blood into the aorta [129], [130]. Recently, a research group combined the sensor into a wristband for limb BCG measurement [131], [132].
b. Phonocardiogram (PCG) was also applied as the proximal timing reference [117], [133], which could detect two dominant types of sounds corresponding to the closure of mitral and tricuspid valves, and the closure of aortic and pulmonary valves.
c. Seismocardiogram (SCG) is a non-invasive measurement to capture cardiac vibrations transmitted due to the heart's mechanical activities from the chest wall by using accelerometers or gyroscopes [134]. It was recently applied to replace ECG as a surrogate proximal reference, cooperating with PPG to determine PTT in a wrist-watch BPM [135]. The SCG waveform includes waves associated with the opening of the aortic valve, which was marked as the characteristic point in this study. Furthermore, this research group applied a gyroscope to estimate and eliminate the interferential PEP [136]. Their recent custom watch (SeismoWatch) could take multiple ambulatory BPM over 24 hours, paving another promising way toward long-term hemodynamic monitoring using PWPM [137].
d. The two-PPG system was proposed by Yan Chen and his colleagues [138] to measure two independent pulse waves from the ear and toe and then found a non-linear relationship between PWV and BP by pulse contour analysis. They also pointed out

shortcomings of the conventional ECG-PPG method, such as it was easily affected by PEP and ECG signal was sensitive to other electrical instruments in clinical conditions. The two-PPG system is one feasible approach to detect PEP-free PTT, which was also able to be determined by time delay from the earlobe to fingers [103], from fingertips to the forehead temple [139], from shoulder to fingertips [140], or from the left hand to the right hand [141]. A commercial wrist watch (Biobeat BB-613WP, Biobeat Technologies Ltd, Israel) can track changes in BP based on PTT obtained by pulse measurements from the integrated SpO_2 sensor [142], which has been indicated as accurate by two validation studies [143], [144]. Moreover, it has been cleared by the FDA. However, it requires an initial calibration process and recommended re-calibration every three months using oscillometry BPM to maintain accuracy.

e. Impedance plethysmography (IPG) is a typical application of BIM for hemodynamic monitoring by detecting the volume change of the electrically conductive blood [79]. It has been considered a promising technique to substitute for either ECG or PPG to track blood pulse propagation in the last decade due to the capability to sense the change of impedance of blood vessels caused by the cross-section variations [82]. For example, BIM can be applied as a proximal reference (at the subclavian artery), and then PTT determined from the impedance signal to the PPG signal at the radial artery [145]. BIM could also be placed at the wrist as the distal reference, and then PTT indicated by the time interval from the R-peak of ECG to the peak of the bio-impedance signal [146], [147]. Compared with the conventional PPG, BIM has four benefits: 1) Low power consumption; 2) Low-cost materials of sensors; 3) Higher portability due to small areas of electrodes; and 4) The electrodes can be placed at most body parts where the arteries are close to the surface. Additionally, a research team reported that the ECG-IPG system showed a higher correlation between measured PTT and reference BP than the ECG-PPG system [148].
f. Flexible sensors have been also considered and investigated, such as textile triboelectric nanogenerators, which are emerging as compelling biotechnology for wearable pulse wave monitoring [149]. It is believed that flexible materials could crucially support the realization of wearable cuffless BPM, providing more comfort to wear and more cardiovascular health assessment as well as more electronics functionalities [150].

2.2.2 Local pulse wave propagation methods

In recent years, the importance of local PWV has been gradually recognized as an alternative physiological parameter to aortic-peripheral PWV. Measuring local PWV is an emerging method for determining a host of cardiovascular events such as arterial hemodynamic and local vessel pathologies [151]. The processes of local-PWPM are similar to the central-to-peripheral arteries PWPM: 1) measure waveforms located at two different sites along an artery; 2) calculate PTT/PWV from waveforms; 3) estimate BP values from PTT/PWV by algorithmic models.

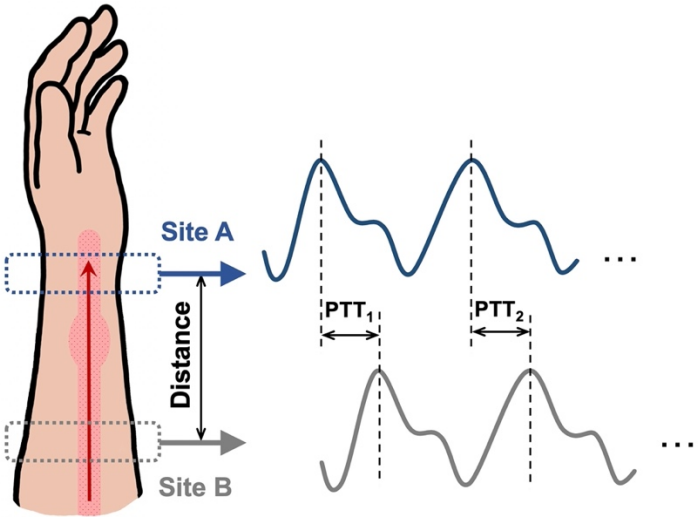

Figure 6. The primary principle of the local-PWPM.

The inherent advantage of the local-PWPM is that it only requires a small area to place the sensors (see Figure 6), while the cross-body configuration of the ECG-PPG system is more challenging to integrate into a wearable device for continuous monitoring. Moreover, the distance of the local artery is more specific, whereas the distance of the central artery to peripheral arteries is subject-dependent and much more complex. Therefore, the main purpose of local-PWPM is to develop a wearable device for BPM. Now smartwatches and sport-bands are the mainstream in the health care market, and can track HR and activities by many kinds of sensors. This has caused the wrist to become the most popular research region. Generally, the radial artery is a common measured position to detect pulse waves due to the thin surrounding tissue layers. The radial artery has been a significative region in medicine. For instance, in traditional Chinese medicine, radial artery pulse diagnosis was widely used by an experienced physician who placed fingertips over the wrist radial site for palpation [152]. One research group developed a wrist BPM to measure the radial artery pressure based on the volume-compensation

method [153]. Subsequently, several techniques have been embedded in a wearable wristband for local-PWPM:

- BCG-PPG system [131]
- BIM-PPG systems [154], [155]
- Two pressure sensor system [156]
- Two PPG system [157]
- Two BIM systems [88], [158], [159]
- Two PPG-ultrasound system [160]

BIM was usually applied as one time reference point to determine pulse wave propagation in above studies. The detailed description and other applications of BIM will be introduced in the following section.

2.3 Bio-impedance measurement

2.3.1 Physical applications

In order to meet the requirements of long-time wearable BPM, high portability and low power consumption are the key factors of the potential techniques. BIM was widely applied along the radial artery at the wrist in this field because the entire BIM system is small enough to be designed as a sports band. Several previous studies that detected blood pulse using BIM are listed in Table 2. They can be categorized into two groups: the component method and the BIM-only method. The component method is defined as using a BIM signal to replace one PPG or ECG signal as a reference point to determine PAT/PTT. Different studies had their own reason for choosing feasible components.

Bang et al. [146] claimed the PPG sensor was unsuitable for a portable system because it has to be clipped on a finger, and it cannot be integrated into an IC. Considering the cost, the light source and photo detector of the PPG device are much more expensive than the BIM sensor [147]. Additionally, Liu et al. [148] reported that the ECG and IPG systems showed a higher correlation between measured PTT and reference BP than ECG and PPG systems. However, the disadvantages of the ECG method cannot be neglected. Huynh et al. [161] abandoned the typical ECG method due to the potential errors from PEP. To overcome the drawbacks of PPG sensors, a four LED structure was designed as a PPG sensor and integrated into a wrist prototype with IPG sensors by Rachim et al. [162].

To overcome the complex configurations of the component method, the BIM-only method was developed. The common measured position is along the radial artery near the wrist. An earlier study has presented a portable BIM system for HR and PWV [82]. First, they used an electrical impedance model to simulate the blood, as shown in Figure 7, where R_i and R_p were the resistance of the inner area of blood cell and blood plasma, respectively, and C was the capacitance of the blood cell membrane. The parameters with "Δ" were the impedance change caused by the variation of the arterial cross-section. Then, the HR was directly related to the impedance variation, and PWV was obtained by dividing the distance between two sensor sites by signal lags. They investigated various locations along the radial artery and ulna artery and then determined the best signal quality appeared in the lower forearm along the radial artery.

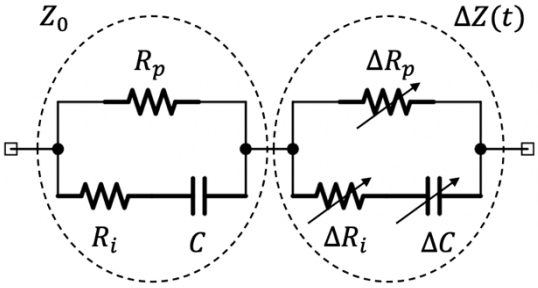

Figure 7. The equivalent circuit of the blood described by Cho et al. [82].

Min and his colleagues [80] proposed a tetra-polar BIM to track impedance signal along the radial artery as a complementary or even substituting a tonometry sensor. Compared to the tonometry method, BIM electrodes almost did not disturb the original blood flow due to the slight contact force on the skin. Metshein and his colleagues [163] observed the pulse wave most clearly when electrodes were placed on top of the radial artery within 5 mm in either transverse direction.

In 2017, Ibrahim and his team [158] proposed a regression model to estimate PTT based on the features extracted from the first and second derivatives of the bio-impedance signal, achieving a high correlation coefficient between estimated PTT and the reference PTT measured by the typical ECG-PPG system. Additionally, they indicated the measurement on the radial artery at 4 kHz was the best configuration to track the bio-impedance signals. Then, this team added a new pair of electrodes along the ulnar artery and applied the AdaBoost model to estimate BP based on multi-features from the time delays, amplitudes, slopes and areas of bio-impedance signals [159], [164]. Post-exercise BP could be accurately estimated with an average correlation coefficient, and root mean square error (RMSE) of 0.77 mmHg and 2.6 mmHg for the DBP and 0.86 mmHg and

3.4 mmHg for the SBP. Later, various electrode configurations were investigated using a 3D circuit model based on a time-varying impedance grid [91]. Recently, they utilized a multi-electrodes array at the wrist to achieve the calibration-free BP estimation by using a convolutional neural network (CNN) autoencoder with fairly low average errors of 0.5 $\pm$ 5.0 mmHg for DBP and 0.2 $\pm$ 6.5 mmHg for SBP.

Different from the studies above, the horizontal electrode structure was applied by Huynh et al. [88]. They suggested the horizontal direction had an advantage in length, which was more suitable for a wearable device. They also tested various different distances between two pairs of sensing electrodes. The results demonstrated the most optimal distance between two channels was 2 cm, with a more stable signal and more accurate estimation. However, tracking local PWV faced a challenge that the time delay between two pairs of electrodes might be much smaller than the descending time from peak to the foot of one bio-impedance signal. As a result, a small variation in the bio-impedance descending slopes between two signals would cause different time delays between different characterized points.

Table 2. Implementation of BIM at the wrist

Reference	Number of electrodes	Injecting current	Frequency [Hz]	Location	Measurement system
Bang et al. 2009 [146]	4	0.05 mA	10 k	Radial artery at the wrist	ECG-IPG
Lee and Cho 2013 [165] Lee and Cho 2015 [147]	4	0.25 mA	64 k	The wrist	
Liu, Cai, et al. 2017 [148] Liu, Cheng, and Su 2017 [166]	4	5 mA	100 k	Left arm	
Rachim, Huynh, and Chung 2018 [162]	4	0.5 mA	100 k	Radial artery at the wrist	PPG-IPG
T. H. Huynh, Jafari, and Chung 2018 [161]	4	0.5 mA	100 k	Radial artery at the wrist	
Metshein et al. 2018 [163]	4	-	8 to 2048 k	Top of radial artery (shift within 5 mm in the transverse direction)	Single-BIM
Min et al. 2017 [80]	4	0.2 mA	125 k	Radial artery at the wrist	
Ibrahim, Akbari, and Jafari 2017 [158]	6	0.4 mA	4 k	Radial artery at the wrist	Two-channels BIM
Cho, Kim, and Cho 2009 [82]	6	1 mA	100 k	Along the radial or ulna artery	
Huang, Huang, and See 2017 [167]	8	1 mA	50 k	Radial artery and middle finger	
T. Huynh, Jafari, and Chung 2018 [168]	8	0.5 mA	100 k	Radial artery at the wrist	
Ibrahim and Jafari 2018 [159]	12	0.8 mA	2 to 9.75 k	Along the radial and ulnar artery within 8 cm along the wrist	Four-channels BIM

2.3.2 Computational simulation

The finite element analysis (FEA) is a common method for computational/ numerical simulation, providing a more accessible and time-saving approach than experiment to verify research hypotheses and can also provide insights into further research methodology, especially to an immature technology. Several previous computational studies are summarized in Table 3. The models were various, including from two-dimensional (2D) geometry to three-dimensional (3D) geometry, from a single tissue to multi-tissues, and from simplified structure to relatively realistic structure. Studies were categorized into three groups according to their research objectives:

- **Diagnosis of vascular diseases:**

BIM can access the impedance changes caused by pathophysiological processes in blood vessels. Therefore it has become a promising technique for the diagnosis of several vascular disorders and diseases, such as stenosis, thrombosis [169], atherosclerosis, wall swelling (aneurysm), and occlusion [170]. These cases could cause the changes in mechanical properties of the arterial or venous wall, which were represented as different Young's modulus, shapes and dimensions of tissues in the simulations.

- **Tracking blood flow:**

Monamed and his group [171] tried to represent the heart pulsations in 2D FEA by applying blood pressure inside the artery. However, the pressure changes did not show any influences on the impedance signals in COMSOL Multiphysics® 5.0 (COMSOL Inc). They suggested a more feasible approach would be to change the arterial diameters rather than applying blood pressure in the artery. The blood flow was reflected as the changes in blood volume (arterial diameter) by Anand et al. [172]. The negative correlation between arterial diameter and measured impedance was observed and further validated using a multi-tissues forearm phantom [173].

- **Sensitivity of signals:**

BIM as a non-invasive sensing technique is highly sensitive to noise, which might cause unreliable acquired signals. Therefore, it is worth searching for the best sensors setup for high quality signals. FEA can provide a visual approach to plot the electrical information, such as the current density. Thereby, a 3D upper arm model was structured to optimize the signal acquisition of BIM by Shuvo and Islam [174]. In this study, the sensitivity (S)

of tetrapolar BIM (four electrodes under linear conditions) was expressed as the following equation:

$$S = \frac{J_1 \cdot J_2}{I^2} \qquad \textit{Equation 8}$$

where J_1 was the current density between CC electrodes when a current I was injected, and J_2 was the current density between two PU electrodes when the same current was applied. In their research, the distance between each electrode was set up as 50 mm. A positive linear correlation was observed between the dimension of electrodes and the integrated sensitivity. Moreover, they indicated that the maximum average sensitivity was approximately at a depth of 15 mm (one-third of the electrode spacing) for the homogenous mediums and 25 mm (half of the electrode spacing) for the heterogenous mediums. Later, a more realistic 3D forearm model was developed with six different configurations of tetrapolar sensors by Pesti et al. [175]. The results indicated most of the measurement sensitivity was concentrated in regions close to the surface of forearm and the radial artery was located near the surface in the positive sensitivity region.

Table 3. Computational simulations of BIM

Reference	Tissue domains	Software	Excitation value	Frequency	Research objectives
Anand, Lowe, and Al-Jumaily 2016 [172]	fat, muscle, blood	ANSYS HFSS	1mA	1 kHz to 2 MHz	Simulated the electrical response of a section of the human forearm and obtain the values of impedance over a wide frequency range
Mohamed, El Dosoky, and El-Wakad 2017 [171]	skin, fat, muscle, blood	COMSOL Multiphysics	1mA	1 kHz to 2 MHz	Studied the effect of the heart pulsatile on the measurements of artery bioimpedance
Shash, Eldosoky, and Elwakad 2018 [170]	skin, fat, muscle, bone and blood vessel	COMSOL Multiphysics	1mA	50 kHz, 100 MHz, 1 GHz	Investigated the effects of vascular diseases on vessel impedance
Shuvo and Islam 2016 [174]	skin, fat, muscle, cortical bone, bone marrow	COMSOL Multiphysics	1A	100 kHz	Investigated the sensitivity distributions in a tetrapolar measurement system
Pesti, Koiv, and Min 2019 [175]	skin, fat, muscle, tendons, cortical bone, bone marrow, blood vessels and blood	COMSOL Multiphysics	1V	10 kHz	Described the spatial sensitivity field for four electrodes placed on the radial artery.

2.4 Mathematical models: the relationship between blood pressure and pulse wave propagation

In Chapter 1, Equation 6 demonstrates the positive correlation between BP and PWV, providing the initial theoretical basis that has driven the subsequent research on estimating BP via pulse wave propagation. However, it does not consider the actual structures of the arterial system, such as branches, tapers, and microcirculation. Furthermore, it was challenging to model the arterial blood flow due to difficulties in describing the individual variations of arterial geometry, the nonlinear wall viscoelasticity, and non-Newtonian rheological properties of blood [176].

This section will introduce various algorithmic models that have been proposed to estimate BP values (i.e., SBP, DBP, MBP, and instantaneous BP) from the pulse wave propagation (i.e., PWV, PTT or PAT). According to the components of formulas, the mathematical models were classified into three categories: pulse wave propagation-only models (see Table 4), augmented components models (see Table 5) and machine learning-based models (see section 2.4.3). Almost all listed models used the ECG-PPG system and contained subjects' coefficients which could be obtained from regression analysis using reference blood pressure measurement (RBPM). The procedure to obtain regression coefficients was called the initial calibration. The accuracy of the initial calibration by reference sphygmomanometers normally determined the accuracy (e.g., bias and variance) of the final BP estimation. Even though the calibration procedure to obtain regression coefficients was a conventional machine learning method, it was not considered a machine learning-based model in this thesis. The relative performance of these mathematical models will be further analysed and discussed combined with clinical protocols in Section 2.5.

2.4.1 Pulse wave propagation-only models

In this section, five types of basic models will be introduced, which only contain PWV/PTT/PAT. Model numbers refer to those shown in Table 4.

- **Proportional model**

The most straightforward algorithm is the proportional model (Model 1), which obtained subjects' parameters A and B from linear regression analysis between measured PWV/PTT/PAT and corresponding reference BP values. For instance, the PWV-based proportional model was investigated during the post-exercise recovery time after indoor

cycling by Marcinkevics et al. [177]. This study verified the reasonable applicability of the proportional model in a higher SBP range after exercise (from around 110 to 150 mmHg). However, one-time calibration might be insufficient. The repeatability of the proportional model was investigated by Wong et al. [115]. The repeatability tests were carried out half a year after the first experiment for 14 normotensive subjects. They found that the SBP showed a higher correlation with PTT, but a new calibration procedure was required after six months for a reliable estimation. Additionally, another work observed that the shorter period of recalibration could increase the accuracy of estimated BP [98]. In order to improve the recalibration performance, they employed a "multi-innovation recursive least square algorithm" to update the subject-dependent parameters and showed a significant improvement in accuracy.

- **Inverse model**

The inverse model (Model 2) is the simplest expression of the reciprocal relationship between PTT and BP. The wider application range of the inverse model was verified during increasing stress exercise, which indicated its potentiality for clinical applications [112].

- **Inverse squared model**

The basic inverse squared model (Model 3) was proposed by expressing the pulse wave as the sum of the kinetic energy of the wave and the gravitational potential energy [102]. Here, the arterial BP was equal to the total BP change divided by 0.7 (considering approximately 70% of the total pressure in the body is dropped in the arteries). Their preliminary results suggested the capacity of this model to capture both hypotension and hypertension conditions. However, this model did not perform better than the inverse model in a recent evaluation study [178]. Another empirical non-linear model (Model 4) was proposed and compared to the simple proportional model based on the same set of data by Wibmer et al. [52]. The results showed its more effective estimation than the proportional model.

- **Logarithmic model**

The logarithmic model was another typical non-linear algorithm to estimate BP via pulse wave propagation. Based on Bramwell-Hills and Moens-Kortweg's formula, a logarithmic relationship can be obtained, and if the physical properties of the artery were

constant for one subject, the simplified relationship between BP and PTT could be expressed as Model 5 [114]. One drawback was that the correlation coefficient between $ln(PTT)$ and BP decreased with increasing number of heart beats, suggesting that the subjects' coefficients were changing at a relatively fast rate.

- **Exponential model**

An ordinary differential equation (Model 6) based on fundamental physics and physiology expressing the relationship between BP, Young's modulus and PWV was proposed by Chen et al. [97] In this model, the age-/gender-dependent factors were combined in coefficients *b* and *k*. They used a benchmark model to calibrate the *b* and *k* for different age and gender groups. Once the parameters were obtained, this model would be reliable for this whole group to avoid the recalibration for individuals. However, the accuracy of this method relied on the number of calibration subjects which means a large amount of clinical data is required for each group.

Table 4. Pulse wave propagation-only models.

Algorithm	Model number	Formula	Coefficients	Measured index	Reference
Proportional model	Model 1	$BP = A \cdot PTT + B$ $BP = A \cdot PAT + B$	A and B: subjects' coefficients	PTT/PAT	[42], [50], [88], [95], [96], [98], [115], [130], [131], [140], [148], [162], [179], [101]
		$BP = A \cdot PWV + B$		PWV	[88], [145], [177], [180]
Inverse model	Model 2	$BP = \frac{A}{PTT} + B$		PTT	[99], [100], [112], [133], [137], [141], [181], [182]
Inverse squared model	Model 3	$BP = \frac{\Delta BP}{0.7} = \frac{\frac{1}{2}\rho\frac{d^2}{PTT^2} + \rho gh}{0.7} = \frac{A}{PTT^2} + B$	d: the blood flow distance, g: gravitational acceleration, h: the height between two measured sites, ρ: blood density, $A = (0.6 \times height)^2 \times \frac{\rho}{1.4}$, B: subjects' coefficient	PTT	[99], [102]
	Model 4	$BP = a + (\frac{b}{PTT - c})^2$	a, b and c: subjects' coefficients	PTT	[52]
Logarithmic model	Model 5	$BP = A \cdot ln(PTT) + B$	A and B: subjects' coefficients	PTT	[99], [103], [114], [129]
Exponent model	Model 6	$p = be^{-\frac{k}{PWV}}$	b, k: subjects' coefficients depend on age and gender	PWV	[97]

2.4.2 Augmented components

During the investigation of PWPM, more and more researchers realised that the simple models with only PWV/PTT/PAT might not be adequate to accurately estimate BP. In this section, numbers of other components augmented in the basic models will be introduced. Model numbers refer to those shown in Table 5.

- **Subject features**

Several studies tried to improve the accuracy and practicability of the proportional model by adding other parameters associated with BP. For example, two characteristic physical parameters (e.g., height and arm length of different subjects) were added into the proportional model by Park et al. [101]. Moreover, HR was taken into account for developing the model because HR was one of the factors that could also correlate with BP (Model 7) [111]. The adaptive kalman filter (AKF) algorithm and maximum-likelihood estimation (MLE) methods were applied to obtain the subjects' coefficients in their calibration procedure. They found that the AKF could decrease the frequency of recalibration significantly.

Recently, the height and a body correlation factor were combined with the PWV-based logarithmic model proposed by Dong et al. [117]. As they reported, this model (Model 8) was robust enough to consistently estimate both SBP and DBP within grade A of the BHS protocol. Additionally, there was only a one-time calibration procedure for each individual. However, they only recruited healthy subjects and did not report the duration of such accuracy.

- **PPG features**

A multiple linear regression combined with the foot to peak amplitude of rising edge of the PPG waveform (Model 9) was proposed by Chua and Heneghan [107]. The performance of estimated BP showed better results than using PAT-only model, whereas this model still had several drawbacks: 1) It was not sensitive enough to detect short-term BP changes within 30 seconds; 2) individual calibration and intermittent recalibration was required; 3) separate calibration for different positions was also required.

A novel indicator named the photoplethysmogram intensity ratio (PIR) was proposed to evaluate the arterial diameter change [183]. Subsequently, this research group suggested DBP was related to PIR, and SBP corresponded to the PTT (Model 10). Their estimated SBP and DBP showed higher accuracy than other studies [109]. A recent article applied the multi-adaptive regression spline (MARS) method based on the PIR model to achieve longer-time reliable BP estimations [184]. They indicated that the effective parameters (PTT and PIR) could represent the strong effects of the last state of the cardiopulmonary system on BP values.

- **Basal conditions**

Model 11 was proposed by simplifying the well-known Bramwell-Hills and Moens-Kortweg's formula (i.e., equation 6) in 2000 [106]. Besides the pulse wave propagation (i.e., PAT change), this research intermittently calibrated the estimation using the low-frequency component (basal SBP) measured by a standard sphygmomanometer, achieving a high correlation between estimated SBP and invasive BP method. However, the accuracy of BP estimations highly relied on the re-calibration interval, inducing inconveniences for long-time monitoring.

In order to reduce the inconvenience of interval calibration, Model 12 was presented as a combination function consisting of an exponential term, a second non-linear term, and a one-point correction constant [23]. The one-point correction constant was the difference between estimated BP and reference BP, aiming to offset the individual BP-PWV relation. Nevertheless, the differences in estimated SBP from reference values were up to 20 mmHg.

It is worth clarifying that equation 5 described the exponential relationship between Young's modulus of the arterial wall and MBP. Based on the assumption that the MBP is approximately the sum of a third of SBP and two-thirds of DBP, Poon and Zhang [12] estimated SBP and DBP based on the logarithmic relationship between MBP and PTT with an initial calibration of SBP and DBP (Model 13). Some studies also specified $A = \frac{2}{\gamma}$ [108], [116]. An overnight investigation of 10 healthy young subjects was carried out by Zheng et al. [116]. Their results showed no consistent correlations between estimated BP values and the RBPM during the daytime while obtaining a better negative correlation during night time. They explained two main factors that influenced the relationship between PTT and BP: 1)

the vascular tone caused by daytime activities, and 2) the physiological status such as stress and emotion. Lately, the impact of heart disease on the accuracy of Model 13 was investigated by Ding et al. [108], observing a more accurate DBP estimation in patients, whereas lower effectiveness of overall SBP estimation since the predicted SBP was derived from DBP and pulse pressure (PP). As a result, they suggested more relevant parameters should be added into the model to suit a wider range of the population.

- **PTT variability**

Ma [100] indexed the variation and variability of PTT (the definition of VPTT and PTTV was shown in Table 5) as the indication of neural control and integrated this with the original inverse model to obtain Model 14, providing a better estimation, especially for DBP. This improvement demonstrated neural control as one crucial BP regulation mechanism and should be considered in future research.

- **Blood volume/ arterial diameter**

As introduced in Chapter 1, blood volume change also showed a strong relationship with BP change. As early in 2000, Heard and his colleagues [110] achieved accurate estimation in DBP and MBP by using Model 15 and ECG-PPG system "DxTek monitor" (DxTek, Inc., Chestnut Hill, MA). Besides adding HR component, the parameter C_{dx} was related to both PAT and $\frac{\Delta V}{V}$. Lately, this model was also applied to a "smart vest" for wearable monitoring by Pandian et al. [113].

Arterial diameter change could represent the blood volume change. A novel ultrasound-PPG bi-modal probe was designed for real-time evaluation of carotid SBP and DBP by Pm et al. [160]. The arterial diameter related components could be directly determined by ultrasound measurement. Different from other models, their Model 16 did not contain any subjects' coefficient, while still requiring an initial BP calibration.

For a specific segment, if PWV was assumed as a relative constant within a cardiac cycle, the pressure can be expressed in terms of local PWV and the cross-sectional area [185]. Huynh and his group [154] presented the cross-sectional area using the variation of magnitude impedance, as shown in Model 17. Their proposed method appeared to offer

superiority compared to PTT-only approaches, proving that the arterial impedance signal was an adequate indicator to estimate BP.

- **Hybrid selective PWV and PWA**

As introduced in the techniques section (2.2), different studies had inconsistent opinions of the superior characteristic point to determine the pulse wave propagation information. The correlation between measured time-based pulse wave propagation and BP might depend on individuals and employed equipment. One recent research sifted the best PWV value from the six channels of flexible polyaniline sensors according to their signal-to-noise ratio, avoiding the errors caused by poor signal qualities [186]. Moreover, they complemented nine other time-based parameters based on the fiducial points from the pulse wave signal and pulse wave analysis (PWA), such as the systolic peak, diastolic peak, and dicrotic notch, the second derivative maximum point, and valley point or systolic notch. The hybrid selective PWV and PWA model (Model 18) showed relatively higher accuracy than the single PWV model, providing a potential solution to improve the reliability of PWPM.

Table 5. Augmented components models

Augmented components	Model number	Formula	Coefficients	Measured index	Reference
Subject features	Model 7	$BP = A \cdot PTT + B + C \cdot HR$	A, B and C: subjects' coefficients	PTT, HR	[111]
	Model 8	$BP = \beta_1 \ln\left(\frac{Hf}{PTT}\right) + \beta_2$	H: height of subjects, f= 0.5, body correlation factor for adults to detect their peripheral pulse wave by fingers, β_1 and β_2: subjects' coefficients	PTT/PAT	[117]
PPG features	Model 9	$BP(i) = b_0 + b_1 PPG(i) + b_2 PAT(i) + b_3 PPG(i-1) + b_4 PAT(i-1)$	i: indicated beat-by-beat samples, PPG: the foot to peak amplitude of rising edge of the PPG wave, b_0, b_1, b_2, b_3 and b_4 : subjects' coefficients	PAT, PPG amplitude	[107]
	Model 10	$DBP = DBP_0 \cdot \frac{PIR_0}{PIR}$ $SBP = DBP_0 \cdot \frac{PIR_0}{PIR} + PP_0 \cdot (\frac{PTT_0}{PTT})^2$ $PIR = \frac{I_H}{I_L} = e^{\alpha \Delta d}$	I_H: peak intensity of PPG signal, I_L: valley intensity of PPG signal, α: a constant related to the optical absorption coefficients in the light path, The parameters with "0": the initial calibration values by reference BP sphygmomanometer, Δd: diameter changes of the artery	PTT, PIR, Calibrated BP	[109], [184]
Basal conditions	Model 11	$P_e = P_b + \Delta P = P_b - \frac{2}{\gamma \cdot PAT_b} \cdot \Delta PAT$	P_b: the base SBP level, PAT_b: the time delay corresponding to P_b γ: range from 0.016 to 0.018/mmHg	PTT, Base BP	[106]
	Model 12	$BP_{ptt} = P1 \times PWV \times e^{P3 \times PWV} + P2 \times PWV^{P4} - (BP_{ptt,cal} - BP_{cal})$	P1 to P4: subjects' coefficients, $BP_{ptt,cal}$: the calculated BP from PTT corresponding to the BP measured by the reference method, BP_{cal}: initial calibrated BP using the reference BPM.	PWV, Calibrated BP	[23], [187]
	Model 13	$DBP = \frac{SBP_o}{3} + \frac{2DBP_o}{3} + A\ln\left(\frac{PTT_o}{PTT}\right) - \frac{SBP_o - DBP_o}{3}\frac{PTT_o^2}{PTT^2}$ $SBP = DBP + (SBP_o - DBP_o)\frac{PTT_o^2}{PTT^2}$	A: subjects' coefficient, parameters with "o": initial calibration with reference BP measurements,	PTT	[12], [108], [116], [188]

PTT variability and variation	Model 14	$BP = \frac{A}{PTT} + B + C \cdot VPTT + D \cdot (PTTV - PTTV_0)$ $PTTV = \sqrt{\frac{\sum_{i=1}^{N}(\Delta PTT_i - mean(\Delta PTT))^2}{N-1}}$ $VPTT = \frac{PTT - PTT_0}{PTT_0}$	A, B, C and D: subjects' coefficients ΔPTT: the difference between any two continuous PTTs, The parameters with "0": the initially calibrated values in sitting postures, N: the number of PTT used for variability calculation $PTTV$: PTT variability during the signal recording, $VPTT$: the PTT variation at the measurement time.	PTT, VPTT, PTTV	[100]
Blood volume change	Model 15	$SBP_i = k_s(C_{dx})_i^2 + a$ $DBP_i = k_d(C_{dx})_i^2 + k_{IHR}IHR_i + b$	IHR: the instantaneous heart rate, i: the number of pulses, k_s, k_d, k_{IHR}: fixed constants, a and b: subjects' coefficients C_{dx}: related to both PWV and blood volume changes	PWV, Wave shape, HR	[110], [113]
	Model 16	$P_D = \frac{2\rho C_D^2}{\beta}$ $P_S = P_D e^{\beta\left(\frac{\Delta D}{D_D}\right)}$ $\beta = \frac{\ln\left(\frac{P}{P_D}\right)}{\left(\frac{D-D_D}{D_D}\right)}$	P_D: end-diastolic pressure corresponding to the diameter D_D, P_S: systolic-peak pressure, P: arterial pressure corresponding to lumen diameter D, ρ: density of blood, C_D: local PWV measured from the diastolic point, β: stiffness index ΔD: distension of arterial diameter	PWV, arterial diameters	[160]
	Model 17	$p(t) = p_0 + \rho\frac{D^2}{PTT^2}ln[1 + K(Z_0 - Z(t))]$	p_0: base BP corresponding to Z_0, ρ: density of blood, D:distance between two sites, K: constant, Z_0: impedance of the body segment, $Z(t)$: measured impedance	PTT, impedance	[154]
Pulse wave analysis	Model 18	$BP = k_a + k_b \cdot sPWV + k_c \cdot sPWA$	k_a, k_b and k_c: subject-specific multi regression model parameters, $sPWV$: selective PWV from six single local-PWV, $sPWA$: selective time-based pulse wave analysis parameters, including systolic peak, diastolic peak, dicrotic notch, second derivative maximum point, and valley point or systolic notch.	PWV and other time-based features	[186]

2.4.3 Models based on machine learning

Recently, with the significant advance in artificial intelligence, machine learning has been widely applied for data processing in many fields [189]. Machine learning was pioneered by Arthur Samuel in 1959 [190]. The primary process of machine learning can be briefly described as that the programmed algorithm can automatically help the system to gather and learn data for prediction or classification. This learning process is called data training [191]. Typically, the machine learning approach has two main steps: a learning group with large numbers of subjects to train the system and a test group with a small number of subjects to verify the proposed method. With the help of existing machine learning algorithms, some studies achieved highly accurate BP estimation and even meet the requirements of ANSI/AAMI/ISO and BHS standards.

There is evidence that machine learning -based models performed more effectively than traditional mathematical models for some problems. Jung Yi Kimet al. [192] compared artificial neural network (ANN) with multiple linear regression and multiple non-linear regression methods, and the results indicated the better performance of the ANN method for SBP estimation. With the help of the ANN method, both SBP and DBP were estimated accurately from 21 time-scale PPG features without PTT information [193]. Additionally, one following study replaced the ANN with support vector regression (SVR) and added 14 new features from the second derivative of the PPG signal [194]. They reported that the BP estimation could be improved by 40%. Moreover, the AdaBoost regression model was used to estimate SBP and DBP in a BIM local-PWPM [159]. Its correlation coefficient, mean absolute error and SD reached 0.94, 2.57, 4.35 mmHg for SBP and 0.92, 1.71 and 2.46 mmHg for DBP, respectively. Furthermore, multi-machine learning models “genetic algorithm-mean impact value-support vector regression” (GA-MIV-SVR) were built and achieved impressive accuracy [195]. In their work, the GA-MIV-SVR method included: 1) GA was used to optimize the parameters; 2) MIV method was utilized to verify the validity of the potential features and remove redundant features; 3) SVR was applied to construct the BP estimation models. Another recent work applied two double-layer multilayer perceptron ANN to estimate BP values; in the meantime, they used the moving backward algorithm and genetic algorithm to sift the optimum set of features out of 34 potential features from signals [157]. Another recent study achieved a high accuracy of BP estimation (86.3%) by using a

deep convolutional neural network without employing any features from waveforms [196]. Other machine learning algorithms for regression tasks have been compared by Kachuee et al. [197], such as decision tree regression and random forest regression. As the focus of this thesis is not on machine learning, readers who want to understand more details about machine learning-based modelling, are referred to other recent review articles for continuous non-invasive BPM [156, 157].

2.4.4 Comparison studies between models

In order to identify the more reliable mathematical models, several articles have carried out comparisons. A comparison study investigated Model 1 and Model 4 based on the same set of data in human subjects [52]. They pointed out that the major limitation of the proportional model was that negative PTT values would be present when BP increased and vice versa. This conflicted with reality. Although the non-linear model showed higher efficiency in estimating BP in their experiments, they thought the linear model could be considered an alternative option in some typical cases. Another paper with a similar opinion believed that the proportional model has the best applicability and the most straightforward operation for coarse BP trend indications [179]. Furthermore, a research group applied three models (Models 2, 3 and 5) with three healthy subjects [99]. They found that these models appeared to differ from person to person and trial to trial. Even though these models could provide insights into the present health status of the individual, the experimental errors exposed that the BP system is more complicated than a simple linear model. They advised that further optimization of BP calculation was required.

A meta-analysis of the proportional model was carried out from 2005 to 2017 [199]. They released several limitations that appeared in previous papers: 1) The non-uniform approach to determine the characteristic points for PAT/PTT/PWV; 2) Some simplifications of blood flow theory were unreliable such as the omission of the effects of surrounding tissues; 3) The high correlation always appeared in slight variations of BP cases; 4) This method might only suit SBP estimation, not DBP because of different PTT-SBP and PTT-DBP relations. A previous review article [10] compared models 1, 2, 3, and 5 using a Physionet online database [200] as a source for the ECG, PPG and arterial BP. The database contains time-stamped nurse-verified physiological readings of patients in the intensive care unit at Boston's Beth

Israel Deaconess Medical Centre (BIDMC) from 2001 to 2008. They found that the model that included HR showed higher accuracy for BP estimation.

2.4.5 Promising methods to improve accuracy

After further comparison, it was proved that the significant contribution of mathematical models to the whole estimation. Even though the simplest proportion relationship (model 1) and inverse relationship (model 5) were able to estimate BP in a few cases, overall, they were not reliable. Therefore, several key elements that constitute a promising model are desired to be indicated.

The overriding criterion of a mathematical model is that its upper and lower limits should be within a reasonable range. For instance, model 13 was a bounded formula with a limited range and always maintained positive. This standard could ensure that the estimated BP corresponds to the actual BP conditions mathematically.

Several studies have shown that a primary method to improve accuracy is to combine other relevant parameters into a simple model. One successful study integrated PTTV and VPPT with model 5 to express the effects of neural control, which is one important BP regulation mechanism [100]. After adding these two parameters, the mean estimation error reduced to -0.2 ± 2.4 mmHg and -0.5 ± 3.9 mmHg from 0.1 ± 2.5 mmHg and 1.3 ± 7.4 mmHg for the SBP and DBP, respectively. Moreover, the correlation coefficient for SBP estimation increased slightly to 0.9607 ($P < 0.001$) from 0.9573 ($P < 0.001$), more significantly, the new model appeared higher improvement for DBP estimation, from 0.27 ($P < 0.01$) to 0.71 ($P < 0.001$). Furthermore, one recent study indicated the positive effect of adding HR [10]. Similarly, another research suggested that both current HR and the average values should be considered in the algorithm to increase the efficiency of BP indirect estimation [201].

Additionally, the PPG waveform could provide more information besides a time reference of PTT:

- Amplitude information: PPG amplitude as a sympathetic marker was considered a component of BP estimation by Chua and Heneghan [107]. They found using a combination model of PAT and PPG amplitude could obtain better BP estimation than using only one of them, especially in the supine position. PPG amplitude showed a

negative linear relationship with BP, which was considered a more robust measurement than PAT. Analogously, PIR was also used to evaluate the modulation of sympathetic nervous activity on BP [109]. Their proposed model (model 15) performed better than the other two algorithms (models 4 and 11) for about 2 mmHg in SD and MAD.

- Horizontal information: time-scale parameters can be extracted from the PPG waveform, such as cardiac period, systolic upstroke time and diastolic time [193]. Recently, seven hemodynamic features were taken into consideration to improve the performance of model 7 [202]. After evaluating correlations of those features to BP, they indicated four covariates were based on their clinical and biological plausibility besides PTT and HR. Specifically, for healthy subjects, stiffness index was applied to SBP estimation, which was determined as the time interval between an early systolic peak and a later diastolic peak of the PPG signal [203], and the descent time from diastolic peak to the end of diastole was utilized to estimate DBP [204]. For subjects with cardiovascular diseases, the rise time from the nadir to the systolic peak of the PPG waveform was selected to improve SBP estimation, which is associated with left ventricular function [205], and the total peripheral resistance was used to optimize DBP estimation [206]. This method could not only increase accuracy but also decrease the re-calibration frequency.
- Features based on the amplitude and time can also be obtained from the second derivative of the PPG signal [194]. A recent work extracted totally 34 potential features from the measured signals and determined several important features for BP estimation, including the weight, age and gender of subjects, the crest time, slop, and the ratio of diastolic amplitude to systolic amplitude of PPG waveform, and the information from acceleration plethysmographs (APG).

The primary purpose of adding other meaningful parameters was to offset the low-frequency influences, which cannot be tracked by pulse wave propagation. The rhythmic oscillations of BP can be identified with the appearance in its spectrum as individual peaks, which reflect: 1) High frequency: the oscillation frequency is normally between 0.2 and 0.35 Hz, which is similar to that of respiratory activity; 2) Low frequency: oscillations with a frequency approximately from 0.1 to 0.15 Hz are associated with vasomotion waves caused by an oscillation of the sympathetic vasomotor tone. The mechanisms of the fluctuation of BP with respiration can be explained as the intrathoracic pressure change with breathing which has a mechanical impact on venous return, pulmonary vascular, and aortic pressure, therefore,

causing the oscillations of BP [207]. Early research evidenced the low-frequency component of BP variation caused by local changes in smooth muscle constriction and dilation through the modulation of the sympathetic nervous activity [208]. The small variation in peripheral arterial diameter caused by smooth muscle represents a large change in the arterial cross-sectional area and produces a large impact on the resistance of blood flow [209]. Therefore, the diameter change of the artery is one component that can reflect the low-frequency effects on BP. Moreover, the similarity between pressure waveform and diameter waveform has been demonstrated [87]. Recently, the arterial diameter variation was directly measured using ultrasound [160] and indirectly expressed as magnitude impedance [154] or PPG intensity ratio [109].

The BP estimation also depends on the calibration procedure. The long-term accuracy always requires frequent calibration (recalibration) [106], [115]. A novel multi-point calibration procedure was presented that accounted for the effects of the sympathetic nervous system (SNS) on the BP-PTT relationship [188]. This procedure selected the most appropriate point from a cluster of several calibration points by identifying the similarity of the state of SNS between the new measurement and each calibration point based on heart rate, respiratory rate (RR), and PTT itself. This proposed method could improve precision over 4 weeks without recalibration. However, the most effective calibration approach might be machine learning-based calibration. An earlier research group utilized the MLE and AKF methods to reduce the number of calibration processes and achieved very high correlation coefficients (over 0.97) and low SD (within 5 mmHg) for BP estimation via model 2 [111]. Additionally, the basic inverse model (model 5) could achieve higher correlative coefficients for both SBP and DBP by adaptively trained using the Ordinary Least Squares [182] or Gradient Descent optimization algorithm [181].

2.5 Clinical protocols

2.5.1 Summary of previous studies

The evaluation of the actual performance of a new BPM depends on many factors rather than its techniques and mathematical models. The most convincing approach to appraising the accuracy of a BPM device is the clinical validation. Unlike theoretical models and computational simulations, clinical validation can provide results without too many

assumptions. Therefore, it is necessary to consider clinical validation protocols. Generally, researchers were more inclined to evaluate their results according to ANSI/AAMI/ISO, BHS and ESH protocols. These criteria provide the most authoritative approach to methodological–statistical, and practical–clinical issues, such as the minimum number of the subjects, the type of reference sphygmomanometer, number of observers, validation process, etc. Even though these standards have similarities in the main concept and procedure, their methodology details are different. This non-uniform situation might confuse researchers and consequently cause omnifarious clinical protocols. Moreover, there is not mandatory for manufacturers or researchers to follow a specific standard or validation process to assess the accuracy of the proposed BPM. Many published articles, therefore, deviated from these protocols. As a result, their conclusion might be questionable and unjustified.

This chapter attempted to summarize the detailed clinical protocols/ validation process of previous studies comprehensively to provide a more objective evaluation. Table 6 organized the original details of clinical protocols carried out in previous studies, while several articles were not included acquired the clinical data via the Multiparameter Intelligent Monitoring in Intensive Care (MIMIC) online databases [210]. In this table, several articles did not describe clearly the specific model of reference sphygmomanometers, which thus were filled with the general word “cuff-based”. In this table, numbers linked by “-” presented the range of parameters, and numbers lined by “±” presented the means ± standard deviation (SD) of the data, BP range marked with “*” was the approximate value estimated from the charts/figures in articles.

Table 6. Clinical protocols of previous studies

Studies	Participant information						Measurement method				Accuracy[1] (Statistical analysis)
	N[2]	Sex	Age[3]	Healthy conditions	Measured condition	BPR[4] SBP / DBP	Techniques	Measured index	Model	RBPM[5]	
[106]	14 6	M[6] F[7]	48 ± 22	patients	During cardiovascular surgery	75-175* / -	ECG-PPG	PAT, base BP	11	invasive	SBP: R = 0.97±0.02 RMSE = 3.70±1.85 Mean±SD = 0.06±0.68
[192]	45	M	22-32	healthy	-	91.5-131 / -	ECG-PPG	PTT, 7 biometric parameters	ML	oscillometry (BM3 Patient Monitoring)	Multiple linear regression: Mean±SD = 6.31±3.89 (SBP) Multiple non-linear regression: Mean±SD = 5.67±3.71 (SBP) Artificial neural network: Mean±SD = 4.53±2.68 (SBP)
[12]	36 49	M F	57±29	Healthy (37) Hypertensive (39) Congestive heart failure (9)	Three trails: first day; once each week for 2 weeks; after 1 month	122±21 / 63±9	ECG-PPG	PTT	13	mercury, oscillometry (Colin BP-8800, Japan and Omron HEM-907, Japan)	Mean±SD = 0.60±9.80 (SBP), 0.90±5.60 (DBP)

[1] **RE**: Relative error; **MAD** (mmHg): mean absolute difference / mean absolute errors / mean estimation errors between estimated BP values and reference BP values; **SD** (mmHg): standard deviation; **Mean ± SD** (mmHg): mean ± standard deviation for estimated BP values against reference BP values; **RMSEs** (mmHg): Root-mean-squared-errors between estimated BP and reference values; **R**: correlation coefficients between estimated BP values and reference BP values; $\mathbf{r}^*$: correlation coefficients between *changes* of PAT/PTT and *changes* of reference BP values; **r**: correlation coefficients between measured parameters (e.g. PWV, PAT, PTT, etc.) and reference BP values; $\mathbf{r^2}$: correlation coefficients between the PAT/PTT and reference BP values; $\mathbf{R^2}$ (Mean±SD): coefficients of determinations between PTT and reference BP values.

[2] N, numbers of subjects

[3] Values are mean±SD

[4] BPR, blood pressure range, values are mean±SD (minimum-maximum) (mmHg), the data marked with * is the approximate value estimated from the chart in the article

[5] RBP, reference blood pressure measurement

[6] M, male

[7] F, female

			Diabetes mellitus (13)								
[101]	Model study with PTT only									oscillometry (Bionet Co. BM3 Patient Monitoring)	
	10 M	25-28	healthy	Relax for 10 minutes; Run up and down stairs	-	-	ECG-PPG	PTT	1		Mean±SD = 9.49±6.03 (SBP)
	Model study with valid physical parameters										
	45 M	22-32	healthy	Relax for 10 minutes	113.371 ± 8.024	-	ECG-PPG	PTT, several physical characteristic parameters			Mean±SD = 5.81±4.16 (SBP)
[107]	7 M	29±4	healthy	Paced and spontaneous breathing in the and standing position	110-145*	-	ECG-PPG	PAT, PPG amplitude	9	Portapres (Finapres)	R = 0.59±0.16 (SBP), 0.59±0.18 (DBP) Mean±SD = 0.70±5.90 (SBP), 0.30±3.60 (DBP)
[113]	25 M	21-60	healthy	Standing	102-128*	58-87*	ECG-PPG	PWV, HR	15	oscillometry (Lloyds Pharmacy Ltd. Model KD 525)	Mean±SD = -0.46±8.00 (SBP), -0.57±6.00 (DBP)
				Walking for 30 minutes	103-129*	61-87*					Mean±SD = -0.56±10.00 (SBP), -0.29±8.00 (DBP)
[97]	5 M	17-23	patients	Undergoing surgical operations	-	42-125	ECG-PPG	PWV	6	invasive and cuff-based	DBP: Mean±SD = 1.40±7.50
	7 M	56-64									
	5 F	18-24									
	6 F	56-65									
[177]	10 M 10 F	19-21	healthy	Seated comfortably from 1 minute after a graded bicycle exercise to baseline at 23 to 25 ℃	110-150*	-	PPG/SFG-ECG	PWV	1	oscillometry (UA-767 Plus, A&D Instruments LTD®)	PPG method r = 0.86±0.11 (SBP), 0.81±0.10 (MBP) SFG method r = 0.85±0.09 (SBP), 0.82±0.07 (MBP)
[115]	22 M		healthy	Pre-exercise:	First test Pre-exercise		ECG-PPG	PTT	1		r = -0.92 (SBP), -0.38 (DBP)

	19 F	25±4		3-min rest Post-exercise: Running at 10km/h for 3-min, 8km/h for 3-min Recovery: 15,20,25,40 min after exercise	103.9±9.6	59.8±8.9				oscillometry (Model HEM-907, OMRON, Japan)	Mean±SD = 0.00±4.00 (SBP), 0.00±3.50 (DBP)
	6 M				After half year Pre-exercise						Re-fitted r = -0.87 (SBP), -0.30 (DBP) Mean±SD = 0.00±5.30 (SBP), 0.00±2.9 (DBP)
	8 F	26±4			103.0±11.3	59.3±8.1					Use old regression coefficients Mean±SD = 1.40±10.20 (SBP), 2.10±7.30 (DBP)
[103]	14 M 6 F	28.8±8.4	healthy	At rest; during exercises (25W, 45W, 65W) on an ergometer for 6 minutes; 5 minutes recovery	increment: 30±13(25w) 39±20(45W) 54±30(65W)	-	ECG-PPG; Two-PPG	PAT/PTT	5	Portapres (Finapres)	SBP: r = -0.84±0.09 (PAT), 0.85±0.09 (PAT ln), - 0.19±0.45 (PTT), 0.22±0.46 (PTT ln)
[112]	19 M 14 F	39±12.5	healthy	Rest; 4 steps increasing stress cycling; 5 minutes after exercise	Rest (33): 121.4±17.6 (86-155) Exercise: normal (19) 120-139 (10) 140-159 (4)	76.7±10.5 (49-99) normal (19) 80-89 (10) 90-99 (4)	ECG-PPG	PTT	2	oscillometry (A&D UA-767; A&D Company, Ltd, Tokyo, Japan)	Mean±SD = -0.06±6.63 (SBP), - 0.25±5.63 (DBP) R = 0.89 (SBP), 0.78 (DBP)
[23]	Determine function 7 M 6 F Verify applicability 29 M 21 F	- - -	healthy	Undergo a physical examination on a bicycle ergometer	95-235*	-	ECG-PPG	PWV, initial BP	12	cuff-based	SBP: R = 0.75-0.99 SBP: R = 0.69-0.99 Mean±SD = 0.00±10.10
[111]	10 -	20-33	healthy	-	90-115*	50-75*	ECG-PPG	PTT, HR	7	oscillometry	AKF algorithm:

										(Microlife BP A100)	R = 0.98 (SBP), 0.99 (DBP) RMSEs = 1.69 (SBP), 1.04 (DBP) SD ≤ 5.00 (SBP, DBP) MLE algorithm: R = 0.98 (SBP), 0.97 (DBP) RMSEs = 1.80 (SBP), 1.57 (DBP) SD ≤ 5 (SBP, DBP)
[116]	10	-	27±3	healthy	Keep still for 24 hours of ambulatory monitoring	Overnight 80-145	-	ECG-PPG	PTT	13	oscillometry (Oscar 2, SunTech Medical®, US)	Night-time SBP: r = -0.62±0.21 Mean±SD = 2.80±8.20 RMSEs = 8.70
[100]	31	M, F	23-25	healthy	Refrain from coffee and alcohol for at least 2 hours at 24±2 ℃	87-133*	53-87*	ECG-PPG	PTT, PTTV, VPTT	2 and 14	oscillometry (OMRON HEM-7012, Japan)	Mean±SD = -0.20±2.40 (SBP), 0.50±3.90 (DBP)
[52]	14 6	M F	51± 18.4	patients	At rest; During an incremental cardiopulmonary exercise on a cycle ergometer; Recovery	Rest: 128±16 Exercise: 197±35 Recovery: 128±15	 88±11 92±14 83±13	ECG-PPG	PTT	1 and 4	oscillometry (Dinamap, ProCare 100, General Electric, Milwaukee, Wisconsin, USA)	Linear regression R^2 = 0.94±0.03 (SBP), 0.38±0.25 (DBP) Mean±SD = 0.00±6.73 (SBP) Non-linear regression R^2 = 0.95±0.03 (SBP), 0.46±0.21 (DBP) Mean±SD=0.00±5.56 (SBP)
[129]	10 5	M F	24±3	healthy	Standing still (60s), deep breathing (60s), resting (60s), sustained handgrip (60s), Resting (60s)	130.2±16.0	89.5±11.1	BCG-ECG	PTT/PAT	5	finger-cuff (ccNexfin, Edwards Lifesciences, Irvine, CA)	PTT Method: R = 0.84 (SBP), 0.79 (DBP), 0.83 (MBP) PAT Method: R = 0.75 (SBP), 0.59 (DBP), 0.69 (MBP)
[126]	30 49	M F	20-83	Healthy and hypertension	Meet the requirement of ISO 81060-2:2013			*ViSi Mobile System (ECG-PPG)*	PAT	ML	Oscillometry (GE DINAMAPTM CARESCAPETM V100)	Mean±SD = -4.20±8.70 (SBP), -3.80±5.80 (DBP)

[109]	14 M 13 F	25.6±2.1	healthy, non-smoker	Seated position	115.19±4.87	73.25±2.98	ECG-PPG	PTT, PIR, base BP	10	Finapres	Mean±SD = -0.37±5.21 (SBP), -0.08±4.06 (DBP) MAD = 4.09 (SBP), 3.18 (DBP)
[108]	21 M 16 F	27.4±10	healthy	Seated at rest (three trails: first trail, 2 weeks, one month after)	105.65±10.70	62.50±7.50	ECG-PPG	PTT, initial BP	13	mercury	Mean±SD = 0.50±11.55 (SBP), 1.19±9.07 (DBP)
	16 M 32 F	80.7±12	patients		134.03±17.28	63.00±9.55					Mean±SD = -3.6±16.02 (SBP), -1.06±7.92 (DBP)
[130]	19 M 3 F	25±3.5	healthy	Standing still (60s), mental arithmetic (60s), standing still (60s), cold pressor (60s), standing still (120s), stair climbing (60s) and recovery	increased about 30 mmHg	increased about 20 mmHg	BCG-PPG; ECG-PPG	PTT; PAT	1	finger-cuff (ccNexfin, Edwards Lifesciences, Irvine, CA, USA)	PTT method: r^2 = -0.80±0.04 (SBP), -0.80±0.02 (DBP) RMSEs = 11.8±1.6 (SBP), 7.6±0.5 (DBP) PAT method: r^2 = -0.66±0.04 (SBP), -0.60±0.04 (DBP) RMSEs = 18.50±1.80 (SBP), 14.60±1.50 (DBP)
[133]	24 M, F	21-50	healthy	Sit upright after with 3-min running at 8 km/h	106-197	51-93	PCG-PPG	PTT	2	oscillometry (Model M3, OMRON, Japan)	MAD=7.47 (SBP), 3.56 (DBP) R=0.84 (SBP), 0.86 (DBP) Mean±SD= 0.00±11.08 (SBP), 0.00±4.53 (DBP)
[181]	24 M 8 F	21-50	healthy	Sit upright after with 3-min running at 8km/h; Train group: 17 Test group: 15	106-197	51-93	PCG-PPG; ECG-PPG	PTT; PAT	2	oscillometry (Model M3, OMRON, Japan), mercury	PCG-PPG (PTT) method: Mean±SD = -0.28±9.44 (SBP), 1.03±5.15 (DBP) MAD = 6.22 (SBP), 3.97 (DBP) R = 0.89 (SBP), 0.84 (DBP) ECG-PPG (PAT) method: Mean±SD = 0.12±6.15 (SBP), 1.31±5.36 (DBP) MAD = 4.71 (SBP), 4.44 (DBP) R = 0.95 (SBP), 0.84 (DBP)

[117]	26	M, F	21-50	healthy	-	103-192	51-93	ECG-PPG, PCG-PPG, FSR	PAT/PTT, height	8	cuff-based	PTT method: R=0.93 (SBP), 0.87 (DBP) MAD±SD = 5.23±4.28 (SBP), 3.32±2.66 (DBP) PAT method: R = 0.95 (SBP), 0.87 (DBP) MAD±SD = 4.46±3.67 (SBP), 3.27±2.85 (DBP)
[88]	9 6	M F	30±5	healthy	Seated with the arm resting on a table; handgrip exercise	95-165*	50-110*	BIM	PWV	1	oscillometry (Oscar 2, SunTech Medical®, US)	Mean±SD = 0.01±8.10 (SBP), -0.06±5.46 (DBP) R = 0.81±0.08 (SBP), 0.84±0.07 (DBP) RMSEs = 7.48±2.15 (SBP), 5.17±1.81 (DBP)
[159]	3	-	-	healthy	5 minutes cycling and then recovered to normal value	98-163*	53-93*	BIM	PTT, BI signals	ML	Finapres	Mean±SD = -0.46±4.35 (SBP), -0.08±2.46 (DBP) R = 0.94 (SBP), 0.92 (DBP) MAD = 2.57 (SBP), 1.71 (DBP)
[187]	36 35	M F	49.3±15.1	healthy and patients	After 5 min of sitting: Test BP recorded beat-to-beat for 24 hours; Reference BP was recorded every 20 minutes from 8 am to 10 pm; every 30 minutes for the remaining time.	134±17.3	79.3±11.7	ECG-PPG	PTT/ calibrated BP	12	oscillometry (Omron HBP-1300)	Mean±SD = 10.20±7.20 (SBP), 8.20±5.5 0(DBP) MAD ≤ 5.00 mmHg: 32.40% (SBP), 33.80% (DBP) ≤ 10.00 mmHg: 60.60% (SBP), 71.80% (DBP) ≤ 15.00 mmHg: 74.60% (SBP), 91.60% (DBP)
[188]	6 4	M F	37±9	four hypertensives	Calibration: every 2 days for 2 weeks; Validation: 1 time per week for 4 weeks	136±14	84±12	ECG-PPG	PTT, HR, respiratory rate	13	mercury	Mean±SD = 1.04±6.88 (SBP), -2.16±6.60 (DBP)

[160]	63 M ——— 20 F	57±12 (24-85)	Healthy (40), Hypertensive (43)	Seated at rest after 3-5 minutes relax	144±19	85±12	Ultrasound-PPG	PWV, artery dimensions	16	oscillometry (SunTech 247, SunTech Medical, North Carolina, US)	DBP: R = 0.86 RMSEs = 8.30 Mean±SD = 3.80±1.96
[162]	6 M	25±4	healthy	Seated at rest; After a 10-minute arm exercise	121.3±16	72±9	IPG-PPG	PTT	1	oscillometry (Oscar 2, SunTech Medical®, US)	R = 0.51±0.05 (SBP), 0.42±0.19 (DBP) MAD±SD = 4.16±5.23 (SBP), 2.44±3.12 (DBP) Mean±SD = 0.00±6.12 (SBP), 0.00±3.16 (DBP)
[182]	21 M ——— 21 F	25.6±2.1 (21-31)	healthy	Non-smokers without caffeine ingestion within 6h, sitting quietly	108-132*	77-86*	ECG-PPG	PTT	2	Finapres	R = 0.90±0.07 (SBP), 0.79±0.10 (DBP) Mean±SD = -0.36±2.37 (SBP), 1.07±3.23 (DBP) MAD = 1.95 (SBP), 2.15 (DBP)
[157]	100M ——— 11 F	32.63±15.82	healthy	Without any specific medicine	85-185*	60-110*	Two-PPG	PWV, PTT and other features from signals	ML	oscillometry (Model M6 Comfort, OMRON, Japan)	MAD = 4.94 (SBP), 4.03 (DBP) Mean±SD = 0.00±5.90 (SBP) 0.53±5.50 (DBP) R = 0.94 (SBP), 0.84 (DBP)
[154]	10 M ——— 5 F	29±5	healthy	Relax, handgrip exercise, and recovery in the seated position	85-160*	55-115*	IPG-PPG	PTT, radial impedance	17	oscillometry (Oscar 2, SunTech Medical®, US)	Mean±SD = 0.31±8.55 (SBP), -0.5±5.07 (DBP) R = 0.88±0.07 (SBP), 0.88±0.06 (DBP) RMSEs = 8.47±0.91 (SBP), 5.02±0.73 (DBP)
[131]	16 M	24±5	healthy	Resting: standstill for 1.5 minutes	Resting: 119±2	78±1	Scaled BCG-PPG; Wrist BCG-PPG	PTT	1	Finapres	Wrist BCG-PPG: R = 0.79 (SBP), 0.81 (DBP) MAD = 5.10 (SBP), 7.60 (DBP)

	6	F			Changes: 2-min cold pressor; 3-min mental arithmetic; 3-min slow breathing; Breath-holding.	Changes: 56±3	38±2				Mean±SD = 0.00±9.54 (SBP), 0.00±6.58 (DBP)
[141]	6	-	-	healthy	Sit relaxed	76-145*	55-96*	Two-PPG using smartphones' cameras	PTT	2	oscillometry (OMRON 10 series)	R = 0.89 (SBP), 0.87 (DBP) MAD = 2.07±2.06 (SBP), 2.12±1.85 (DBP)
[132]	17 6	M F	23±5	healthy	Resting: standstill Changes: cold pressor; mental arithmetic; slow breathing; breath-holding.	70-190*	40-120*	Wrist BCG-PPG	PTT and six BCG features	ML	Finapres	R = 0.77±0.04 (SBP), 0.80±0.04 (DBP) RMSE = 9.10±1.10 (SBP), 6.00±0.70 (DBP) MAD = 7.20±0.90 (SBP), 4.70±0.50 (DBP) Mean±SD = 0.00±9.30 (SBP), 0.00±6.20 (DBP)
[186]	6 2	M F	25.2±3.62	healthy	Baseline: sit related for 5 minutes Lower-body exercise: 2 minutes Rest for 5 minutes Repeat one more time	90-170*	55-100*	MultiPANI: Six polyaniline sensors at the wrist	Hybrid selective PWV-PWA	18	Finapres (Monitor 500, CNSystems)	RMSE=3.94±0.5 (SBP), 1.88±0.9 (DBP) MAD=2.91±0.2 (SBP), 1.42±0.2 (DBP) Mean±SD= 0±5 (SBP) 0±4.08 (DBP)
[137]	16 5	M F	25.9±3.4	healthy	12 measurements over 24 hours except sleeping	80-140*	50-100*	SCG-PPG	PTT	2	oscillometry	RMSE = 4.75 (SBP), 2.72 (DBP) MAD = 4.03 (SBP), 2.24 (DBP) Mean±SD = 0.00±5.44 (SBP), 0.00±2.88 (DBP)

2.5.2 Recommendations of clinical protocols

This section outlines key features of clinical protocols based on the latest AAMI/ESH/ISO collaboration statement (validation study) [211] because it is expected to supersede previous validation protocols.

Sample size and population: this statement requires at least 85 general population participants and a minimum of 35 special population subjects (45 for pregnancy) intended for use in all patient populations. Nevertheless, around 63.16% of previous studies (shown in Table 6) involved less than 30 subjects, and only 9 studies investigated unhealthy subjects (patients) with cardiac diseases. It is understandable that there was no need for all works to recruit large numbers of subjects for the initial research and development phase because a smaller sample size can reduce the cost of validation. However, an adequate sample size could increase the statistical power and accuracy and allow more investigation of subgroups in the long term. In other words, the more participants, the closer the estimated probability will approach the actual probability and vice versa. To some extent, if only healthy young participants are recruited, the measured BP range will be much narrower than that of the world population, which will reduce the applicability of the results. The standard also suggests that the percentage of males and females should be at least 30%. Overall, it is necessary to recruit diverse participants (i.e. broad age group, balanced male to female ratio) because it is evidenced that the age, gender and subregion show considerable variation in BP levels [212].

Reference BPM: In the above summarized clinical studies, the commonest device to obtain reference BP values was the oscillometry sphygmomanometer (approximately 60.53%), followed by Finapres (approximately 26.32%). However, some of these cuff-based devices might not be appropriately used as a reference. Standards suggested that the mercury sphygmomanometer with two professional observers or validated nonmercury devices shall be performed as the critical reference. Regrettably, the mercury sphygmomanometer cannot provide continuous reference BP values. Therefore, several works selected Finapres to provide the beat-to-beat reference BP values, while the inherent unreliability of Finapres might not be able to take this responsibility. The “gold standard” was applied as the BP reference in two studies. In these studies, the invasive method was used on patients in ICU or undergoing a surgical operation and provided the reference BP values to the existing ECG-

PPG system. In addition to invasive methods, it is currently challenging to select a reference sphygmomanometer that is entirely suitable for PWPM. Thus, this re-evaluation did not account for the effects of the accuracy of RBPM on the clinical validation.

Validation process: the target working environment determines the specific validation process. For a normal static BPM, the subjects should seat comfortably and relax for at least 5 minutes before measurement. Talking and any other interference needs to be avoided throughout the clinical validation procedure. The PWPM is particularly relevant to portable and ambulatory monitoring. Thereby, in order to simulate the actual activities in daily life, researchers investigated a more comprehensive range of BP variations by testing during some physical exercises, such as running, bicycle ergometer, handgrip, stair climbing and walking. In this way, three measured conditions could be achieved: baseline BP at rest, during exercise and during the recovery period. The exercise phase can not only validate the adaptability of the system to the higher BP level but also verify the effective response to sudden changes in BP.

Validation criteria and reporting: the AAMI/ESH/ISO collaboration statement required that the mean BP difference for both SBP and DBP (test versus reference) should be within ±5 mmHg (±0.67 kPa) with its SD no greater than 8 mmHg (1.07 kPa). Furthermore, the number of absolute differences (test device differing from the reference BP) within 5, 10, and 15 mmHg shall be reported. Additionally, standardized Bland–Altman scatterplots are required to be presented. There are ten statistical analysis methods (parameters) presented in Table 6. Typically, according to the specific research objectives, researchers usually evaluate their accuracy from three views: (1) Bias: the difference between their results (estimated BP values) and their targets (reference BP values); (2) Variation/dispersion: standard deviations of the difference between various methods; (3) Correlation: the linear relationship between estimation values and target values, which was a common approach to select more relevant features.

Efficacy measure: considering the variability of validation methodology, a threshold of acceptable BPM was set that the estimated probability of a tolerable error (within 10 mmHg) is at least 85%. The main function of this threshold was to separate the high/moderate accurate devices from poor devices. It is also the primary basis to re-evaluate the previous clinical studies in this review.

2.6 Limitations of previous studies and suggestions for future work

This section will summarise several limitations of current PWPM and highlight suggestions for future work based on the research gaps identified in the literature review.

A. Limitations of techniques

In recent years, PWPM has provided a promising concept for cuff-less continuous BPM. The most typical measurement is the ECG-PPG system. Such techniques can easily determine the time delay between the proximal-distal signals, while it is worth noting that the measured time delay contains irrelevant PEP. ECG-PPG method is also compromised by non-uniform standards for PTT/PWV determinations, such as various characterized points on waveforms and the treatment of the effects of PEP, etc. Even though other substitutions were attempted, the accuracy of the proposed systems all suffered from substantial signal noises caused by motion artefacts and position changes.

Regarding the portability of the measurement, BIM is one promising technique that deserves to be investigated further because of its promising capability to track blood flow. Besides being utilized as the time reference for pulse wave propagation, BIM could provide more critical information for blood volume change, connecting the arterial diameter to BP. For example, Ibrahim and Jafari [213] has recently evidenced that continuous BP could be estimated via BP features extracted from BIM waveform.

B. Simplifications of mathematical models

One inherent drawback of PWPM is that the BP values are estimated instead of measured. As a result, the critical link between BP values and pulse wave propagation is the mathematical model. Almost all models were based on excessive simplifications of blood flow and artery theories. Additionally, as mentioned above, the PTT/PAT/PWV is inadequate for accurate BP estimation. Future work is expected to acquire more BP-relative information from the measured waveform, such as other factors that can reflect the neural control, sympathetic system, and arterial diameter changes. Machine learning-based method might be a more effective approach to estimate BP to some extent, opening an opportunity for the shortcut in selecting relevant features, which is also a general trend in many fields nowadays. Remarkably, several studies could achieve much higher accurate BP estimation with only

one single PPG sensor by utilizing deep learning methods [71], [214], [215]. Nevertheless, from the biomedical engineering perspective, further research should keep focusing on employing arterial hemodynamic principles to explore the relationship between blood pressure and pulse wave propagation. The readers are referred to one comprehensive review [176] for more detailed knowledge and discussion of the physical and mathematical modelling of pulse wave propagation.

C. Inevitable calibrations

According to the present research progress and products in the market (e.g. *ViSi Mobile System* [125]*, Biobeat wristwatch* [142]*, and Aktiia 24/7 BPM* [216]), it may be difficult to avoid the calibration procedure. The initial calibration is necessary to determine the subject-depended coefficients by using conventional BPM. These subject-depended coefficients typically corresponded to the subjects' ages, genders and state of health. A particular population always has some commonalities. Thus, if a large number of participants are investigated to set up a massive database for different populations (e.g., age groups, gender groups, and health condition groups), it could be possible to reduce reliance on the initial calibration procedure for individuals. In this way, users are only required to input basic personal information before wearing the device. The accuracy of the estimation depends on the precision of the initial calibration, and the durability of estimation always depends on the frequency of recalibration. In other words, without recalibration, the accuracy would decrease over time. Several advanced calibration methods (e.g., machine learning) have been tried to achieve long-term monitoring. However, the ideal BPM should be reliable without recalibration. As a matter of fact, recalibration is a manifestation of the flawed mathematical model, which is another reminder of the importance of adequate mathematical models.

D. Lack of specific clinical standards

A serious problem during summarizing Table 6 was that lots of studies did not provide adequate statistical data to prove their accuracy due to omnifarious clinical protocols. It cannot exclude the possibility that unsatisfactory validation testing results inadvertently give readers an illusion that this method is accurate. Moreover, even though the latest AAMI/ESH/ISO collaboration statement was used as the reference protocol in this review, its intrinsic purpose mainly focused on cuff-based auscultatory/oscillometric BPM. In other

words, parts of this protocol might be not fully applicable for PWPM. For example, current conventional sphygmomanometers cannot provide beat-to-beat BP references.

The lack of rigorous and comprehensive clinical standards for these burgeoning BPM might blur and mislead the actual accuracy of proposed devices, such as the Instant Blood Pressure smartphone application [217]. Most insidiously, if inaccurate devices are sold on the market, the inappropriate result could result in mismanagement of BP and even cause serious clinical consequences. Therefore, in order to standardize the procedures for the development of PWPM, a specific revision of the current authoritative standard is desired to guide manufacturers and clinicians in the future. PWPM-based BPM are expected to be widely adopted once the ISO standard has been established [218]. Furthermore, related organizations should provide a more accessible way for the public to help potential customers inquire about devices' actual clinical validation results, such as a list of validated devices [219].

This problem already exists in the current market of sphygmomanometers. Some devices have passed the regulatory requirements for sale and their accuracy might be not guaranteed [40]. The fundamental issue is that regulatory authorities always concentrate on the safety features of devices rather than their accuracy and performance characteristics [220]. For instance, the FDA assess sphygmomanometers for the market based on 'substantial equivalence' but not clinical accuracy, which means 'FDA-cleared' is not the label for an accurate product [221]. One latest review article summarized several FDA-approved cuffless BPMs [222], including the above mentioned Biobeat wristwatch [142] and ViSi Mobile System [125]. However, more detailed and precise evaluation of these devices is needed to confirm their clinical efficacy. Additionally, manufacturers are not required to share the accuracy with the public [223]. Consequently, consumer organizations cannot know whether the product performs accurately. In order to protect users from severe consequences caused by inaccurate BPM devices, four steps were suggested by O'Brien et al. [224] as follows:

1) A universal protocol is desired to regulate the requirement for mandatory independent validation of all BPM devices.
2) Accreditation laboratories should validate the performance of BPM.
3) The validation studies should be evaluated online using a specific standard and then eliminate protocol violations before publishing the results.
4) An independent scientific forum should list accurate BPM devices publicly.

2.7 Research gaps

The literature review has highlighted a number of previous systems (i.e., techniques and mathematical models) that attempt to estimate BP via pulse wave propagation information (i.e., PTT, PAT and PWV). The limitations of current PWPM have been reviewed in section 2.6, revealing various research gaps in this area:

- Even though many studies have applied other techniques to replace the typical ECG-PPG system (see section 2.2.1.2), the acquired signals were mainly utilized as a time reference to determine pulse wave propagation time. Much less literature explored deriving other critical information from measured signals, such as the absolute arterial diameter changes.
- Although many previous works have attempted to improve the accuracy of BP estimation by augmenting other parameters (see section 2.4.2), only a few studies included the absolute values of arterial diameter in the mathematical model. However, arterial diameter information is directly related to BP, as introduced in section 1.5.
- Almost all previous mathematical models contained subject-specific coefficients, requiring an initial calibration for individuals and re-calibration for long-term measurement. More advanced systems are desired to avoid such steps.
- As a tool for monitoring hemodynamic information, BIM could potentially provide arterial diameter information to enhance the BP estimation. However, according to section 2.3, very few investigations have been directed toward estimating arterial diameter change via bio-impedance signals.
- Several studies have investigated various electrode configurations to obtain a better quality of bio-impedance waveform. However, few describe whether the obtained waveforms can accurately represent the responses of measured tissues and pulsatile blood from a mathematical perspective.
- The geometry of the human forearm has been represented by a few previous studies in computational simulation. However, no works presented two synchronously pulsatile arteries (i.e., both radial artery and ulnar artery). The effects of a contralateral conductive artery on the conventional 4-spot electrodes BIM are still unclear.

- For novel PWPM-based BPM, there is inconsistent clinical validation between studies. A universal protocol is desired to regulate the requirement for mandatory independent validation of novel PWPM-based BPM.
- Even though a few studies claimed that they met the international standard (i.e., ANSI/AAMI SP10) with fairly high accuracy in BP estimation, their recruited subjects were fewer than the required subject number (i.e., 85), leaving results open to interpretation. A more robust statistical treatment needs to be developed to re-evaluate the literature less subjectively.

The work presented in this thesis does not attempt to address all of the above research gaps. The specific research objectives are presented in section 2.8.

2.8 Research objectives

The main objective of this research is to **accurately estimate radial artery diameter from bio-impedance signals by reaching a consensus between simulated/measured impedance values and mathematical modelling of BIM at the human wrist**. This thesis focuses on the effects of different electrode configurations on current density and electric field (E-field) distribution within the wrist. The aim is to achieve a reasonably uniform E-field distribution such that the cross-sectional area changes of the blood can be estimated more accurately. The following objectives support the main goal of this study:

- Quantify the individual and overall contribution of different tissues (i.e., skin, fat, muscle and bones) and the pulsatile blood under BIM on the human wrist from a mathematical perspective.
- Develop the most appropriate electrode configuration to estimate the cross-sectional area of tissues and the arterial diameter change via simulated impedance change by using FEA.
- Analyse different dielectric responses of tissues to explore their contribution under BIM and explore the effects of a contralateral pulsatile artery on acquired signals.
- Validate the proposed mathematical modelling and simulation results using phantom experiments, using suitable tissue-mimicking materials for human wrist phantom fabrication and constructing experimental setups to simulate artery contraction during BIM.

CHAPTER 3. MATHEMATICAL MODELLING

3.1 Introduction

In previous studies, the bio-impedance signal was often used only as a time reference for pulse wave propagation detection, while this thesis focuses on its numerical value. The primary objective of this chapter is to explore and quantify the contribution of soft tissues and the pulsatile blood under BIM on the human wrist.

The first section of this chapter describes the theoretical relationship between the overall measured impedance and dielectric properties of measured tissues. A mathematical model is proposed to estimate the cross-sectional area of each tissue by using multi-frequency measurement. In the second section, a developed mathematical model is described to estimate arterial cross-sectional area change via a real-time bio-impedance signal, aiming to estimate the real-time arterial diameter more accurately.

3.2 Wrist tissue electrical modelling

The anatomical structure of the human wrist can be reasonably assumed to be a uniform geometry with multiple lumped domains, such as skin, fat, skeletal muscle, bone, and blood-filled artery, as shown in Figure 3. The arterial wall can be reasonably neglected because the thickness of the radial artery wall is relatively thin compared with the surrounding tissues. Moreover, the arterial wall shows similar dielectric properties to the skeletal muscle.

The current conduction inside the human wrist mainly depends on tissues' electrical properties and geometric structures, making the equivalent circuit complicated to represent. To simplify the analysis, the current density inside the human wrist was considered uniform, as shown in Figure 8 (B). Additionally, the human tissues were considered homogeneous with bulk electrical properties. As a result, alternating current can be regarded as injecting from both ends of the measured segment, and different tissues can be regarded as connected in parallel. For tissue components connected in parallel, the inverse overall measured impedance ($Z_{overall}$) equals the summation of the inverses of the component impedances:

$$\frac{1}{Z_{overall}} = \frac{1}{Z_{\text{skin}}} + \frac{1}{Z_{fat}} + \frac{1}{Z_{blood}} + \frac{1}{Z_{muscle}} + \frac{1}{Z_{bone}} \qquad \text{Equation 9}$$

The β-dispersion (from 1 kHz to 100 MHz) accounts for passive cell membrane capacitance, intracellular organelle membranes and protein molecule response. In this frequency range, human tissues are dielectric materials with both resistance and capacitance. Therefore, it is reasonable to describe it as a parallel resistor-capacitor (RC) circuit. For individual tissue, the electrical resistance (R_{tissue}) can be computed by its electrical conductivity (σ_{tissue}), cross-sectional area (A_{tissue}) and the measured length (l_m) based on the assumed uniform current density distribution.

$$R_{tissue} = \frac{l_m}{\sigma_{tissue} A_{tissue}} \qquad \text{Equation 10}$$

For the bio-impedance measurement at the wrist, the length of the measured segment can be assumed to be the spacing between PU electrodes (L_{PU}). The frequency-dependent conductivity can be acquired via the database parametrically modelled and compiled by Gabriel et al. [225]–[227]. Therefore, the hypothesis was that the cross-sectional areas of tissues can be estimated from the resistance component of measured impedance by applying multi-frequency measurement. The cross-sectional area of each tissue ($A_1, A_2, \cdots A_n$) can be obtained by solving the following matrix:

$$\begin{bmatrix} \sigma_{1,f1} & \sigma_{2,f1} & \cdots & \sigma_{n,f1} \\ \sigma_{1,f2} & \sigma_{2,f2} & \cdots & \sigma_{n,f2} \\ \vdots & \vdots & \ddots & \vdots \\ \sigma_{1,fn} & \sigma_{2,fn} & \cdots & \sigma_{n,fn} \end{bmatrix} \begin{bmatrix} A_1 \\ A_2 \\ \vdots \\ A_n \end{bmatrix} = L_{PU} \begin{bmatrix} {R_{f1}}^{-1} \\ {R_{f2}}^{-1} \\ \vdots \\ {R_{fn}}^{-1} \end{bmatrix} \qquad \text{Equation 11}$$

n is the number of applied frequencies which is at least the number of tissue types to be estimated. R_{fn} is the resistance value of measured impedance at the n^{th} frequency. $\sigma_{1,fn}$ is the conductivity of the first type of tissue at the n^{th} frequency. Taking the parallel combination in Figure 9 as an example, there are six types of tissues. Thus n is equal to six.

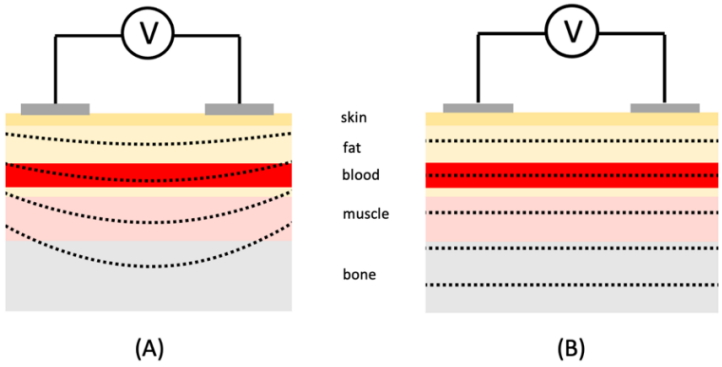

Figure 8. Current flow under PU electrodes: (A) normal condition; (B) idealised parallel condition.

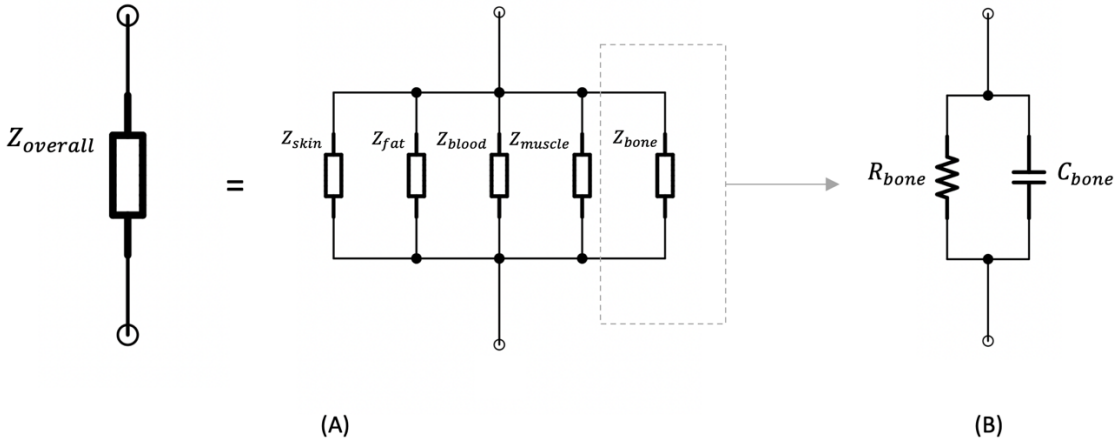

Figure 9. Equivalent circuit of measured impedance at the human wrist: (A) parallel combination of tissues; (B) parallel RC circuit.

3.3 Modelling blood flow in the wrist

Even though there is evidence for the effects of RBC orientation on measured impedance changes [84], it is challenging to represent such contribution in FEA and artificial tissue phantom experiments. Thus, blood volume change in the radial artery is considered as the major contribution to bio-impedance signal change in this thesis. The modelling of blood flow in the wrist was inspired by Nyboer's theory proposed in 1950 [228], which was used to represent stroke volume from impedance variation by using an expansible tube. In order to separate the impedance contribution of blood flow in the artery (AC component) from the overall measured impedance of the whole wrist (DC component), a parallel combination of the impedance of the pulsatile blood and the static condition of all tissues was assumed, as shown in Figure 10. At any time, the overall impedance ($Z(t)$) during blood flow is modelled as a parallel combination of the basal impedance (Z_0), which corresponds to the static

impedance of all surrounding tissues and static (perfused) blood, and the real-time pulsatile blood impedance ($Z_p(t)$), which is the variable impedance of flowing blood.

$$\frac{1}{Z(t)} = \frac{1}{Z_0} + \frac{1}{Z_p(t)} \qquad \text{Equation 12}$$

Therefore, the measured real-time change in impedance ($dZ(t)$) can be given by:

$$dZ(t) = Z(t) - Z_0 = \frac{Z_0 Z_p(t)}{Z_0 + Z_p(t)} - Z_0 = -\frac{{Z_0}^2}{Z_0 + Z_p(t)} \qquad \text{Equation 13}$$

The pulsatile blood impedance $Z_p(t)$ can either be positive or negative depending on the increase and decrease in the blood volume, respectively. Previous studies usually used the conductivity to calculate the magnitude impedance values, which can cause confusion and errors. Strictly speaking, according to Equation 10, only the resistance of the pulsatile blood ($R_p(t)$) is related to the conductivity of the blood (σ_b), which can be expressed as:

$$R_p(t) = \frac{L_{PU}}{\sigma_b \cdot dA_b(t)} \qquad \text{Equation 14}$$

where $dA_b(t)$ is the cross-sectional area changes of the blood ($dA_b(t) \neq 0$). Equation 13 can be rewritten by substituting the resistance components:

$$dR(t) = R(t) - R_0 = -\frac{{R_0}^2}{R_0 + R_p(t)} \qquad \text{Equation 15}$$

Next, after substituting Equation 13 into Equation 14, the cross-sectional area changes of the blood (dA_b) is thereby:

$$dA_b(t) = -\frac{L \cdot dR(t)}{\sigma_b \cdot R_0 \cdot R(t)} \qquad \text{Equation 16}$$

where R_0 is the basal resistance corresponding to the basal tissues and basal cross-sectional area of the blood A_0. $R(t)$ is the resistance measured as a function of time, while dR is the difference between the measured basal resistance and the resistance measured at time t. If the basal inner diameter of the artery can be calibrated through other measurement techniques (e.g., ultrasound image), then the real-time inner arterial diameter can be calculated from the cross-sectional area of the blood:

$$d(t) = 2\sqrt{\frac{A(t)}{\pi}} = 2\sqrt{\frac{A_0 + dA_b(t)}{\pi}} \qquad \text{Equation 17}$$

The proposed mathematical modelling is based on four main assumptions: 1) the geometry of the artery is a uniform cylindrical plastic tube; 2) the blood is homogeneous with frequency-dependent (but time-invariant) conductivity, 3) the volume increment in the blood caused by the pulse is uniformly distributed within the measured segment, and 4) the current distribution is parallel to the blood flow.

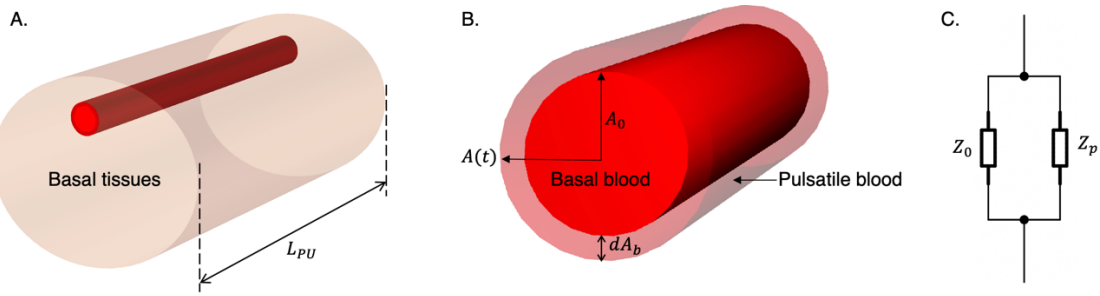

Figure 10. The relationship between the impedance changes and the artery diameter change: (A) measured segment of the human wrist; (B) cross-sectional area change of the artery; (C) equivalent circuit of the pulsatile blood.

3.4 Closure

This chapter simplified the complex anatomical structure of the wrist into a multi-tissue uniform model and proposed two main mathematical models based on equivalent electrical circuit models: 1) estimation of the cross-sectional areas of each tissue (see Equation 11); 2) estimation of the inner diameter change of the artery (see Equation 17).

However, these mathematical models are based on some assumptions. One of the most important prerequisites is that the current flowing into the wrist is parallel to each tissue domain. In other words, the current density in the measured region needs to be uniform along the length, which is not always true in practical situations, especially considering the actual anatomy and tissue properties of human body. In addition to the anisotropic properties and geometric structures of the human tissues, the placement and shape of electrodes can affect the current distribution inside the wrist. Therefore, in the next chapter, an FEA will be applied to initially explore the impact of different electrode configurations on current distribution. Moreover, the most suitable electrodes setup will be developed to verify the accuracy of the proposed mathematical modelling.

CHAPTER 4. SIMULATION ANALYSIS OF ELECTRODE CONFIGURATIONS

4.1 Introduction

This chapter attempts to initially substantiate how accurate of the mathematical modelling described in Chapter 3 to represent the electrical contribution of multi-tissues and pulsatile blood. Before physical experiments, it is advisable and timesaving to investigate the effects of various experimental setups on the ultimate objectives using computational simulation. In this chapter, a FEA of the static simplified human wrist segment (wrist model 1) was constructed using the HFSS design type in ANSYS Electronics Desktop (2021 R2), which included fat, muscle and one blood-filled artery. This simulation was used to analyse different dielectric responses of these three main tissue regions in the β-dispersion (from 1 kHz to 100 MHz), particularly the blood inside the radial artery. Figure 11 illustrates the overall simulation process in this chapter. Various electrode configurations were investigated to explore the effects of electrode materials, shapes, dimensions, types and spacings (CC electrode spacing (L_{CC}) and PU electrode spacing (L_{PU})) on the uniformity of current density distribution. The primary objective of this chapter was to develop the most appropriate electrode configuration to estimate the cross-sectional area of tissues and the arterial diameter change via simulated impedance change based on the mathematical modelling in the previous chapter.

Section 4.2describes simulation settings in ANSYS HFSS, including the geometry of the 3D model, mesh quality, material assignment and excitation. Then, Section 4.3introduces the data processing and analysing methods. Next, three main research outcomes are stepwise discussed based on the corresponding simulation results from the Section 4.4to Section 4.6.

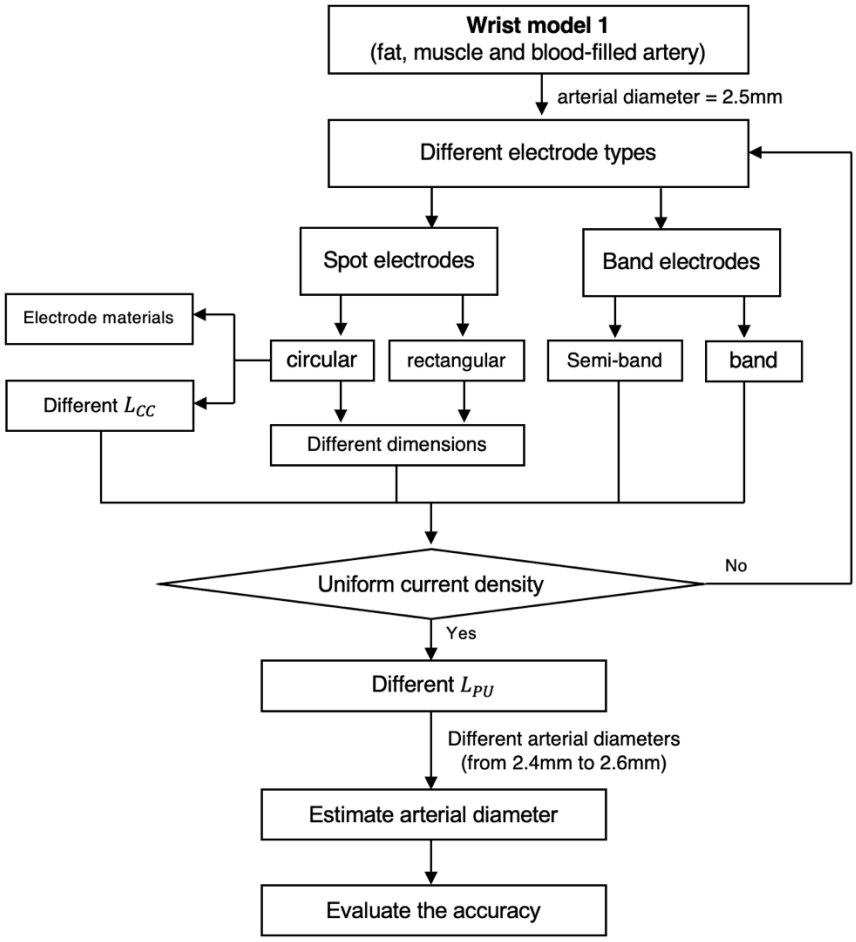

Figure 11. The flowchart of the simulation process in Chapter 4.

4.2 ANSYS HFSS setup

4.2.1 Geometry

The static FEA of a 3D cuboid model (30 mm×50 mm×100 mm) of the human forearm segment near the wrist was constructed using the HFSS design type in ANSYS Electronics Desktop (2021 R2). The overall 3D model was composed of two sections, including experimental apparatus (i.e., electrodes and cables) and the human tissues (e.g., fat, muscle, and a blood-filled artery).

4.2.1.1 3D wrist model

The dimensions of the simplified human forearm model near the wrist was based on several studies and reports of the relative proportions of tissues in the standard human forearm [229],

depth and diameter of the human radial artery [230], human forearm anatomy scanned by MRI (Magnetic Resonance Imaging) [231]–[233], the average diameter of radial artery [234]–[239] and human wrist circumference [240]. As shown in Figure 12, the reddish muscle tissue section in the middle was wrapped by the outermost yellowish adipose tissue layer. The radial artery was at the bottom of the fat layer, close to the muscle domain. The thickness of the volar aspect fat layer was 6 mm, while other aspects were 3 mm. However, the thickness change from proximal to distal was not represented here. In this initial geometry, the depth and diameter of the radial artery were 3 mm and 2.5 mm, respectively.

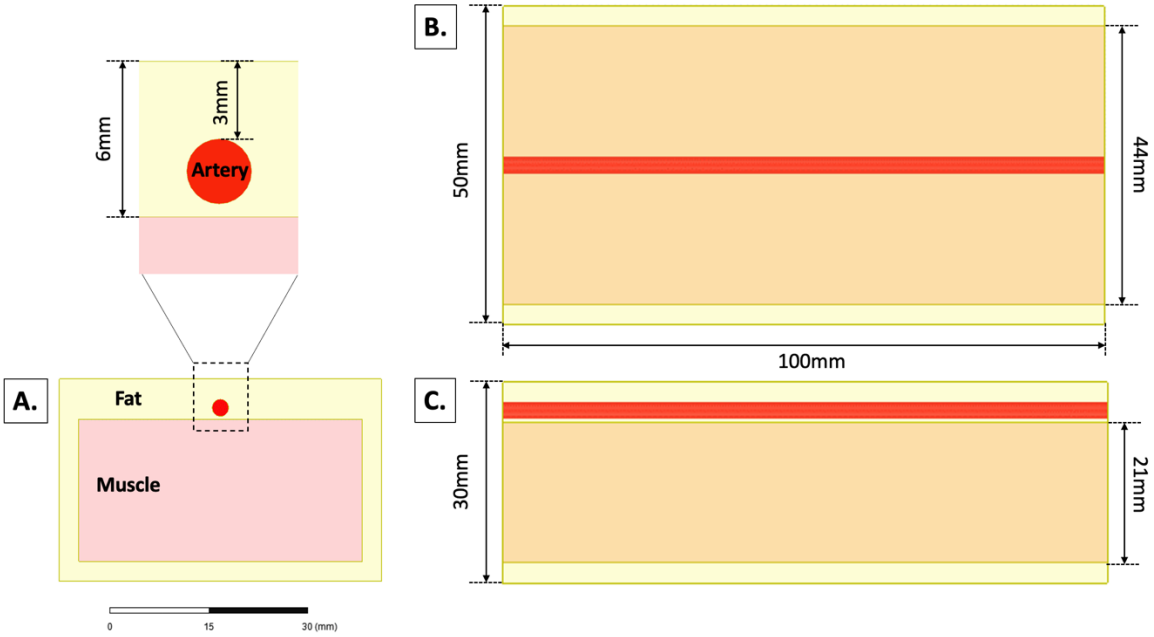

Figure 12. The dimension of the wrist model 1: (A) the top view; (B) the front view; (C) the left view.

In this simulation stage, unlike actual anatomy, the ulnar artery and other vessels were not considered in the initial model in order to focus on the pulsatile blood volume inside the radial artery. Moreover, bones with relatively low and almost unchanged conductivity in the frequency range of interest were not taken into account. Additionally, the skin layer that would be wet by the electrolyte of gel electrodes was represented as dry electrodes directly in contact with the underlying fat domain.

The time-varying blood volume change in the artery caused by ejection of blood from the heart was regarded as the only contribution to bio-impedance signal change. Five different static arterial diameters were modelled as 2.4 mm, 2.45 mm, 2.50 mm, 2.55 mm, and 2.60 mm based on the human radial artery's actual vasoconstriction and vasodilation range

[93]. The arterial diameter of 2.50 mm was defined as the basal condition, while other variables were used to calculate the increment/decrement in simulated impedance and estimate the contraction/expansion of the blood cross-sectional area.

4.2.1.2 Current-carrying electrodes

In the original configuration, the typical 4-electrodes vertical configuration aligned above the radial artery was employed, as shown in Figure 13. Two outer CC electrodes were settled directly on the surface above the artery with a thin cylinder shape (circular electrode) with a diameter of 10 mm and a thickness of 1 mm to represent the conventional dry Ag/AgCl electrode, connecting with a thin wire, while PU electrodes are not represented visually. HFSS can calculate and export the complex electric field (E-field) values between any two points of the 3D model. Therefore, the potential differences across PU electrodes were calculated by integrating the E-field instead of measuring defined PU electrodes. The calculation process will be described in detail in the data processing section 4.3.2.Multiplicate electrode configurations were stepwise modelled in order to explore the promising configuration to generate the uniform E-field, including varied materials, shapes, dimensions, types and spacings, as shown in Table 7.

Table 7. Various CC electrode configurations modelled in Chapter 4.

Step	**Electrode configurations**	**L_{CC} [mm]**	**Materials**	**Shape and dimension [mm]** *diameter (D) and width (W)*	**Types**
1	Materials	90	Copper, silver, platinum (Table 9)	Circular D = 10	spot
2	L_{CC} [mm]	90, 70, 50 (Figure 13)	platinum		
3	Shapes and dimensions	90		Circular D = 10, 9 and 8 (Figure 14) Rectangular W = 10, 30 and 50 (Figure 15)	
4	Types			Semi-band and band (Figure 16)	Band-type

- **Step 1**: three different metal materials were assigned on the CC electrodes and wire, which will detailly described in following section 4.2.4.2.
- **Step 2**: three different L_{CC} from the centre to the centre were modelled, including 90 mm, 70 mm and 50 mm, as shown in Figure 13.

- **Step 3**: the circular electrode was re-modelled with different diameters of 9 mm and 8 mm, as shown in Figure 14. In addition to the circular electrodes, a cuboid shape (rectangular electrode) was also modelled with the same thickness of 1 mm and a side length of 10 mm to investigate the effects of electrode shape on current propagation. Similarly, the rectangular electrode was further modified to different widths of 10 mm, 30 mm and 50 mm (see Figure 15).
- **Step 4**: Besides the conventional spot electrodes mentioned above, two band-based electrode types were also investigated. As shown in Figure 16, the left method was "semi-band electrode", and the right one was "band electrode". As their names imply, the band electrode was an extension of the wider rectangular electrode encircling the whole wrist, and the semi-band electrode was half of the band electrode located at the volar aspect of the wrist.

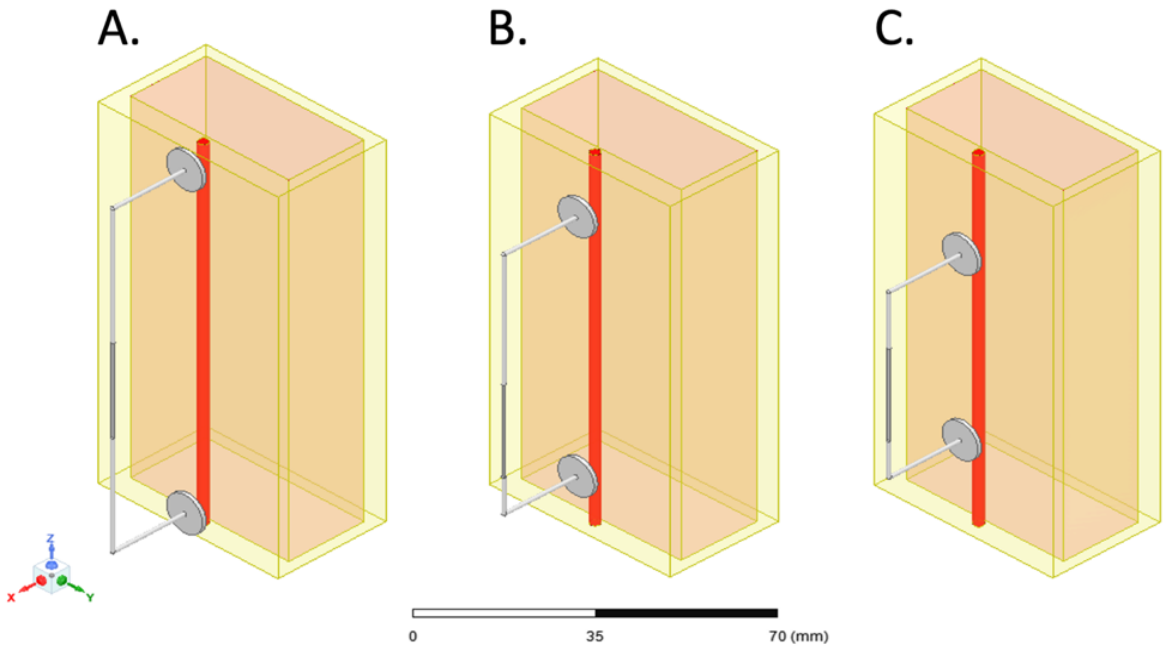

Figure 13. Three different L_{CC}: (A) 90 mm; (B) 70 mm; (C) 50 mm.

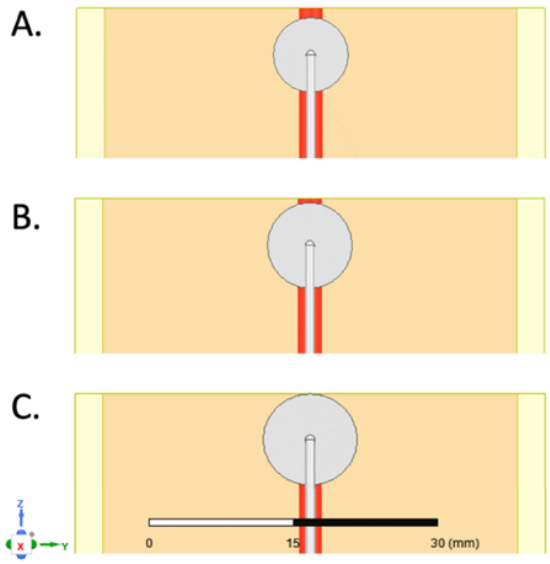

Figure 14. Different diameters of the circular electrodes: (A) 8 mm; (B) 9 mm; (C) 10 mm.

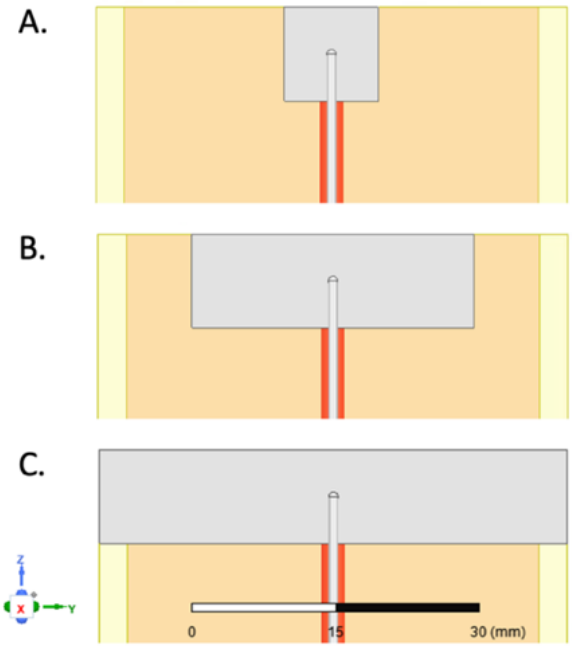

Figure 15. Different widths of the rectangular electrodes: (A) 10 mm; (B) 30 mm; (C) 50 mm.

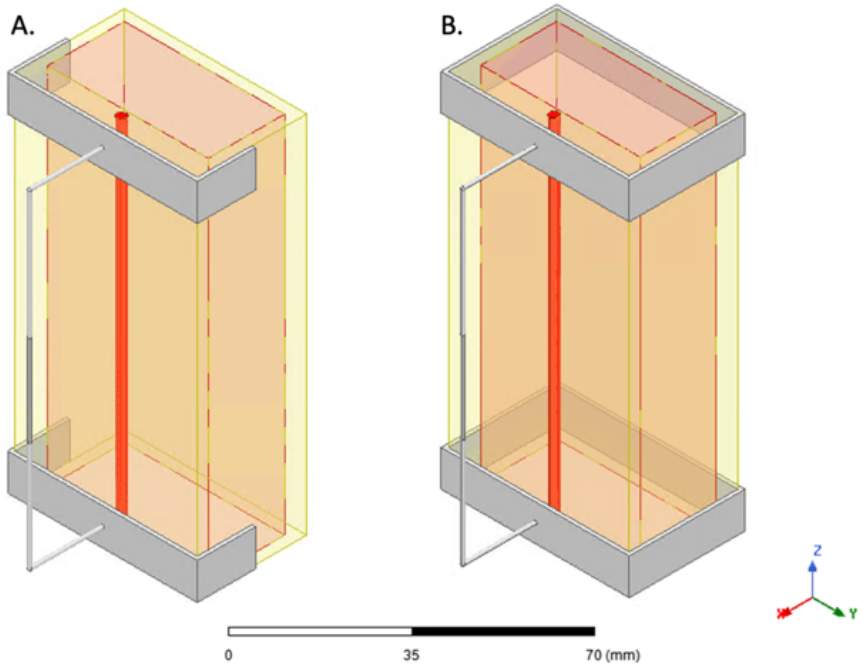

Figure 16. Band-type electrodes: (A) semi-band electrodes; (B) band electrodes

4.2.2 Mesh

In order to find a balance between solving time and accuracy, the *Length-based Mesh Refinement* of 0.5 mm was assigned inside the radial artery. Furthermore, *Curvilinear Elements* were applied to the artery domain to represent its curved geometry more accurately. Table 8 lists an example of the total number of mesh elements in each tissue domain of the initial model at step 1. Figure 17 shows an example of the mesh distribution of wrist geometry. The mesh density increased around the CC electrodes to increase accuracy of the simulation results.

Table 8. The number of mesh elements of the initial model at step 1.

Tissue domains	**Fat**	**Artery**	**Muscle**
Number of elements	185481	39408	114402

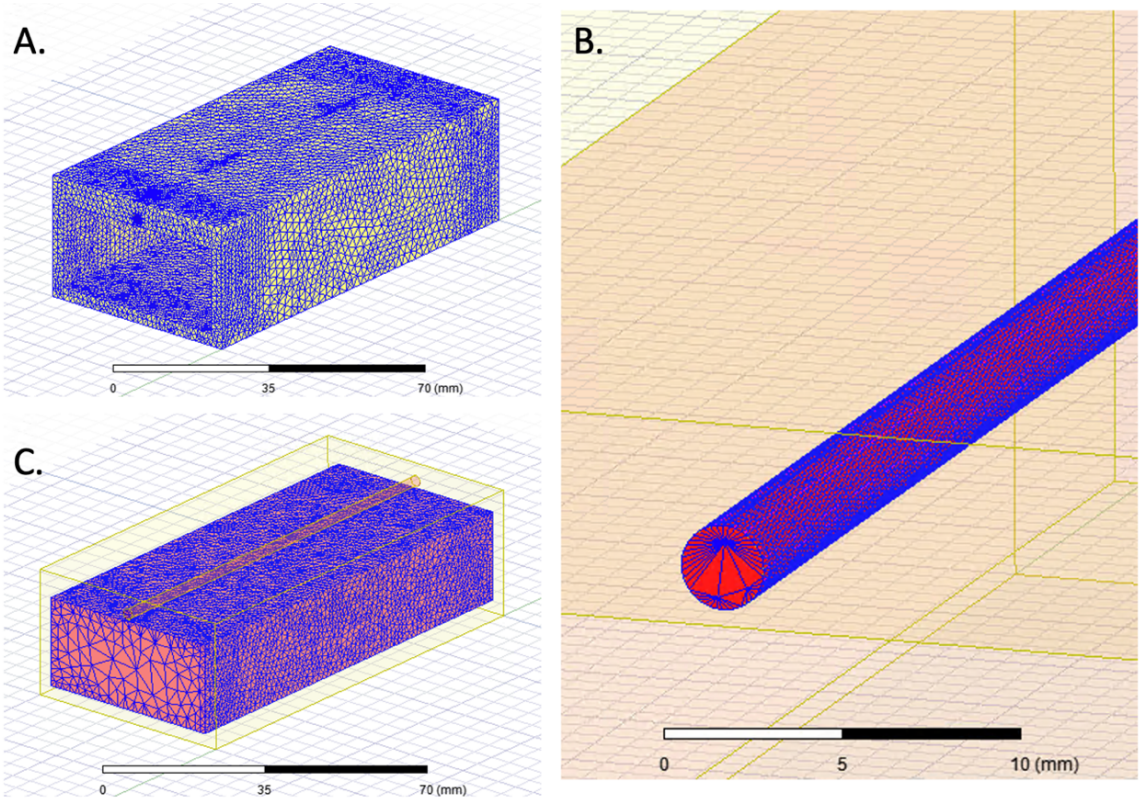

Figure 17. Mesh quality of each tissue domain: (A) fat; (B) blood; (C) muscle.

4.2.3 Excitations

The *Current Excitation* was applied on the modelled wire between CC electrodes as 1 mA within prescribed allowable current ranges for the safety of medical equipment according to IEC 60601 technical standards [240]. The *Discrete Frequency Sweep* was chosen. The setup of the current injection frequency was divided into two steps: first, the basal simulation (artery diameter = 2.5 mm) was performed across the entire frequency range in the β-dispersion with nineteen points (1 kHz, 10 kHz, 50 kHz, 100 kHz, 200 kHz, 300 kHz, 400 kHz, 500 kHz, 600 kHz, 700 kHz, 800 kHz, 900 kHz, 1 MHz, 1.5 MHz, 2 MHz, 5 MHz, 10 MHz, 50 MHz and 100 MHz); second, four specific frequencies (1 kHz, 100 kHz, 500 kHz and 1 MHz) were utilised for following simulations with different diameters in accordance with Figure 18. The partial derivatives of tissues' conductivity were calculated to indicate different frequency-dependent relationship between fat, muscle and blood, bringing specific interests in these four frequencies for multi-frequency BIM. For instance, the blood shows nearly constant conductivity between 1 kHz and 31.6 kHz, while it shows the most significant

changes around 1 MHz. By comparison, 100 kHz is the most widely utilised frequency in BIM according to literature (see Table 2 and Table 3). The whole wrist model was enveloped within a radiation boundary and a vacuum region to simulate the prevention of any electromagnetic interference from an outside source. Moreover, this boundary could reduce the space of the overall region to ensure adequate simulation speed.

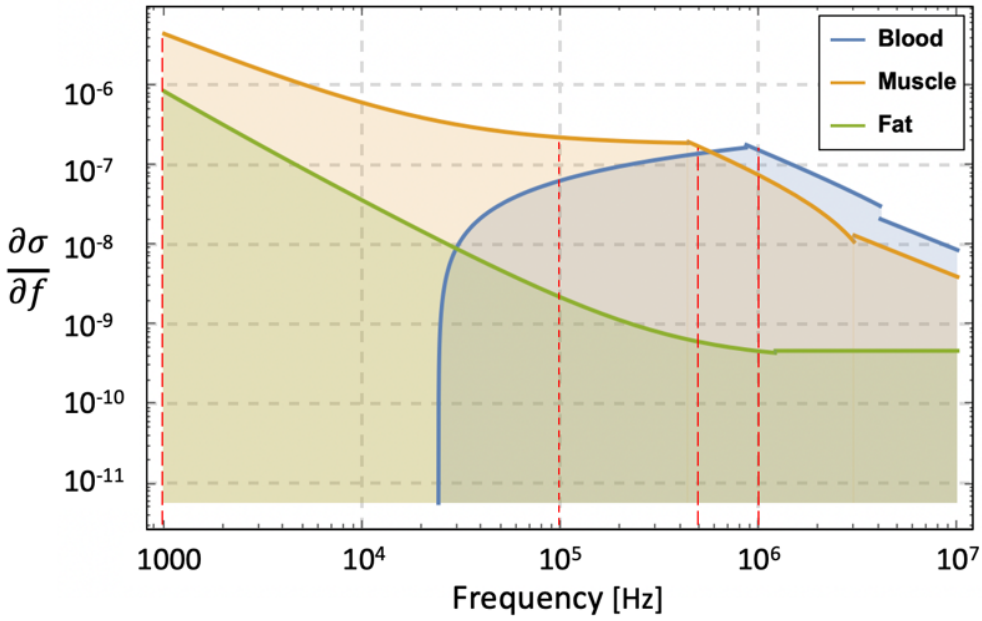

Figure 18. Calculated partial derivative of tissues' conductivity.

4.2.4 Material assignment

4.2.4.1 Tissues

In this simulation, tissue domains were considered homogeneous with bulk electrical properties. The frequency-dependent bulk conductivity and relative permittivity (see Table 36 in the Appendix) of each tissue were separately assigned according to the database proposed by Gabriel et al. [225]–[227], as shown in Figure 19 .

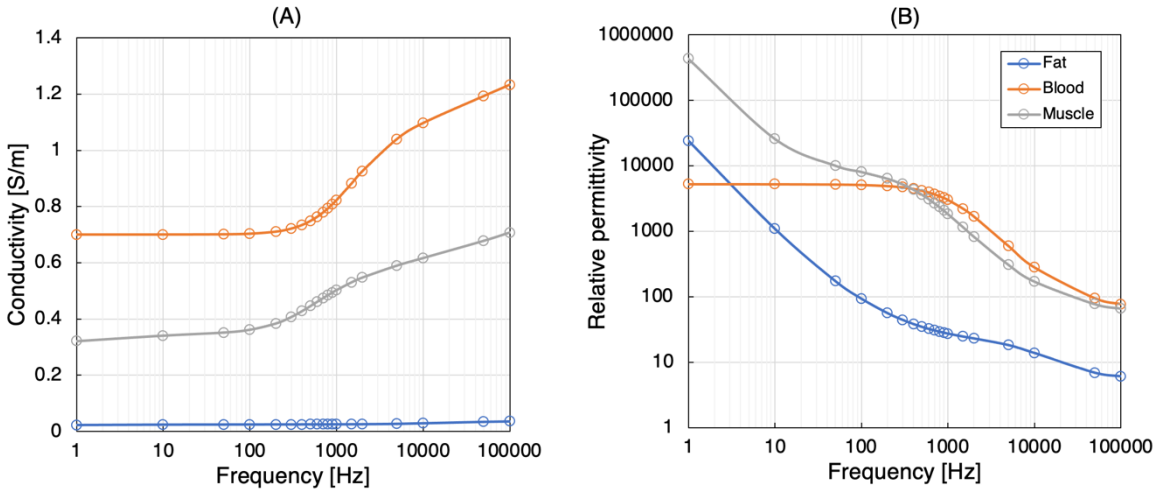

Figure 19. Dielectric properties of human fat, blood and muscle in the β-dispersion: (A) conductivity; (B) relative permittivity.

4.2.4.2 Electrodes

In electrical experiments, the electrode usually plays the role of a conductor with electrons as the dominant charge carrier. However, for BIM on human subjects, electrodes have another critical property called biocompatibility, which must be considered if the electrode comes in contact with living tissue [242]. Moreover, skin-electrode contact impedance caused by electrode polarization is a nuisance in most cases, introducing errors in tissue impedance measurements. This simulation did not model the electrolyte between solid electrode and tissue, thereby it was expected to eliminate the effects of different polarizable materials first. For this reason, three common metal materials were separately assigned on electrodes, including silver, copper, and platinum. Platinum is a type of biocompatible material commonly used for invasive electrodes and implants. Silver shows bactericidal properties as well. Copper is selected because it is a common low-cost electrode that can be used in bench testing. The bulk conductivity and relative permittivity of selected metal materials are listed in Table 9.

Table 9. Electrical properties of electrode materials

Materials	**Bulk conductivity [S/m]**	**Relative permittivity**
Platinum	9300000	1
Sliver	61000000	1
Copper	58000000	1

4.3 Data processing

4.3.1 Current density

In this simulation, the current density (J_{vol}: the complex magnitude of the current density over the volume) was utilised to distinguish whether the injected current propagated in parallel with tissue domains. This can help predict the most suitable electrode configuration for a uniform current distribution throughout the initial wrist model. The colour maps of current density were plotted on non-model planes A and B, and the numerical values along the parallel direction (z-axis) in non-model lines A and B were exported as data tables for further processing (see Figure 20).

Section 4.4presents the simulation results from aspects including the following:

- **The current density vector throughout the entire wrist model** was plotted to explore the overall direction of current flow from the front, left, and top views.
- **The current density overlay on plane A** was plotted to present the current density distribution in the horizontal middle region.
- **The current density overlay on plane B** was plotted to present the current density distribution in the vertical middle region.
- **The proportion of current in each tissue domain on plane B** was listed to indicate the relative current distribution in tissues.
- **Current density along the Z-axis on line A** was plotted to indicate the horizontal current density distribution inside the radial artery numerically.
- **Current density along the Z-axis on line B** was plotted to numerically to indicate the vertical current density distribution of each tissue domain with depth.

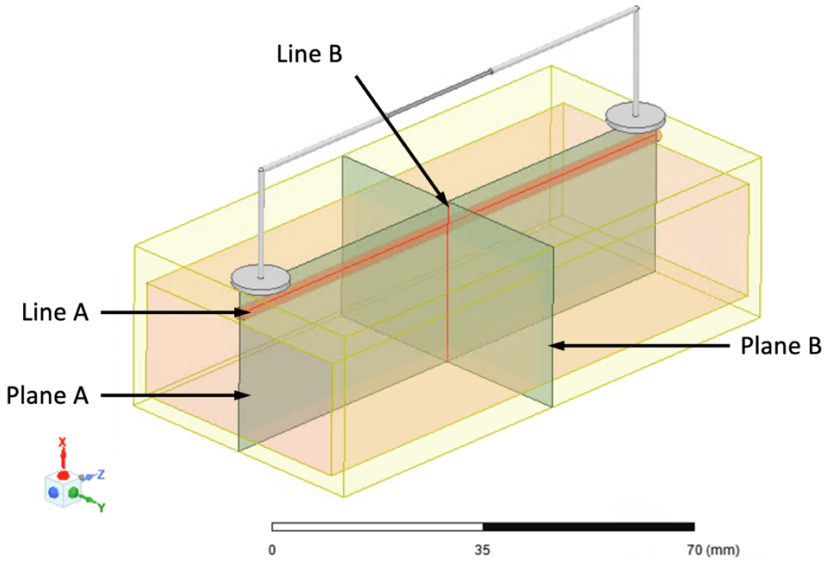

Figure 20. Analysis objects in chapter 4.

4.3.2 Simulated impedance

First, the magnitude value of the complex E-field was plotted in the whole wrist model. Furthermore, a non-model line (100 mm) was drawn between the centres of the two CC electrodes. The real and imaginary parts of the complex E-field at zero degrees along the z-axis were separately exported at 0.1 mm intervals at each frequency. Then, the first numerical derivative of the magnitude E-field ($f'(E)$) was calculated to determine the uniform E-field region (results are shown in Figure 34).

$$f'(E) = \frac{E_{n+1} - E_n}{0.1 \times 10^{-3}} \qquad n = \{1, 2, 3, \cdots 1000\} \qquad \text{Equation 18}$$

where n is the number of E-field points along the non-model line. Next, the real and imaginary parts of the potential difference were consequently calculated by computing the approximate cumulative integral of the real part of E-field ($\overrightarrow{Re(E)}$) and imaginary part of E-field ($\overrightarrow{Im(E)}$) via the trapezoidal method using MATLAB (R2019a, The MathWorks, US).

$$Re(U) = \int_a^b \overrightarrow{Re(E)} \cdot d\vec{l} \qquad \text{Equation 19}$$

$$Im(U) = \int_a^b \overrightarrow{Im(E)} \cdot d\vec{l} \qquad \text{Equation 20}$$

where a and b were any two points on the non-model line and $d\vec{l}$ was the vector between two adjacent points (0.1 mm). Then the real and imaginary part of impedance "measured" by PU electrodes can be calculated by dividing the potential difference by the amount of excitation current (I=1 mA):

$$Re(Z) = \frac{Re(U)}{I} \qquad \text{Equation 21}$$

$$Im(Z) = \frac{Im(U)}{I} \qquad \text{Equation 22}$$

Next, the Nyquist plot (Cole plot) was constructed to analyse whether the simulated impedance follows the Cole-type responses. As introduced in Chapter 3, the equivalent circuit of human tissues was described as a resistor connected in parallel with a capacitor. Thus, the real and imaginary part of impedance can also be expressed as follows:

$$Re(Z) = \frac{R_s}{1 + (\omega R_s C_s)^2} \qquad \text{Equation 23}$$

$$Im(Z) = -\frac{\omega R_s^2 C_s}{1 + (\omega R_s C_s)^2} \qquad \text{Equation 24}$$

where ω was the angular frequency, which is equal to $2\pi f$. Then the simulated resistance R_s and capacitance C_s can be obtained by solving the above equations:

$$R_s = Re(Z) \cdot \left(1 + \left(\frac{Im(Z)}{Re(Z)}\right)^2\right) \qquad \text{Equation 25}$$

$$C_s = -\frac{Im(Z)}{\omega(Re(Z)^2 + Im(Z)^2)} \qquad \text{Equation 26}$$

4.3.3 Estimation of the radial artery diameter change

According to Equation 16 and Equation 17, the real time diameter can be estimated by:

$$\hat{d}_i = 2\sqrt{\frac{\hat{A}_i}{\pi}} = 2\sqrt{\frac{A_0+\widehat{dA}_i}{\pi}} = 2\sqrt{\frac{A_0+\frac{0.1(b-a)\cdot(R_0-R_i)}{\sigma\cdot R_0\cdot R_i}}{\pi}} \qquad \text{Equation 27}$$

where R_0 is the basal simulated resistance corresponded with the basal cross-sectional area A_0 and R_i are the simulated resistance corresponding with modelled diameter d_i. The percent error (PE_d) can be calculated to evaluate the accuracy of the estimated diameter:

$$PE_d = \frac{|d_i - \hat{d}_i|}{d_i} \times 100\% \qquad \text{Equation 28}$$

4.3.4 Estimation of the cross-sectional area of each tissue

As described in Figure 9 in Chapter 3, different tissue domains were considered as parallel connection circuits. Therefore, in theory, the overall resistance ($R_{theory,i}$) can be expressed by the conductivity, cross-sectional area, and the length of the measured region. The simulated resistance was assumed to be equal to the theoretical resistance at each frequency:

$$R_{sim,i} = R_{theory,i} = \frac{l}{\sigma_{b,i}A_b + \sigma_{f,i}A_f + \sigma_{m,i}A_m} \qquad \text{Equation 29}$$

where i can be any three of the investigated frequencies (i.e., 1 kHz, 100 kHz, 500 kHz and 1 MHz). There are three unknown parameters (A_b, A_f and A_m), which can be obtained by solving the following equations at any three different frequencies

$$\begin{bmatrix}\sigma_{b,1} & \sigma_{f,1} & \sigma_{m,1}\\ \sigma_{b,2} & \sigma_{f,2} & \sigma_{m,2}\\ \sigma_{b,3} & \sigma_{f,3} & \sigma_{m,3}\end{bmatrix}\begin{bmatrix}A_b\\ A_f\\ A_m\end{bmatrix} = l\begin{bmatrix}R_{sim,1}{}^{-1}\\ R_{sim,2}{}^{-1}\\ R_{sim,3}{}^{-1}\end{bmatrix} \qquad \text{Equation 30}$$

The accuracy of the solutions highly depends on the difference between the simulated resistances and the theoretical values. To find out the threshold of accurate estimation, the expected error was calculated by the propagation of uncertainty/error:

$$\mu_{A_b} = \sqrt{(\Delta R_1)^2\left(\frac{\partial Ab}{\partial R_{sim,1}}\right)^2 + (\Delta R_2)^2\left(\frac{\partial Ab}{\partial R_{sim,2}}\right)^2 + (\Delta R_3)^2\left(\frac{\partial Ab}{\partial R_{sim,3}}\right)^2} \qquad \text{Equation 31}$$

This formula describes the error/tolerance of the estimated cross-sectional area of the blood (μ_{A_b}) caused by the independent uncertainty in the simulated resistance at different frequencies. The uncertainty of simulated resistance at each frequency was assumed to be the same ($\Delta R_i = \Delta R_1 = \Delta R_2 = \Delta R_3$), representing the absolute error between actual simulated resistance and theoretical resistance. In this chapter, the ΔR_i of 0.001 Ω, 0.005 Ω, 0.01 Ω, 0.05 Ω and 0.1 Ω were separately substituted in Equation 31.

4.4 Results and discussion section 1: The effects of electrode configurations on the current distribution

4.4.1 Electrode material

In the beginning, copper circular electrodes with a L_{CC} of 90 mm were simulated. Figure 21 illustrates the current density on plane A and plane B at 100 kHz. The overall current density distribution was symmetrical in plane A. The current was injected from the positive CC electrode into the outer fat layer and then conducted to the underlayers, reaching a maximum value of around 16 A/m^2 at the blood domain, directly below the inner side of CC electrodes. Then it gradually decreased in tissues at farther distances from CC electrodes, reaching the lowest value of approximately 0.068 A/m^2 at the fat domain in the middle region. The blood domain had the maximum current density of around 2.081 A/m^2 compared with other tissues, followed by the muscle domain.

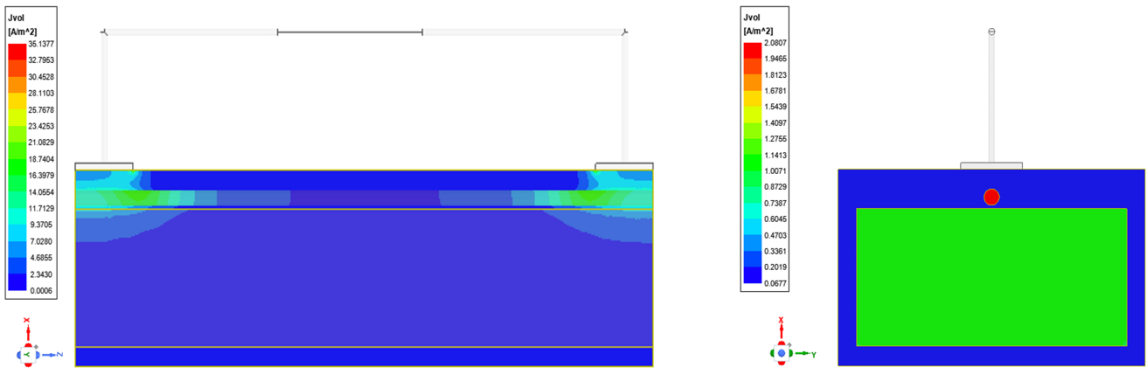

Figure 21. A typical current density overlay on plane A (left) and plane B (right) at 100 kHz.

However, different metal electrode materials did not exhibit any perceptible differences, as shown in Figure 22 where the current density curves of the three materials overlapped each other at all frequencies on both planes. This phenomenon can be explained as the HFSS platform simulated and analysed the model under ideal conditions without the effect of skin-

electrode contact impedance. As a result, electrodes here only played the role of the conductor. Therefore, the influence of the electrode materials could be ignored, and platinum was assigned in all subsequent simulations.

Table 10 exhibits the average current density values in each tissue layer and its standard deviation (SD) on line B at 100 kHz. The SD indicates the amount of variation and dispersion of current density within the same tissue domain. In addition to numerically showing the differences between tissue domains, it was found that within the same tissue (fat), deeper regions have a slightly lower current density.

Table 11 lists the proportion of injected current (1 mA) in each tissue with four different frequencies, indicating the effects of frequency on the current distribution of different tissues. Even though the blood domain showed the highest current density, the vast majority of current (around 95%) flowed in muscle domain because of its fairly high conductivity and the largest volume percent of the whole wrist model.

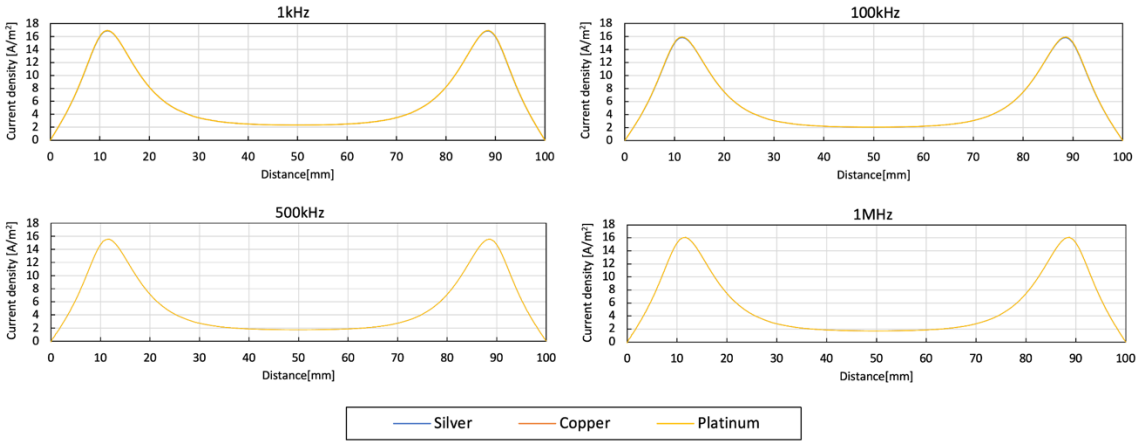

Figure 22. Current density distribution inside the artery with different electrode materials.

Table 10. The current density in each tissue domain with platinum electrode materials at 100 kHz.

Depth [mm]	**Tissues**	**Current density [A/m^2]**	
		Mean	**SD**
0-3	fat	0.072	4.25×10^{-5}
3-5.5	blood	2.063	1.67×10^{-3}
5.5-6	fat	0.071	4.58×10^{-4}
6-27	muscle	1.021	9.01×10^{-3}
27-30	fat	0.068	1.08×10^{-5}

Table 11. The proportion of injected current in each tissue domain with platinum electrode materials.

Tissues	Proportion of current			
	1 kHz	**100 kHz**	**500 kHz**	**1 MHz**
fat	4.17%	4.04%	3.37%	3.05%
blood	1.14%	1.02%	0.89%	0.88%
muscle	94.68%	94.94%	95.73%	96.07%

4.4.2 The spacing between CC electrodes

Figure 23 illustrates the significant impacts of L_{CC} on the current density distribution from both horizontal and vertical aspects. Figure 24 shows the current vector throughout the whole wrist model from the front, left and top views, respectively. The injected current propagated from the edge of the positive CC electrode to the surroundings and converges at the edge of the negative CC electrode. With L_{CC} of 90 mm, the direction of passing current was constantly changing during the conduction and tended to be parallel to each tissue in the middle region. The parallel region became larger in deeper tissue domains. However, this parallel trend was inconspicuous with shorter L_{CC} of 70 mm and almost disappears with L_{CC} of 50 mm.

Figure 25 shows various current density curves in the centre of the artery. The arc of the density curve increased with decreasing L_{CC}. The maximum current density appeared nearby the CC electrodes and gradually decreased to the minimum value in the middle region between CC electrodes. The peak current density with L_{CC} of 90 mm was higher than two others because the outer edge of CC electrodes coincided with the wrist model's outer edge, inducing the only positive direction propagation.

Table 12 illustrates the average current density in each tissue domain at 100 kHz. L_{CC} of 50 mm showed the highest value in all tissues, especially in the blood domain (3.726 A/m^2), almost twice as much as that in L_{CC} of 90 mm (2.065 A/m^2). However, it showed more significant discrepancies within the same tissue region. For example, in the blood domain, the SD in L_{CC} of 50 mm (2.82×10^{-2} A/m^2) is around 22 times larger than that in L_{CC} of 90 mm (1.27×10^{-2} A/m^2), indicating a less uniform current distribution. According to Table

13, more current flowed into the superficial region (fat and blood) with decreasing L_{CC}, demonstrating a negative relationship between current propagation depth and L_{CC}.

A shorter L_{CC} usually means the overall system could take up less space with higher portability in actual measurement. However, an excessive shortening limited the path of current propagation, weakening the required uniform region for impedance measurement.

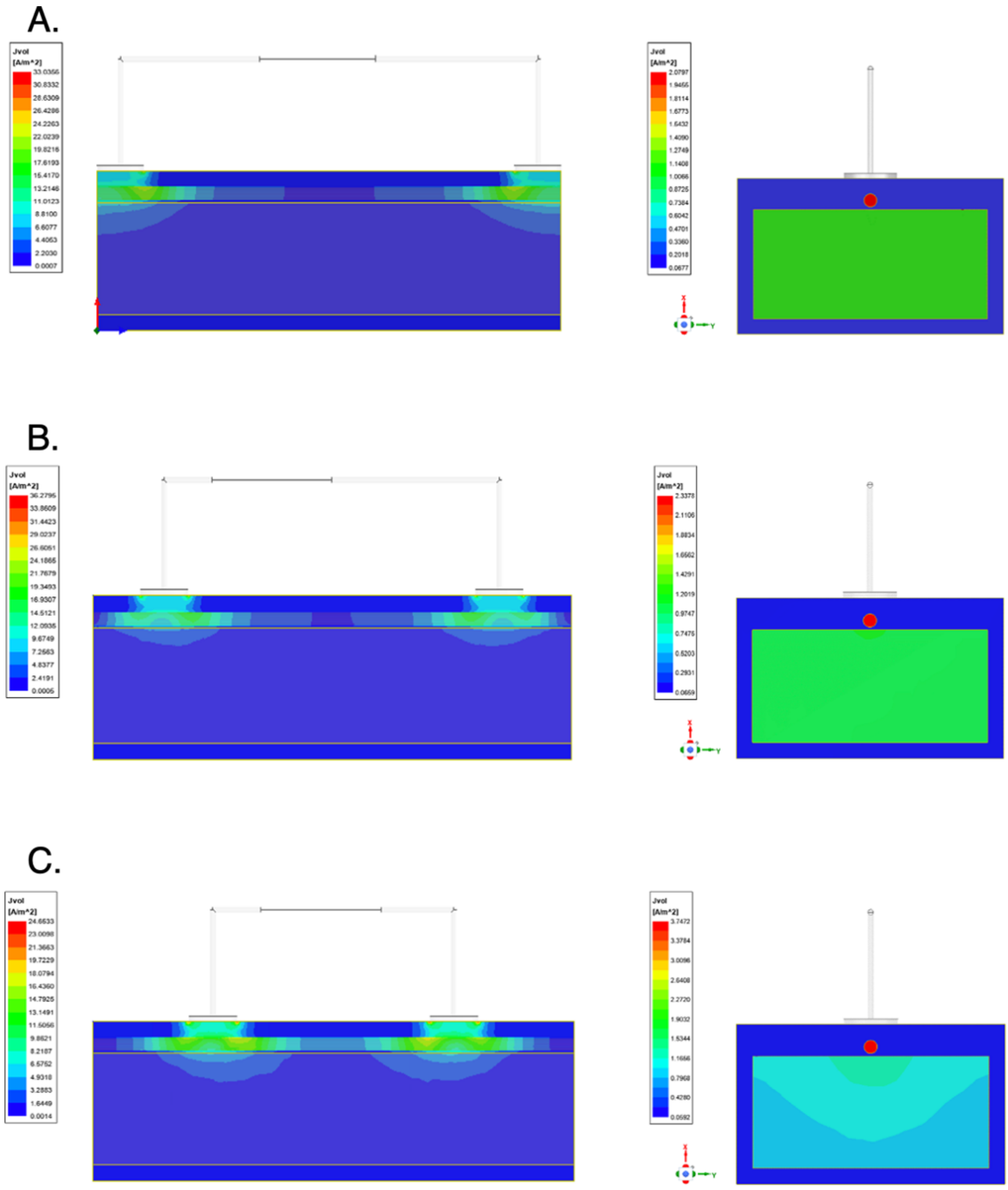

Figure 23. Current density overlays with different L_{CC} at 100 kHz: (A) L_{CC} = 90 mm; (B) L_{CC} = 70 mm; (C) L_{CC} = 50 mm.

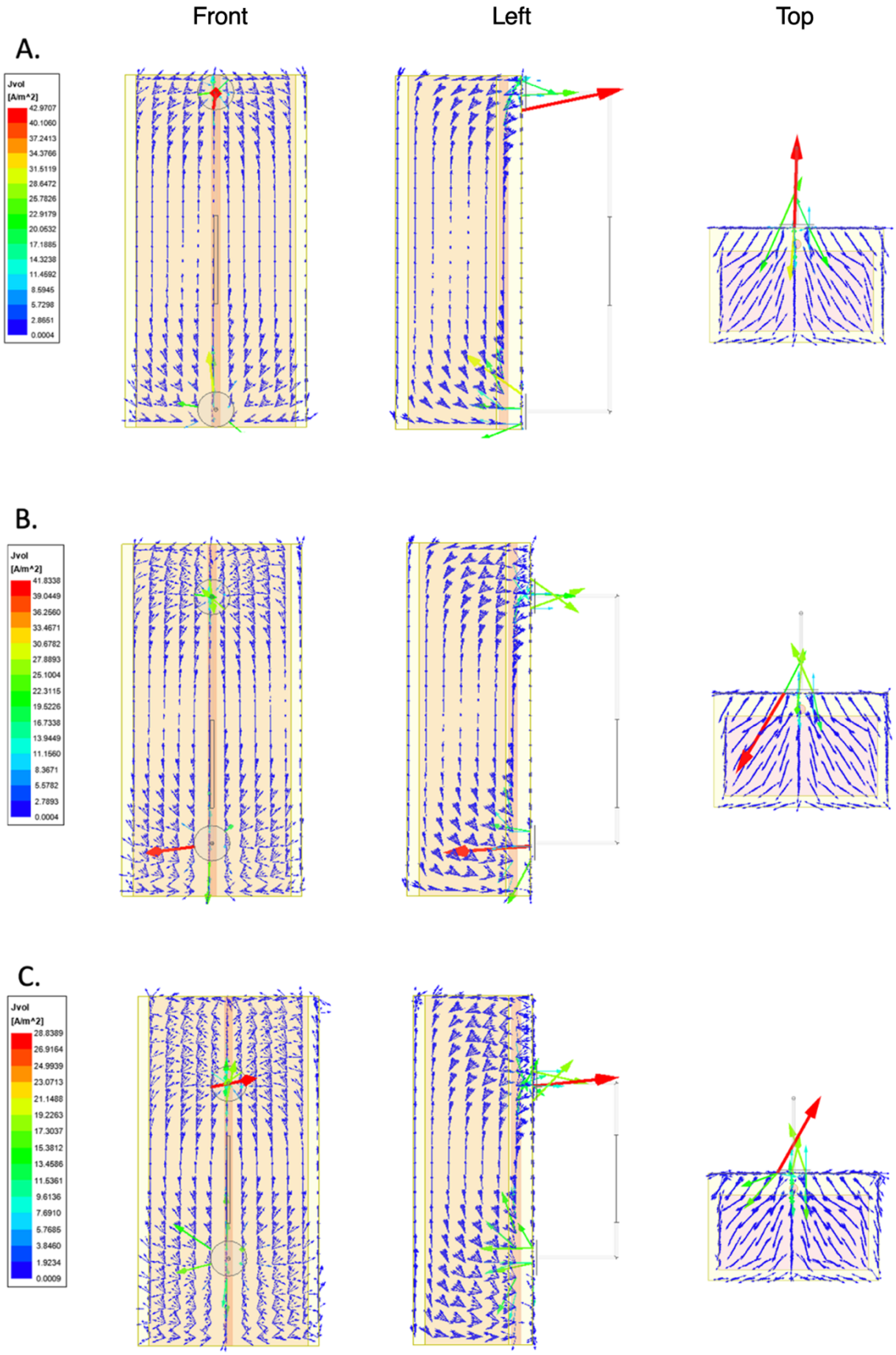

Figure 24. The current density vector of different L_{CC} at 100 kHz: (A) L_{CC} = 90 mm; (B) L_{CC} = 70 mm; (C) L_{CC} = 50 mm.

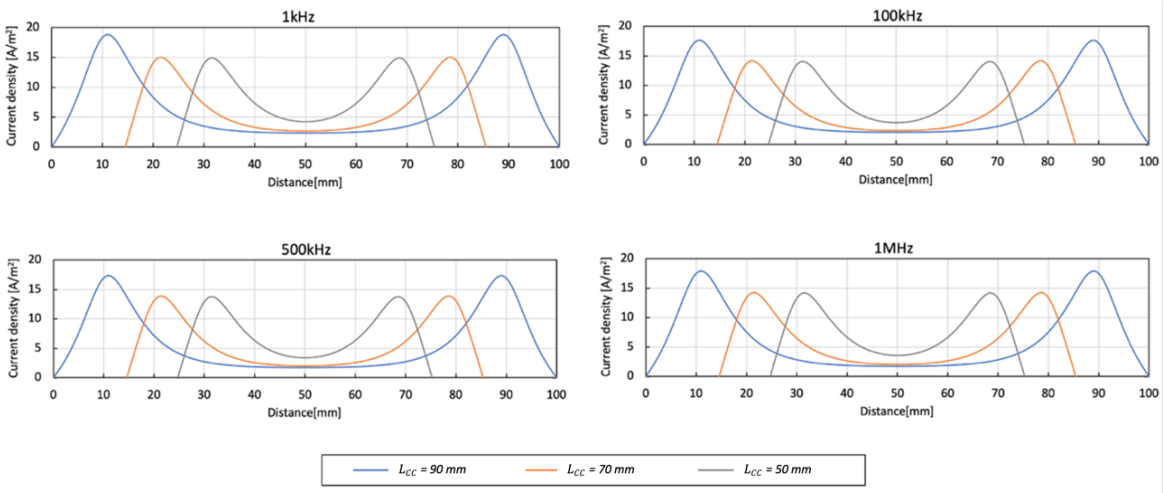

Figure 25. Current density distribution inside the artery with different L_{CC}.

Table 12. The current density in each tissue domain with different L_{CC} at 100 kHz.

Depth [mm]	Tissues	Current density [A/m²]					
		L_{CC} = 90 mm		L_{CC} = 70 mm		L_{CC} = 50 mm	
		Mean	SD	Mean	SD	Mean	SD
0-3	fat	0.072	7.08×10^{-5}	0.080	2.30×10^{-4}	0.129	4.88×10^{-3}
3-5.5	blood	2.065	1.27×10^{-3}	2.329	5.04×10^{-3}	3.726	2.82×10^{-2}
5.5-6	fat	0.071	4.84×10^{-4}	0.076	2.01×10^{-3}	0.105	1.11×10^{-2}
6-27	muscle	1.021	8.75×10^{-3}	1.034	2.90×10^{-2}	1.080	0.116
27-30	fat	0.068	1.83×10^{-5}	0.067	6.15×10^{-5}	0.063	1.48×10^{-4}

Table 13. The proportion of injected current in each tissue domain with different L_{CC}..

Tissues	Frequency [Hz]	Proportion of current		
		L_{CC} = 90 mm	L_{CC} = 70 mm	L_{CC} = 50 mm
fat	1k	4.17%	4.37%	5.44%
	100k	4.04%	4.21%	5.27%
	500k	3.37%	3.55%	4.61%
	1M	3.05%	3.23%	4.29%
blood	1k	1.14%	1.28%	1.92%
	100k	1.02%	1.13%	1.70%
	500k	0.89%	1.01%	1.61%
	1M	0.88%	1.01%	1.67%
muscle	1k	94.68%	94.35%	92.64%
	100k	94.94%	94.66%	93.02%
	500k	95.73%	95.44%	93.79%
	1M	96.07%	95.76%	94.04%

4.4.3 Electrode shape

The rectangular electrode caused slight differences in current density curves compared to the circular electrode model, as shown in Figure 26. The primary distinction of around 2 A/m^2 appeared in regions near CC electrodes, while this divergence gradually disappeared in the middle area. The initial understanding of this appearance was that the current density of surrounding sections of CC electrodes was affected by the dimension of CC electrodes. In these two simulations, the contact area of the rectangular electrode was 100 mm^2, whereas the circular electrode had a smaller contact area, which is approximately 78.54 mm^2. Therefore, the smaller contact area has a greater current density for the same amount of injected current (1 mA), but it gradually diluted through tissues. To confirm the preliminary explanation, various dimensions of both rectangular and circular electrodes were simulated and will be discussed in the next section.

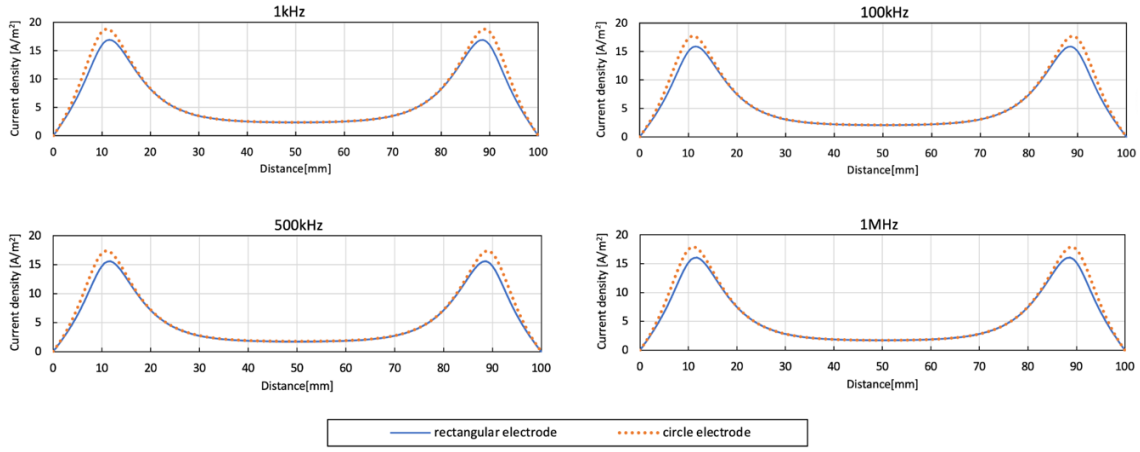

Figure 26. Current density distribution inside the artery with different electrode shapes.

4.4.4 Electrode dimension

The influence of electrode contact area on current distribution was initially noticed when comparing rectangular and circular electrodes. The circular electrodes were thereby tested with three different diameters: 10 mm, 9 mm, and 8 mm to further confirm this finding. Figure 27 indicates that the smaller contact area induced a greater current density near CC electrodes. However, this difference was not apparent in the middle of the region.

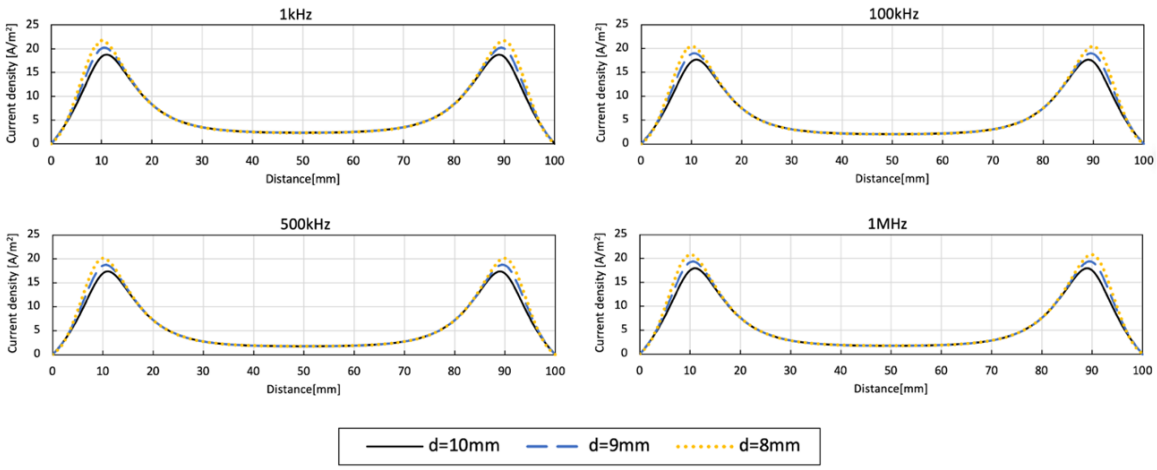

Figure 27. Current density distribution inside the artery with different diameters (d) of circular electrodes.

Furthermore, the rectangular electrode was extended to three times (30 mm) and five times (50 mm) of the original width. Figure 28 shows the current vectors from the front, left and top views. The variation in current distribution caused by the changes in width was significant. The larger contact area dramatically reduced the peak value of current density near the CC electrodes, as shown in Figure 29. At the same time, the overall current distribution became more uniform. The current density changes more gently from both ends of CC electrodes to the middle area. Table 14 numerically demonstrates that the SD of current density in each tissue decreased with increasing width, indicating a more consistent current density within each tissue domain. Furthermore, wider electrode spacing induced slightly more current to flow into deeper regions (muscle), as shown in Table 15. These results revealed that in addition to increasing L_{CC}, the uniformity of current distribution can be further improved by increasing the contact area, driving the subsequent simulations.

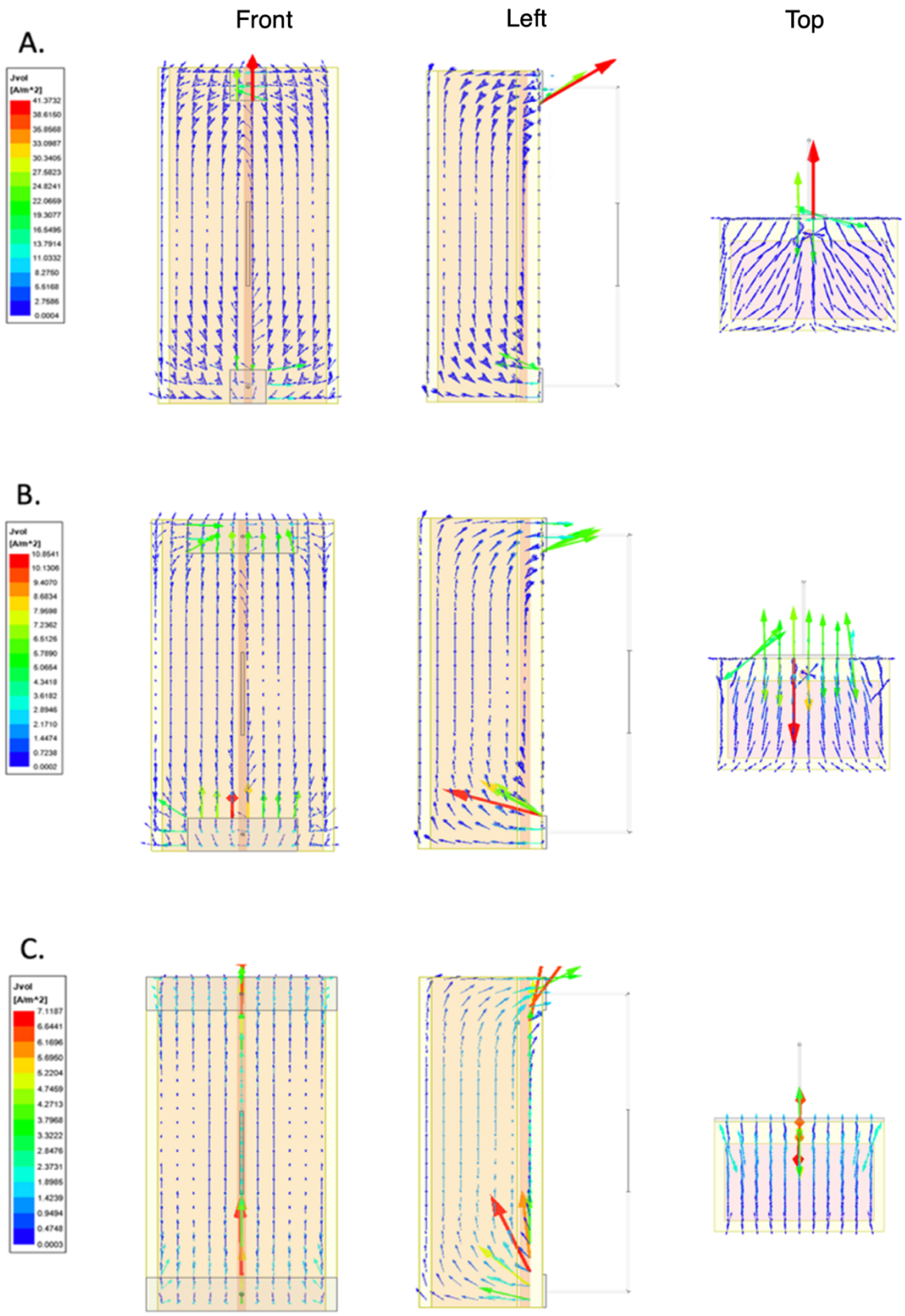

Figure 28. The current density vectors with different widths of rectangular electrodes at 100 kHz: (A) 10 mm; (B) 30 mm; (C) 50 mm.

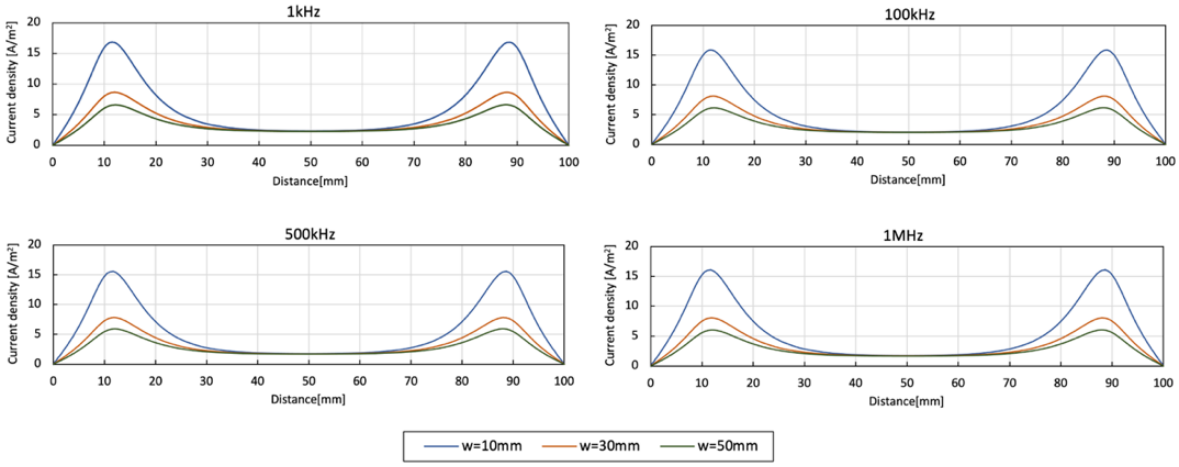

Figure 29. Current density distribution inside the artery with different widths (W) of rectangular electrodes.

Table 14. The current density in each tissue domain with different widths of rectangular electrodes at 100 kHz.

Depth [mm]	Tissues	Current density [A/m^2]					
		Width=10 mm		Width=30 mm		Width=50 mm	
		Mean	SD	Mean	SD	Mean	SD
0-3	fat	0.071	4.26×10^{-5}	0.070	1.30×10^{-5}	0.070	6.76×10^{-6}
3-5.5	blood	2.063	1.64×10^{-3}	2.027	7.74×10^{-4}	2.011	5.14×10^{-4}
5.5-6	fat	0.071	4.59×10^{-4}	0.070	2.85×10^{-4}	0.069	2.20×10^{-4}
6-27	muscle	1.021	8.99×10^{-3}	1.016	6.87×10^{-3}	1.014	6.04×10^{-3}
27-30	fat	0.068	1.04×10^{-5}	0.068	3.20×10^{-5}	0.068	1.48×10^{-5}

Table 15. The proportion of injected current in each tissue domain with different widths of rectangular electrodes.

Tissues	Frequency [Hz]	Proportion of current		
		Width=10 mm	Width=30 mm	Width=50 mm
fat	1k	4.17%	4.14%	4.13%
	100k	4.02%	4.01%	4.00%
	500k	3.37%	3.35%	3.34%
	1M	3.05%	3.02%	2.99%
blood	1k	1.15%	1.13%	1.12%
	100k	1.02%	1.01%	1.00%
	500k	0.89%	0.88%	0.87%
	1M	0.88%	0.86%	0.86%
muscle	1k	94.68%	94.73%	94.75%
	100k	94.96%	94.99%	95.00%
	500k	95.73%	95.77%	95.79%
	1M	96.07%	96.11%	96.15%

4.4.5 Band-type electrodes

In addition to the conventional 4-spot electrode configuration, this research also investigated two band-type electrodes inspired by the discovery from the previous section that the direction of ejected current flow can be altered by changing the electrode-tissue contact area. It was expected that the current source could be designed to uniformly distribute throughout the wrist by expanding the width of CC electrodes.

Figure 30 illustrates the horizontal and vertical current density overlays with band-type electrodes. The magnitude of current density with the band electrode was more uniform than the semi-band electrode in all tissue domains. Consistent with the expected result, the band electrode changed the injected direction of the current so that more tissue regions were in parallel with the current flow (see Figure 31).

Figure 32 demonstrates the specific current density inside the blood domain. The rectangular electrode model with a width of 50 mm was re-produced for comparison purposes. Both semi-band and band electrodes could reduce the significant differences in the current density near the CC electrodes. The adjustment effect of applying band electrodes was more significant in contrast with semi-band electrodes. The range of the horizontal section (i.e., distance from 25 mm to 75 mm on the x-axis) extended to around 50 mm in the middle, indicating a wider uniform region.

Table 16 illustrates the vertical current density differences between tissue domains. Compared to the spot electrode, the band electrode slightly augmented the current density of around 0.0002 A/m^2 (0.2%) in the deepest fat layer between 27 mm and 30 mm. Furthermore, the band electrode showed a slightly higher current density in the muscle domain than the semi-band electrode. The band electrode can ensure that the same amount of current was evenly injected into the outermost fat layer around the wrist. Furthermore, the current density inside each tissue domain was more consistent. The semi-band electrode decreased the SD by about 40% compared with the rectangular electrode. More impressively, the band electrode reduced the SD to only 6.09% and 0.81% of the original SD (4-spot electrodes configuration) in the blood and muscle domains, respectively. No significant difference in the proportion of current was found between semi-band electrode and band electrode according to Table 17.

The band electrode exhibited outstanding performance compared to the conventional 4-spot electrodes approach in this simulation. The current was reasonably regarded as uniform in all tissues within the middle 75% region between CC electrodes.

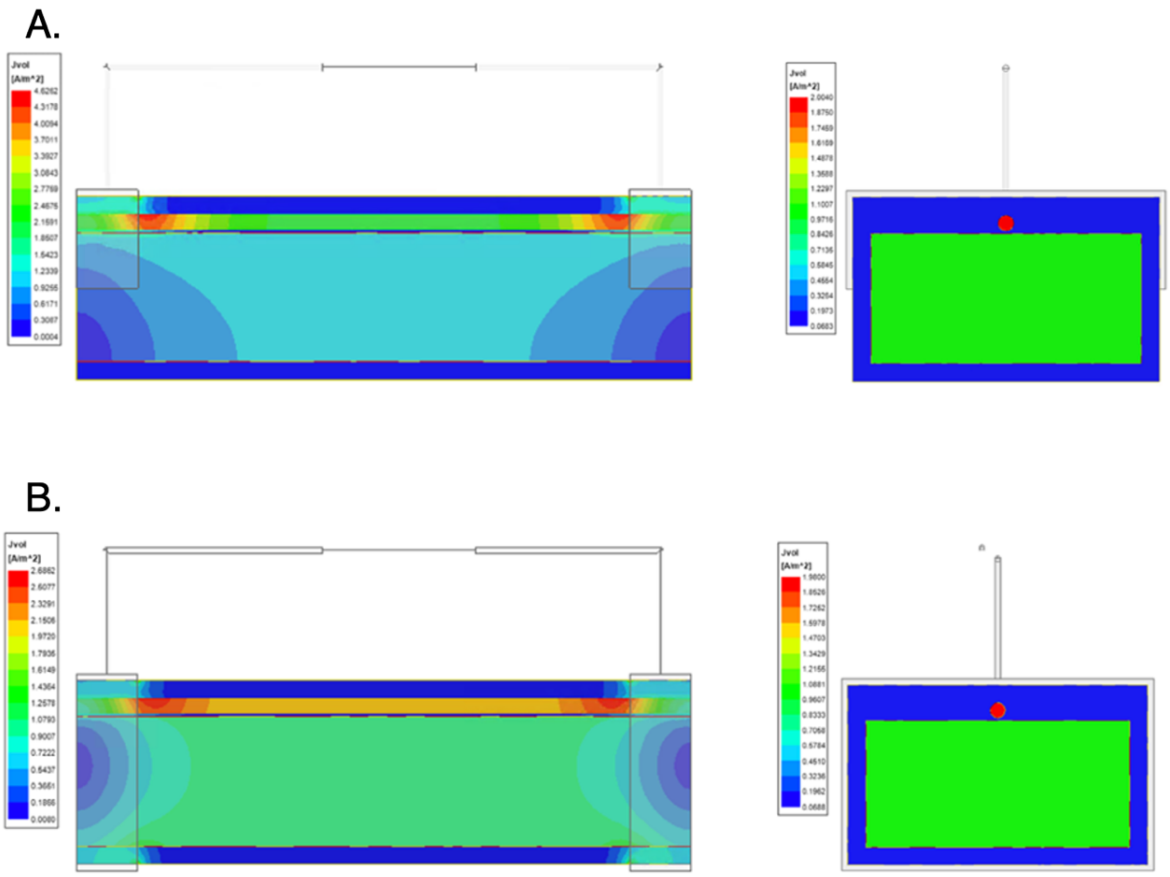

Figure 30. Current density overlays with band-type electrodes at 100 kHz: (A) semi-band electrode; (B) band electrode.

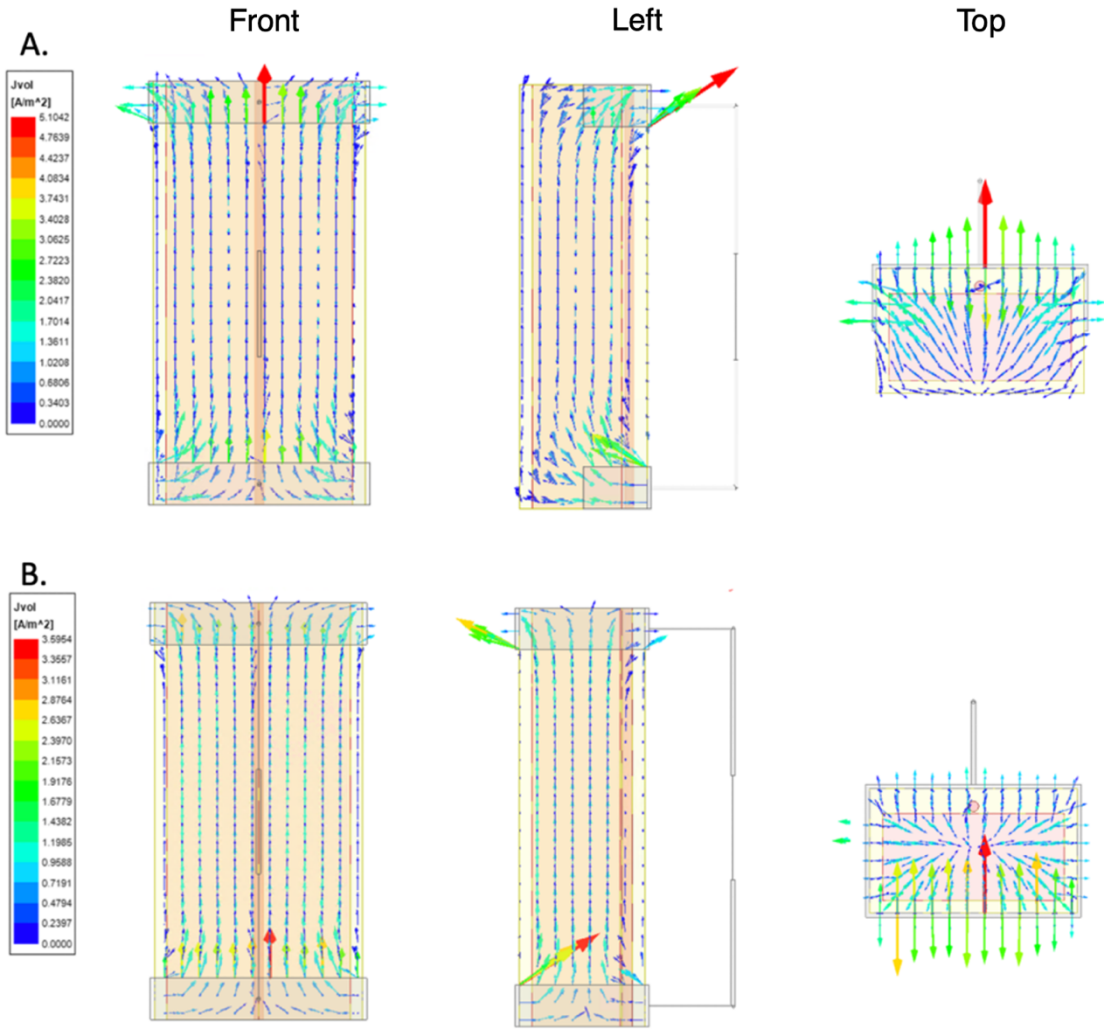

Figure 31. The current density vectors with band-type electrodes at 100 kHz: (A) semi-band electrode; (B) band electrode.

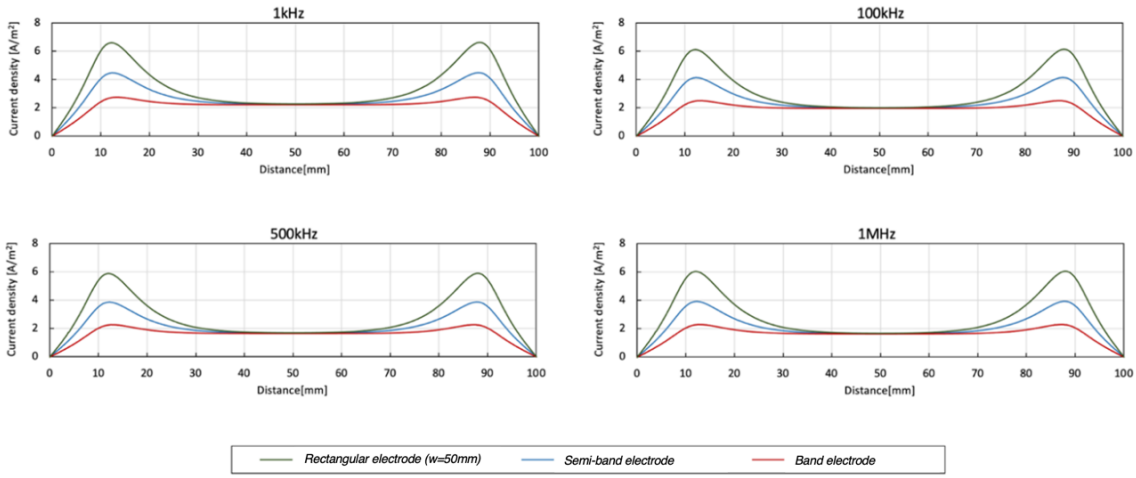

Figure 32. Current density distribution inside the artery with band-type electrodes.

Table 16. The current density in each tissue domain with band-type electrodes at 100 kHz.

Depth[mm]	Tissues	Current density [A/m^2]			
		Semi-band electrode		Band electrode	
		Mean	SD	Mean	SD
0-3	fat	0.069	1.25×10^{-5}	0.068	6.54×10^{-6}
3-5.5	blood	1.989	3.45×10^{-4}	1.966	3.09×10^{-5}
5.5-6	fat	0.068	1.16×10^{-4}	0.068	3.13×10^{-7}
6-27	muscle	1.011	4.13×10^{-3}	1.012	2.62×10^{-5}
27-30	fat	0.068	1.11×10^{-5}	0.068	5.86×10^{-7}

Table 17. The proportion of injected current in each tissue domain with band-type electrodes.

Tissues	Frequency [Hz]	Proportion of current	
		Semi-band electrode	Band electrode
fat	1k	4.09%	4.09%
	100k	4.01%	3.95%
	500k	3.31%	3.30%
	1M	2.98%	2.98%
blood	1k	1.11%	1.10%
	100k	0.99%	0.98%
	500k	0.87%	0.85%
	1M	0.85%	0.84%
muscle	1k	94.80%	94.81%
	100k	95.00%	95.07%
	500k	95.83%	95.84%
	1M	96.17%	96.18%

4.5 Results and discussion section 2: Estimation of arterial diameter change

4.5.1 E-field distribution

Figure 33 illustrates the E-field distribution with eight different electrode configurations. The E-field was mathematically proportional to the current density when the conductivity was constant. Therefore, the distribution of E-field showed a similar trend to the current density discussed in the previous section. The maximum E-field appeared near the CC electrodes and gradually decreased to the surrounding regions. The peak value of E-field reduced with increasing contact area between electrodes and the tissue surface. The band electrode generated the most uniform field as expected.

In this section, the most suitable region in the middle was explored to place PU electrodes by comparing the uniformity of the E-field. Figure 34 presents the scatter plots of the first numerical derivative of the E-field between CC electrodes. The E-field changes significantly within a few millimetres of nearby CC electrodes. Comparing the charts in the first column, in the entire range (from the inner edge of the positive CC electrode to the inner edge of the negative CC electrode), the circular electrode showed the highest changing range, twice larger than the wide rectangular electrode and fifteen times larger than the band electrode. However, there were no significant impacts from different frequencies. As the spacing gradually approached the middle, the magnitude of the change became smaller, indicating a more uniform E-field. The range of numerical derivatives reduced to ± 10 V/m^2 when the distance fell between 30 mm and 50 mm with the circular electrode. However, in this distance range, the ranges of the numerical derivative were ± 3 V/m^2 and ± 0.1 V/m^2 with the wider rectangular electrodes and band electrodes, respectively. Thereby, band electrode configuration with a L_{cc} of 90 mm (i.e., Figure 16 (B)) was selected for the following simulation.

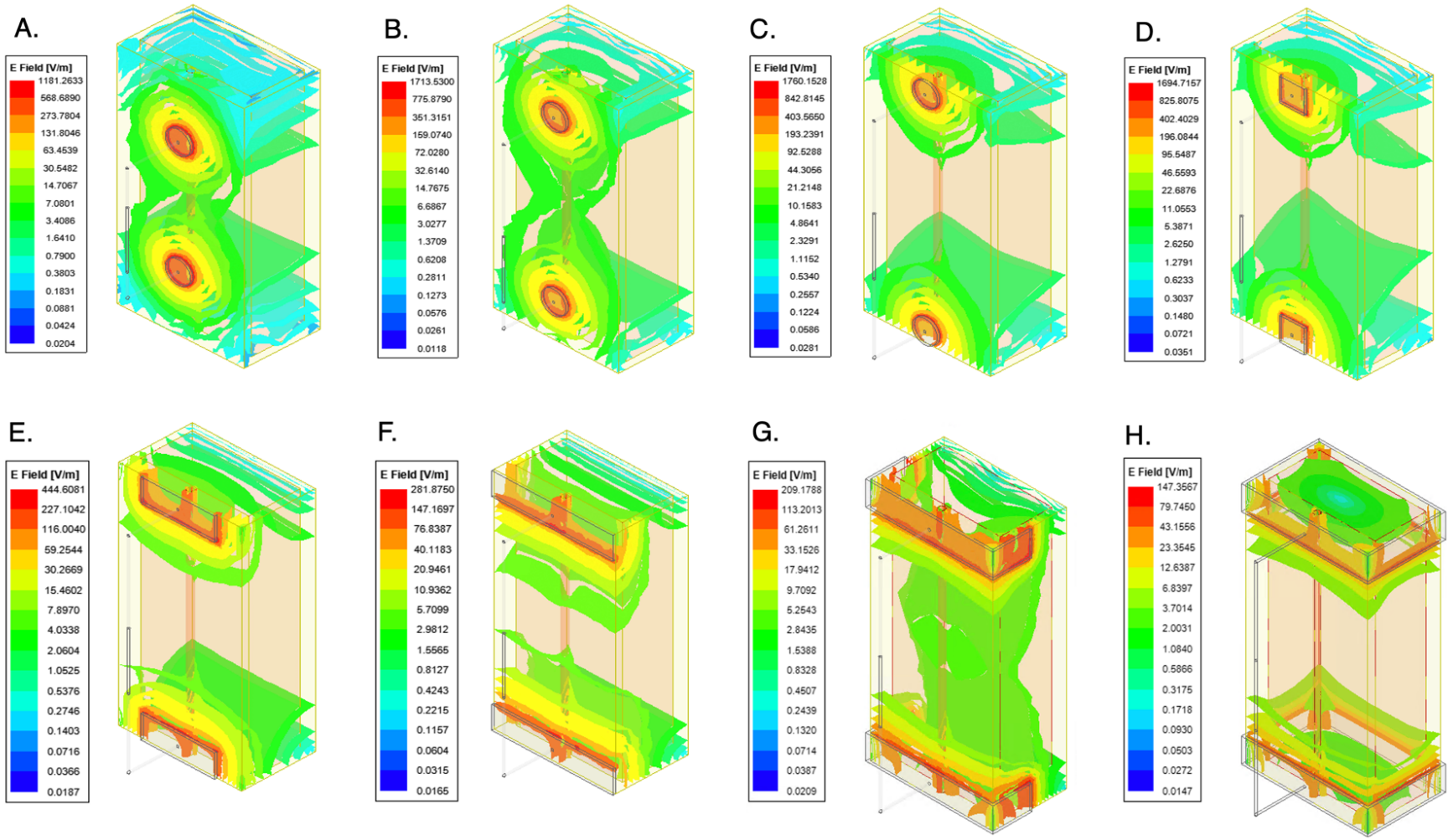

Figure 33. The colour maps of E-field distribution throughout the wrist model 1 at 100 kHz: (A) circular electrodes (d=10 mm, L_{CC}=90 mm); (B) circular electrodes (d=10 mm, L_{CC}=70 mm); (C) circular electrodes (d=10 mm, L_{CC}=50 mm); (D) rectangular electrodes (w=10 mm, L_{CC}=90 mm); (E) rectangular electrodes (w=30 mm, L_{CC}=90 mm) (F) rectangular electrodes (w=50 mm, L_{CC}=90 mm) (G) semi-band electrodes (L_{CC}=90 mm); (H) band electrodes (L_{CC}=90 mm)

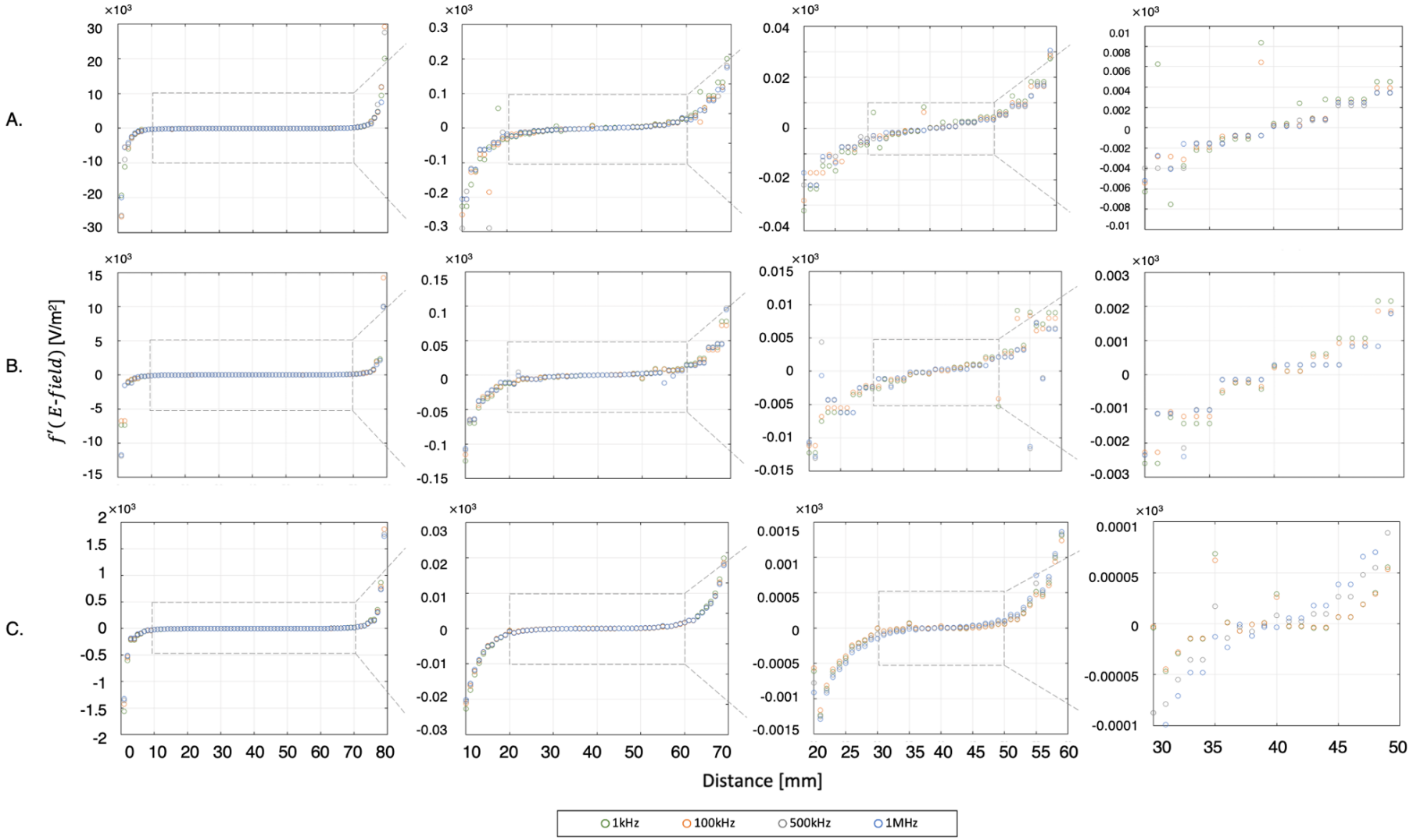

Figure 34. The first numerical derivative of the E-field between CC electrodes: (A) circular electrodes (d=10 mm, L_{CC}=90 mm); (B) rectangular electrodes (w=50 mm, L_{CC}=90 mm); (C) band electrodes (L_{CC}=90 mm).

4.5.2 Simulated impedance

Unlike the CC electrodes, the PU electrodes were not structured in a specific geometry in the model. More flexibly, the simulated impedance between PU electrodes was calculated using Equation 19 to Equation 22 without changing the 3D model. Based on the results concluded in the previous section, three locations of PU electrode pairs were investigated: 15 mm and 65 mm, 25 mm and 55 mm, and 35 mm and 45 mm, corresponding to different PU electrode spacings (L_{PU}) of 50 mm, 30 mm and 10 mm.

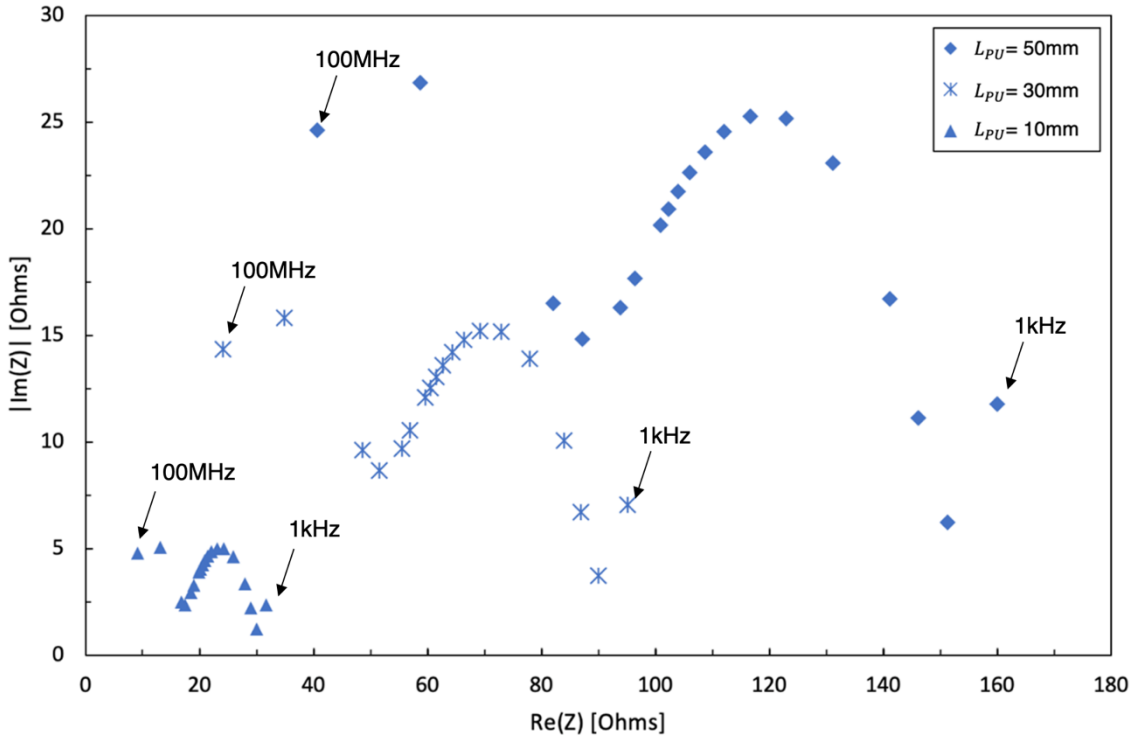

Figure 35. Nyquist plot (Cole plot) of the simulated $Re(Z)$ and $Im(Z)$ of the wrist model 1 (arterial diameter = 2.5 mm) with different L_{PU}.

The wrist model 1 showed a Cole-type dielectric response in the way the real part of the impedance ($Re(Z)$) and imaginary part of impedance ($Im(Z)$) varied with frequency, as shown in Figure 35. The semi-circular shape of the major portion of the plots (between 10 kHz to 2 MHz) agreed with the Cole model, indicating the bio-tissue behaviour of the simulated 3D model. Nevertheless, the simulation diverged from the Cole model at 1 kHz and higher frequencies above 5 MHz. Consistent with the theory, both $Re(Z)$ and $Im(Z)$ showed nearly proportional relationship with increasing L_{PU}. Moreover, $Re(Z)$ decreased as the frequency increased, corresponding with the increasing conductivity.

The wrist model 1with an artery diameter of 2.5 mm (i.e., simulated and analysed in section 4.4) was defined as the basal condition, while the expansion and contraction of the radial artery were represented by simulations conducted for the varied diameters: 2.60 mm, 2.55 mm, 2.45 mm, and 2.40 mm. Figure 36 demonstrates that the simulated $Re(Z)$ and $Im(Z)$ were negatively correlated with the arterial diameter. As the arterial diameter increased, the simulated impedance decreased, and vice versa, confirming the main contribution of blood volume change on the overall measured impedance due to its significantly higher conductivity than other tissues. Furthermore, the range of the $Re(Z)$ over the maximum to minimum diameters reduced with decreasing L_{PU} and increasing frequency. In other words, a larger impedance amplitude in response to a pulse could be sensed in the actual BIM on human body by increasing the L_{PU} and using a lower frequency. However, no consistent trends were found in $Im(Z)$.

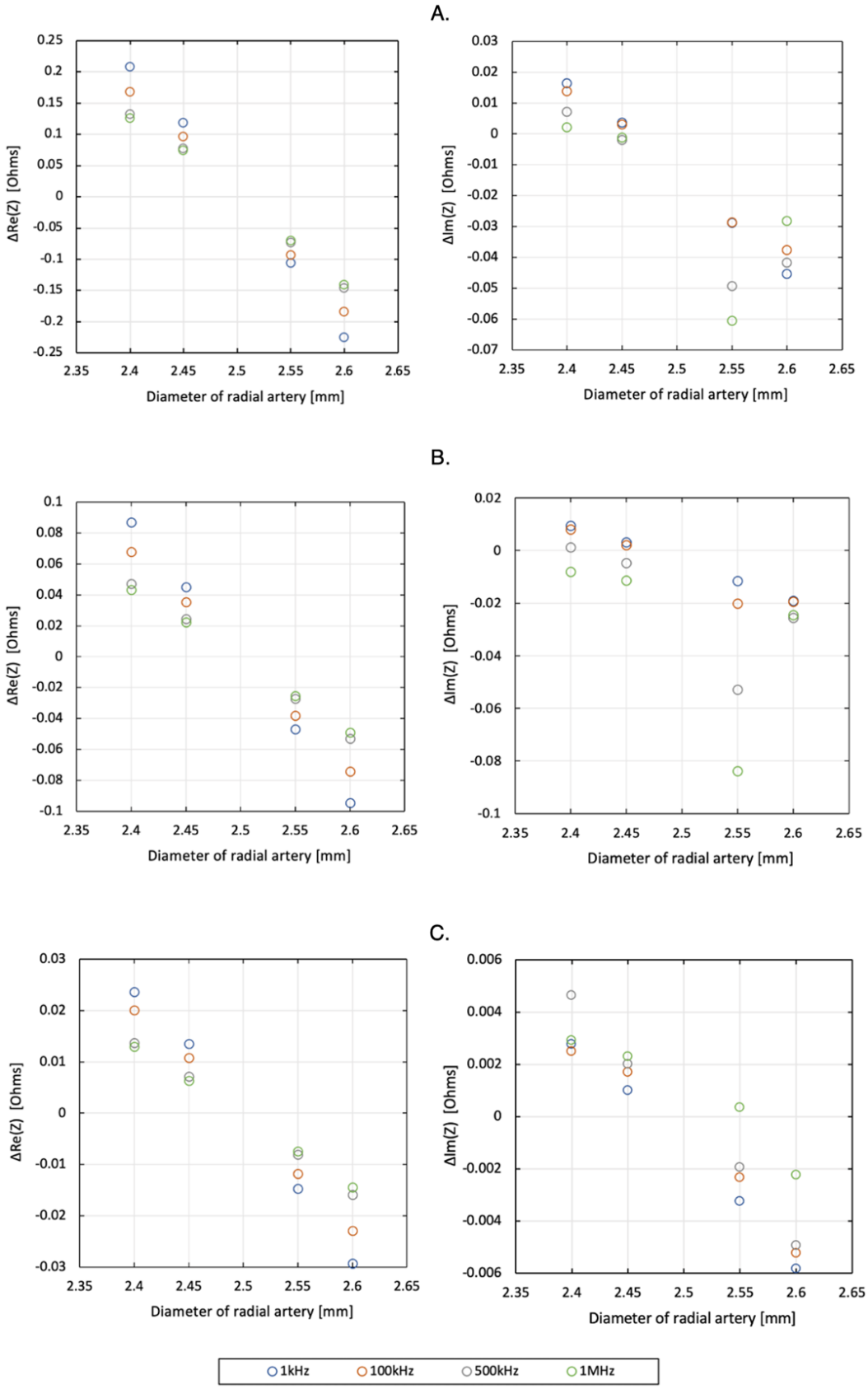

Figure 36. The variation of the simulated $\mathrm{Re}(Z)$ and $\mathrm{Im}(Z)$ of the wrist model 1 caused by arterial diameter changes with different L_{PU}: (A) L_{PU} = 50 mm; (B) L_{PU} = 30 mm; (C) L_{PU} = 10 mm.

4.5.3 Estimated arterial cross-sectional area change

The modelled cross-sectional area changes were 0.4006 mm^2, 0.1983 mm^2, -0.1944 mm^2 and -0.3848 mm^2. Figure 37 shows the estimated cross-sectional area changes with three different L_{PU}. The red line provides the reference/target values. Even though larger L_{PU} was found more sensitive to blood volume changes, it did not lead to a more accurate estimation. Conversely, shortest L_{PU} of 10 mm induced the closest estimated cross-sectional area changes. According to the analysis of the E-field distribution in the previous section, it can be explained that the shorter L_{PU} covered a more uniform E-field region in the middle, which was more in line with the assumption in the proposed mathematical modelling.

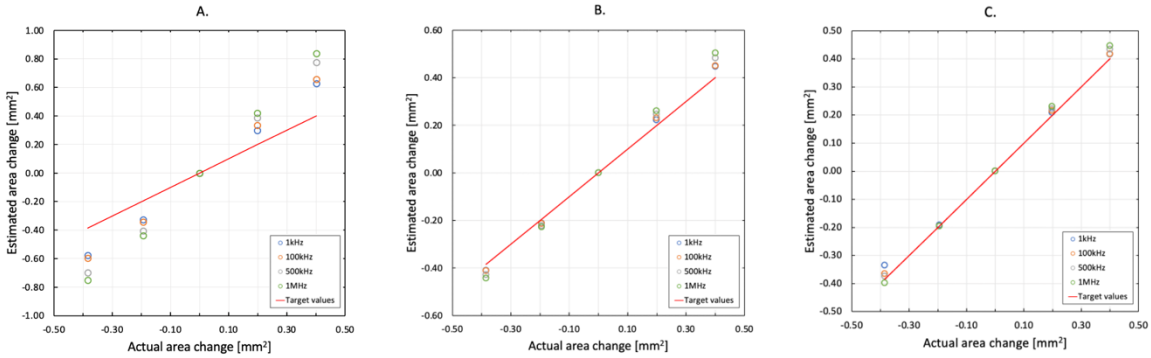

Figure 37. The estimated arterial cross-sectional area changes with different L_{PU}: (A) L_{PU} = 50 mm; (B) L_{PU} = 30 mm; (C) L_{PU} = 10 mm.

4.5.4 Estimated artery diameter

The real time arterial diameter can be obtained from the impedance variances if we know the initial/basal arterial diameter. In this simulation, the basal arterial diameter of 2.5 mm was assumed to be a known parameter for calibration. Figure 38 demonstrates the percent error between estimated and actual arterial diameter. In accordance with the estimated cross-sectional area change, the shortest L_{PU} of 10 mm showed the lowest error. It is found that percent errors gradually increased with increasing diameter variation. The primary source of this error was the inherent difference between the simulation condition and the theoretical condition: The proposed mathematical modelling assumed the pulsation led to an additional volume change in the original geometry. However, in the simulation setup, the arterial diameter change was implemented by re-assigning the surrounding region (i.e., fat) of the artery, which means the overall volume of the wrist was kept the same as the original

geometry. For instance, when the arterial diameter increased to 2.6 mm from 2.5 mm, a tiny fat domain of 4.005 mm^3 (L_{PU} = 10 mm) was replaced by the blood. From a theoretical perspective, this missing volume of fat could induce a small drop in simulated resistance change (i.e., $R_0 - R_i$ in Equation 27), causing a slight percent error of 0.12% in estimated arterial diameter.

It was also found that the simulation at 1 kHz usually obtained the best estimation of all frequencies. It can be explained by the fact that 1 kHz showed a more significant $Re(Z)$ change responding to the same diameter variation under the same electrode configuration, as shown in Figure 36.

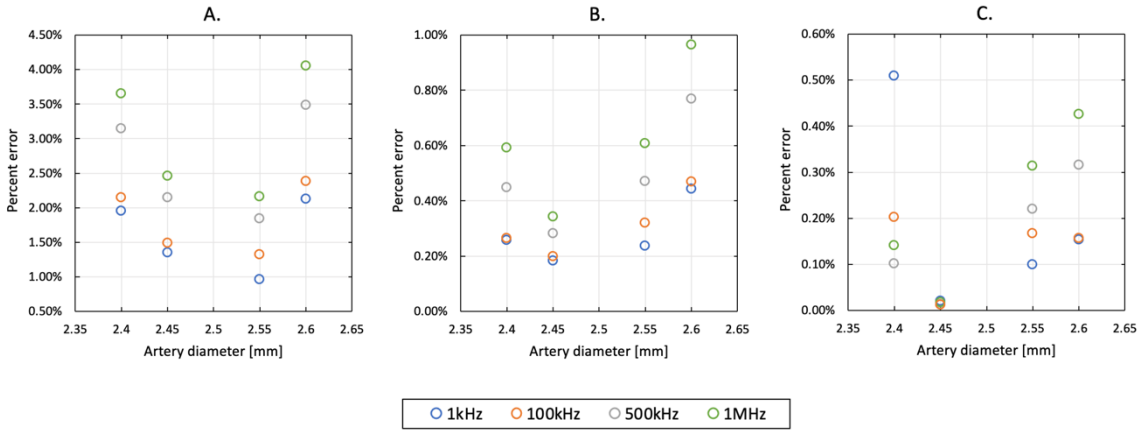

Figure 38. Percent errors of the estimated arterial diameters with different L_{PU}: (A) L_{PU} = 50 mm; (B) L_{PU} = 30 mm; (C) L_{PU} = 10 mm.

4.6 Results and discussion section 3: Estimation of the cross-sectional areas of tissues via multi-frequency impedance

In section 4.5.4, it was shown that the proposed mathematical model can accurately estimate the diameter change of the radial artery. However, an additional technique was required as an initial calibration for basal arterial diameter. This thesis also attempted to use the multi-frequency BIM to estimate the absolute cross-sectional areas of different tissues using their conductivities at different frequencies, as described in section 4.3.4. Figure 39 illustrates the differences between simulated (R_{sim}) and theoretical resistance (R_{theory}) with different L_{PU} at each frequency. The shortest L_{PU} of 10 mm exhibited the lowest absolute differences at all

frequencies as expected. R_{sim} at 1 kHz has a minimal error of 0.2311 Ω, while the error was over 1 Ω at 500 kHz.

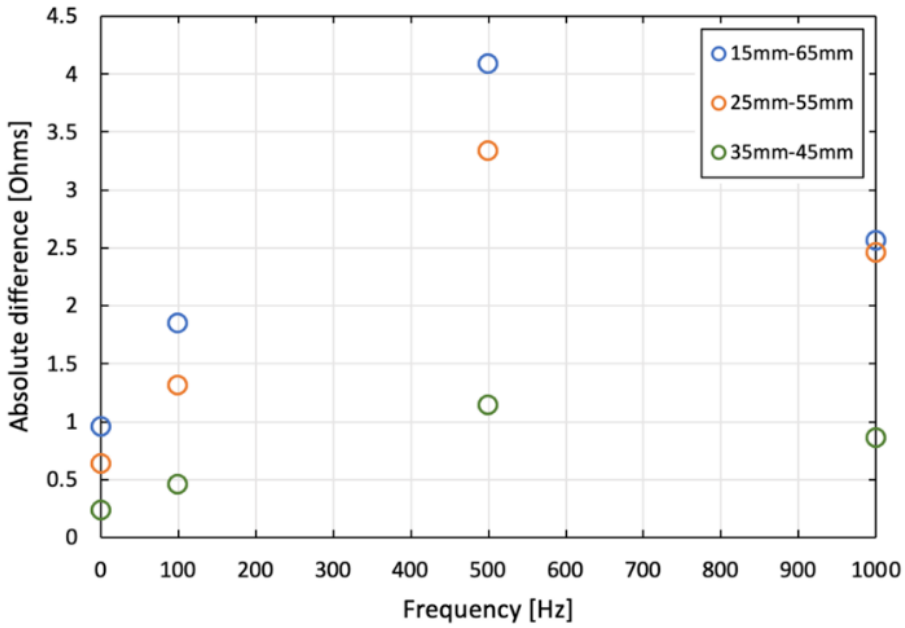

Figure 39. The absolute difference between the simulated and theoretical resistance with different L_{PU}.

The propagation of error was used to evaluate the assumed absolute differences (ΔR_i) between R_{theory} and R_{sim}, as shown in Table 18. The target cross-sectional area of the artery was 4.91 mm^2. The impact of uncertainty of R_{sim} on the final estimation was significant. For instance, when the uncertainty of the resistance was 0.01 Ω, the expected error of the estimated area (μ_{A_b}) would rise to around 50% of the true value. The expected error was even twice larger than the target value when the uncertainty ΔR_i was over 0.05 Ω. However, the actual absolute differences of R_{sim} were much bigger than the threshold of the simulated resistance error (i.e., assumed ΔR_i) according to Figure 39. It appears that the arterial cross-sectional area cannot be estimated based on the existing simulation results. Even if the accuracy of the simulation can be gradually improved by continuing to refine the mesh, there are more unavoidable factors that would cause higher experimental errors in the actual measurement. For example, one of the most common sources of errors would be the challenging contact impedance between electrodes and human skin.

Table 18. Expected errors of the estimated cross-sectional area of the artery

	Applied frequencies [Hz]	**Uncertainty of simulated resistance ΔR_i**				
		0.001Ω	**0.005 Ω**	**0.01 Ω**	**0.05 Ω**	**0.1 Ω**
Expected errors of artery cross-sectional area μ_{A_b}	1 k, 100 k, 500 k	0.24 mm^2	1.19 mm^2	2.38 mm^2	11.95 mm^2	23.90 mm^2
	1 k, 100 k, 1 M	0.23 mm^2	1.17 mm^2	2.33 mm^2	11.66 mm^2	23.33 mm^2
	1 k, 500 k, 1 M	0.22 mm^2	1.10 mm^2	2.19 mm^2	10.95 mm^2	21.90 mm^2
	100 k, 500 k, 1 M	0.20 mm^2	1.04 mm^2	2.07 mm^2	10.35 mm^2	20.70 mm^2

4.7 Closure

This chapter provided an insight into simulation performed for the initial verification of the proposed mathematical modelling described in Chapter 3. The initial human wrist segment was constructed using HFSS ANSYS. The basic wrist model (wrist model 1) was simplified as a cuboid geometry with outer fat layer, middle muscle domain, and one uniform blood-filled radial artery. The simulation setups were described, including the 3D model, the mesh setting, excitations, and the material assignment. Then, the data processing method was represented in detail. According to the simulation results and analysis, several outcomes were observed:

1. Different metal materials of electrodes did not affect the simulation results because the electrode-skin contact impedance did not exist in the simulation environment.
2. The current density in each tissue domain mainly depended on the conductivity of tissues. The higher conductivity of the tissue, the higher current density inside the tissue. However, this does not imply a higher proportion of current, which also depended on the relative tissue volume. Muscle is the main volume component of the initial wrist model and thereby contained most of the current.
3. The CC electrode spacing significantly affected the current density distribution: the larger L_{CC}, the more uniform the current density distribution in the middle region.
4. The contact area between CC electrodes and the outer tissue (fat layer in this chapter) affected the maximum value of current density near the CC electrodes. The larger size of CC electrodes, the larger the contact area, and the lower the current density below the CC electrodes.
5. The band electrode had the largest contact area wrapped around the entire wrist, generating a more parallel current flow and the most uniform E-field throughout all tissues. Thus, the band electrode configuration was selected for subsequent simulation.

6. According to the uniformity of E-field, PU electrodes should be placed in the middle, between CC electrodes, with a shorter L_{PU}.
7. Simulated $Re(Z)$ and $Im(Z)$ of the wrist model 1 showed a Cole-type response in the β-dispersion (from 1 kHz to 100 MHz). Additionally, both $Re(Z)$ and $Im(Z)$ showed a nearly proportional relationship with increasing L_{PU}.
8. Simulated $Re(Z)$ and $Im(Z)$ were negatively correlated with the arterial diameter. As the arterial diameter increased, the simulated impedance decreased.
9. The diameter of the simulated radial artery can be accurately estimated with the band electrode configuration (L_{CC} = 90 mm and L_{PU} = 10 mm) by using the proposed mathematical modelling. The percent errors were below 0.6% at all frequencies.
10. The accuracy of estimated cross-sectional areas of each tissue highly depended on the difference between R_{theory} and R_{sim}. According to the propagation of error analysis, it will be challenging to use the multi-frequency method to accurately estimate the cross-sectional area of each tissue in both simulation and actual measurement.

In conclusion, this chapter utilised a simplified human wrist model to simulate and analyse various electrode configurations (e.g., spacing, materials, shape, and dimension), helping in understanding the dielectric response of a multi-tissue domain and blood flow, the current distribution throughout the wrist region, and the optimisation of electrode setup for arterial pulse sensing, without the need for extensive experimentation. The band electrode configuration was selected because of its promising capability to generate a more uniform E-field than the conventional 4-spot electrode configuration. Furthermore, longer L_{CC} of 90 mm and shorter L_{PU} of 10 mm in the middle region were recommended to probe more accurate impedance changes. By applying this configuration, the arterial diameter can be accurately estimated. However, in terms of estimating the cross-sectional area of tissues, simulations uncovered challenges that are difficult to overcome, leaving a research gap worth exploring in the future.

CHAPTER 5. SIMULATION ANALYSIS OF DIFFERENT TISSUE DOMAINS

5.1 Introduction

The primary purpose of this chapter was to further validate the capability of the proposed mathematical modelling to estimate the blood cross-sectional area change and arterial diameter by stepwise adding other accessorial tissue domains and complexity. The promising band electrode configuration (L_{CC} = 90 mm and L_{PU} = 10 mm) determined in Chapter 4 continued to be utilised. Another objective of this chapter was to analyse different dielectric responses of other tissues (i.e., skin, bones and contralateral blood-filled artery) to explore their contribution under BIM, providing evidence to model tissue domains in future simulations more reasonably.

The overall simulation was divided into five stages, as shown in Table 19. Stage 1 has been described in Chapter 4, and the rest will be introduced in this chapter, including the geometrical modifications of the wrist model and analyses of corresponding simulation results in sequence.

Table 19. Stages for computational simulation.

Stages	**3D models**	**Tissue domains**						**Geometry boundary**	**Electrode configurations**	**Chapter**
		Fat	Muscle	Radial artery	Skin	Bones	Ulnar artery			
1	Wrist model 1	✓	✓	✓				Linear	Various	4
2	Wrist model 2	✓	✓	✓	✓				Band electrode L_{CC} = 90 mm L_{PU} = 10 mm	5
3	Wrist model 3	✓	✓	✓	✓	✓				
4	Wrist model 4	✓	✓	✓	✓	✓		Curve		
5	Wrist model 5	✓	✓	✓	✓	✓	✓	Linear		

5.2 Updated wrist model with the skin

5.2.1 Modified geometry with skin

The overall dimension of the wrist model 2 maintained the same cuboid geometry (30 mm × 50 mm × 100 mm), as shown in Figure 40. The outermost 0.5 mm section of the fat layer was used to represent skin tissue, based on data from ultrasonic imaging of the human volar forearm [243]. The frequency-dependent bulk conductivity and relative permittivity (see Table 37 in the Appendix) of human skin tissue were assigned, as shown in Figure 41.

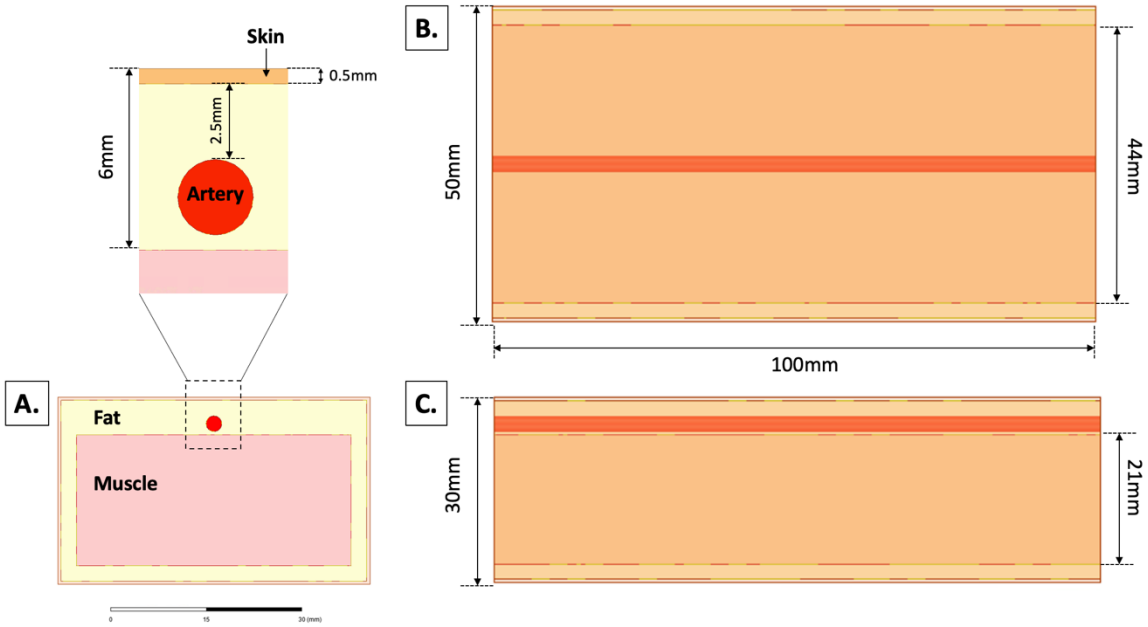

Figure 40. The dimension of the updated wrist model 2 with the skin: (A) the top view; (B) the front view; (C) the left view.

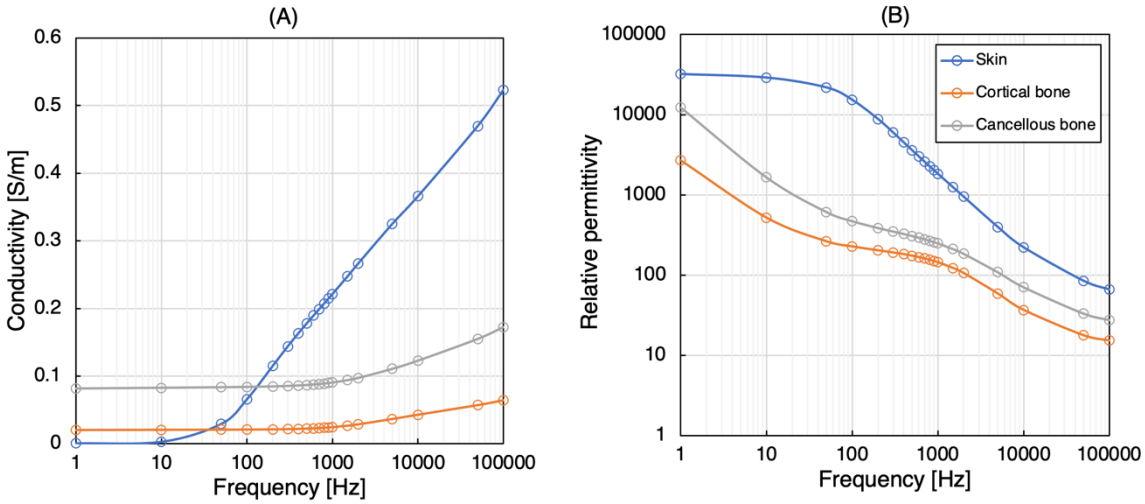

Figure 41. Dielectric properties of human skin, cortical bone and cancellous bone in the β-dispersion: (A) conductivity; (B) relative permittivity.

5.2.2 Results and discussion

5.2.2.1 Current density

The overall current density throughout the wrist model 2 maintained a uniform distribution as for wrist model 1, as shown in Figure 43. The blood domain had the maximum current density compared with other tissues, followed by the muscle domain. However, the current densities of the skin and fat domains had different magnitude relationships at different frequencies. The current density in the fat domain was higher than that in the skin layer at 1 kHz, while it was smaller than the skin layer at higher frequencies (i.e., 100 kHz, 500 kHz and 1 MHz). As observed in Chapter 4, the amounts of current density depended on the conductivity of tissues. The skin had significantly lower conductivity at 1 kHz, even 100 times lower than the fat tissue. Then the skin gradually became more conductive with increasing frequency, becoming similar to muscle at 1 MHz. This noteworthy conductivity change caused a significant current density variance within the muscle domain at 1 MHz (see Figure 43. D). The added skin layer also impacted the current density inside the blood domain, as shown in Figure 42. As the conductivity of the skin increased with increasing frequency, both the current density and the proportion of current inside other tissues decreased, according to Table 20 and Table 21. In a sense, the outermost skin layer 'occupied' a small amount of the current from other tissue domains.

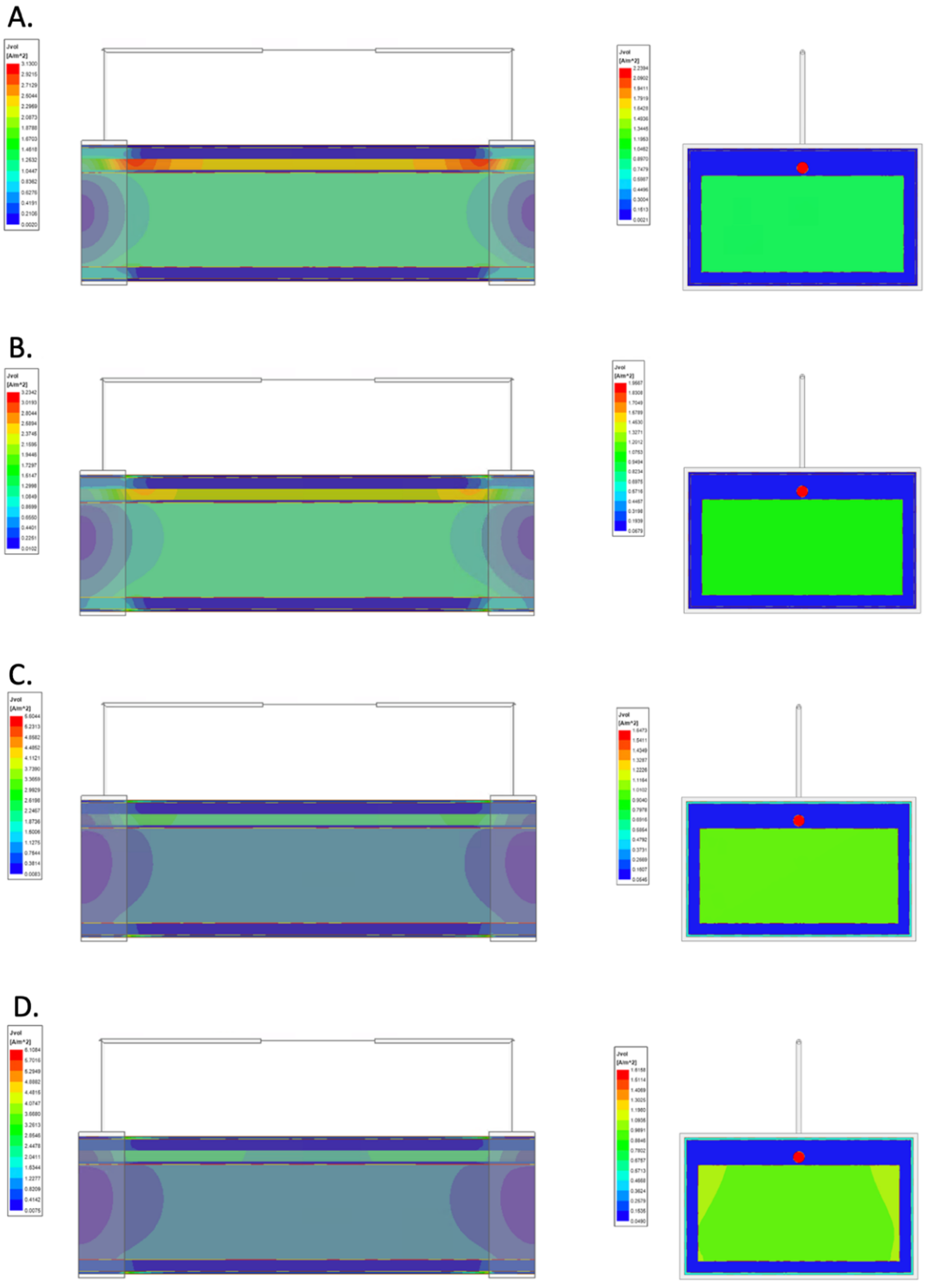

Figure 42. Current density overlays of the wrist model 2 with different frequencies: (A) 1 kHz; (B) 100 kHz; (C) 500 kHz; (D) 1 MHz.

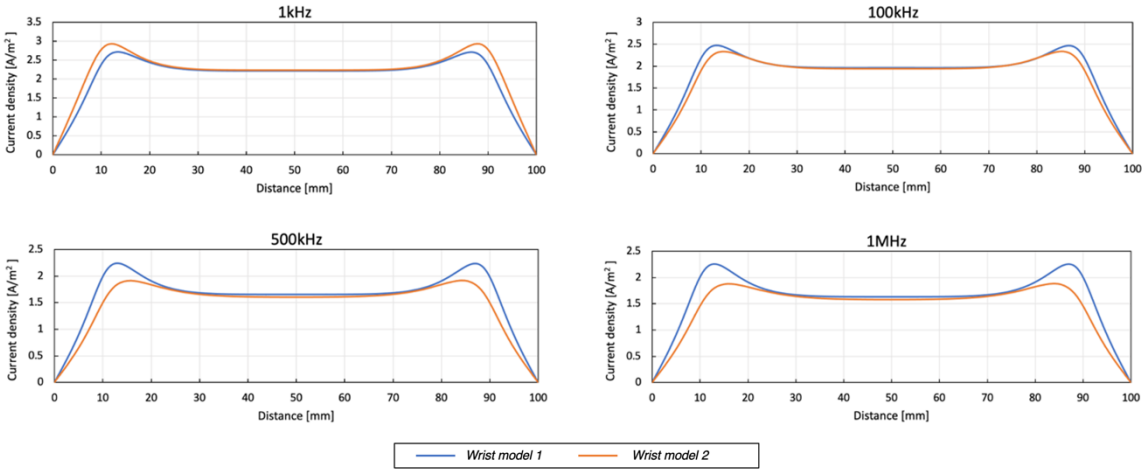

Figure 43. Comparison between current density distributions inside the artery between the wrist model 1 and the wrist model 2.

Table 20. The current density in each tissue domain of the wrist model 2 at 100 kHz.

Depth [mm]		0-0.5	0.5-3	3-5.5	5.5-6	6-27	27-29.5	29.5-30
Tissues		skin	fat	blood	fat	muscle	fat	skin
Current density [A/m²]	**Mean**	0.182	0.067	1.938	0.067	0.998	0.067	0.182
	SD	1.59×10^{-6}	1.04×10^{-6}	4.40×10^{-5}	6.82×10^{-7}	5.75×10^{-5}	1.79×10^{-7}	8.49×10^{-7}

Table 21. The proportion of injected current in each tissue domain of the wrist model 2.

		Proportion of current			
Frequency [Hz]		**1k**	**100k**	**500k**	**1M**
Tissues	**skin**	0.02%	1.47%	3.20%	3.55%
	fat	3.52%	3.37%	2.76%	2.48%
	blood	1.10%	0.97%	0.83%	0.82%
	muscle	95.36%	94.19%	93.20%	93.15%

5.2.2.2 Estimation of arterial diameter

Figure 44 demonstrates that the wrist model 2 also showed a Cole-type dielectric response in the way $Re(Z)$ and $Im(Z)$ varied with frequency. Compared with the wrist model 1, the simulated $Re(Z)$ was slightly greater at 1 kHz and 10 kHz due to the lowest conductivity of the skin at low frequencies.

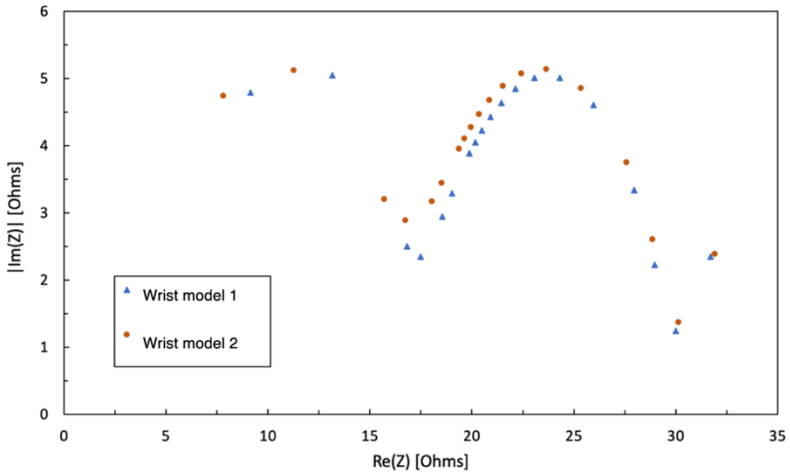

Figure 44. Comparison between Nyquist plots (Cole plots) of the simulated $Re(Z)$ and $Im(Z)$ between the wrist model 1 and the wrist model 2 (arterial diameter = 2.5 mm).

The simulated $Re(Z)$ changes caused by the arterial diameter changes did not show any significant differences from the wrist model 1, as shown in Figure 45. However, the estimated cross-sectional area changes and the estimated artery diameter exhibited larger errors at 500 kHz and 1 MHz (see Figure 46). The estimated area changes were 0.1 mm^2 and 0.2 mm^2 higher than the actual values at 500 kHz and 1 MHz, respectively. As a result, the percent errors of estimated arterial diameter at 500 kHz and 1 MHz were greater than 0.5%, even higher than 1.5% at 1 MHz. As observed before, the increasing errors might be caused by the deteriorative uniform current density in the middle region at these two frequencies, highlighting the impacts of the conductive skin on the overall uniformity of the E-field, especially at higher frequencies.

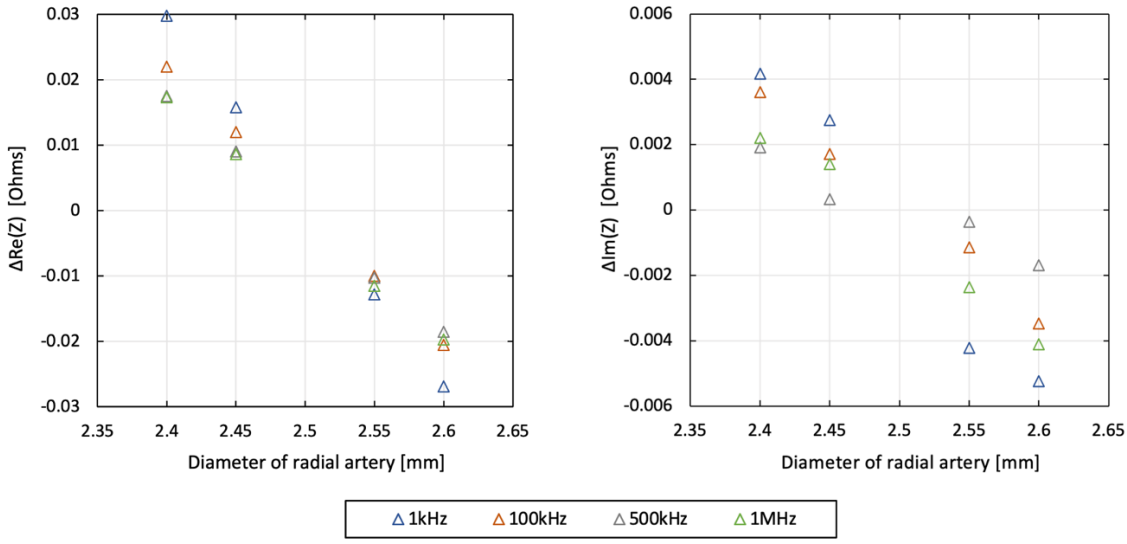

Figure 45. The variation of simulated impedance caused by arterial diameter changes of the wrist model 2.

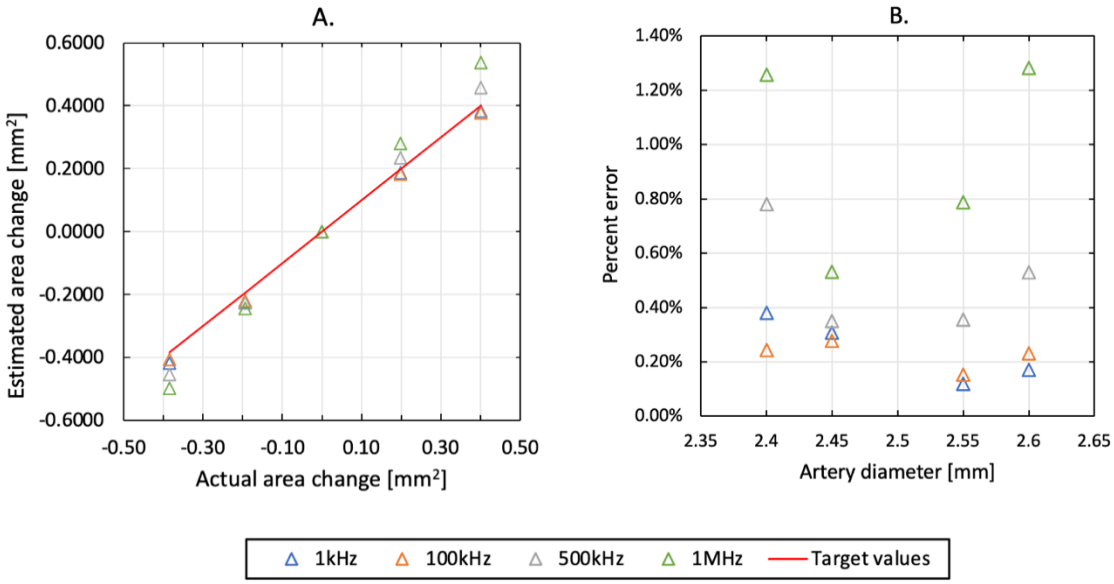

Figure 46. Estimation results of the wrist model 2: (A) estimated cross-sectional area changes; (B) percent errors of the estimated arterial diameters.

5.3 Updated wrist model with bones

5.3.1 Modified geometry with bones

The influence of the bones on the current distribution throughout the wrist model was still unknown. This simulation stage investigated whether the bones would change the uniformity of the current distribution and how would the added bones impact the accuracy of the estimation.

The overall dimension of the wrist model 3 maintained the same cuboid geometry (30 mm × 50 mm × 100 mm), as shown in Figure 47. In addition to the added skin layer analysed in the previous stage, a cuboid bone domain was further complemented in the centre of the whole wrist model. The radius and ulna were merged into one domain in this simulation instead of separate. According to the anatomy of the forearm [231], [244], the added bone domain contains the inner cancellous bone enwrapped by the outer cortical bone. The thickness of cortical bone was 1.5 mm. The frequency-dependent bulk conductivity and relative permittivity of the cancellous bone and cortical bone (see Table 37 in the Appendix) were assigned.

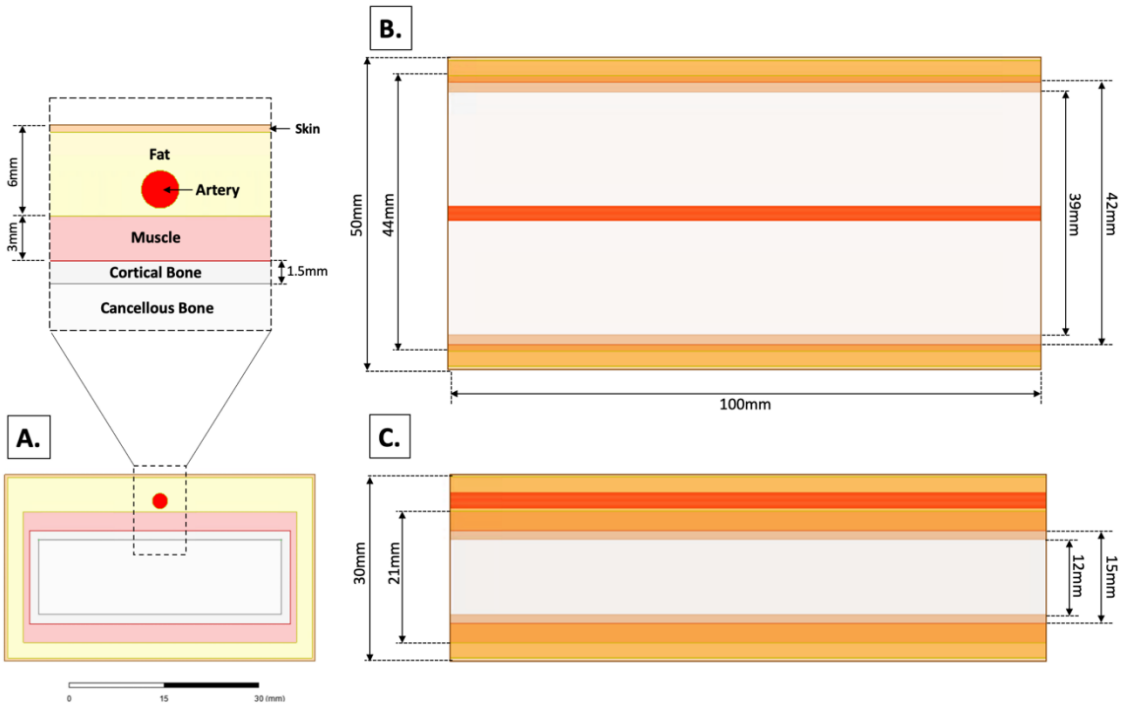

Figure 47. The dimension of the updated wrist model 3 with bones: (A) the top view; (B) the front view; (C) the left view.

5.3.2 Results and discussion

5.3.2.1 Current density

Bones, are a sizeable component of the human wrist, and have relatively lower conductivity. The outside cortical bone domain was a kind of low conductive material similar to the fat tissue, while the inner cancellous bone was around four times more conductive than cortical bone. Both cortical and cancellous bones showed less frequency-dependent conductivity than other tissues across the frequency range of interest. The added bone domains accounted for about 68% of the original muscle domain, causing the high conductive region in the centre of the whole wrist to become resistive. As a result, more amounts of injected current flowed in other conductive domains, such as the blood-filled artery and muscle, as shown in Figure 48. Different from wrist models 1 and 2, the maximum current density appeared in the middle of the entire blood region rather than under the CC electrodes at both ends (see Figure 49). Moreover, the peak values were approximate twice greater than for wrist model 1. In addition to the blood domain, the current density values also increased in other tissues, including the muscle, fat, and skin domains, as shown in Table 22. Even though the fat and cortical bone have the similar conductivity in the frequency range, more current flowed in the fat domain

because of its larger volume, indicating the importance of tissue volume (besides the conductivity) to the relative current distribution, as shown in Table 23.

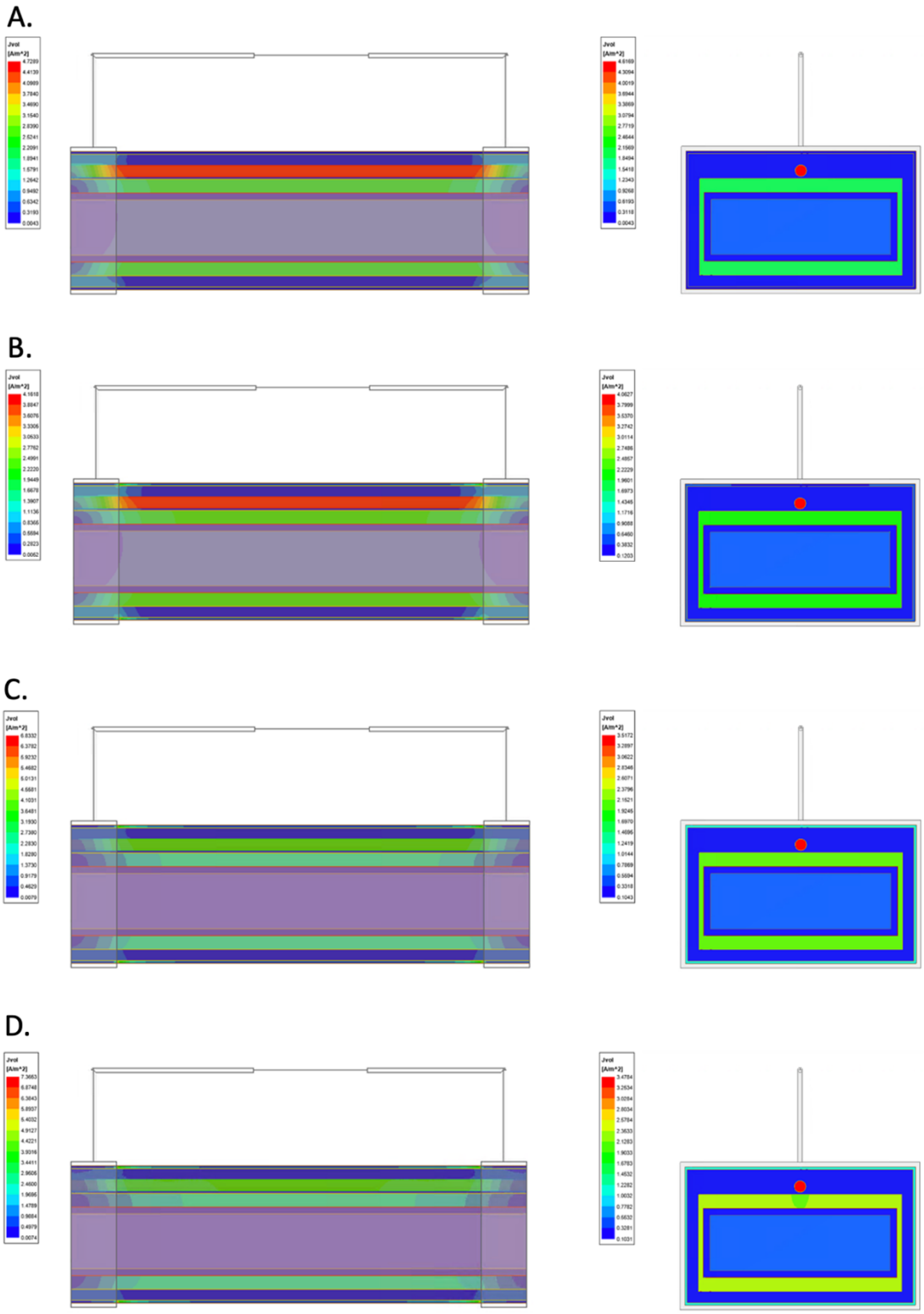

Figure 48. Current density overlays of the wrist model 2 with different frequencies: (A) 1 kHz; (B) 100 kHz; (C) 500 kHz; (D) 1 MHz.

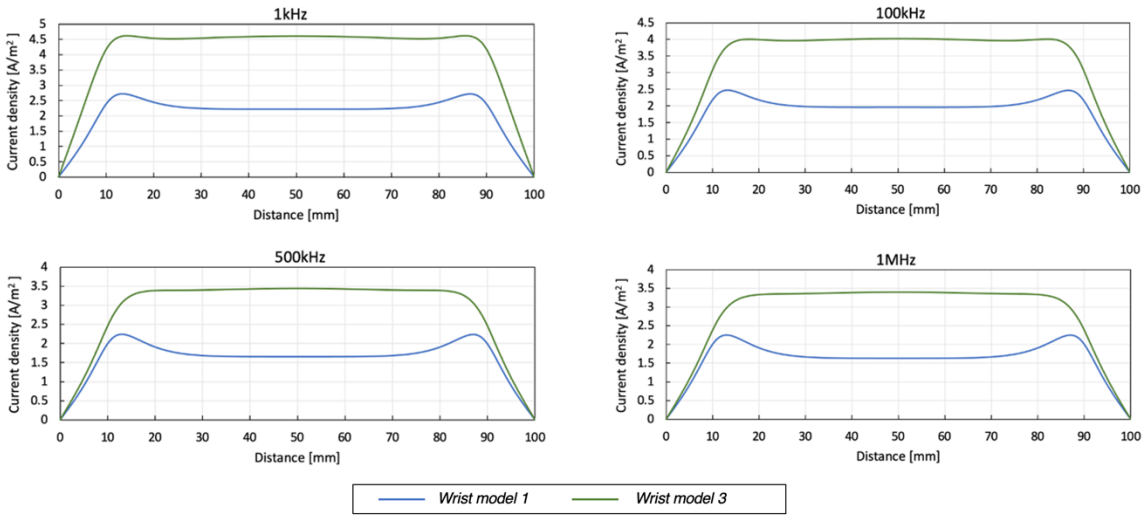

Figure 49. Comparison between current density distributions inside the artery between the wrist model 1 and the wrist model 3.

Table 22. The current density in each tissue domain of the wrist model 3 at 100 kHz.

Depth [mm]	**Tissues**	**Current density [A/m^2] (Mean±SD)**
0-0.5	skin	$0.377 \pm 2.86 \times 10^{-6}$
0.5-3	fat	$0.140 \pm 1.98 \times 10^{-5}$
3-5.5	blood	$4.026 \pm 5.51 \times 10^{-4}$
5.5-6	fat	$0.140 \pm 9.05 \times 10^{-5}$
6-9	muscle	$0.891 \pm 2.09 \times 10^{-4}$
9-10.5	Cortical bone	$0.120 \pm 8.91 \times 10^{-5}$
10.5-22.5	Cancellous bone	$0.484 \pm 9.84 \times 10^{-4}$
22.5-24	Cortical bone	$0.121 \pm 1.41 \times 10^{-4}$
24-27	muscle	$2.105 \pm 1.52 \times 10^{-4}$
27-29.5	fat	$0.142 \pm 1.39 \times 10^{-5}$
29.5-30	skin	$0.383 \pm 1.11 \times 10^{-6}$

Table 23. The proportion of injected current in each tissue domain of the wrist model 3.

		Proportion of current			
Frequency [Hz]		**1k**	**100k**	**500k**	**1M**
Tissues	**skin**	0.03%	3.03%	6.78%	7.60%
	fat	7.27%	7.01%	5.88%	5.37%
	blood	2.27%	2.01%	1.77%	1.75%
	muscle	62.93%	62.94%	64.16%	65.11%
	Cortical bone	2.16%	1.98%	1.73%	1.72%
	Cancellous bone	25.34%	23.04%	19.68%	18.46%

5.3.2.2 Estimation of arterial diameter

Figure 50 illustrates a Cole-type dielectric response in the way $Re(Z)$ and $Im(Z)$ varied with frequency for the wrist model 3. The highly resistive bones significantly increased the simulated $Re(Z)$ by around 20 to 30 Ω across the frequency range. Unlike the added skin discussed in the previous stage, the low variability of conductance of cortical and cancellous bones only changed the magnitude of the simulated impedance but not its behaviours.

Compared with the wrist model 1, the simulated $Re(Z)$ in the wrist model 3 showed more drastic responses to the pulsating blood (i.e., the diameter changes of the radial artery), as shown in Figure 51. The amplitude of $Re(Z)$ was about four times greater than that in the initial model. The reason was that the higher current density inside the blood induced a higher increment in impedance, highlighting the major contribution of the pulsating blood to the impedance change.

However, the cross-sectional area change was likely to be overestimated in the wrist model 3 as well, as shown in Figure 52. The estimation of arterial diameter was more accurate than that in wrist model 2. The percent errors were mostly below 0.8%. The results at 500 kHz and 1 MHz were worse for arterial diameters of 2.4 mm and 2.45 mm. No significant effects of the added bones were found on the overall accuracy of the estimated arterial diameter.

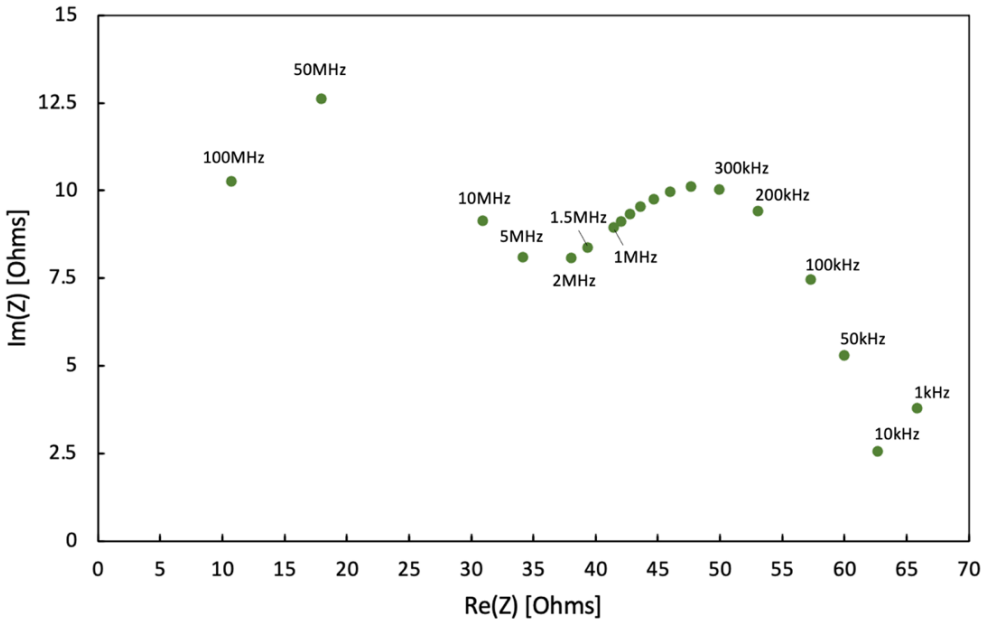

Figure 50. Nyquist plots (Cole plots) of the simulated $Re(Z)$ and $Im(Z)$ of the wrist model 3 (arterial diameter = 2.5 mm).

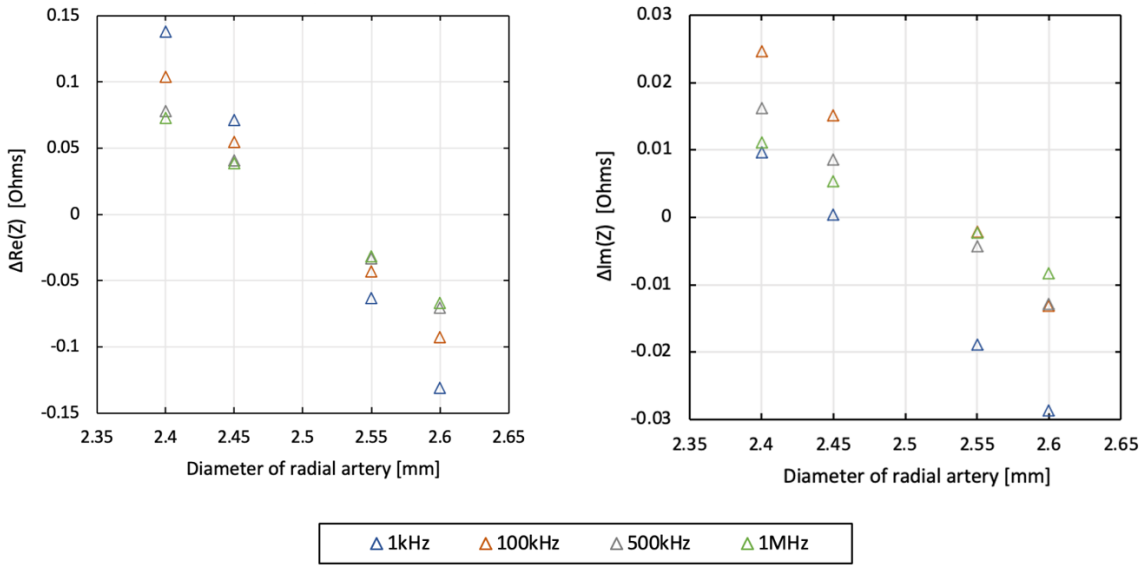

Figure 51. The variation of simulated impedance caused by arterial diameter changes of the wrist model 3.

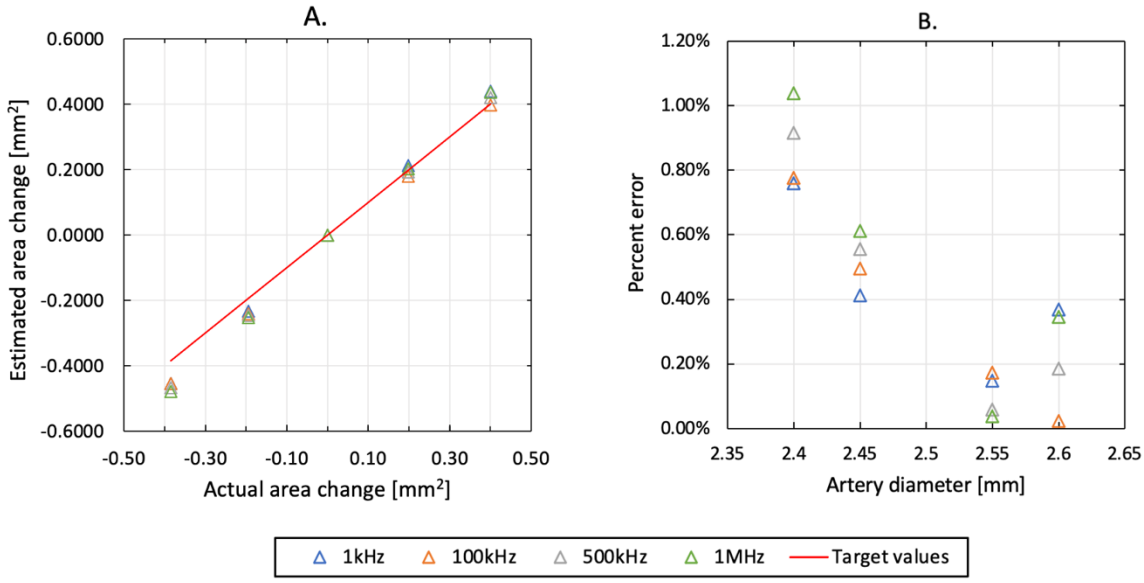

Figure 52. Estimation results of the wrist model 3: (A) estimated cross-sectional area changes; (B) percent errors of the estimated arterial diameters.

5.4 Cylindrical wrist model

5.4.1 Modified geometry with a curvilinear shape

The cuboid wrist model was selected in the previous simulation stages because linear geometry would be easier to mesh accurately. It struck a balance between the accuracy of simulation and the time required for simulation. In this stage, all tissue domains were replaced by cylindrical geometry, as represented in Figure 53, to explore how the curvilinear

surface would impact the simulated results and the accuracy of the estimation. The transformation of the wrist model from a cuboid to a cylinder applied the following principles:

1) The length of the entire wrist segment was kept the same, 100 mm.
2) The outer perimeter of the wrist model was unchanged as the contact area between the CC electrodes and the skin could affect the current density near the CC electrodes. Moreover, the aspect ratio of the cross-section remained unchanged (5:3). Thus, the cross-sectional area of the whole wrist model was re-designed as an ellipse with a width of 30 mm and a height of 18 mm. Its circumference was only around 1 mm longer than the previous cuboid model.
3) The thickness of skin and cortical bone domains was kept the same on all sides, whereas the muscle and fat layers maintained the same thickness as the cuboid model on the major and minor axes.
4) The depth and the dimensions of the artery remained the same.

All tissue domains were assigned with the same dielectric properties as before. The cross-sectional areas of each domain are listed in Table 24. Some differences between the wrist model 4 and the previous cuboid model geometry need to be noticed. Firstly, the fat and the cancellous bone areas had the most significant area increments. Additionally, the maximum and minimum thickness of the dorsal fat layer was kept the same as the volar region because of the new elliptical periphery.

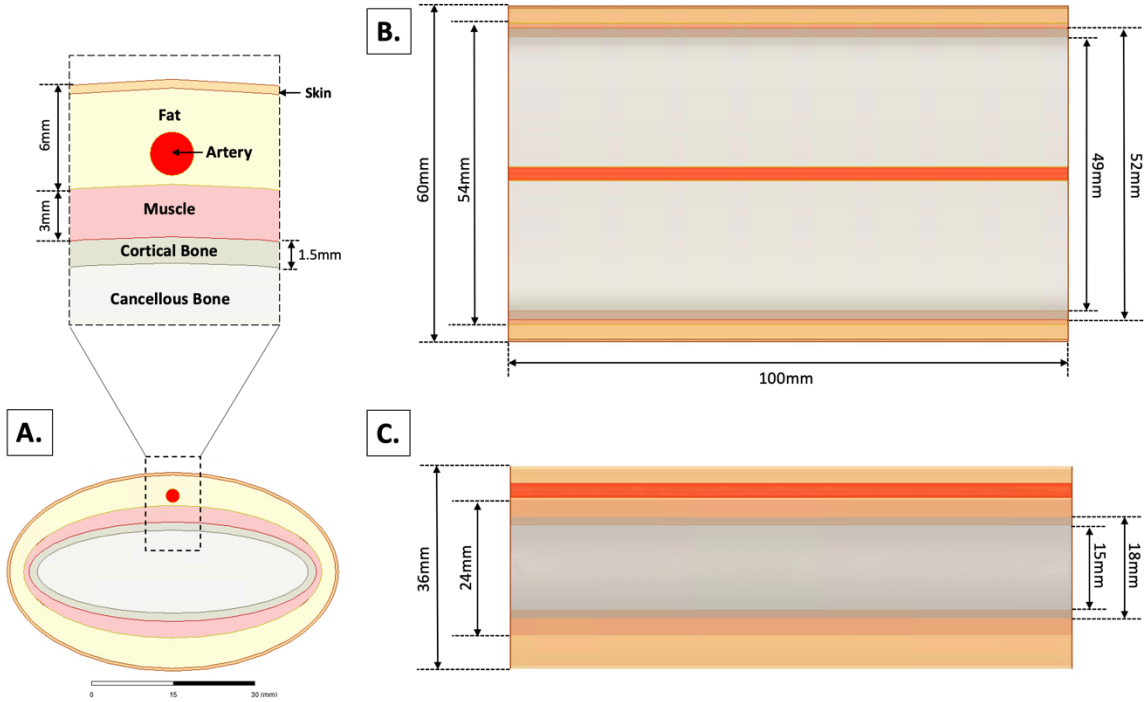

Figure 53. The dimension of the cylindrical wrist model 4: (A) the top view; (B) the front view; (C) the left view.

Table 24. The cross-sectional area of each tissue.

	Cross-sectional area [mm^2]						
Tissue domains	**skin**	**fat**	**blood**	**muscle**	**Cortical bone**	**Cancellous bone**	**Total**
Cuboid model	79.00	492.09	4.91	294.00	162.00	468.00	1500.00
Cylindrical model	74.61	599.06	4.91	282.74	157.87	577.27	1696.46

5.4.2 Results and discussion

5.4.2.1 Current density

Compared with the cuboid wrist model 3, the current density values on both planes did not show any significant differences, as shown in Figure 54, confirming the current density distribution throughout the cylindrical wrist model was decided by the conductivity of each tissue instead of the geometry. Specific to the blood domain, the horizontal current density distribution was not affected by curvilinear geometric changes, remaining uniform in the middle region from the distance of 30 mm to 70 mm (see Figure 55). However, according to the higher SD of the current density in the blood domain shown in Table 25 (around 20 times greater than that in Table 22), the curvilinear geometric changes influenced the depth-dependent uniformity of current density in the blood, while other tissue domains were not impacted. This variance might be caused by the gradually decreasing fat layer thickness with

the depth. Table 26 indicates the slight differences in proportion of current in each tissue from the wrist model 3, corresponding to the variant cross-sectional areas/volumes of the new cylindrical geometry (see Table 24).

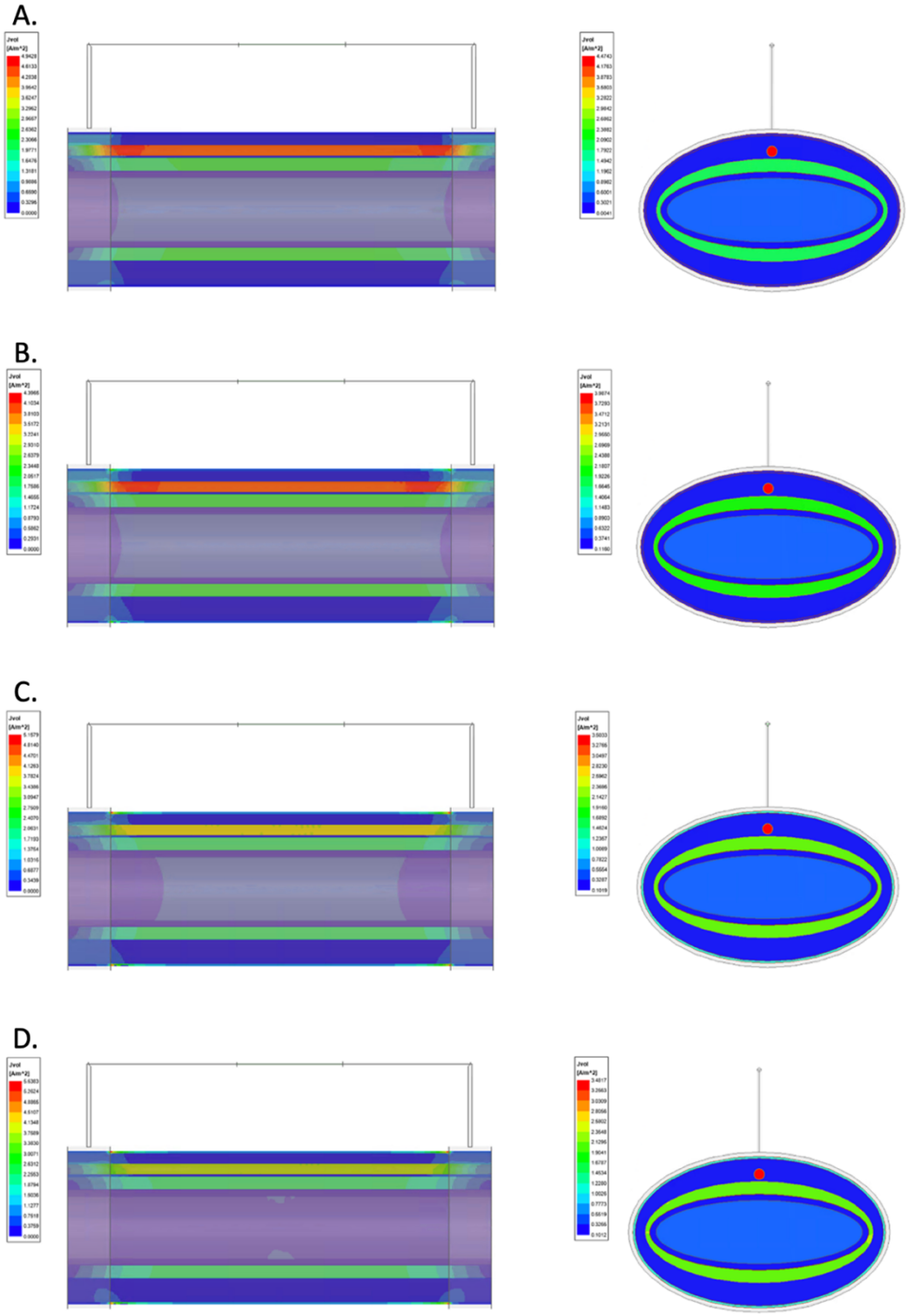

Figure 54. Current density overlays of the cylindrical wrist model 4 with different frequencies: (A) 1 kHz; (B) 100 kHz; (C) 500 kHz; (D) 1 MHz.

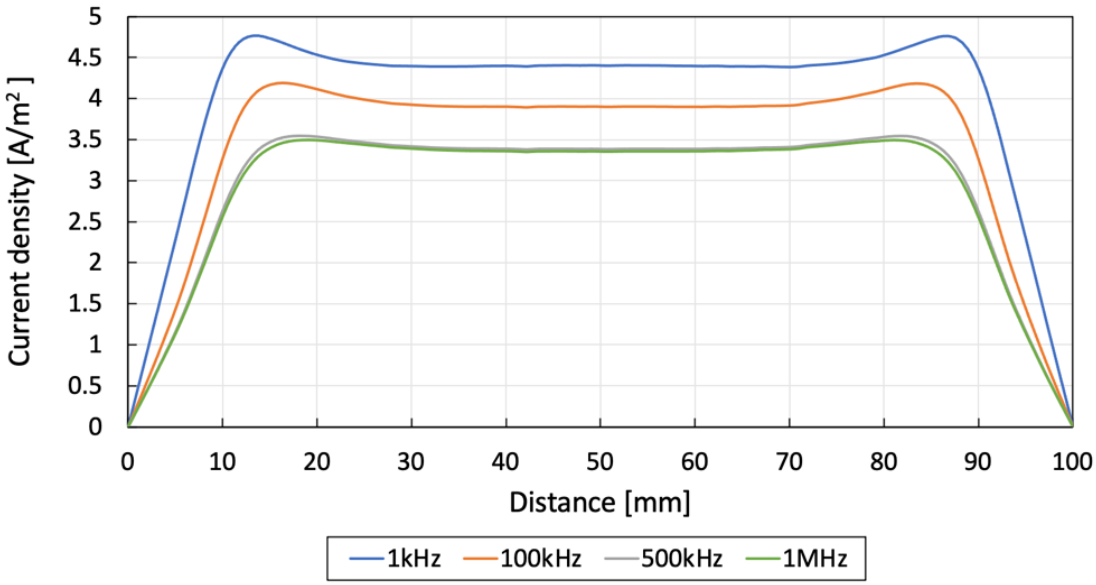

Figure 55. Current density distribution inside the artery of the cylindrical wrist model 4.

Table 25. The current density in each tissue domain of the cylindrical wrist model 4 at 100 kHz.

Depth [mm]	**Tissues**	**Current density [A/m^2] (Mean±SD)**
0-0.5	Skin	0.366±2.70E-05
0.5-3	Fat	$0.135\pm6.56\times10^{-4}$
3-5.5	Blood	$3.900\pm1.12\times10^{-2}$
5.5-6	Fat	$0.135\pm1.25\times10^{-4}$
6-9	Muscle	$0.635\pm6.68\times10^{-4}$
9-10.5	Cortical bone	$0.115\pm5.90\times10^{-5}$
10.5-25.5	Cancellous bone	$0.465\pm1.27\times10^{-4}$
25.5-27	Cortical bone	$0.115\pm7.48\times10^{-5}$
27-30	Muscle	$2.010\pm4.19\times10^{-5}$
30-35.5	Fat	$0.135\pm3.47\times10^{-5}$
35.5-36	skin	$0.365\pm1.97\times10^{-6}$

Table 26. The proportion of injected current in each tissue domain of the wrist model 4.

		Proportion of current			
Frequency [Hz]		**1k**	**100k**	**500k**	**1M**
Tissues	**skin**	0.03%	2.78%	6.30%	7.10%
	fat	8.49%	8.23%	7.03%	6.41%
	blood	2.17%	1.95%	1.74%	1.73%
	muscle	57.55%	57.86%	59.68%	60.87%
	Cortical bone	2.01%	1.85%	1.65%	1.64%
	Cancellous bone	29.75%	27.33%	23.59%	22.24%

5.4.2.2 Estimation of arterial diameter

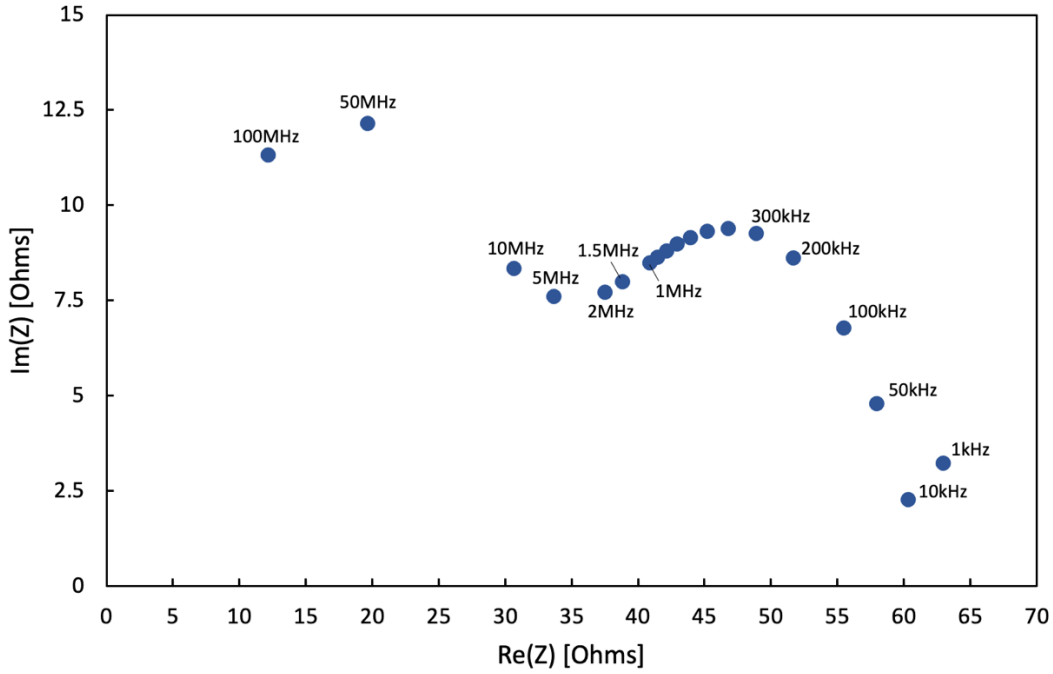

Figure 56. Nyquist plots (Cole plots) of the simulated $Re(Z)$ and $Im(Z)$ of the wrist model 4 (arterial diameter is 2.5mm).

The wrist model 4 exhibited a similar Cole-type response to the wrist model 3 across the β-dispersion, as shown in Figure 56, proving the curvilinear geometric changes did not change the overall dielectric response. Compared with the wrist model 3, both simulated $Re(Z)$ and $Im(Z)$ were slightly smaller in the new cylindrical wrist model. This decrement in impedance corresponded to the negative relationship between the cross-sectional areas of tissues and impedance.

As observed in previous stages, the simulated $Re(Z)$ changes were more significant than the $Im(Z)$ changes, as shown in Figure 57. Moreover, $Re(Z)$ decreased as the frequency increased as observed in section 4.5.2, corresponding with the increasing conductivity. The accuracy of the estimated cross-sectional area change was impacted by the lower uniformity of current density inside the blood, as shown in Figure 58. Different from previous models, the cross-sectional area changes were underestimated when the arterial diameters were 2.4 mm and 2.45 mm. Moreover, except for the diameter of 2.55 mm, other estimations showed larger percent errors, which were over 0.5%. Abnormally, two estimations at 1 kHz obtained the worst accuracy (1.47% and 2.23%), which might be caused by less simulation accuracy (worse mesh quality) due to the curvilinear geometry.

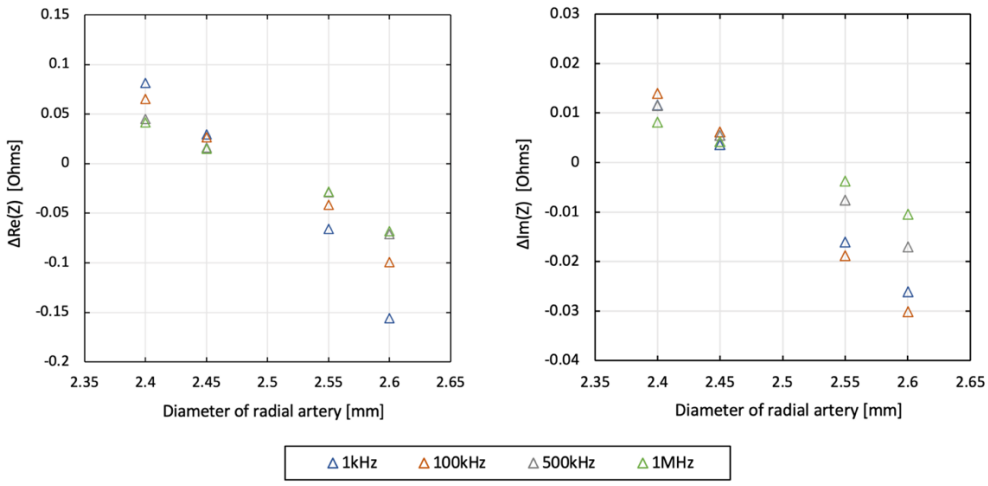

Figure 57. The variation of simulated impedance caused by arterial diameter changes of the wrist model 4.

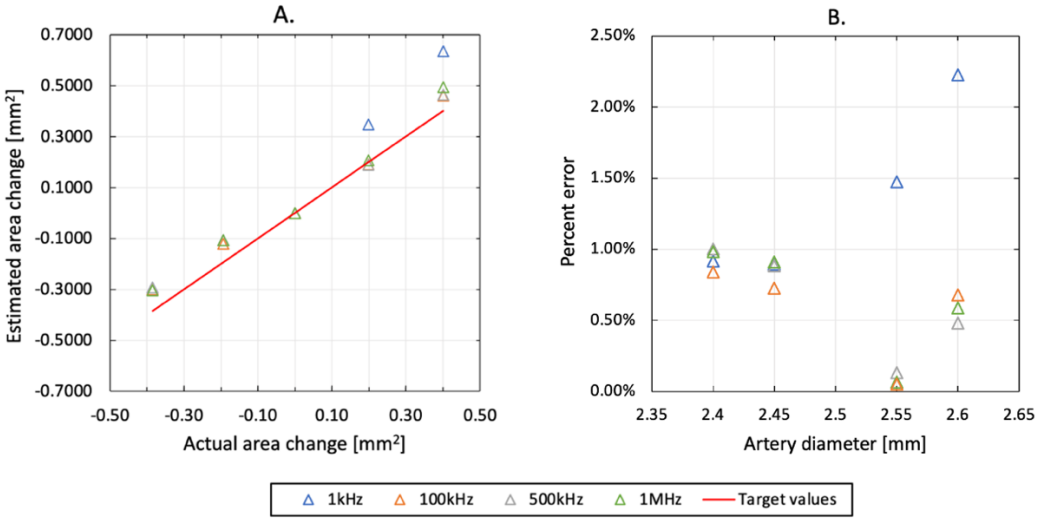

Figure 58. Estimation results of the wrist model 4: (A) estimated cross-sectional area changes; (B) percent errors of the estimated arterial diameters.

5.5 Two-arteries wrist model

According to the literature review, previous studies mainly focused on one artery measurement by placing conventional 4-spot electrodes above the radial artery near the wrist. Researchers have always regarded the measured bio-impedance signal as a reflection of the pulsatile blood inside the radial artery. However, the ulnar artery, as another major artery of the lateral aspect of the forearm arising from the bifurcation of the brachial artery, has been rarely modelled and considered. BIM at the distal forearm for hemodynamic monitoring is highly sensitive to surrounding large blood volume change. Therefore, both radial artery and

ulnar artery are desired to be investigated. This last simulation stage is intended to explore the effects of another pulsatile artery on the simulated results and the accuracy of estimation.

5.5.1 Modified geometry with the ulnar artery

The previous stage demonstrated no significant differences between the cuboid and cylindrical geometries in the simulation. However, it was noticed that complex 3D models with more tissue domains and curvilinear geometry had higher failure rate or requested overnight computing times to remain the fine mesh quality. Therefore, considering the computing time and simulation accuracy, the cuboid shape was maintained in this stage for wrist model 5 (30 mm × 50 mm × 100 mm), as shown in Figure 59. The ulnar artery is another major artery of the forearm and has a similar diameter to the radial artery [237], [238], [245]. Because of inter-individual differences, the consensus on the size differences between the radial artery and the ulnar artery was not found from the literature. Therefore, the additional ulnar artery was also modelled with the same dimension as the radial artery in the basal condition (arterial diameter = 2.5 mm). Furthermore, slightly different diameter changes were modelled to represent different synchronously pulsatile volumes, which were 2.6 mm and 2.55 mm for the radial artery and the ulnar artery, respectively. In addition to the band electrode setup, the conventional 4-spot electrode configuration on the radial artery was also simulated for comparison purposes.

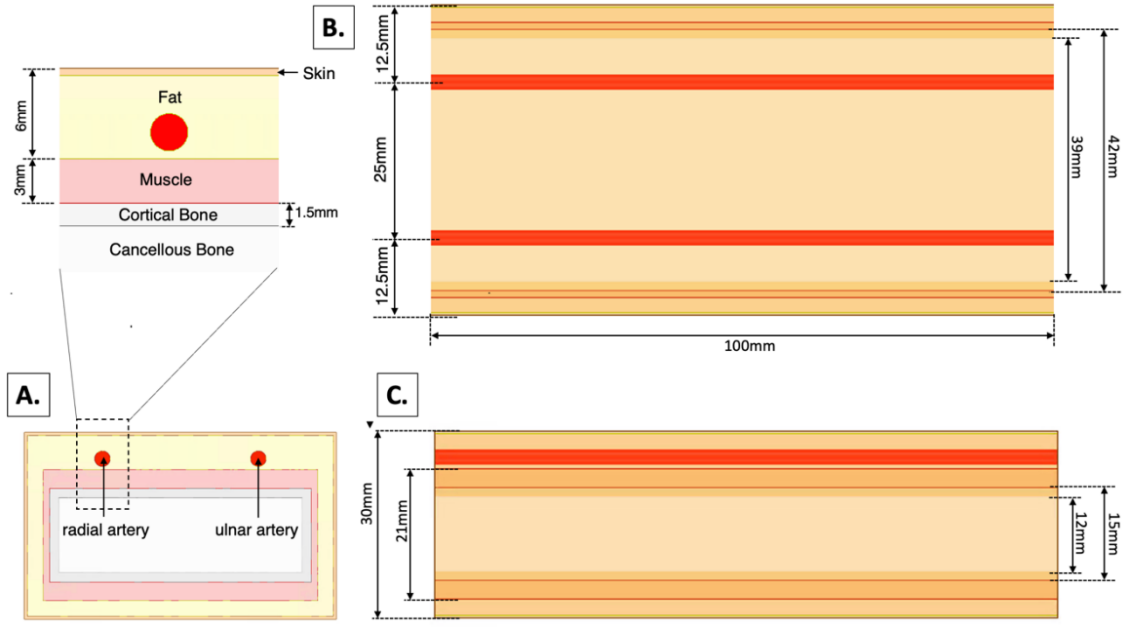

Figure 59. The dimension of the updated wrist model 5 with two arteries: (A) the top view; (B) the front view; (C) the left view.

5.5.2 Results and discussion

5.5.2.1 Current density

Figure 60 indicates a totally different current density distribution between the conventional 4-spot electrode configuration and the proposed band electrode configuration. The band electrode configuration generated horizontally and vertically symmetrical current density throughout all tissue domains, while the current density on the side of spot electrodes was significantly higher than on the other side. The maximum current density in each tissue domain with the 4-spot electrode configuration was higher than the band electrode configuration. As observed in Chapter 4, the radial artery with the 4-spot electrode configuration showed more significant changes in current density than band electrodes (see Figure 61). The maximum value appeared at both ends of the radial artery and then dropped to the lowest in the middle part (still over 4 A/m^2). However, the ulnar artery had an entirely different current density distribution. The maximum current density of the ulnar artery appeared in the middle part, which was still smaller than the minimum value of the radial artery at the same frequency. For the band electrode configuration, the current density curves inside two arteries were overlapped, demonstrating the equal current density distribution between the radial artery and ulnar artery. Furthermore, their uniformities of current density were consistent with the previous one-artery wrist model, showing a significantly wider uniform range along the blood flow direction (from the distance of 10 mm to 90 mm) than the spot electrode configuration.

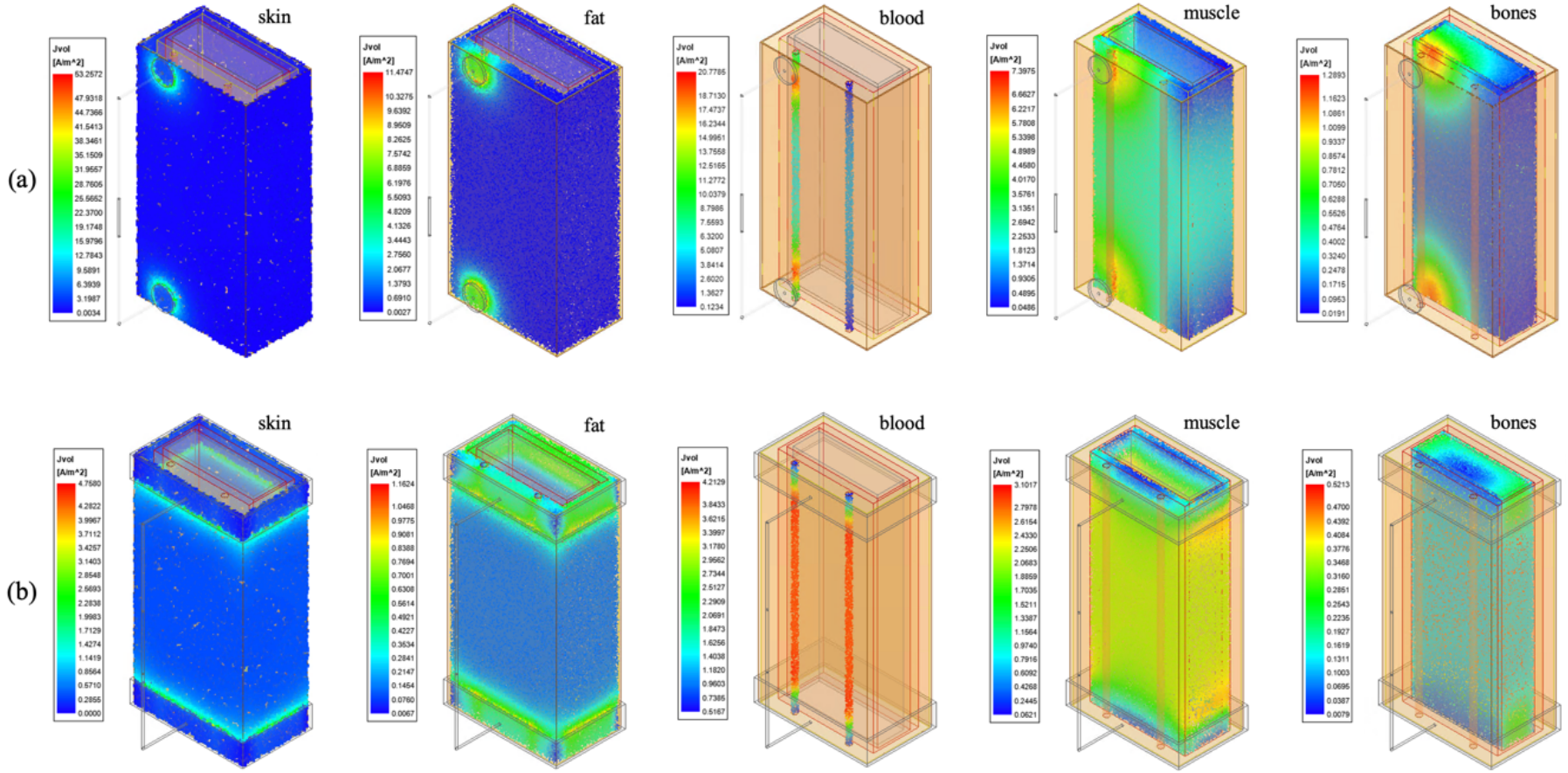

Figure 60. Current density in each tissue domain of the wrist model 5 with two arteries at 100 kHz: (a) conventional 4-spot electrode configuration; (b) band electrode configuration.

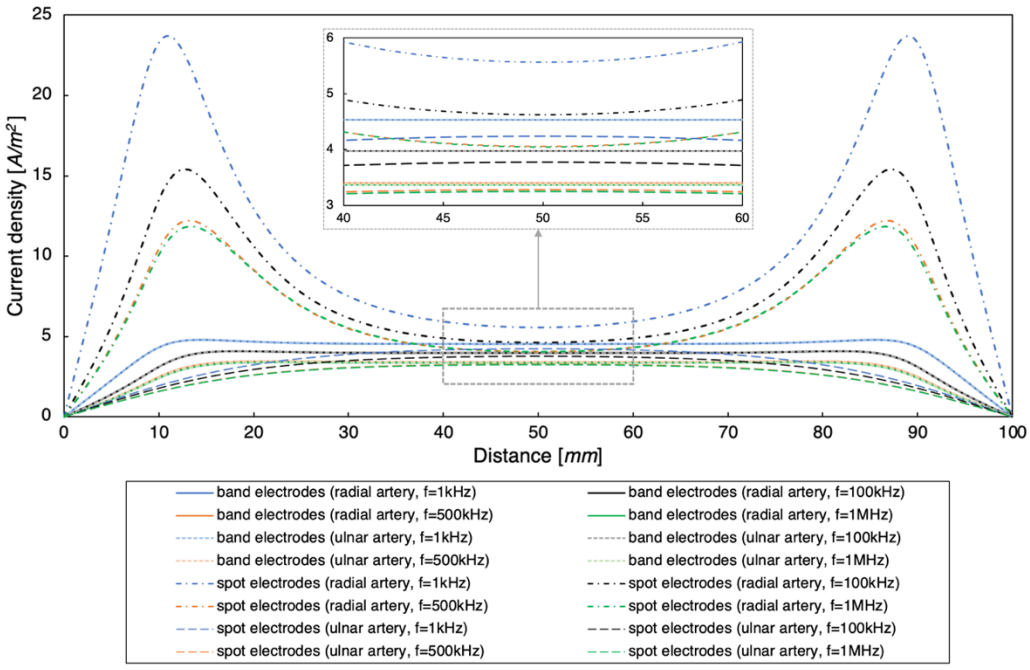

Figure 61. Current density distribution inside two arteries with different CC electrodes.

5.5.2.2 Simulated impedance with different locations of PU electrodes

Figure 63 demonstrates the influence of the added ulnar artery on the simulated $Re(Z)$ and $Im(Z)$ with the band electrodes. The semi-circular shape plot was still observed in the wrist model 5, agreeing with the Cole model. The additional ulnar artery reduced both $Re(Z)$ and $Im(Z)$ across the frequency range due to the higher conductivity of the blood.

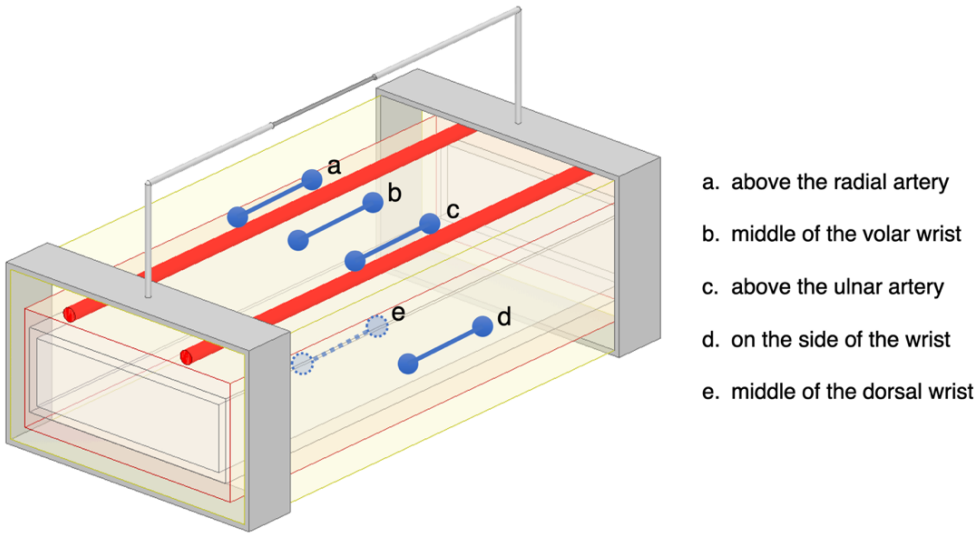

Figure 62. Various PU electrode locations of the wrist model 5 with two arteries.

According to the previous simulation results analysed in Chapter 4, PU electrodes were supposed to be placed in the middle between two CC electrodes with shorter L_{PU} of 10 mm to sense the most uniform E-field. In previous stages, PU electrodes were only placed on the radial artery aligned with outer CC electrodes according to the common placement in literature. In this stage, in addition to measuring the impedance above the radial artery, the resistance from other locations were also investigated as shown in Figure 62, including above the ulnar artery, in the middle of the volar aspect of the wrist, on the side of the wrist, and in the middle of the dorsal aspect of the wrist. Then, the overall theoretical resistance R_{theory} (according to Equation 9 and Equation 10) of the measured wrist segment was calculated by considering each tissue was connected in parallel based on Figure 63. Both simulated resistance and R_{theory} (red point line) were plotted in Figure 64. The simulated resistance values using band electrodes were very close to the theoretical values at all measurement locations, and the overall MAD was 0.637 Ω. Except for the simulated resistance at 10 MHz and 100 MHz, the MAD of other simulations was only 0.298 Ω. In contrast, the measurement position severely affected the simulated resistance when applying conventional spot electrodes. The closer the PU electrodes were to the radial artery, the higher the measured resistance. However, simulated resistance values under the conventional electrode setup showed a higher MAD of 6.098 Ω.

More remarkably, the most commonly used measurement location (4-spot electrodes on the radial artery) showed greater deviations with a MAD of 11.747 Ω. The Bland–Altman plots of all simulated resistance values versus R_{theory} at all frequencies with various locations of PU electrodes is shown in Figure 64. The overall mean $\pm$ SD of the simulated resistance under conventional 4-spot electrodes configuration and band electrode configuration against R_{theory} were 0.519 $\pm$ 7.083 Ω and -0.464 $\pm$ 1.291 Ω, respectively.

The conventional 4-spot electrode configuration focused the injected current more on the radial artery than the ulnar artery, which could obtain higher impedance values. However, as shown in the simulation results, the ulnar artery was also within the measurement range, even if its current density was lower than that of the radial artery. In other words, the measured bio-impedance signal contained the hemodynamic information of both the radial artery and the ulnar artery.

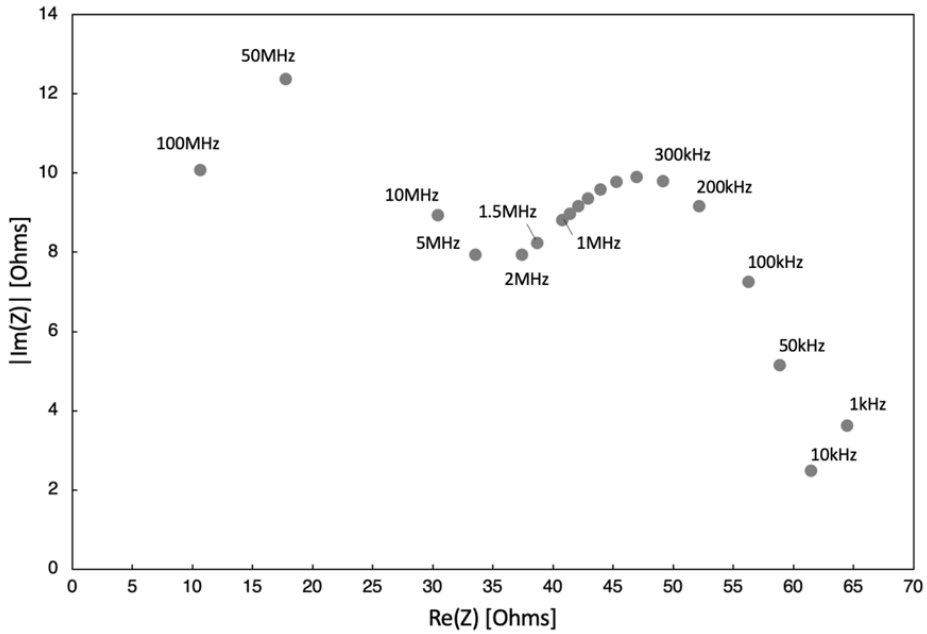

Figure 63. Nyquist plots (Cole plots) of the simulated $\mathrm{Re}(Z)$ and $\mathrm{Im}(Z)$ of the wrist model 5 with band electrodes (arterial diameters = 2.5 mm).

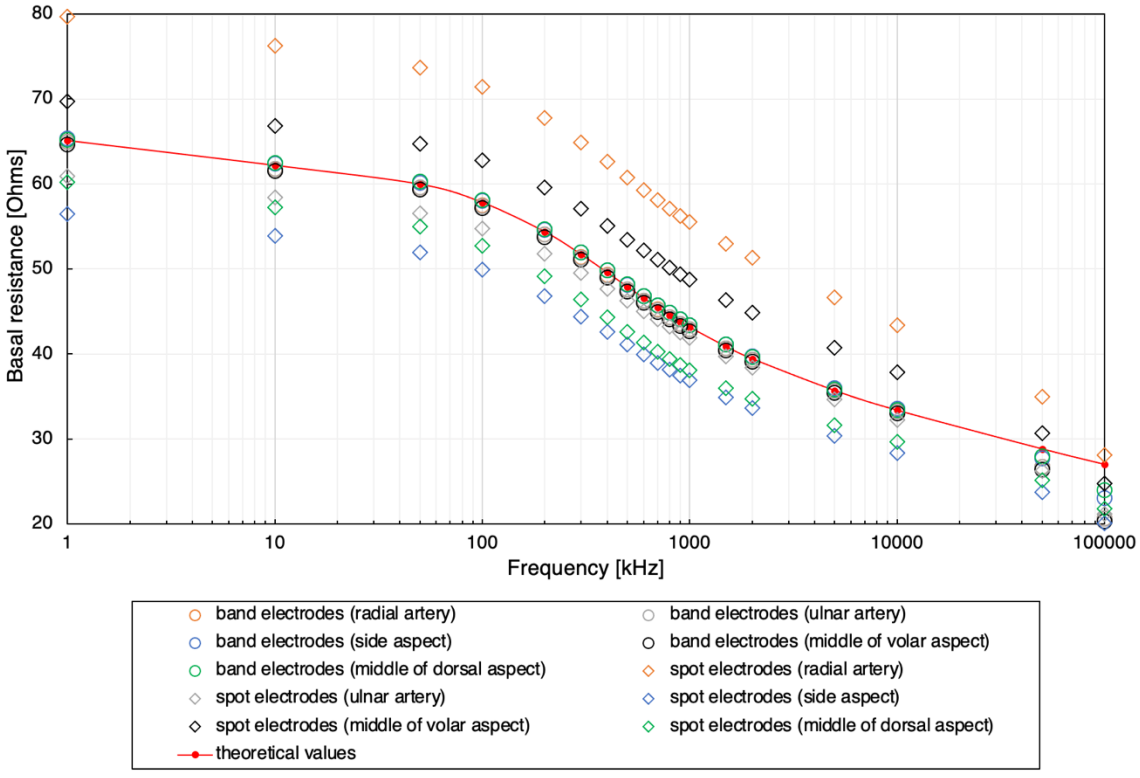

Figure 64. Simulated basal resistance of the wrist model 5 with different CC electrodes from different locations of PU electrodes.

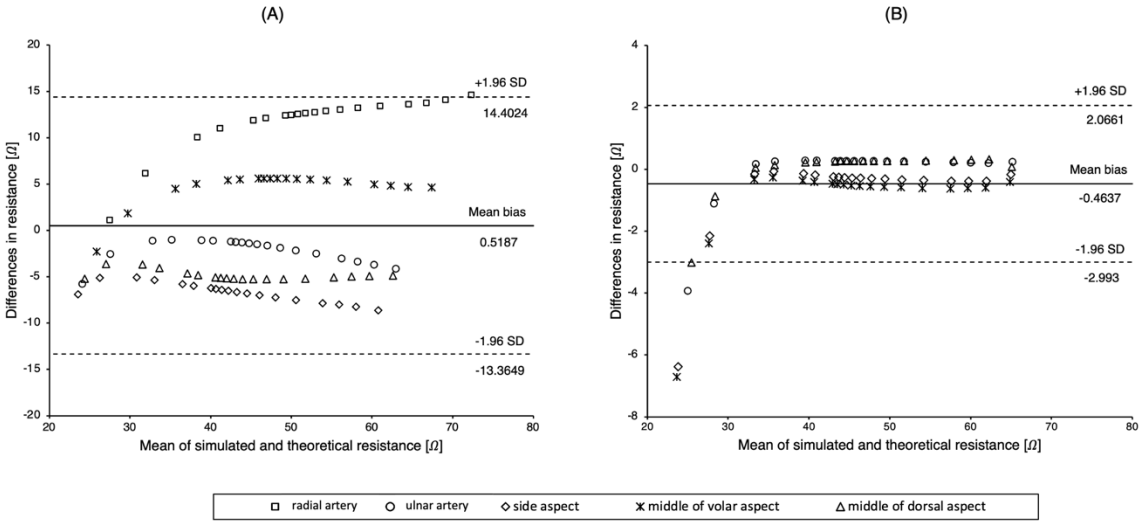

Figure 65. Bland–Altman plots between simulated and theoretical resistance: (A) conventional 4-spot electrode configuration; (B) band electrode configuration.

5.5.2.3 Estimation of cross-sectional area change

Different from previous stages, two pulsatile arteries induced difficulties in estimating the individual arterial diameter changes. Therefore, in the stage, only the overall cross-sectional area change of the blood was estimated with various PU electrode locations (aspects of the wrist) to indicate how would these values represent the pulsation. As shown in Figure 66, for the band electrode method, the simulated absolute resistance changes remained similar when the PU electrodes were placed on the volar aspect of the wrist, while a slight drop appeared for the side and dorsal aspects. However, for the conventional spot electrode method, the influences of measured locations on the resistance changes were more significant.

In this stage of simulation, the cross-sectional area changes of the radial artery and the ulnar artery were 0.4006 mm^2 and 0.1983 mm^2, respectively. Therefore, the reference overall increment in blood was 0.5989 mm^2. As mentioned in the previous section, the band electrodes could generate a more uniform E-field throughout the wrist, inducing the promising capability to sense the overall blood volume changes from both arteries. The most accurate estimation of the overall cross-sectional area changes was 0.5967 ± 0.0061 mm^2 measured in the middle of the volar aspect between two arteries, followed by measuring on the ulnar artery of 0.6074 ± 0.0069 mm^2 and on the radial artery of 0.6305 ± 0.0138 mm^2. The measurement from the side aspect and the middle of the volar aspect showed a higher bias.

In contrast, spot electrode configurations did not exhibit obvious regularity with different measured locations. The spot electrode method was more likely to overestimate the cross-sectional area change by placing the PU electrode on the ulnar artery, the side aspect, and the middle dorsal aspect of the wrist. According to the information from Figure 64, the larger deviation in estimation using spot electrodes was caused by the large differences in simulated (basal) resistance between different measured locations, inducing the overestimation and underestimation of the area changes.

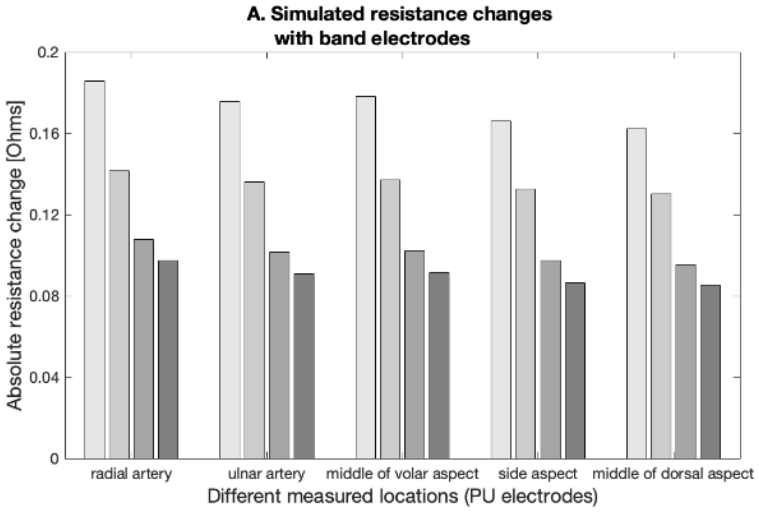

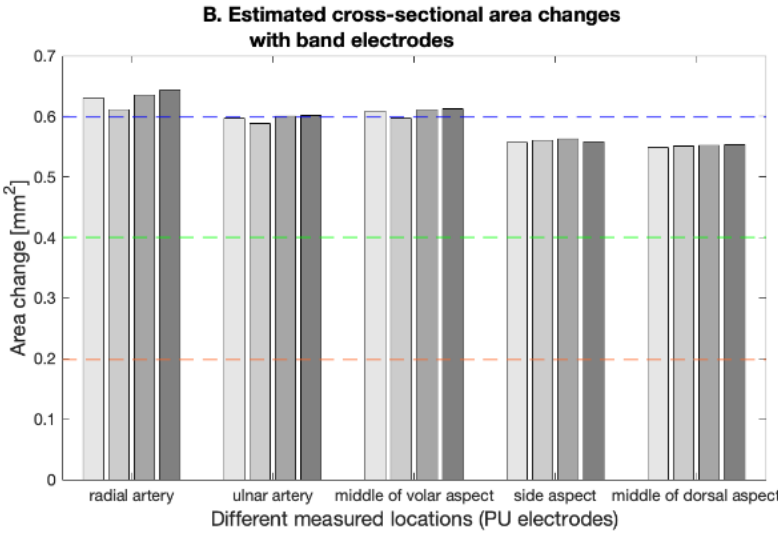

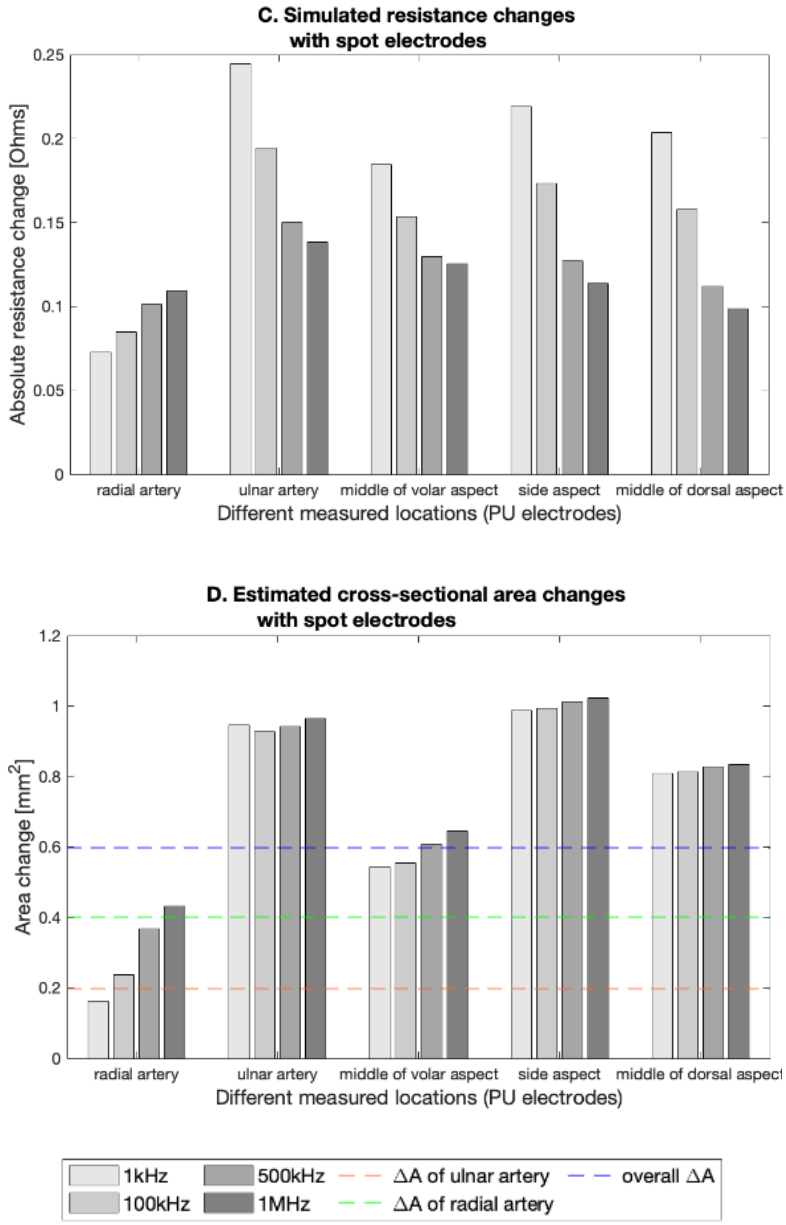

Figure 66. Simulation results of the wrist model 5: (A) simulated absolute resistance changes using band electrodes; (B) estimated cross-sectional area changes using band electrodes; (C) simulated absolute resistance changes using spot electrodes; (D) estimated cross-sectional area changes using spot electrodes.

5.6 Closure

In this chapter (simulation stages 2 to 5), the effect of multiple tissue domains was investigated to improve the understanding of their contributions to BIM. It helped to explore the feasibility of accurately estimating artery diameter changes under the conditions of more complex geometrical considerations.

As determined in Chapter 4, the amounts of current density in each tissue domain were decided by the conductivity of tissues. Specifically, the skin appeared to have significantly lower conductive at 1 kHz, even 100 times lower than the fat, and then gradually became more conductive as the frequency increased, surpassing the fat and cortical bone at 50 kHz and exceeding the cancellous bone at 200 kHz. Bones had relatively lower conductivity with less frequency-dependent changing across the frequency range of interest. The added bone domains accounted for about 68% of the original muscle domain, causing larger simulated basal resistance. Consequently, more amounts of injected current flowed into the blood domain, inducing higher resistance change caused by arterial diameter change. Therefore, for future investigations that want to focus on the contribution of pulsatile blood, it is recommended to include the bones in the human 3D model to highlight the contribution of conductive blood.

Typically, containing more tissue domains could represent the human body more realistically. However, in certain conditions, adding components might require significantly higher computing power and even reduce the accuracy of the simulation. Compared with the wrist model 1 (in Chapter 4), the wrist model 2 with added skin showed larger errors of the estimated arterial diameter, especially at 500 kHz and 1 MHz. Such a tiny component (skin layer) required a much higher mesh quality to accurately represent the geometry, causing slightly fluctuating errors in ANSYS HFSS. Therefore, future research should pay attention to such impacts of skin domain on the computing time and accuracy of the overall 3D model. Although the conductivity of the skin showed a dramatic change with the frequency, it did not significantly affect the overall impedance/resistance of the body in the simulation condition due to the much thinner volume of the skin compared with other tissues. In the actual measurement, the effects of the stratum corneum layer of the skin can be discounted through skin preparation. The skin-electrode contact impedance can be reduced by applying gel-electrodes. However, the influence of skin should be considered with dry electrodes.

Additionally, the whole 3D model was reshaped as cylindrical geometry. The results did not reveal any significant influences on the simulated values and the accuracy of estimation. Thereby, it was reasonable to simplify the human wrist with either linear or curvilinear geometry. Nevertheless, both the small volume domain and curvilinear geometry required

finer mesh quality to simulate the 3D model accurately, making the trade-off between accuracy and running speed more difficult.

Most importantly, the impacts of pulsatile ulnar artery on the signal acquirement from the radial artery were investigated by modelling another blood-filled artery domain in the 3D model. As far as I know, this simulation is the first investigation into two synchronously pulsatile arteries in the forearm near the wrist. The simulation results revealed the significant influences of another adjacent artery on the overall current distribution, weakening the capability of conventional spot electrode configuration to accurately represent the electrical responses of tissues and cross-sectional area change of the blood from the mathematical perspective. However, the band electrode configuration could be used to accurately estimate the overall blood volume change, including both pulsatile radial artery and ulnar artery. The above outcomes drove the interest in the next investigation by constructing the equivalent human wrist phantom for further verification.

CHAPTER 6. EXPERIMENTAL INVESTIGATION OF HUMAN WRIST PHANTOM

6.1 Introduction

In physical measurement, due to regulation and legal, ethical, safety and humanitarian concerns, it is often expedient and reasonable to utilise tissue phantoms instead of living human tissues for experimental purposes. Consequently, tissue-mimicking materials have been created and developed since the early 20th century. To simulate the behaviours of human tissues, tissue phantoms are developed with similar electrical or mechanical properties to human tissues for long-term experimentation and reproducible analysis. To validate the simulation results in the previous two chapters, two different phantom models were fabricated to simulate the human forearm near the wrist, including *one-artery model* and *two-arteries model*. A desktop injection pump was applied to change the blood simulant volume inside the artery. Meanwhile, the impedance signal was measured by multi-frequency impedance analyser (MFIA, Zurich Instruments, Switzerland). The phantom experiments aimed to substantiate the feasibility of the proposed BIM setup (i.e., mathematical modelling, frequency range and electrode configurations) before attempting measurement of the human body, which is expected to be performed in the future.

In this chapter, the overall experimental arrangement and process will be introduced first, and then each experimental procedure will be described in detail, including the design of 3D printed moulds, the fabrication of wrist phantom and the impedance measurement during pumping. The last part will exhibit and discuss the experimental results regarding the measured impedance and the estimated arterial diameter.

6.2 Experiment process

Figure 67 illustrates the entire phantom experimental process. The whole process can be primarily divided into two stages: the fabrication of the human wrist phantom and the estimation of arterial diameter using BIM. First, to materialise the human wrist model simulated in ANSYS HFSS, two 3D moulds were separately designed and printed. Various proportions of tissue-mimicking materials were tested for suitability as the human wrist phantom. A desktop injection pump was utilised to change the volume in the blood phantom

to simulate the dynamic arterial diameter change. The dynamic impedance signal was measured to estimate the arterial diameter using the mathematical modelling proposed in Chapter 3. Then, the accuracy was evaluated and analysed. The following sections will describe the experimental process of each step in detail.

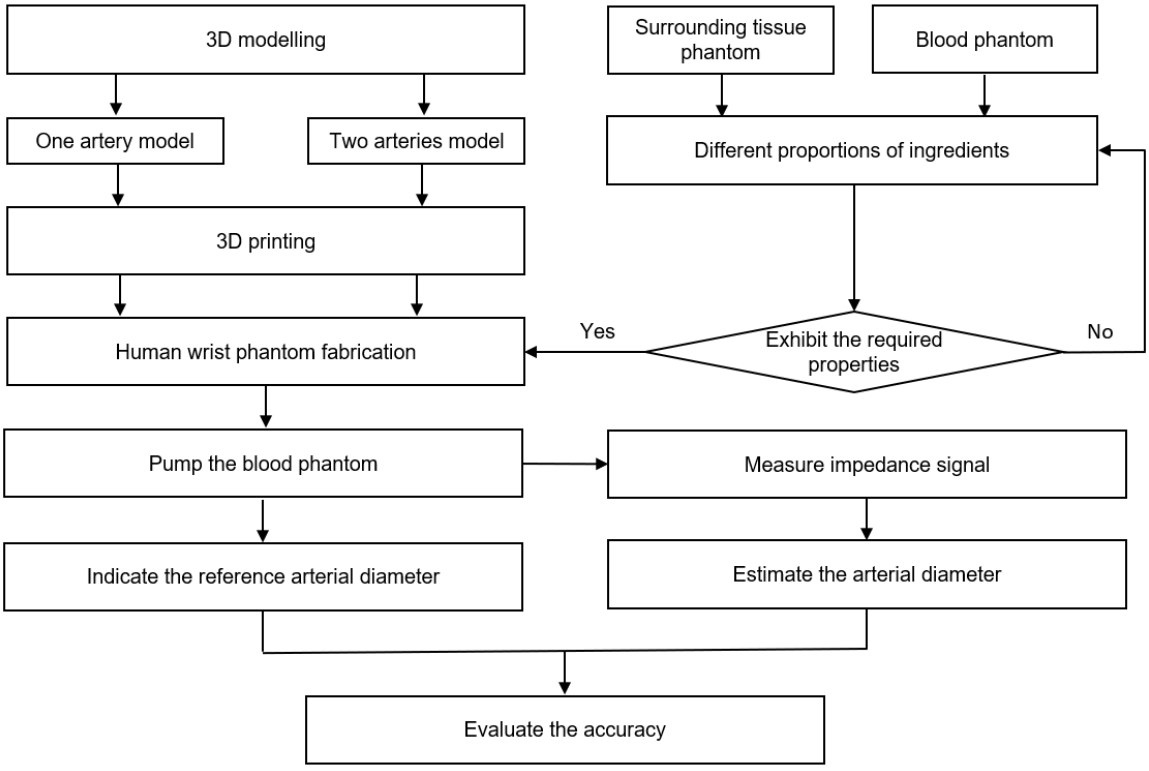

Figure 67. Experimental process flow chart.

6.2.1 Mould design and fabrication

At the beginning of mould design, several schemes were considered. The first consideration was the placement of the electrodes. Unlike the models in computational simulation, if we want to investigate different locations of the electrodes, it complicates the experimental operation and increases the experimental uncertainty, for example, by sacrificing the stable contact between the electrode and phantom surface. To ensure a long-term stable attachment during the measurement, all conventional electrodes were placed on a single printed circuit board (PCB) and fix it at the bottom of the phantom. Figure 68 illustrates the structure of the electrode plate in this phantom experiment. Six metal holes with 18 mm spacing on the PCB (115 mm × 27 mm) was designed to solder six metal snap fasteners. The advantage of the

metal snap fastener is that it is easier to replace the new ECG dry electrodes, considering the electrode surface may be oxidised and corroded when in contact with the phantom for a long time. A six-pin PCB terminal block (MPT 0.5/5- 2.54, Phoenix Contact) was soldered on another side of the PCB to connect to the multi-frequency impedance analyser. Six pins were connected to six ECG dry electrodes through the PCB.

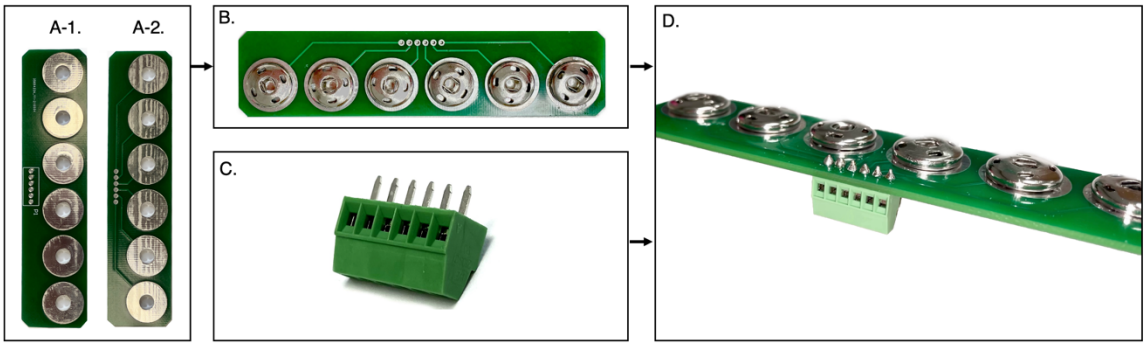

Figure 68. The structure of the electrode plate: (A-1) PCB side 1; (A-2) PCB side 2; (B) PCB soldered with six metal snap fasteners; (C) terminal block; (D) assembled electrode plate.

Based on the parallel-tissues modelling, multi-tissue domains are reasonably regarded as a single component once the uniform E-field is generated in the region. According to Equation 16 described in Chapter 3, the estimation of arterial diameter change only requires three types of parameters (i.e., overall resistance, measured length between PU electrodes and the conductivity of blood) rather than the conductivities of other tissues (i.e., skin, fat, muscle, and bones). Moreover, the results observed in Chapter 4 and Chapter 5 indicated that other tissue domains would not affect the final estimation significantly, except for the remarkable influences in wrist model 5 (with two arteries). Considering the complexity of the moulding process, different tissue layers were neglected in phantom experiments. It was reasonable to consider all other tissues as one uniform component with lower conductivity in this project. Therefore, two different wrist phantom moulds were designed and fabricated: *one-artery model* (according to Figure 47) and *two-arteries model* (according to Figure 59).

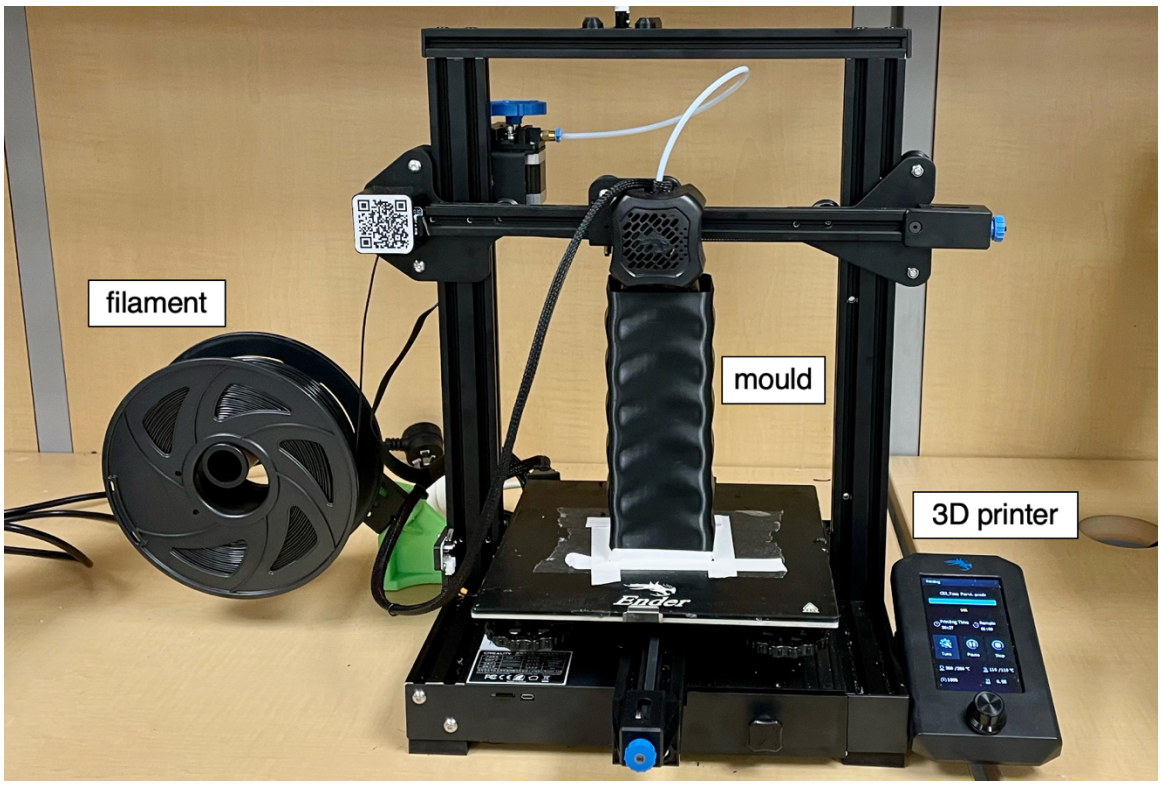

Figure 69. Mould printing process

All moulds for the wrist phantom were designed by SOLIDWORKS 2019 (Dassault Systèmes) and printed by a 3D printer, as shown in Figure 69. The Polyethylene Terephthalate Glycol (PETG) and Polylactic Acid (PLA) filaments were used for the *one-artery model* and *two-arteries model*, respectively. Both materials showed excellent tolerance to high temperature and corrosion during the whole phantom experiment (i.e., heated chemical solution). The dimension and construction of the two moulds will be further described separately.

6.2.1.1 One-artery model

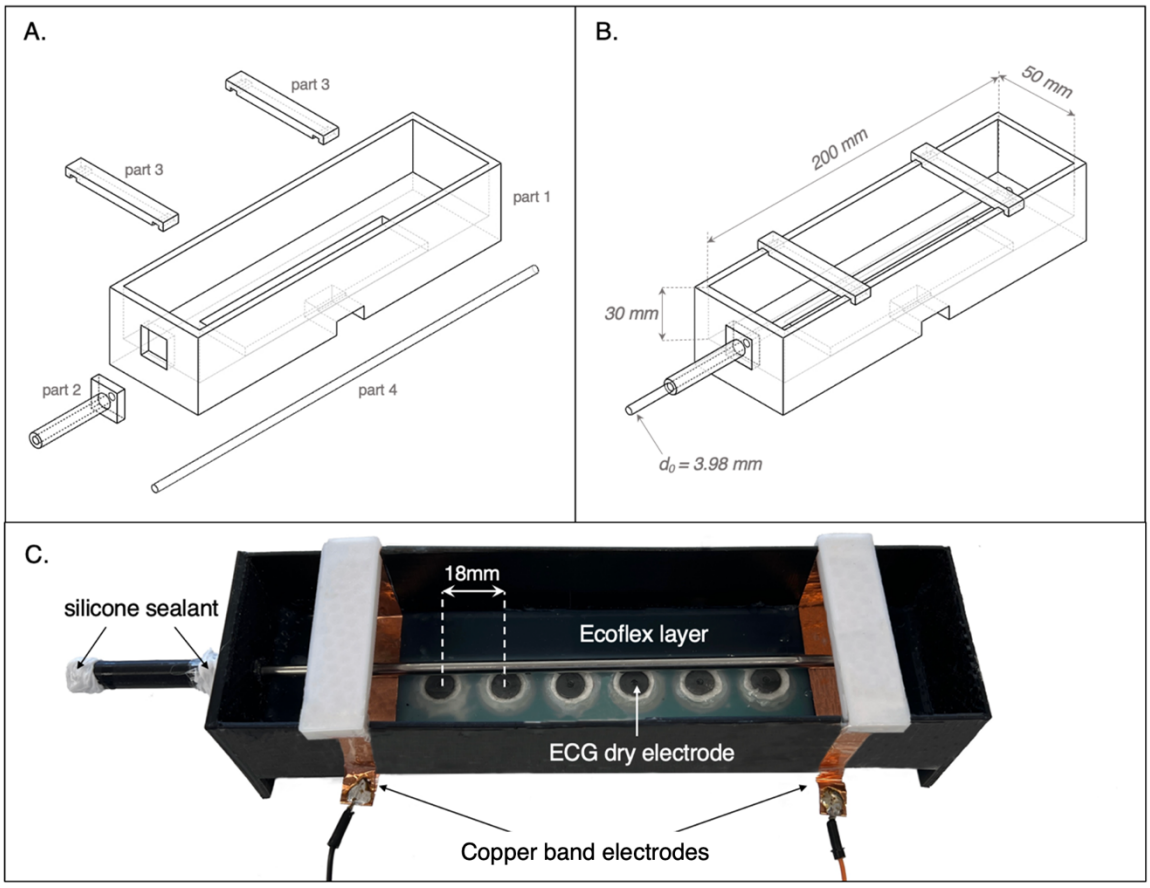

Figure 70. Mould for one-artery model: (A) 3D schematics of separated moulds (parts 1-3) and the metal rod (part 4); (B) 3D schematics of assembled mould; (C) assembled setup for wrist phantom fabrication.

For the *one-artery model* (see Figure 70*)*, the inner width and height of part 1 remained the same as the initial cuboid wrist model simulated in previous chapters, which were 50 mm and 30 mm, respectively. The inner length of part 1 was 200 mm, which was designed twice longer than the simulation (100 mm) to leave adequate space for electrodes and pump operation. I left space and an open port for the electrode plate at the bottom of the part 1, allowing the terminal block to connect wires. Part 2 was designed as a detachable piece to fix and guide part 4 (a straight metal rod with a diameter of 3.98 mm). Furthermore, two pieces of part 3 could clip on part 1 to provide four-sided structures for copper tapes as the band electrodes. After assembling all parts and the electrode plate, a filmy silicon insulating layer (Ecoflex^{TM} 00-50) was poured on the electrode plate to cover all other conductive components except the ECG dry electrodes. This procedure was essential to prevent other conductive components from contacting the phantom, such as the metal snap fasteners.

6.2.1.2 Two-arteries model

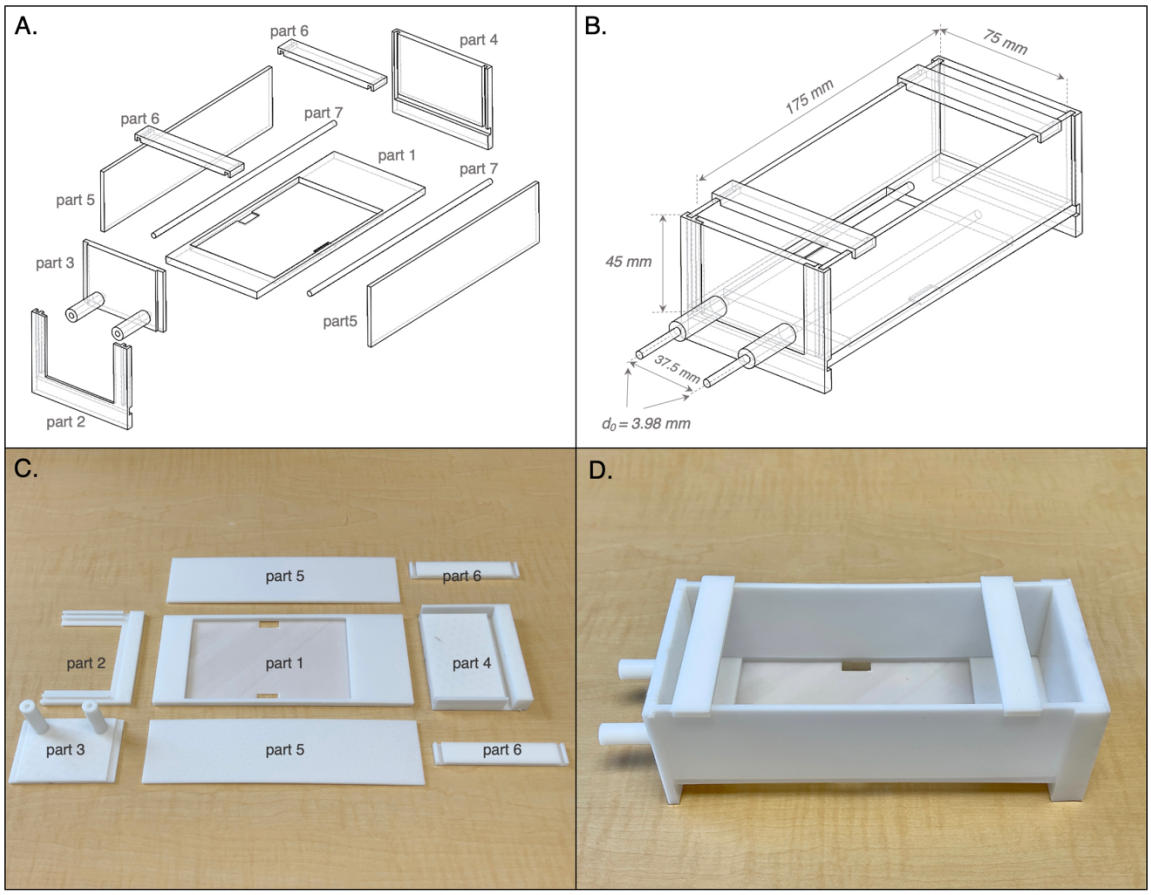

Figure 71. Mould for two-arteries model: (A) 3D schematics of the separated moulds (parts 1-6) and the metal rod (part 7); (B) 3D schematics of the assembled mould; (C) 3D printed parts; (D) 3D printed assembled mould.

Based on the observations from the one-artery experiment, the design ideas were changed for *two-arteries model*. It was noticed that the 3D printing process was more prone to failure when producing an enormous mould with hollow structures. For this reason, the overall mould for the *two-arteries model* was separated into more pieces to ensure more accurate printing. Figure 71 illustrates the schematics and printed parts for the new mould. Considering the more complex experimental operation with two arteries, the whole dimension of the *two-arteries model* was magnified by a factor of 1.5 compared to the simulated model (i.e., Figure 59). The wrist phantom's height, width, and length were 45 mm, 75 mm, and 175 mm, respectively. The diameter of both arteries was 3.98 mm, which was also approximately 1.5 times bigger than the maximum diameter (2.6 mm) in the computational simulation. This magnified factor ensured that the new wrist phantom had the same volume scale as the simulated model for more critical comparison purpose.

Part 1 was the bottom of the whole mould and housed two symmetrical electrode plates. Parts 2, 4, and 5 could snap around part 1 to provide support. They were sealed and fixed using Super Glue (UHU®). Part 3 played the same role as part 2 in the previous mould to fix and guide two metal rods (part 7). A larger open area was left for part 3 to attach the pump device. Two pieces of part 6 were used to provide four-sided structures for copper tapes as band electrodes. A thin silicon insulating layer (Ecoflex™ 00-50) covered the two electrode plates to prevent other unwanted conductive components from contacting the phantom.

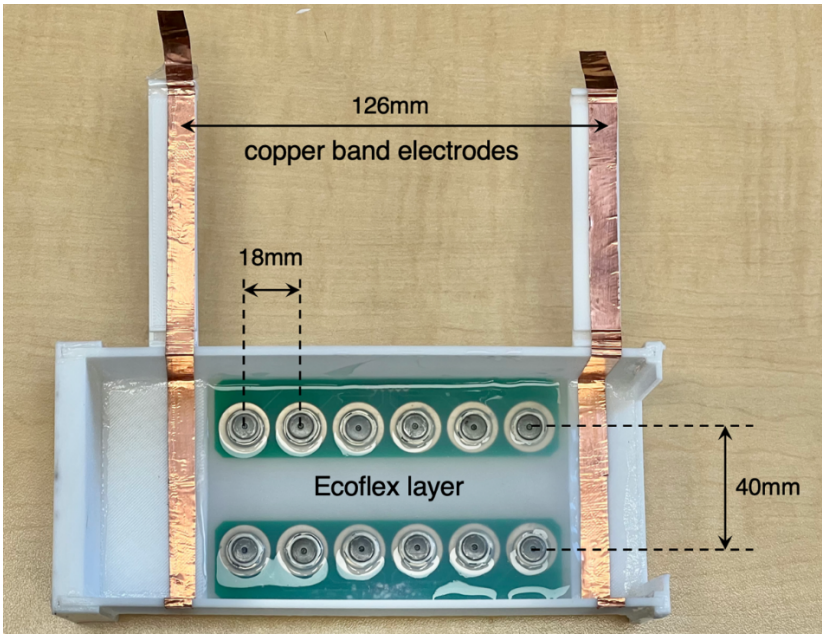

Figure 72. Assembled setup for wrist phantom fabrication.

6.2.2 Phantom fabrication

As mentioned earlier, although the ideal human wrist phantom would contain all the same tissue domains as the simulated model, it is not necessary to address such complex moulding process to prove the concept in this project. Chapter 3 has described the measured tissues as an equivalent parallel circuit. The basal impedance represented both surrounding tissues and the initial blood. Therefore, this project focused on only two material domains:

- Gel-based surrounding tissue simulant

To avoid unnecessary cost, the selection of suitable tissue-mimicking materials for surrounding tissue simulant was referred to my previous master thesis [246], [247], including

the machinal properties (Young's modulus and breaking behaviours) and dielectric properties (bulk conductivity and relative permittivity) of various concentrations of gelatine samples.

- Conductive liquid for blood simulant

A conductivity sensor using the four-electrodes method was constructed to determine the conductivity of the liquid. Different proportions of sodium chloride (NaCl) were mixed with deionized water to simulate the conductivity of human blood.

6.2.2.1 Surrounding tissue simulant

In this phantom investigation, the selected tissue-mimicking materials were expected to exhibit adequate elasticity and rupture strength to maintain the integrity of the artery section during pumping. The required elasticity of artery wall had broader limits because the diameter changes of artery section depended on the conservation of volume instead of the specific elasticity of the arterial wall.

Even though the electrical properties of the surrounding tissue phantom did not dominate the estimation process, its conductivity must be lower than the blood phantom to ensure the dominant contribution of conductive pulsatile blood to the impedance change. Ideally, the conductivity of the surrounding tissue phantom should be close to the overall conductivity of simulated skin, fat, muscle, cortical bone, and cancellous bone domains in Chapter 5.

Gelatine is the most common matrix material used in tissue phantoms and is a heterogeneous water-soluble mixture of high average molecular weight. The advantages of gelatine-based phantoms are that they can be fabricated at a low cost and preserved in a refrigerator for a long time. In my previous research, several trials were performed by mixing various concentrations of gelatine powder from 4 wt.% to 30% wt.% with deionized water to produce gelatine-only samples. The longitudinal compression test was performed to prevent cracking the samples and allow repeatable tests to determine Young's modulus rather than the tensile test. Furthermore, the breaking behaviour of gel-only samples was examined. Each sample was compressed until achieving 100% strain, and the maximum breaking strain was observed. Table 27 lists the mechanical properties of each sample from previous research. A positive correlation between Young's modulus and gel concentration was found. The higher gel concentration resulted in increased stiffness. Moreover, the breaking strains demonstrated

that higher gel concentration shows higher tolerance to deformation. A breaking strain over 80% was achieved in the compression test when the gelatine concentration was over 10 wt.%. Considering the deformation range of the artery, 20 wt.% gelatine powder was selected as the matrix of the surrounding tissue phantom for further experiment in this project.

Table 27. Mechanical properties of gel-only samples from the previous research [246]

Ingredients (percentage by weight)		**Young's modulus (kPa, mean ± SEM)**	**Breaking strain**
Deionized water	**Gelatine powder**		
96.00%	4.00%	3.5±0.066	63.20%
94.00%	6.00%	7.79±0.092	71.21%
92.00%	8.00%	12.9±0.089	76.81%
90.00%	10.00%	18.2±0.215	80.02%
88.00%	12.00%	27.2±0.057	>80.00%
85.00%	15.00%	29.1±0.168	>80.00%
80.00%	20.00%	56.9±0.486	>80.00%
73.00%	23.00%	85.7±0.623	>80.00%
75.00%	25.00%	130.0±0.996	>80.00%
70.00%	30.00%	196.0±1.490	>80.00%

The approximate target conductivity of the surrounding tissue phantom was calculated via the cross-sectional area (see Figure 59) and the individual conductivity of each tissue (see Table 36 and Table 37) simulated in Chapter 5. Based on Equation 9 and Equation 10, the overall conductivity of surrounding tissues (σ_{st}) can be determined by:

$$\sigma_{st} = \frac{l}{R_{st}A_{st}} = \frac{\left(\frac{1}{R_{skin}} + \frac{1}{R_{fat}} + \frac{1}{R_{muscle}} + \frac{1}{R_{cortical}} + \frac{1}{R_{cancellous}}\right) l}{A_{st}} = \frac{\sigma_{skin}A_{skin} + \sigma_{fat}A_{fat} + \sigma_{muscle}A_{muscle} + \sigma_{cortical}A_{cortical} + \sigma_{cancellous}A_{cancellous}}{A_{skin} + A_{fat} + A_{muscle} + A_{cortical} + A_{cancellous}} \quad \text{Equation 32}$$

The calculated overall conductivity of all surrounding tissues in the computational simulation was from 0.099 S/m to 0.150 S/m between 1 kHz and 1 MHz, as plotted in Figure 73. It also became the target conductivity range for the surrounding tissue phantom in this experiment. The gelatine-only samples have been indicated with much lower conductive from approximately 0.016 S/m to 0.030 S/m between 1 kHz and 1 MHz. Therefore, other filler materials were considered to increase the conductivity of gelatine-based phantom. NaCl is a widely used material to increase conductivity, which has also been investigated with various

salt concentrations in the gelatine samples. The conductivity nearly showed a linear relationship with the amount of added NaCl. Therefore, an additional 0.1 wt.% NaCl (approximately 0.017 M) was selected to dissolve into deionized water with gelatine powder as the surrounding tissue simulant in this phantom experiment.

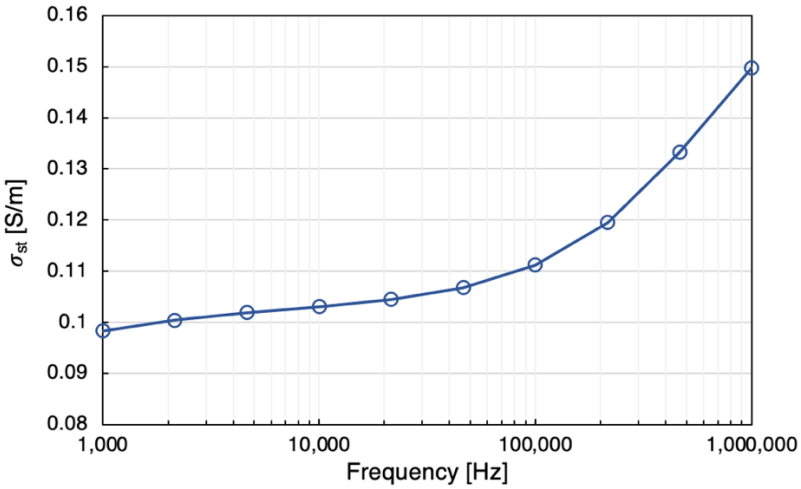

Figure 73. Calculated overall conductivity of simulated surrounding tissues

6.2.2.2 Blood simulant

As mentioned in previous chapters, human blood is a highly conductive tissue with conductivity from 0.700 S/m to 0.820 S/m between 1 kHz and 1 MHz. NaCl solution is a common electrolyte with free-moving ions in which the constituent sodium ion (Na^+) and chloride ion (Cl^-) dissociate entirely. The advantage of the NaCl solution is that it is low-cost, and its conductivity is linearly related to concentration. Even though there have been several studies investigated the conductivity of NaCl solution [248]–[250], it is necessary to calibrate the measurement setup before the phantom fabrication because the liquid conductivity is highly sensitive to the measurement environment, such as the temperature, electrode polarization, cell constant value, the purity of chemicals and other potential instrument errors [251].

Three different concentrations of NaCl solution were prepared by adding the weighed NaCl with 100 mL of deionized water and then fully dissolved by stirring for around 2 minutes using a magnetic stirrer. The concentrations of NaCl solution sample were 0.03 M, 0.05 M and 0.15 M. Samples were prepared shortly before the conductivity measurement at room temperature (22.5°C). This project applied the four-electrodes method to measure the

conductivity of liquid samples (see Figure 74). The inner dimension of the cuboid liquid container was 50 mm × 50 mm × 20 mm (50 mL). In this low-cost apparatus, the outer two copper plate electrodes generated uniform current excitation, and the inner two pin electrodes measured the resulting potential difference. Moreover, a 3D printed grid board was placed on the cuboid liquid container. There were seven rows of small holes (with a spacing of 5 mm) to insert and fix the pin electrodes. The uniformity of the E-field throughout the liquid could be verified by comparing the measured impedance between each row with the same pin electrode spacing.

Furthermore, there were nine small holes with a spacing of 5 mm in each row, aiming to obtain the average conductivity from different cell constant (K) of the same NaCl sample. The cell constant is one important scale factor that depends on the overall geometry of the sample and current paths. Compared with the traditional two-electrodes method, this setup could minimize the errors caused by electrode polarization and address a broader frequency range of measurement. The 4-electrodes setup was connected to the multi-frequency impedance analyser, and the real and imaginary parts of impedance were measured between 1 kHz to 1 MHz and exported for further data processing.

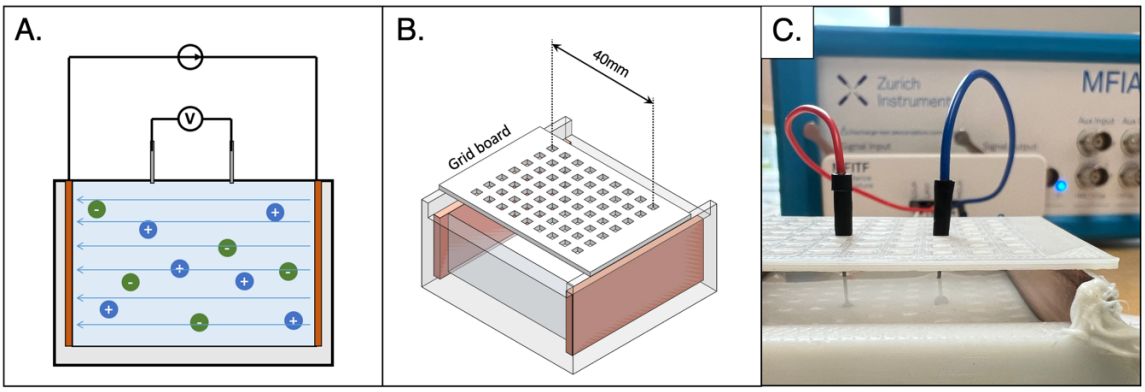

Figure 74. Four-electrodes conductivity measurement: (A) the principle of the four-electrodes method; (B) 3D schematic of the setup; (C) experimental setup for NaCl solution samples.

In this project, tissue simulants were modelled as an RC circuit in parallel. If the cross-section and chemical composition of the liquid were uniform, the E-field generated by two parallel copper plates were constant across the liquid. Then, the conductivity of the NaCl solution (σ_l) was calculated as:

$$\sigma_l = \frac{K}{R_l} = \frac{l}{R_l S}$$ Equation 33

where R_l is the resistance of the measured NaCl sample, l is the distance between two pin electrodes, and S is the cross-section of the current path, which was the area of copper plates (1000 mm^2). The measurement was repeated eight times with different distance l_n from 5 mm to 40 mm with 5 mm steps. The mean conductivity and standard deviation (SD) were calculated by:

$$\overline{\sigma_l} = \frac{1}{n}\sum_{i=1}^{n} \sigma_{l_i} = \frac{\frac{l_1}{R_{l_1}A} + \frac{l_2}{R_{l_2}A} + \cdots + \frac{l_n}{R_{l_n}A}}{n}$$ Equation 34

$$SD = \sqrt{\frac{\sum_{i=1}^{n}(\sigma_{l_i} - \overline{\sigma_l})^2}{n-1}}$$ Equation 35

Figure 75 illustrates the calculated mean conductivity of different NaCl samples between 1 kHz and 1 MHz. The conductivity of NaCl solution exhibited a positive relationship with salt concentration as reported in literature. Although the conductivity slightly increased with the frequency for each sample, the overall values remained relatively constant over the frequency range. As shown in Table 28, compared with two previous studies [248], [249], 0.03 M and 0.15 M samples showed good agreement with literature, whereas the measured conductivity of the 0.05 M sample was slightly higher. Based on the linear regression between NaCl concentration and conductivity, 0.08 M NaCl solution was chose as the blood simulant in further phantom experiments.

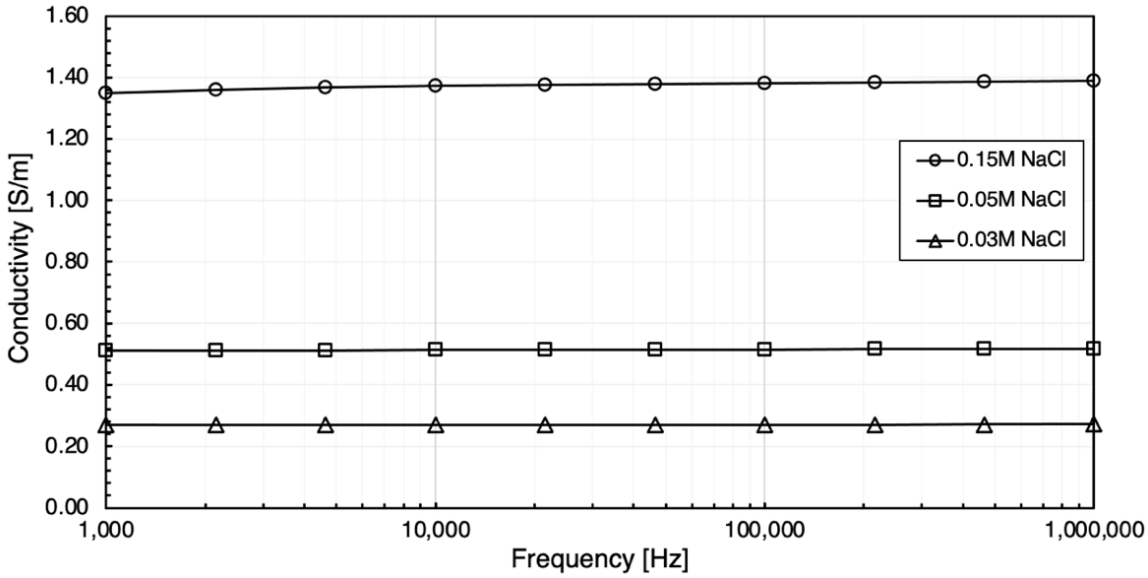

Figure 75. Measured mean conductivity $\bar{\sigma}_l$ of three different concentrations of NaCl solution between 1 kHz to 1 MHz.

Table 28. Comparison between measured mean conductivity and reference values from the literature.

NaCl samples	**Conductivity $\bar{\sigma}_l$ [S/m] (Mean±SD)**	**Reference values**	
		Gabriel et al., 2009 (4-electrodes)	**Peyman et al., 2007 (open-ended coaxial probe)**
0.03 M	0.270±0.002	0.276	0.281
0.05 M	0.514±0.007	0.477	0.466
0.15 M	1.374±0.028	1.392	1.375

6.2.2.3 Human wrist phantom

Figure 76 and Figure 77 illustrate the main experimental steps to fabricate the *one-artery model* phantom and the *two-arteries model* phantom, respectively.

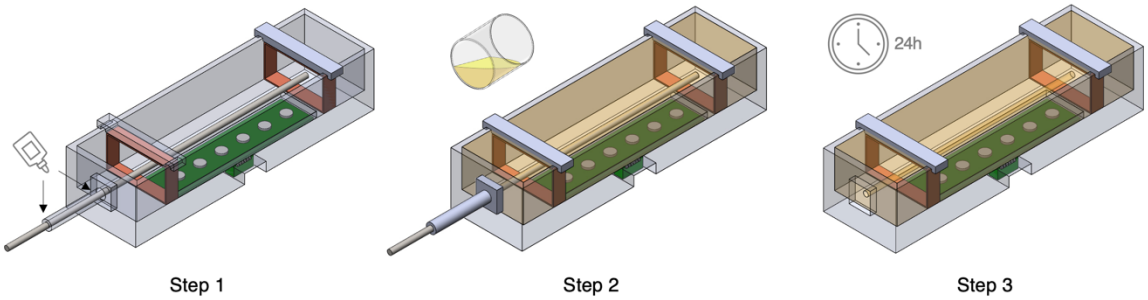

Figure 76. Three main steps of the fabrication of one-artery human wrist phantom.

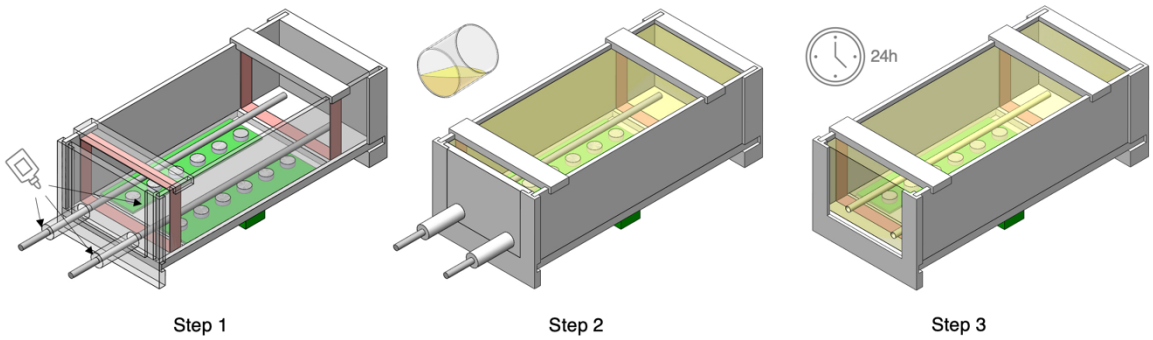

Figure 77. Three main steps of the fabrication of two-arteries human wrist phantom.

1) Step one: assemble and seal the printed mould

After assembling all 3D printed parts introduced in Figure 70 and Figure 71, the electrode plate was settled at the bottom of the mould (one plate for *one-artery model* and two plates for *two-arteries model*) and covered with a thin insulating layer. Then the copper tape with a width of 10 mm was stuck around the inner wall of the mould and soldered to a wire at one end. Next, the metal rod with a diameter of 3.98 mm was inserted into the mould along the hole (one rod for the *one-artery model* and two rods for the *two-arteries model*). Afterwards, all joints between detachable parts were sealed using silicone sealant to prevent the gelatine solution from leaking out. The silicone sealant was cured for 4 to 8 hours at room temperature (22.5°C) and can be easily removed to reuse the mould.

2) Step two: pour the prepared surrounding tissue simulant

To fabricate the surrounding tissue simulant, 20 wt.% gelatine powder and 0.1 wt.% NaCl were selected to dissolve in deionised water. Before preparing the gelatine solution, all experimental equipment was thoroughly cleaned with deionised water and dried using paper towels. The required volume of deionised water was measured using a graduated cylinder and poured into a suitable beaker (250 ml for the *one-artery model* and 650 ml for the *two-arteries model*). Then, weighed gelatine powder (62.5 g for *one-artery model* and 162.5 g for *two-arteries model*) and NaCl (0.25 g for *one-artery model* and 0.65 g for *two-arteries model*) were gradually added to the beaker. Next, the mixture was heated on the hotplate and dissolved completely using a magnetic stirring bar. The solution temperature was controlled between 60°C and 80°C during stirring. After the aqueous gelatine solution became transparent (approximately 10 to 20 minutes depending on the volume), all air bubbles floated on the surface were removed using a plastic Pasteur pipette. Last, the prepared

gelatine solution was gently poured into the mould and left on a level, horizontal surface at room temperature for 24 hours, as shown in Figure 78.

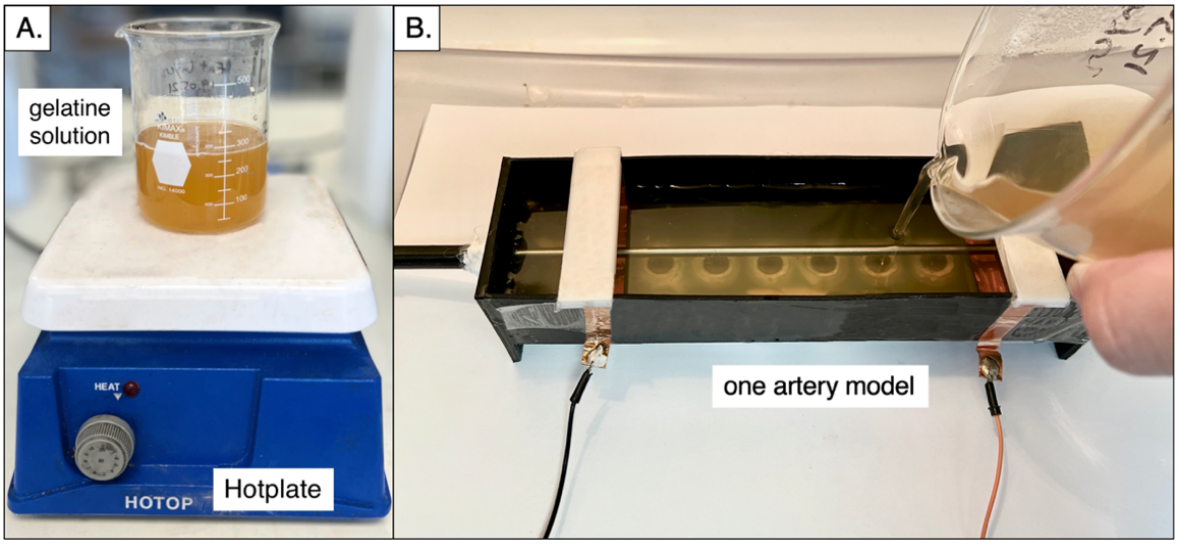

Figure 78. Preparation for surrounding tissue simulant: (A) dissolved gelatine powder and NaCl in deionised water; (B) cast the gelatine solution in 3D printed mould.

3) Step three: remove the metal rod after congealing

Typically, the gelatine solution can be thoroughly coagulated after 24 hours at room temperature. Although this process can be expedited by storing the solution in the fridge, the temperature of the wrist phantom would continue to recover to room temperature after being removed from the refrigerator. During this period, the increasing temperature over time could cause the conductivity change, resulting in fluctuating impedance results. After solidifying, the silicone sealant was cleared away, and the metal rod was carefully pulled out, leaving a uniform, straight hole as the hollow artery. Then the detachable part (part 2 in *one-artery model* and part 3 in *two-arteries model*) was also demounted to uncover the open end of the artery for pump operation.

6.2.3 Phantom-pumping operation and impedance measurement

The basal diameter of the artery phantom was determined by the metal rod as 3.98 mm in this experiment. During the initial period of the phantom-pumping experiment, it was realised that the gelatine-based phantom was more robust under contraction than expansion. In other words, the closed end of the artery phantom was more likely to burst when I attempted to increase the arterial diameter by injecting more volume of blood simulant. Therefore, it was

decided to withdraw a specific volume of blood simulant from the artery section to reduce the arterial diameter.

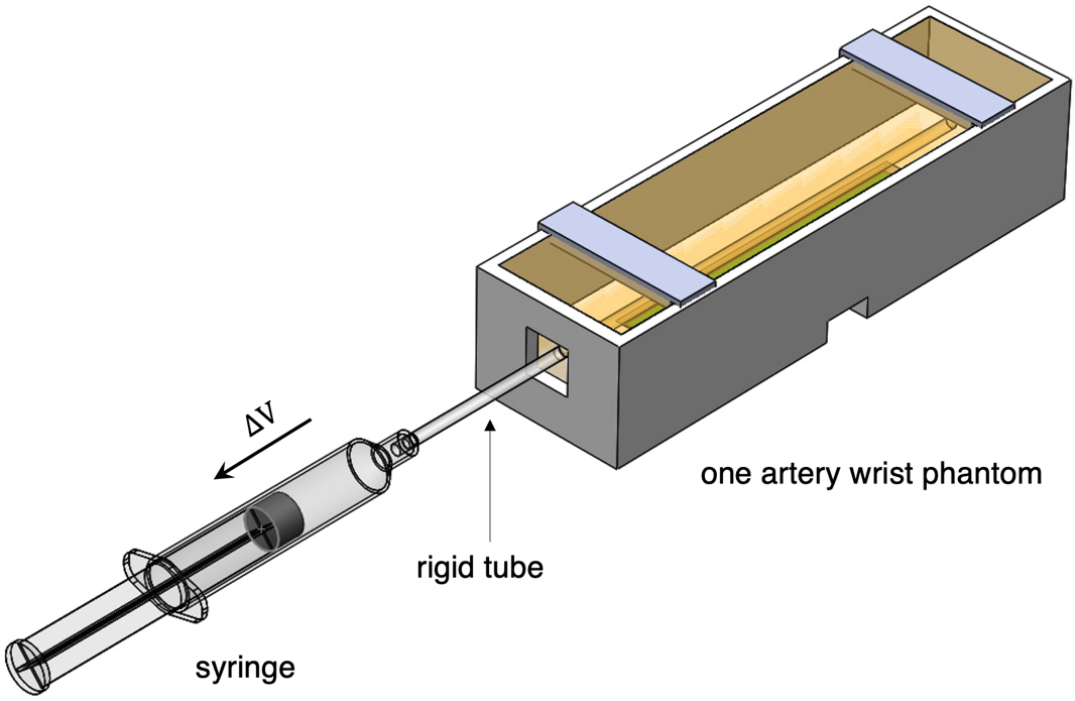

Figure 79. Pump operation of one-artery human wrist phantom.

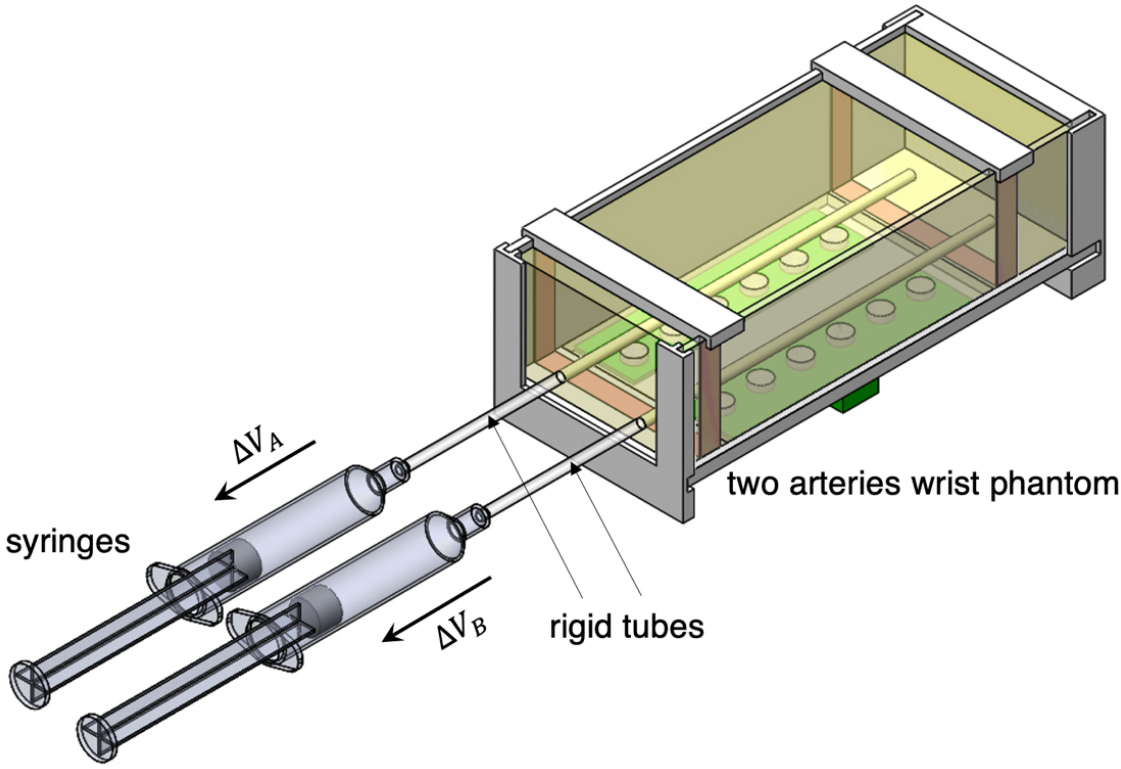

Figure 80. Pump operation of two-arteries human wrist phantom.

Figure 79 and Figure 80 illustrate the setup for phantom-pump experiments. A rigid plastic tube was inserted into the hollow artery section to a depth of around 10 mm. The tube had a slightly bigger outer diameter of 4.5 mm and did not deform during pumping. During the experiment, Super Glue (UHU®) was found as the only type of sealant could firmly bond the plastic tube with a water-based gelatine simulant. Thus, Super Glue was applied between the open end of the hollow artery phantom and the rigid tube to prevent air from entering the artery system, which typically took 24 hours to be fully sealed. Next, the prepared blood simulant was gradually injected into the hollow artery phantom from the bottom of the artery to the open end of the rigid tube by a slender needle. Then, a syringe half-filled with the blood simulant was connected to the open end of the rigid tube. These procedures were sensitively handled to avoid mixing any gas into the artery system, preventing the influence of atmospheric pressure. In this way, increments in volume of the syringe were equal to the decreased blood phantom volume in the artery because of the conservation of volume. The reference cross-sectional area changes in the artery (ΔA_r) can be calculated from the withdrawn volume of the blood phantom (ΔV_b) and the total length of the artery phantom (L_{artery}) by assuming the uniform deformation of the whole artery section:

$$\Delta A_r = \frac{\Delta V_b}{L_{artery}} = \frac{\pi \Delta L_{syringe} {d_{syringe}}^2}{4\, L_{artery}} \qquad \text{Equation 36}$$

where $\Delta L_{syringe}$ was the displacement distance of the plunger and $d_{syringe}$ was the inner diameter of the syringe barrel. Since the initial diameter of the artery phantom (d_0) was known (3.98 mm), the reference absolute diameter of the artery (d_r) could be determined:

$$d_r = \frac{A_0 - \Delta A_r}{L_{artery}} = \frac{\frac{\pi {d_0}^2}{4} - \frac{\Delta L_{syringe} A_{syringe}}{L_{artery}}}{L_{artery}} = \frac{\pi {d_0}^2}{4 L_{artery}} - \frac{\Delta L_{syringe} A_{syringe}}{{L_{artery}}^2} \qquad \text{Equation 37}$$

Figure 81 and Figure 82 represent the integrated experimental apparatus for impedance measurement during phantom pumping. To ensure stable and controllable operation of the syringe, a commercial desktop injection pump was applied to fix the barrel and drive the plunger. The pump controller allowed the plunger can be linearly pulled and pushed along the inside of the barrel with specific speed and time. The multi-frequency impedance analyser was employed to measure the absolute value of the impedance and phase angle of all subjects between 1 kHz and 1 MHz with ten logarithmical steps throughout the phantom experiments,

including 1 kHz, 2.15 kHz, 4.64 kHz, 10, 21.54 kHz, 46.42 kHz, 100 kHz, 215.44 kHz, 464.16 kHz and 1 MHz.

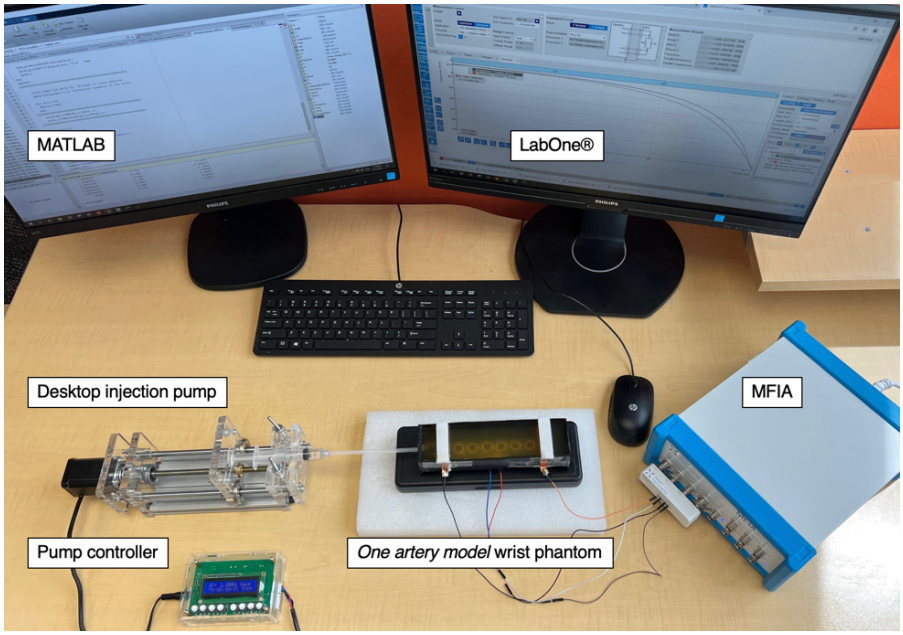

Figure 81. The entire experimental setup for the one-artery model phantom-pumping experiments (Groups A, B and C).

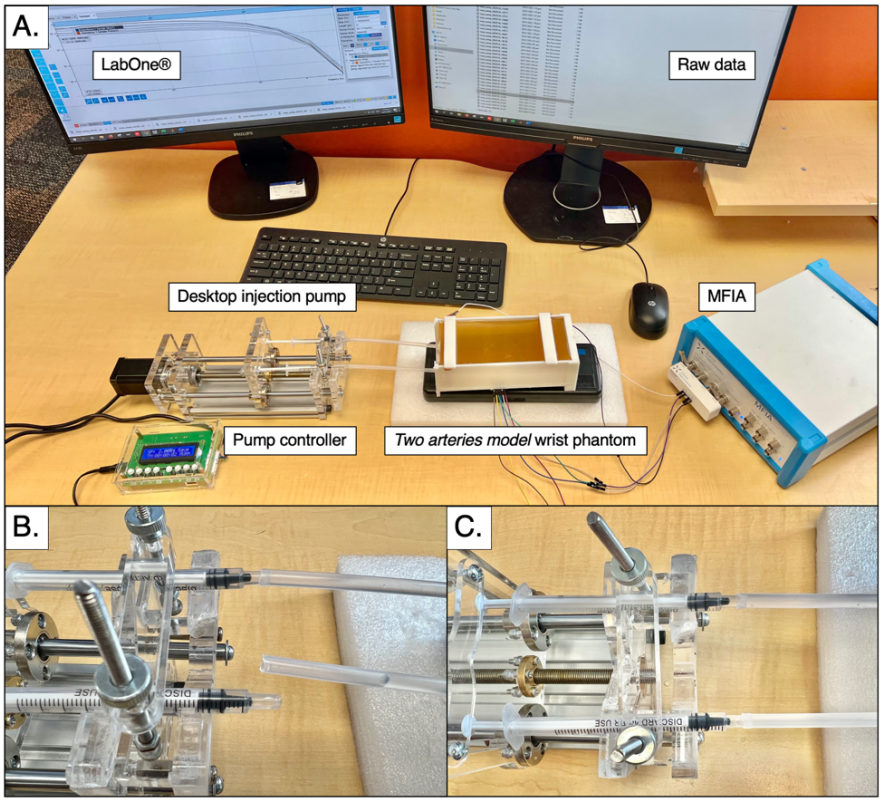

Figure 82. (A) The entire experimental setup for two-arteries model phantom-pumping experiments; (B) specific setup for Groups D and E; (C) specific setup for Group F.

Each electrode was assigned a number to facilitate the description of the different electrode configurations, as shown in Figure 83. Then, electrode configurations that used the conventional 4-spot electrodes method were assigned codes as 'L_{CC}/L_{PU}', where 'L_{CC}' indicated the distance between CC electrodes, and 'L_{PU}' demonstrated the distance between PU electrodes. For those configurations that applied band electrodes, the codes were adjusted as 'B/L_{PU}', where 'B' stood for the band electrode method (see Table 29).

Similar to the computational simulation, the investigation of phantom pumping was divided into six progressive experimental groups. Each experimental group had specific electrode configurations and pumping operations for different objectives. Figure 84 and Figure 85 respectively show the experimental process of six test groups for the *one-artery model* and *two-arteries model*. At the beginning of phantom-pumping experiments, six diverse configurations of the conventional 4-spot electrodes method were assessed (Group A) to corroborate the effects of electrode spacing on the accuracy of estimated arterial diameter. In Group B, three band electrode configurations were tested. According to the results, the most promising electrode configuration was further investigated with ten minor pumping steps to explore the source of errors (Group C). As the influence of another conductive artery on the overall current distribution had been regarded, Group D was first implemented to examine whether an adjacent static blood-filled artery could weaken the estimation. Next, the significance of an adjacent pulsatile artery (contralateral artery) on the measured impedance signal was investigated in Group E. Subsequently, two arteries were simultaneously constricted to simulate the physical pulsatile condition. The original static condition was measured as the basal impedance before contracting the artery in each test. Moreover, the withdrawn blood phantom was entirely injected back into the artery to allow the arterial diameter to restore to the original geometry before the next test.

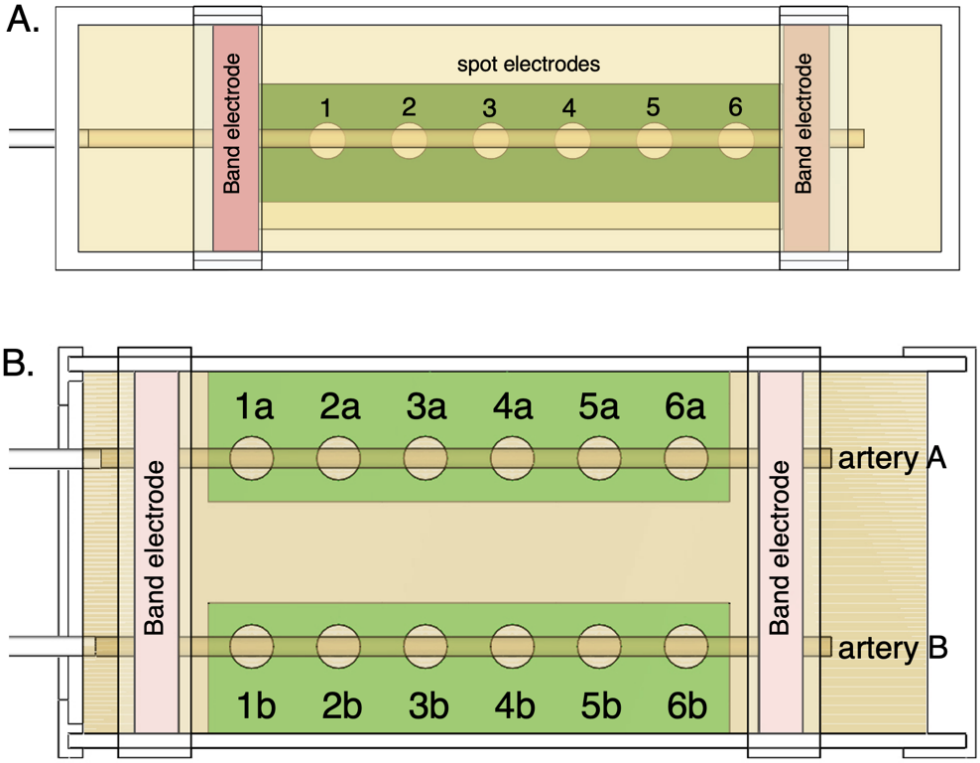

Figure 83. Assigned numbers for electrodes in phantom-pumping experiments: (A) one-artery model for Groups A, B and C; (B) two-arteries model for Groups D, E and F.

Table 29. Assigned codes for various electrode configurations in phantom pumping experiments.

Electrode methods	**Electrode configurations**						
	Locations of CC electrodes (including 1a to 6a and 1b to 6b)		L_{CC} [mm]	Locations of PU electrodes (including 1a to 6a and 1b to 6b)		L_{PU} [mm]	Assigned codes
Conventional 4-spot electrodes method	1	6	90	3	4	18	*90/18*
	1	6	90	2	4	36	*90/36*
	1	6	90	2	5	54	*90/54*
	1	5	72	3	4	18	*72/18*
	1	5	72	2	4	36	*72/36*
	1	4	54	2	3	18	*54/18*
Band electrodes method	Band electrodes		126	1	6	90	*B/90*
	Band electrodes		126	2	5	54	*B/54*
	Band electrodes		126	3	4	18	*B/18*

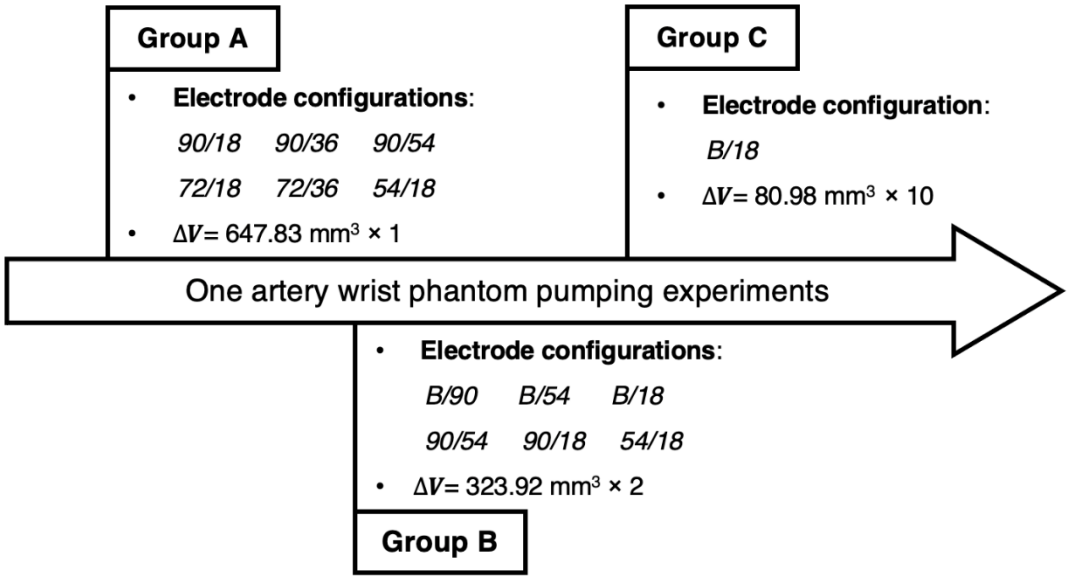

Figure 84. The overall process of one-artery wrist phantom pumping experiments.

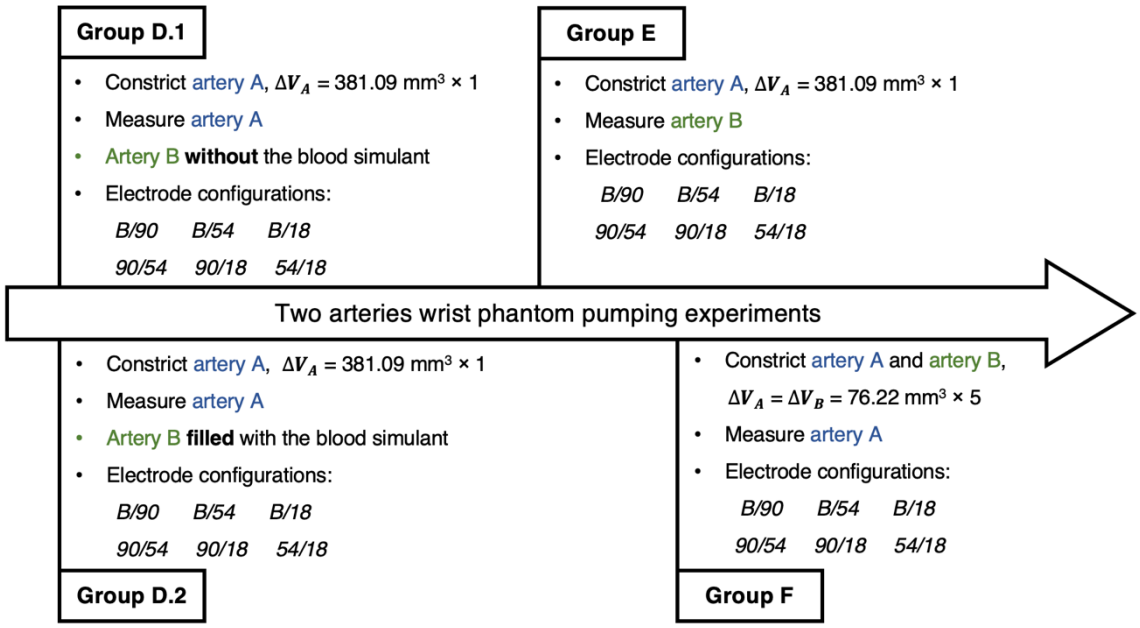

Figure 85. The overall process of two-arteries wrist phantom pumping experiments.

All measured data was exported from the LabOne® (Zurich Instruments, Switzerland) control interface, including frequency (f), absolute impedance ($|Z|$), and phase angle (θ). Then, the raw data were processed and analysed using MATLAB (R2019a, The MathWorks, US). First, the real and imaginary parts of measured impedance were calculated by:

$$Re(Z) = |Z| \cos(\frac{\pi\theta}{180}) \quad \text{Equation 38}$$

$$Im(Z) = |Z| \sin(\frac{\pi\theta}{180}) \quad \text{Equation 39}$$

The electrical response of the wrist phantom was also described using a parallel RC circuit. Thus, the resistance of the whole wrist phantom can be obtained. Afterwards, according to Equation 16 and Equation 17, the diameter of artery phantom after pumping can be estimated by:

$$\hat{d}_{artery} = 2\sqrt{\frac{\hat{A}_{artery}}{\pi}} = 2\sqrt{\frac{A_0 - \widehat{dA}_{artery}}{\pi}} = 2\sqrt{\frac{A_0 + \frac{L_{PU} \cdot (R_0 - R')}{\bar{\sigma}_l \cdot R_0 \cdot R'}}{\pi}} \quad \text{Equation 40}$$

where R_0 was the basal resistance of the whole wrist phantom corresponding to the original cross-sectional area of the artery phantom ($A_0 = \frac{\pi {d_0}^2}{4} \approx 12.44\, mm^2$), R' was the measured resistance of the whole wrist phantom after pumping, and $\bar{\sigma}_l$ was the mean conductivity of the blood simulant (0.08 M NaCl solution) calculated by Equation 34. The percent error (PE_{artery}) was calculated to evaluate the accuracy of the estimated arterial diameter:

$$PE_{artery} = \frac{\left|d_r - \hat{d}_{artery}\right|}{d_r} \times 100\% \quad \text{Equation 41}$$

6.3 Results and discussion

6.3.1 The properties of selected tissue simulants

The mechanical properties of surrounding tissue simulant principally depended on the percentage of gelatine powder. Its strength was likely to increase with a longer storage time as observed before. In the entire experiment, the selected 20 wt.% gelatine phantom showed adequate rupture strength to maintain the integrity of the artery during the contraction without breaking.

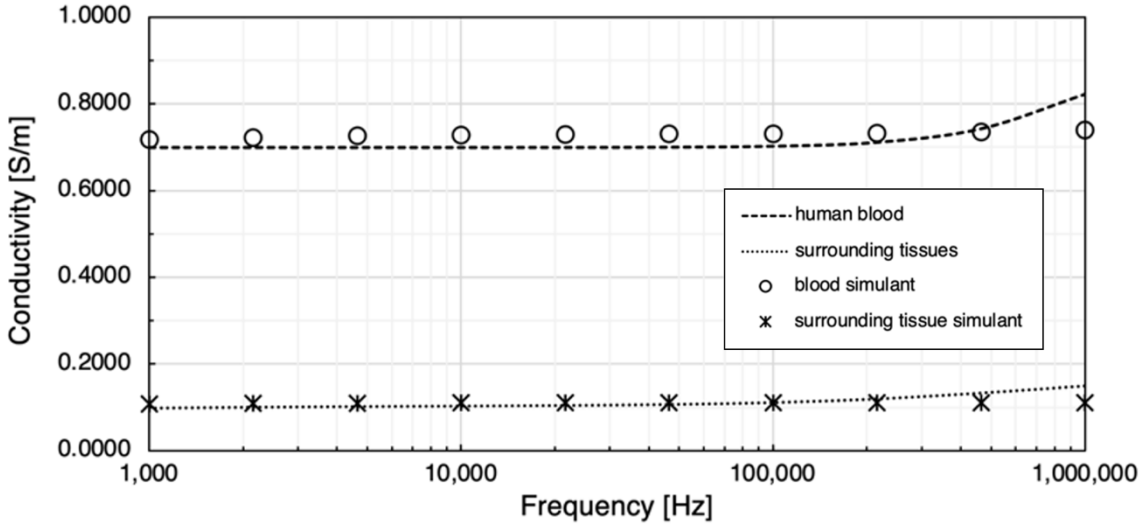

Figure 86. Comparison between prepared tissue simulants and target conductivities.

In the phantom experiments, 0.08 M NaCl solution was prepared as the human blood simulant and 20 wt.% gelatine powder and 0.1 wt.% NaCl were dissolved in deionised water to simulate the overall surrounding tissues. Their bulk conductivities were determined using the multi-frequency impedance analyser before pumping operation at room temperature, as plotted in Figure 86. Both simulants showed ranges of conductivity similar to the target values. The conductivity (mean±SD) of 0.08 M NaCl solution was from 0.717±0.018 S/m to 0.739±0.017 S/m between 1 kHz and 1 MHz, which was marginally higher than the human blood at less than 100 kHz and lower after 100 kHz. The conductivity of the surrounding tissue simulant was between 0.109 S/m and 0.111 S/m between 1 kHz and 1 MHz. Even though the conductivity of the gelatine-based phantom was influenced by water evaporation, such slight variances did not show any significant impacts on the following experiments, indicating its properties were still within the range of target conductivity during several tests. Although these two simulants did not exhibit Cole-type response as they did not emulate the relative permittivity, it was expected to have no impact on the estimation of arterial diameter in this project because the relative permittivity of tissue was not involved in the calculation.

6.3.2 One-artery wrist phantom

6.3.2.1 Test Group A: conventional 4-spot electrodes

Table 30. Experimental details in Group A

Applied electrode configurations	Initial arterial diameter (d_0)	The volume of constricted blood (ΔV)	Reference arterial diameter (d_r)
90/18 90/36 90/54 72/18 72/36 54/18	3.98 mm	647.83 mm^3	3.34 mm

The initial phantom-pumping test was performed on the *one-artery model* phantom with six different conventional 4-spot electrodes configurations, as illustrated in Table 30. For configurations *90/18*, *90/36* and *90/54*, the L_{cc} was 90 mm, corresponding to the maximum spacing in computational simulation, and the PU electrode spacings were 18 mm, 36 mm and 54 mm, respectively. For tests *72/18* and *72/36*, the distance between CC electrodes was reduced to 72 mm, and the L_{PU} were 18 mm and 36 mm individually. The last test *54/18* had the L_{cc} of 54 mm and the L_{PU} of 18 mm. The basal resistance of the wrist phantom (R_0) was calculated via measured absolute impedance and phase angle, as shown in Figure 87(A). The measured range of R_0 agreed with the simulation results. With the same L_{cc} of 90 mm, the resistance measured by the longest L_{PU} *of* 54 mm ($356.58 \pm 1.14\ \Omega$) and medium L_{PU} of 36 mm ($237.38 \pm 0.34\ \Omega$) were approximately 3.10 times and 2.06 times larger than the shortest L_{PU} of 18 mm ($114.97 \pm 0.19\ \Omega$), which showed a proportional relationship with the spacing between PU electrodes. This phenomenon was also observed by comparing *72/18* ($123.49 \pm 0.73\ \Omega$) and *72/36* ($247.05 \pm 1.69\ \Omega$). Furthermore, shorter L_{CC} exhibited higher basal resistance compared to tests *90/18*, *72/18* and *54/18,* with the same L_{PU}.

Figure 87 (B) illustrates the increment in resistance after withdrawing 647.83 mm^3 blood simulant, demonstrating the magnitude of impedance signal responded to pulsatile blood. A significant influence of the spacing between electrodes was found that a longer L_{PU} and a shorter L_{CC} could induce a larger resistance change. In other words, it can obtain more pronounced pulse waves. However, as discussed in the FEA simulation, it might not lead to a more accurate estimation of arterial diameter.

After pumping, the increased volume in the syringe barrel was equal to the decreased volume in the artery section. The reference arterial diameter was 3.34 mm calculated using Equation 37. From Figure 87 (C), almost all estimated diameter values were between 3.40 mm to

3.60 mm. Configurations *90/18*, *72/18* and *54/18* showed relatively similar estimation. They had the shortest L_{PU} of 18 mm in common. According to the percent errors in Figure 87 (D), the most accurate estimation was obtained by configuration *90/18* (around 3% error), which was consistent with previous simulation results that the longer L_{CC} could generate a more uniform field throughout the wrist and a shorter L_{PU} in the middle region was recommended. In contrast, other tests showed larger errors due to longer L_{PU}. It was worth noting that the configuration *90/54* exhibited a shift at the last two frequencies, which seemed to be a systematic error during measurement. According to the manufacturer's specifications of instrument accuracy of the multi-frequency impedance analyser [252], the most accurate (0.05%) measured frequency range is specified between 1 mHz and 500 kHz, as shown in Figure 94 in the Appendix. The shift of measured resistance change at 1 MHz was around 1.5 Ω, which was only approximately 0.4% of the measured absolute resistance (around 350 Ω). Such error is expected to be fairly minimized by reproducing the measurement to increase sample size and averaging data.

In conclusion, a nearly linear relationship between measured R_0 and L_{PU} was found. Although the wider distance between PU electrodes could sense more significant resistance change, their estimations showed less accuracy. The best estimation was achieved using the longest L_{CC} of 90 mm and the shortest L_{PU} of 18 mm.

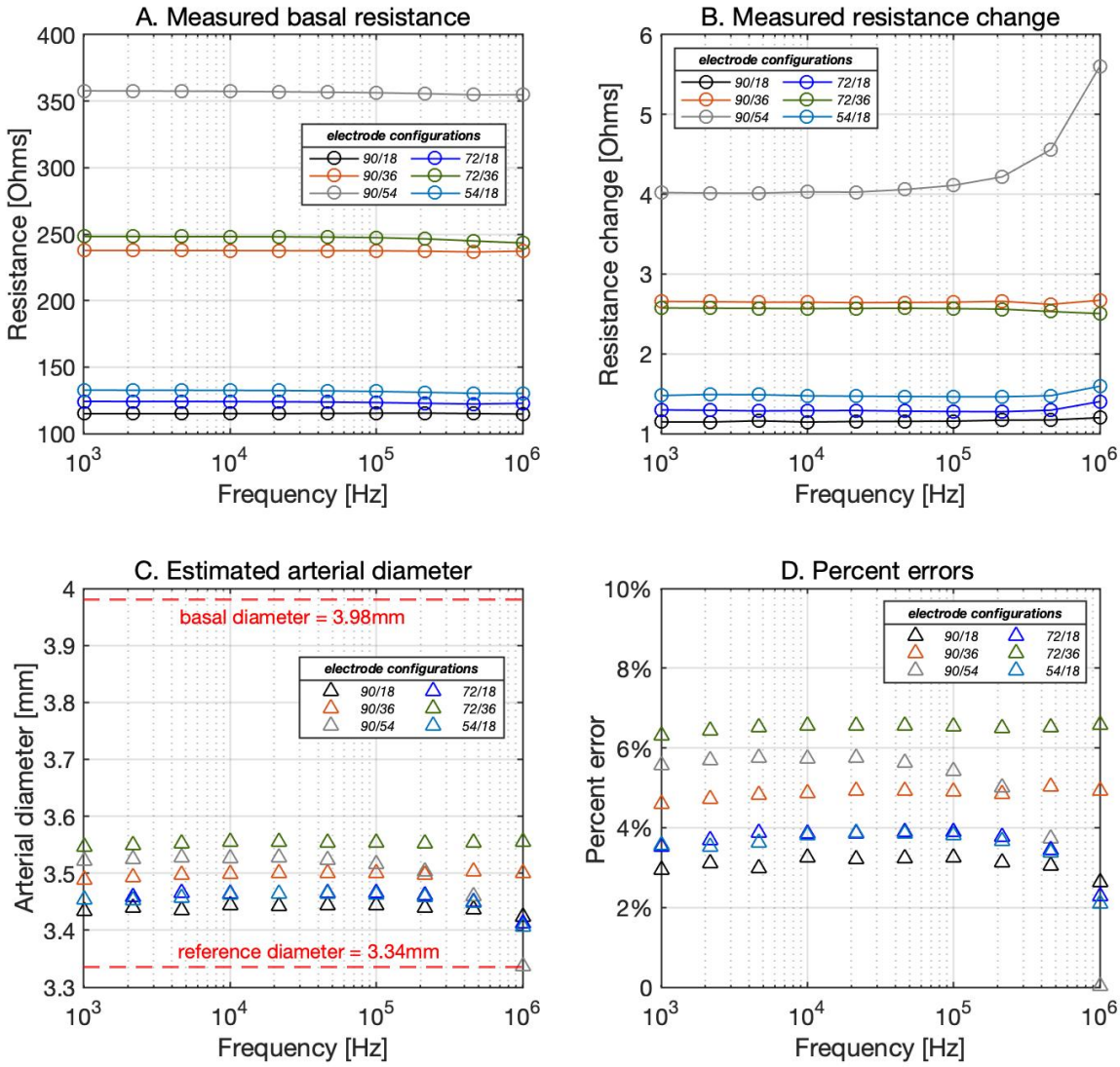

Figure 87. Experimental results of the one-artery wrist phantom in Group A: (A) measured basal resistances; (B) measured resistance changes after pumping; (C) estimated arterial diameters; (D) calculated percent errors of the estimated arterial diameters.

6.3.2.2 Test Group B: band electrodes

Table 31. Experimental details in Group B

Pumping times	Applied electrode configurations	Initial arterial diameter (d_0)	The volume of constricted blood (ΔV)	Reference arterial diameter (d_r)
1	*B/90 B/54 B/18 90/54 90/18 54/18*	3.98 mm	323.92 mm^3	3.67 mm
2			647.84 mm^3	3.34 mm

The band electrode method was first investigated using two copper tapes positioned around the wrist phantom in the test group B of the phantom-pumping experiments. The pumping process was divided into two more minor contractions of 323.92 mm^3 blood simulant in each step. The fixed distance between two band electrodes was 126 mm for configurations *B/90*,

B/54, and *B/18*. Figure 88 (A) shows the nearly proportional relationship between L_{PU} and measured R_0 as observed in Group A. The R_0 of *B/90* ($669.80 \pm 4.63\ \Omega$) and *B/54* ($400.43 \pm 2.43\ \Omega$) were 5.10 times and 3.05 times greater than *B/18* ($131.29 \pm 0.86\ \Omega$). Moreover, three conventional 4-spot electrodes configurations (i.e., *90/54*, *90/18* and *54/18)* were performed for comparison purposes, whereas the measured R_0 values were around 68.51 Ω, 18.37 Ω and 18.37 Ω higher than that in test group A (compared to Figure 87.A), respectively. This phenomenon can be explained as gelatine-based phantom losing some moisture during storage, resulting in a decline in conductivity. Such variances would not impact the measured results in short time intervals within the same group. For different groups, the changes in measured resistance can be regarded as a different measurement for different subjects with various tissue compositions, which is common and expected to have no influences on arterial diameter estimation.

According to all plots in Figure 88, the results between configurations *B/18* and *90/18* only exhibited small differences in basal resistance, resistance change and even the estimated arterial diameter. In other words, the band electrode method did not exhibit superior performance than the 4-spot electrodes method after the first contraction. The highest accuracy was achieved by *B/18* with the percent error of $1.70 \pm 0.08\%$, followed by 90/18 with a slightly higher percent error of $1.75 \pm 0.07\%$.

Figure 89 delineates the experimental results after the second contraction. The increments in resistance of all electrode configurations were roughly twice bigger than the first contraction, showing a practically linear relationship with the blood simulant volume change. The estimated values of arterial diameter were between 3.4 mm and 3.6 mm, which were similar to Group A. The band electrode configurations with the shortest L_{PU} (*B/18*) still presented the highest accuracy, followed by the configuration *90/18*.

In this group, although band electrode configuration (*B/18*) achieved the best estimation throughout pumping, it did not display significantly better estimation than the conventional 4-spot electrodes method (*90/18*). One reasonable explanation was that the longest distance between ECG dry electrodes (90 mm) was able to generate a considerably uniform field in the middle region. Consequently, the theoretical advantages of the band electrode were no longer remarkable. Moreover, it was noticed there might be a positive relationship between the withdrawn volume of blood simulant and the percent error of estimated arterial diameter.

Therefore, the optimum configuration *B/18* was selected for further testing to scrutinize the source of errors.

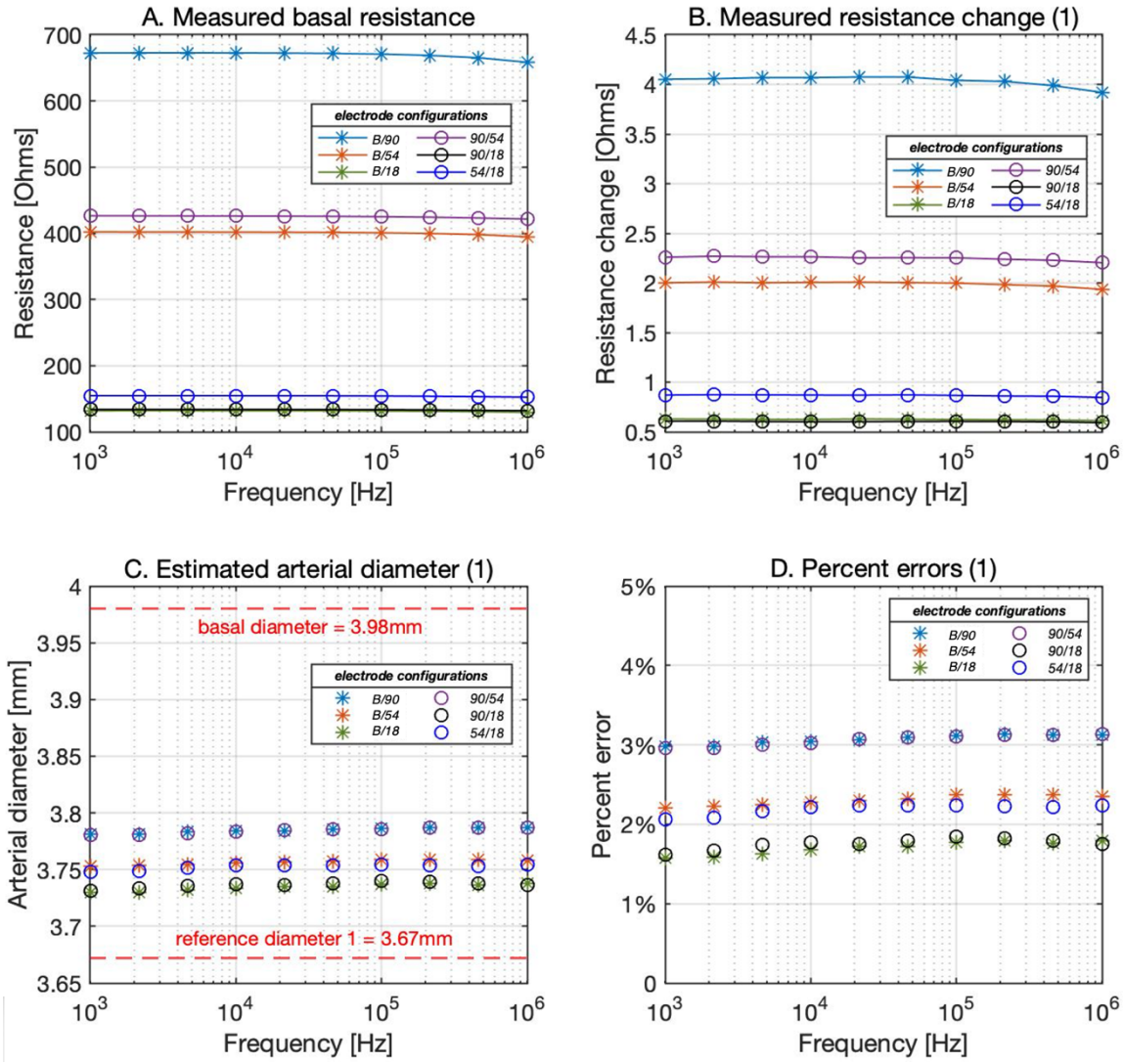

Figure 88. Experimental results of the one-artery wrist phantom after the first contraction in Group B: (A) measured basal resistances; (B) measured resistance changes; (C) estimated arterial diameters; (D) calculated percent errors of the estimated arterial diameters.

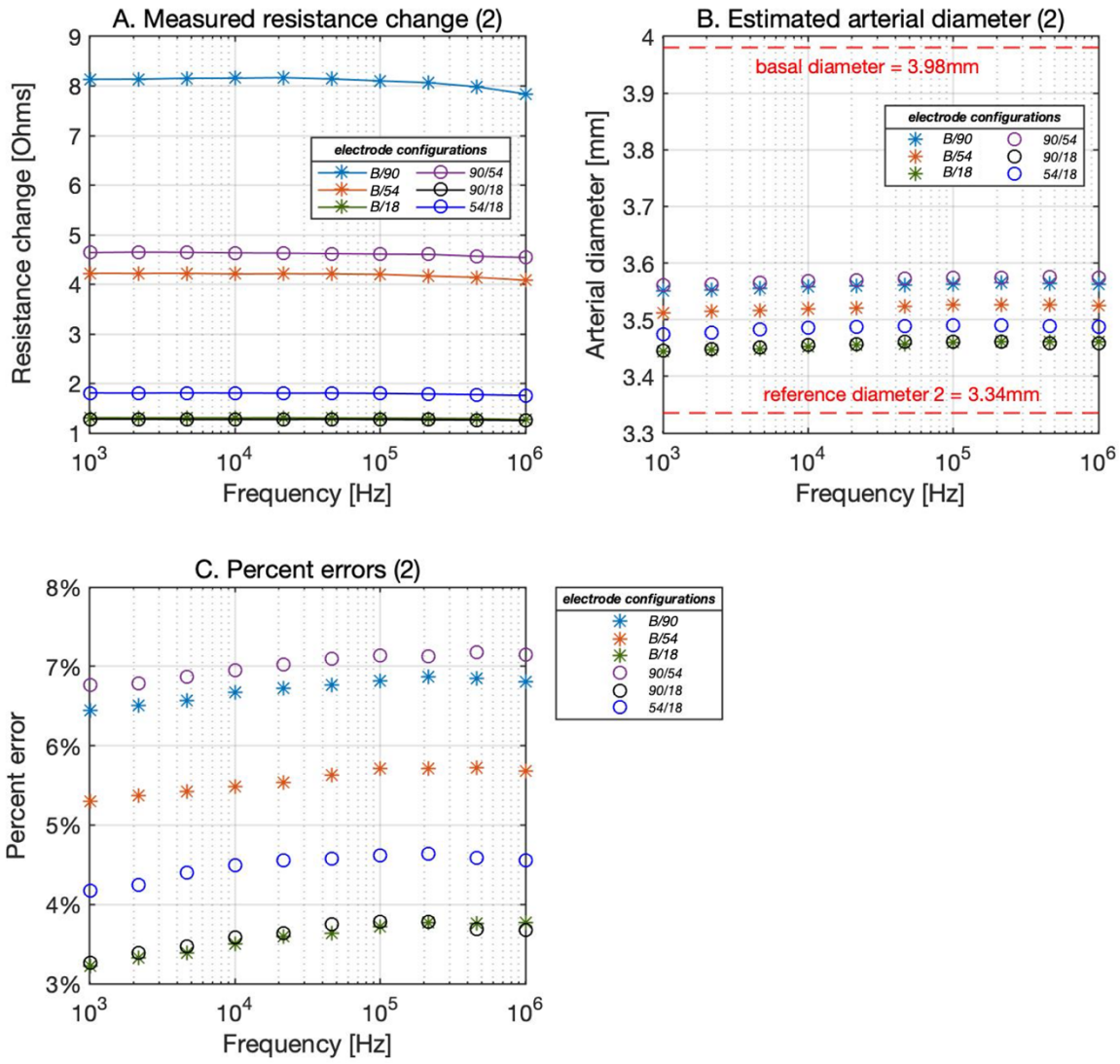

Figure 89. Experimental results of the one-artery wrist phantom after the second contraction in Group B: (A) measured resistance changes; (C) estimated arterial diameters; (D) calculated percent errors of estimated arterial diameters.

6.3.2.3 Test Group C: potential sources of errors

Table 32. Experimental details in Group C

Pumping times	Applied electrode configurations	Initial arterial diameter (d_0)	The volume of constricted blood (ΔV)	Reference arterial diameter (d_r)
1	*B/18*	3.98 mm	80.98 mm^3	3.91 mm
2			161.96 mm^3	3.83 mm
3			242.94 mm^3	3.75 mm
4			323.92 mm^3	3.67 mm
5			404.90 mm^3	3.59 mm
6			485.88 mm^3	3.51 mm
7			566.86 mm^3	3.42 mm
8			647.84 mm^3	3.34 mm
9			728.82 mm^3	3.25 mm
10			809.80 mm^3	3.15 mm

This experimental phase was an extension of Group B and intended to explore the potential source of errors. The band electrode configuration *B/18* was re-tested. Furthermore, the pumping process was finely divided into ten minor contractions of 80.98 mm^3 blood simulant per step.

As shown in Figure 90 (A), the measured R_0 of the wrist phantom decreased from 129.55 Ω to 127.31 Ω between 1 kHz and 1 MHz coinciding with the slightly increasing conductivity of gelatine-base phantom. Additionally, the decreasing resistance might be caused by reduced effects of electrode polarization (electrode-phantom surface) with increasing frequency. The electrode polarization typically occurs at low frequencies (below 100 kHz) caused by the fact that ions are able to build up close to the electrodes, contributing a large additional capacitance to the overall measured impedance [253]. The overall measured impedance (Z_m) can be regarded as the summation of the real impedance of the phantom (Z_r) and the unwanted impedance caused by electrode polarization (Z_{EP}):

$$Z_m = Z_r + Z_{EP} \qquad \text{Equation 42}$$

The measured resistance raised progressively with each equal amount of blood simulant withdrawn and achieved 131.61 Ω to 129.31 Ω after the last contraction. The approximate linear relationship between the increment in resistance and the constricted volume of blood simulant was demonstrated by the linear regression in Figure 90 (B). The average incremental

resistance per contraction was 0.204±0.017 Ω, whereas a lightly decreasing trend of the increment was found from the first contraction to the last contraction. From a mathematical perspective, according to Equation 16, the relationship between the resistance change ($dR(t)$) and blood simulant volume change ($dV_l(t)$) can be expressed as:

$$dR(t) = -\frac{\overline{\sigma_l} \cdot R_0 \cdot R(t)}{{L_{PU}}^2} \cdot dV_l(t) \qquad \text{Equation 43}$$

where the measured resistance ($R(t)$) after constricting blood simulant at time t can be further expressed by:

$$R(t) = \frac{1}{\frac{1}{R_{st}}+\frac{1}{R_l}} = \frac{1}{\frac{1}{R_{st}}+\frac{\overline{\sigma_l}(A_0+dA_l(t))}{L_{PU}}} = \frac{1}{\frac{1}{R_{st}}+\overline{\sigma_l}(V_0+dV_l(t))} = \frac{R_{st}}{1+R_{st}\overline{\sigma_l}(V_0+dV_l(t))} \qquad \text{Equation 44}$$

where R_{st} is the resistance of surrounding tissue simulant, V_0 is the initial volume of the blood simulant before pumping. Then, substituting Equation 44 into Equation 43 obtained:

$$dR(t) = -\frac{\overline{\sigma_l} \cdot R_0 \cdot R_{st}}{{L_{PU}}^2 + {L_{PU}}^2 R_{st}\overline{\sigma_l}\big(V_0 + dV_l(t)\big)} \cdot dV_l(t) \qquad \text{Equation 45}$$

In this formula, the first component of the right side contains a variable $dV_l(t)$, negating the proportional relationship between the increment in resistance and the constricted volume of blood simulant. However, the increment in resistance could be regarded as having a fairly linear relationship with a small amount of blood simulant change, as observed in experimental results.

Figure 90 (C) and (D) demonstrate the accuracy of the estimated arterial cross-sectional area change. The proposed method was likely to underestimate the blood simulant volume change. A significant deviation from the reference values was noticed after the fifth pump (404.90 mm^3) and then became more deflective with the incremental withdrawn blood simulant. The absolute error reached 0.84 mm^2 after the last contraction. The regression analysis was also performed. The absolute errors of estimated cross-sectional area change exhibited a more reliable non-linear fit (quadratic polynomial regression) than the linear fit (first-degree polynomial regression), exposing a non-linear relationship with the blood volume change. The weakened performance of the proposed method in a larger deformation range may reveal the inherent method errors of the mathematical modelling. The proposed

mathematical modelling would be less accurate when the actual situation deviated from the theoretical assumptions (i.e., the current shall be parallel with the blood).

The arterial diameter was estimated from the summation of the basal cross-sectional area and the estimated cross-sectional area change, as introduced by Equation 40. Therefore, the deviation of the estimated area change led to a similar underestimated diameter, as shown in Figure 90 (E). The average deviation of the estimated diameter was only 0.007 mm after the first contraction and then gradually increased to 0.167 mm after the last contraction. Moreover, the estimated values at different frequencies were fairly consistent at the beginning of pumping, while the differences became more significant as the blood simulant continued to be withdrawn. As plotted in Figure 90 (F), the correlation between the percent errors and constricted blood volume showed a non-linear relationship (quadratic polynomial regression) rather than a linear relationship (first-degree polynomial regression), which revealed that the proposed method was relatively accurate within a certain deformation range (below 1% within 323 mm^3), while the accuracy diminished outside of this range. In the previous computational simulation, the range of arterial diameter was modelled from 2.4 mm to 2.6 mm according to the actual vasoconstriction and vasodilation range of the human radial artery. The minimum arterial diameter was 92.3% of the maximum arterial diameter. Based on this ratio, the equivalent range of artery phantom was between 3.67 mm and 3.97 mm, which corresponded to the fourth contraction in this experimental group. Within this deformation range, the band electrode configuration and proposed mathematical modelling could achieve promising accuracy with a percent error of less than 1.00%.

Based on current experiments, the final estimation error was mainly from several systematic errors, such as the lower accuracy of the multi-frequency impedance analyser in the high-frequency range, the effects of electrode polarization and potential environmental impacts (e.g., temperature variation). More potential sources of error will be discussed after all test groups at the end of this chapter.

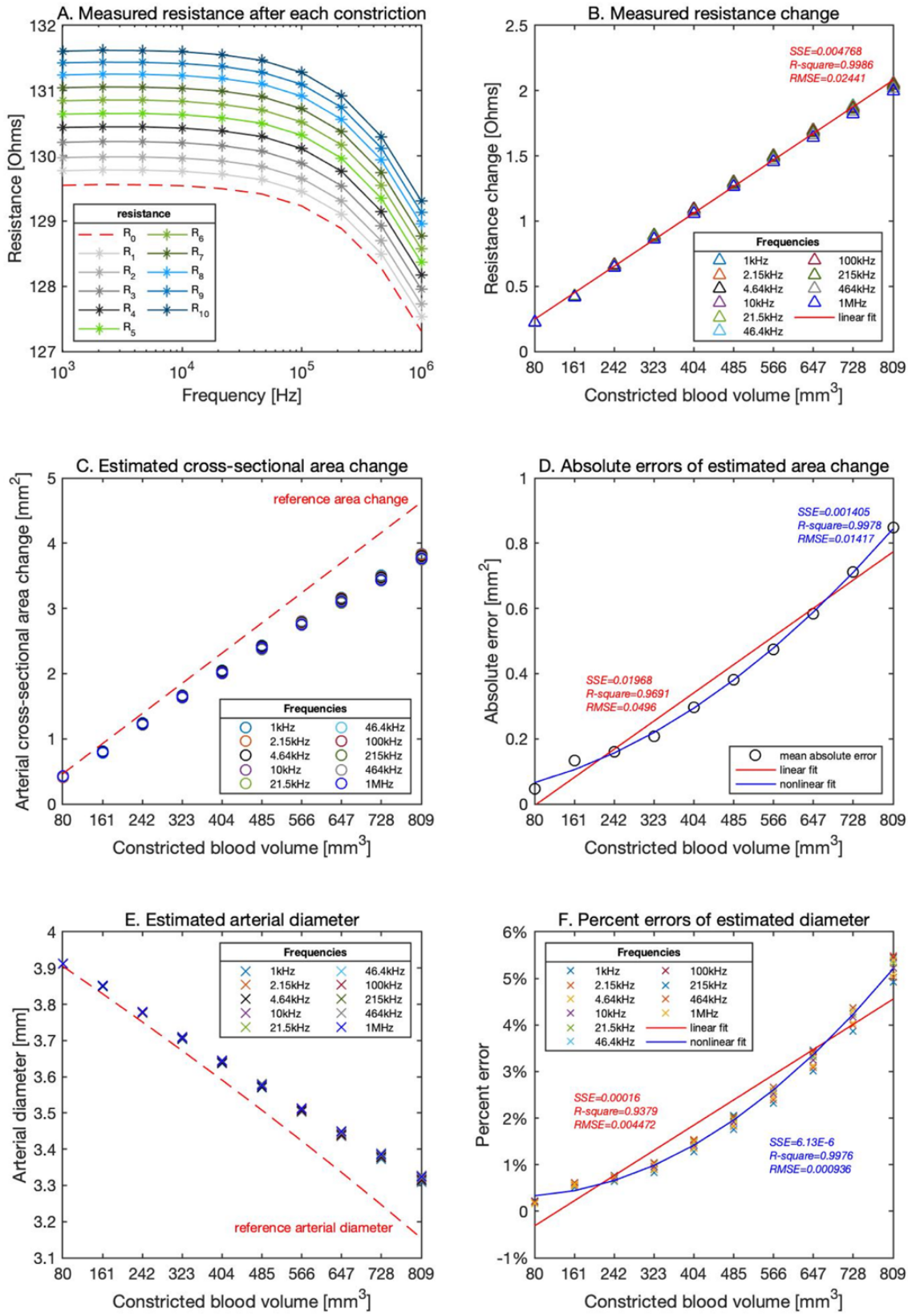

Figure 90. Experimental results in Group C: (A) measured resistances with ten pumping times; (B) measure resistance changes; (C) estimated cross-sectional area changes of the artery; (D) average absolute errors of estimated cross-sectional area changes; (E) estimated arterial diameters; (F) relative errors of estimated arterial diameters.

6.3.3 Two-arteries wrist phantom

The previous three experimental groups have demonstrated the considerable accuracy of the estimated diameter of one artery using the proposed mathematical modelling and recommended electrode configurations, including *B/18* and *90/18*. This section will investigate the same six different electrode configurations with the more realistic two-arteries wrist phantom.

6.3.3.1 Test Group D: ipsilateral measurement

Table 33. Experimental details in Group D

Subgroups	Conditions of artery B	Applied electrode configurations on artery A	The initial diameter of artery A (d_0)	The volume of constricted blood (ΔV_A)	Reference diameter of artery A (d_r)
D.1	Hollow	*B/90 B/54 B/18 90/54 90/18 54/18*	3.98 mm	318.09 mm^3	3.63 mm
D.2	Filled with the blood			318.09 mm^3	3.63 mm

This group was implemented to verify whether an adjacent static blood-filled artery could impact the uniformity of the E-field and thereby weaken the estimation. At the beginning of two-arteries wrist phantom experimentation (subgroup D.1), only one-artery (i.e., artery A) was filled with the blood simulant and connected with the syringe for pumping, while another artery (i.e., artery B) remained hollow. The impedance signal was measured on the same side as pulsatile artery A (ipsilateral measurement). Six different electrode configurations (i.e., *B/90*, *B/54*, *B/18*, *90/54*, *90/18*, and *54/18*) were employed by shifting the wires between band electrodes and ECG dry electrodes numbered 1a to 6a (see Figure 83). In the next subgroup D.2, the blood simulant was injected in artery B, whereas it was still not connected to the syringe. The same six electrode configurations were re-examined. In short, the BIM and the pump were applied on the same side of artery A in two different conditions of artery B: hollow (without the blood simulant) and filled with the blood simulant, as described in Table 33.

Figure 91 (A) illustrates the R_0 of two-arteries wrist phantom measured by six different electrode configurations from 1 kHz to 1 MHz. The proportional relationship between the L_{PU} and the R_0 was also indicated the same as in previous groups. Compared between two blood conditions of artery B, it could be found that the measured R_0 under artery A decreased

after injecting the blood simulant into artery B. The high conductive NaCl solution raised the overall conductivity of the measured region. After withdrawing 381.09 mm^3 blood simulant, the influence of blood-filled artery B was also noticed on the measured resistance change, as shown in Figure 91 (B). For electrode configurations *B/90*, *B/54* and *B/18*, the new injected blood simulant in artery B reduced the increment in resistance from $0.856 \pm 0.015\ \Omega$ to $0.526 \pm 0.007\ \Omega$, from $0.478 \pm 0.006\ \Omega$ to $0.267 \pm 0.003\ \Omega$ and from $0.145 \pm 0.004\ \Omega$ to $0.009 \pm 0.001\ \Omega$, respectively. For the 4-spot electrodes methods *90/54*, *90/18 and 54/18*, the increments in resistance after contraction lessened from $1.093 \pm 0.164\ \Omega$ to $0.876 \pm 0.100\ \Omega$, from $0.233 \pm 0.021\ \Omega$ to $0.162 \pm 0.024\ \Omega$, and from $0.611 \pm 0.017\ \Omega$ to $0.460 \pm 0.010\ \Omega$, respectively.

The outcomes of the estimated diameter of artery A are shown in Figure 91 (C) and (D). For the same electrode configuration, the accuracy of the estimated diameter of artery A was visibly diminished after filling artery B with the blood simulant. In the condition of artery B without the blood, the band electrode with the shortest L_{PU} (*B/18*) achieved the closest estimated arterial diameter with the lowest percent error of $0.99 \pm 0.42\%$, followed by configurations *B/54*, *90/18*, and *54/18*. The performance of all electrode configurations was in consonance with results obtained in Group B. When there was only one blood-filled artery, the whole wrist phantom resembled a *one-artery model* in the current distribution and led to the same estimation accuracy. However, the measurement became divergent after filling the artery B. All estimated diameters of artery A increased. The best estimation was achieved by configuration *90/18* of 3.72 ± 0.03 mm with the lowest percent error of $2.58 \pm 0.77\%$, followed by *B/18* of 3.73 ± 0.01 mm with a slightly higher mean percent error and smaller SD of $2.92 \pm 0.17\%$. Moreover, some noticeable aberration was recognized at the last three frequencies above 100 kHz, causing the high SD in several tests.

In this experimental group, the significant impacts of the adjacent static blood-filled artery on the estimation of ipsilateral arterial diameter were revealed. The conductive blood simulant in artery B "attracted" parts of the exciting current to the opposite side of the phantom, reducing the amount of current flowing into artery A, more importantly, weakening the uniformity of current distribution throughout the wrist phantom. This influence was more significant in the band electrode configurations because the injected current was expected to be equally distributed into two arteries in accordance with the simulation results (see Figure

61). Furthermore, more current flowed into artery B during constricting artery A, leading to the lower accuracy of band electrode methods. In contrast, the current from conventional 4-spot electrodes could focus more on artery A.

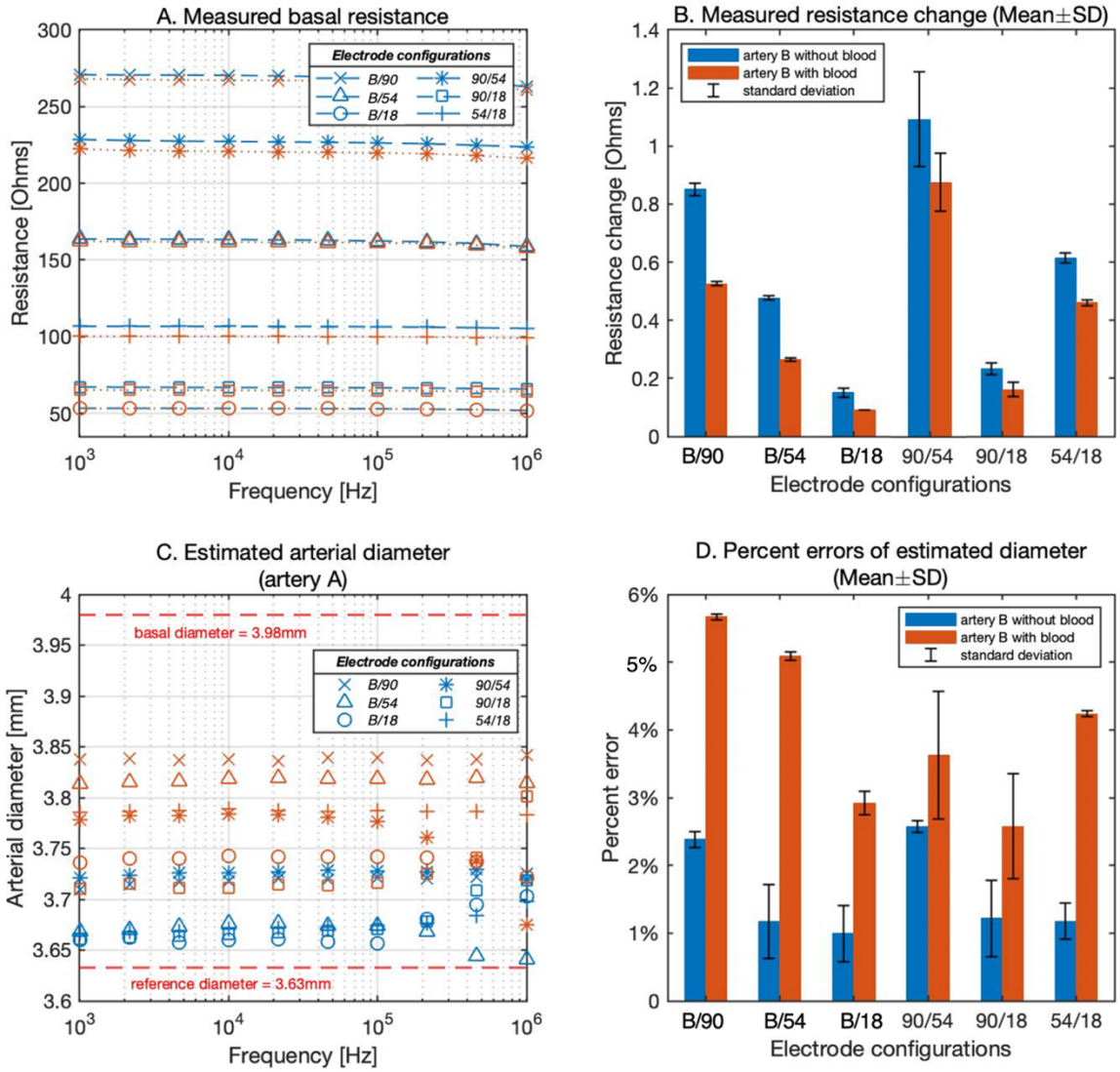

Figure 91. Experimental results of the two-arteries wrist phantom in Group D: (A) measured basal resistance; (B) measured resistance changes; (C) estimated diameter of the artery A; (D) calculated percent error of the estimated diameter of the artery A. (Blue colour indicates the measured condition of artery B without the blood simulant, while orange colour indicates artery B with the blood simulant.)

6.3.3.2 Test Group E: contralateral measurement

Table 34. Experimental details in Group E

Applied electrode configurations on artery B	The initial diameter of artery A (d_0)	The volume of constricted blood (ΔV_A)	Reference diameter of artery A (d_r)
B/90 B/54 B/18 90/54 90/18 54/18	3.98 mm	318.09 mm^3	3.63 mm

The objective of this experimental group was to explore the influences of adjacent pulsatile blood on the measured impedance signals and the estimated diameter of the target artery below the applied electrodes (contralateral measurement). In order to highlight the contribution of contralateral pulsatile blood volume and avoid any fluctuations from the target artery, only artery A was connected to the syringe for pumping, while artery B remained static during the measurement. The multi-frequency impedance analyser was connected to the band electrodes and the electrode board on the side of artery B (i.e., ECG dry electrodes 1b to 6b, see Figure 83). The withdrawn volume of blood simulant remained 381.09 mm^3 as for Group D.

Figure 92 (A) exhibits the measured R_0 of the two-arteries wrist phantom on the side of artery B. Compared with subgroup D.2, the measurement by two-electrode boards did not show significant differences in basal resistance, demonstrating the fairly symmetrical structure of the wrist phantom. Figure 92 (B) indicates how significantly an adjacent pulsatile artery affected the contralateral impedance measurement. With the same L_{PU} of 54 mm, band electrode configuration *B/54* sensed a higher increment in resistance of 0.326 ± 0.004 Ω than the conventional 4-spot electrodes configuration *90/54* of 0.298 ± 0.120 Ω. This phenomenon agreed with the theory and simulation findings that the band electrode could generate a more uniform current distribution and allow the PU electrodes to detect any resistance change throughout the wrist phantom more sensitively. Additionally, there were a few abnormally rising data points at the last three frequencies in configurations *90/54* and *90/18*, which were also noticed and analysed as a type of systematic error caused by weakening instrument accuracy in test group A.

For the conventional 4-spot electrodes configurations, the measured resistance changes from contralateral pulsatile artery were unwanted. Such pulse signals were a kind of noise to the estimation of target arterial diameter. Therefore, it was understandable that inaccurate values

were obtained, as shown in Figure 92 (C) and (D). In contrast, band electrode configurations were supposed to monitor any pulsatile blood within the measured region. The closest estimation of arterial diameter was achieved by configuration *B/18* of 3.75±0.002 mm with a small percent error of 3.24 ± 0.07%, similar to previous subgroup D.2. The results demonstrated the previous hypothesis that PU electrodes could track the pulsatile blood from any aspect once band electrodes formed the uniform field. However, the accuracy always relied on the uniform geometry and homogeneous material properties.

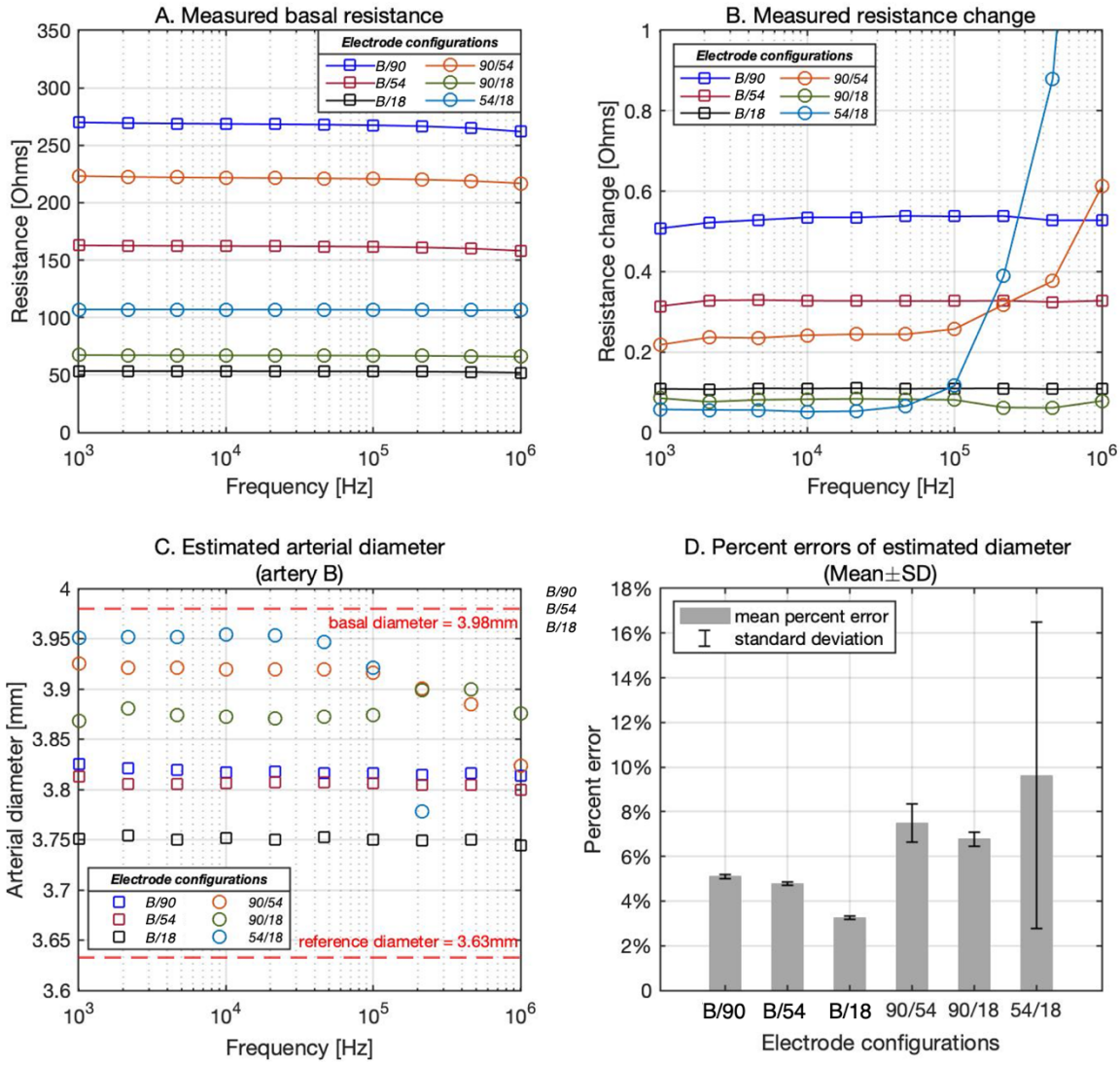

Figure 92. Experimental results of the two-arteries wrist phantom in Group E: (A) measured basal resistance on the side of artery B; (B) measured resistance change after constricting artery A; (C) estimated diameter of the artery A; (D) calculated percent errors of the estimated diameter of artery A.

6.3.3.3 Test Group F: two simultaneously pulsatile arteries

Table 35. Experimental details of Group F

Pumping times	Applied electrode configurations on artery A	Initial diameter of artery A and artery B (d_0)	The volume of constricted blood simulant ($\Delta V_A = \Delta V_B$)	Reference diameters of artery A and artery B (d_r)
1	*B/90 B/54 B/18 90/54 90/18 54/18*	3.98 mm	63.62 mm^3	3.91 mm
2			127.23 mm^3	3.84 mm
3			190.85 mm^3	3.77 mm
4			254.47 mm^3	3.70 mm
5			318.09 mm^3	3.63 mm

The last experimental group simultaneously constricted both arteries to simulate the physical pulsatile condition. In this test group, artery A and artery B had the same initial diameter (d_0) and constricted blood volume ($\Delta V_A = \Delta V_B$). In other words, the differences in arterial diameter and blood flow volume between the radial artery and ulnar artery were not included. As shown in Table 35, the pumping process was divided into five smaller contractions of 63.63 mm^3 each step. Furthermore, three band electrode configurations and three conventional 4-spot electrodes configurations were applied as in previous groups. The multi-frequency impedance analyser was connected to the electrodes on the side of artery A to simulate the most common BIM at the human wrist having four electrodes placed on the radial artery.

The values of R_0 remained the same as previous groups (refer to Figure 91 (A) and Figure 92 (A)); they have not plotted again here. Figure 93 (A) illustrates the reasonably linear relationship between the incremental resistance and the constricted blood volume in all electrode configurations. More importantly, two quantitative relationships of the increments in resistance were observed between Groups D, E and F after withdrawing the same volume of blood simulant, as shown in Figure 93 (B). First, compared between subgroup D.2 and Group E, PU electrodes could sense the similar values of resistance change on artery of either side by employing the band electrode method ($\Delta R_1 \approx \Delta R_2$ for configurations *B/90*, *B/54* and *B/18*). Second, the summation of the individual increments in resistance caused by two separately pulsatile arteries in subgroup D.2 and Group E ($\Delta R_1 + \Delta R_2$) was approximately equal to the measured increasing resistance caused by synchronously pulsatile arteries in this group (ΔR_3), especially for configurations *B/18* and *90/18* with the shortest L_{PU}. This quantitative relationship can establish the fact that for all electrode methods, the measured

impedance signal at the human wrist contains the pulsatile information from both arteries. The difference was that band electrode configurations could equally sense the total impedance change on either side of arteries. In contrast, the conventional 4-spot electrodes methods can primarily detect the single ipsilateral blood volume change below the electrodes but are disturbed by the contralateral pulsatile artery.

After recognizing the components of measured resistance change, the estimated cross-sectional area change shall be the total constricted blood simulant from both arteries. Additionally, the geometry and contraction of artery A and artery B were the same. Therefore, the estimated overall increment in the cross-sectional area was evenly divided among two arteries. Figure 93 (C) and (D) illustrate the estimated arterial diameter and the accuracy. All conventional 4-spot electrodes configurations were unable to estimate reasonable values of arterial diameter as expected. The promising band electrode configuration *B/18* could estimate the diameters of both arteries with the smallest percent errors of $2.95 \pm 0.06\%$ after the final contraction. This level of accuracy was between subgroup D.2 and Group E, demonstrating the superior performance of the band electrode configuration with the shortest L_{PU} in estimating the overall pulsatile artery diameter at the wrist.

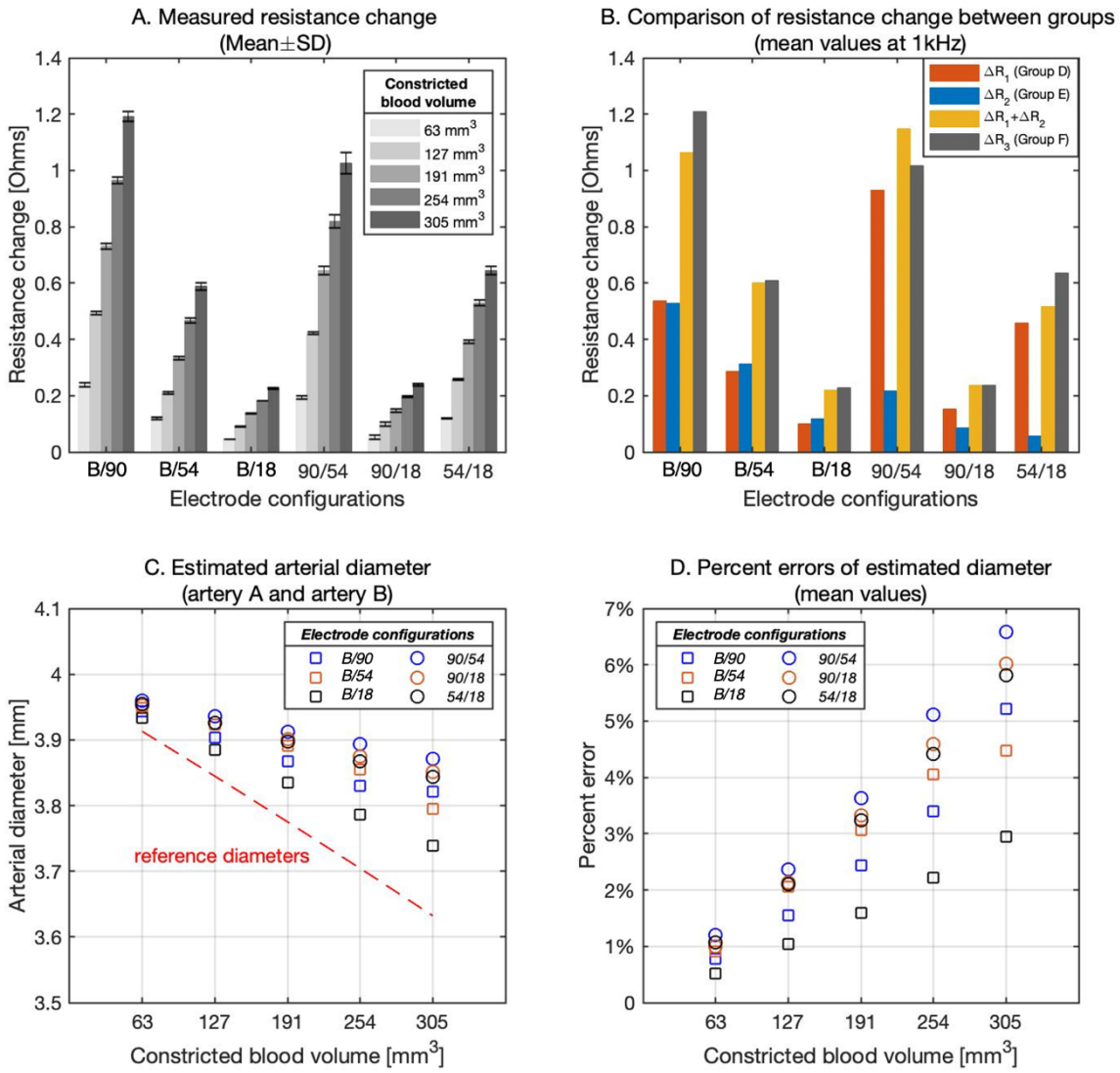

Figure 93. Experimental results of the two-arteries wrist phantom in Group F: (A) measured resistance change; (B) comparison of resistance change after constricting 318.09 mm^3 blood simulant between groups at 1 kHz: ΔR_1 was the incremental resistance caused by artery A in subgroup D.2; ΔR_2 was the incremental resistance caused by artery B in Group E; ΔR_3 was the incremental resistance caused by both artery A and artery B in Group F; (C) estimated diameters of the artery A/B; (D) calculated mean percent errors of the estimated diameters of artery A/B.

6.4 Closure

This chapter constructed the entire setup of BIM at the human wrist simulated in previous FEA. The objective of this chapter was to verify the performance of several electrode configurations in phantom experiments in terms of the estimation of arterial diameter from the measured impedance.

Two types of phantom moulds were designed and printed using a 3D printer to separately construct the simulated *one-artery model* and *two-arteries model*. Six ECG dry electrodes were soldered on one PCB with equal spacing of 18 mm as the conventional 4-spot electrodes method. Copper tapes were stuck around the inner walls of the moulds as the band electrode method. The wrist phantom contained two components: surrounding tissue simulant and blood simulant. The surrounding tissue simulant was fabricated by mixing 20 wt.% gelatine power with 0.017 M NaCl solution, showing an expected conductivity range from 0.109 S/m to 0.111 S/m in the interested frequency range. The human blood was simulated by 0.08 M NaCl solution, exhibiting conductivity from 0.717 ± 0.018 S/m to 0.740 ± 0.017 S/m between 1 kHz and 1 MHz. Then, the open end of the artery was connected with the syringe by a rigid plastic tube. A desktop injection pump was applied to drive the syringe's plunger to withdraw the blood simulant from the artery, and meanwhile, the absolute impedance and phase angle were recorded by the multi-frequency impedance analyser between 1 kHz and 1 MHz with ten logarithmical steps.

The phantom-pumping experiment was divided into six progressive test groups. Each experimental group had specific electrode configurations and pumping operations for individual objectives. The first three test groups were performed on the one-artery wrist phantom. The last three test groups were implemented on the two-arteries wrist phantom with four different conditions: 1) ipsilateral measurement (constricted and measured the same blood-filled artery) while another artery was empty; 2) ipsilateral measurement (constricted and measured the same blood-filled artery) while another artery was filled with the blood simulant; 3) contralateral measurement (constricted one blood-filled artery and measured the other blood-filled artery); 4) simultaneously constricted both blood-filled arteries and measured one artery. The reference diameter was calculated from the constricted volume of the blood simulant as the target value. Then the accuracy of each estimation was evaluated by the percent error of the estimated arterial diameter. The primary outcomes were highlighted as follows:

1. The overall measured resistance of the wrist phantom was in agreement with the simulated resistance in Chapter 5, indicating similar conductivity ranges of the two simulants.

2. The nearly proportional relationship between measured resistance of the wrist phantom and the L_{PU} was indicated in all experimental groups. Furthermore, shorter L_{CC} induced higher measured resistance with the same L_{PU}.
3. Measured resistance increased after withdrawing some of the blood simulant from the artery. The increment in resistance also depended on the electrode configurations. The higher the measured resistance, the higher increment in resistance after constricting the blood simulant, except for the conventional 4-spot electrodes method in Group E.
4. The nearly linear relationship between the increment in resistance and the constricted volume of blood simulant was observed within a small deformation range. However, the overall relationship was indicated as non-linear according to the mathematical analysis (see Equation 45).
5. The equivalent changing range of arterial diameter was between 3.67 mm and 3.97 mm, corresponding to the simulated arterial deformation range in Chapter 4 and Chapter 5. Within this range, the most accurate arterial estimation of the *one-artery model* was achieved by *B/18* (band electrode method with the shortest L_{PU}), followed by *90/18* (4-spot electrodes method with the shortest L_{PU}). Comparing these configurations, the band electrode method did not exhibit exceptionally higher accuracy than the conventional 4-spot electrodes method, because the L_{CC} had adequate length to generate a fairly uniform E-field in the middle region of the wrist phantom.
6. In the first measured condition of the two-arteries wrist phantom, each electrode configuration's experimental phenomenon and performance were similar to the one-artery wrist phantom. After filling the contralateral artery with the blood simulant in the second condition, the measured resistance and increment in resistance were reduced. More importantly, the adjacent conductive artery significantly influenced the distribution of current flow throughout the wrist phantom and thereby weakened the accuracy of estimated arterial diameters.
7. The inevitable impacts from the adjacent pulsatile artery on measured resistance of all electrode configurations were demonstrated in Group E. The band electrode configuration (*B/18*) was more sensitive to tracking overall blood volume change within the measured region. The resistance change measured on the contralateral artery could also be used to reasonably estimate the diameter of the pulsatile artery.
8. The summation of the individual increments in resistance caused by a single pulsatile artery were approximately equal to the measured resistance change caused by two

synchronously pulsatile arteries, establishing the fact that the measured impedance signal at the human wrist contains the pulsatile information from both arteries.

9. Band electrode configurations could sense the similar increments in resistance of a single pulsatile artery from two different sides, indicating a moderately uniform field in the middle region of the wrist phantom.
10. Band electrodes with the shortest PU electrode spacing (*B/18*) could estimate the diameters of both pulsatile arteries, while the conventional 4-spot electrodes configuration failed to produce a reasonable estimation.

For all phantom experimentation (especially Test Group C in section 6.3.2.3), the following potential sources of errors might have affected the final accuracy of the estimation:

- Higher frequencies usually showed poor estimation due to distinct electrical responses of the wrist phantom to different frequencies and poorer instrument accuracy beyond 500 kHz.
- The conductivity of the gelatine-based phantom was sensitive to temperature and moisture content, changes in which were difficult to avoid and thereby slightly impacted the impedance reading.
- As described in section 6.2.1, the electrode plate was placed at the bottom of the phantom to provide a more stable and consistent attachment during the measurement to partly avoid the noises from motions. The effects of electrode polarization from the measured impedance were not eliminated, thereby leading to a higher 'measured' resistance and under-estimating the cross-sectional area change. In the future investigation, polarization should be further addressed in the future, such as through modelling or experimentally eliminating the unwanted electrode polarization impedance.
- The reference arterial diameters were calculated instead of measured. The unnoticed presence of air in the artery-pump system or any faulty sealing at the junction could lead to an over-estimated reference cross-sectional area.

In conclusion, the accuracy of the estimation principally depended on the uniformity of E- field between PU electrodes. Thus, for the single artery wrist phantom, once the longer L_{CC} and shorter L_{PU} were employed, there was no significant difference between the band electrode method and the conventional 4-spot electrodes method. However, if there was more than one pulsatile artery in the measured domain, the conventional 4-spot electrodes methods

would be disturbed by other pulsatile arteries, leading to frustrated estimation. In contrast, the band electrode method appeared to provide reasonably accurate performance under these conditions.

Even though the conventional Ag/AgCl electrode has stable adhesion to the human body and lower skin-electrode impedance, the evaporation of electrolyte gel can reduce its durability for long-term use. In future clinical investigations, the band electrode is readily implementable as a wristband made of types of conductive materials [242]. Textile fabrication of electrodes provides more flexibility and wearability for long-term monitoring by avoiding the use of gels. In recent years, particular attention has been focused on the development of textile electrodes for types of hemodynamic monitoring [254]–[257].

CHAPTER 7. CONCLUSIONS AND FUTURE WORK

The primary motivation of this research was to further improve the performance of PWPM-based BPM and lay new groundwork for cuffless BPM by accurately estimating the arterial diameter (change) from impedance variance on the wrist. A comprehensive systematic review was carried out in Chapter 1, indicating the lack of arterial diameter information in previous BP estimations. This thesis investigated the dielectric response of multi-tissues and pulsatile blood in the wrist to numerically quantify the contribution of the changing arterial diameter to the overall impedance spectrum (Chapter 3). Computational simulation and tissue phantom experiments were carried out from three aspects:

1. An initial FEA of the human wrist segment was performed with various electrode configurations (i.e., materials, shapes, dimensions, and spacings) in the β-dispersion (from 1 kHz to 100 MHz) using ANSYS HFSS in Chapter 4.
2. An updated FEA of the human wrist segment with more complex geometries was investigated to explore the dielectric contribution of different tissue domains to simulated impedance in Chapter 5.
3. Two corresponding wrist phantom models were fabricated with low-cost tissue-mimicking materials (i.e., gelatine and NaCl) to verify the results and behaviours observed in the simulation in Chapter 6.

This chapter will summarise significant outcomes observed in this thesis and suggest a few future directions based on the limitations of this research.

7.1 Main outcomes

- **Efficient 3D model and tissue phantom**

In the FEA, the stepwise simulation approach improves the understanding of individual and overall responses and contributions of tissues under BIM, providing evidence to model tissue domains in future simulations more reasonably. The simplified cuboid geometry has been proved to be time-saving without any significant effects on simulated results compared with curvilinear geometry, striking a balance between the accuracy of simulation and the time required for simulation. The current density simulation results confirmed that the amounts of flowing current within tissues were decided by both volume and conductivity of tissues. This

FEA also verified the modelling of different arterial diameters is an efficient approach to represent the contribution of blood flow-induced cross-sectional area changes to the overall impedance. Bones, as the major volume component of the human wrist, had relatively lower conductivity in the β-dispersion, inducing more amounts of injected current to flow in the conductive blood and thereby emphasizing larger resistance change caused by arterial diameter change. Therefore, for future investigations that want to focus on the contribution of pulsatile blood, it is recommended to include the bones in the human 3D model to highlight the contribution of conductive blood.

In the tissue phantom experiment, the overall conductivity of surrounding tissue (i.e., skin, fat, muscle and bones) can be accurately mimicked by mixing 20 wt.% gelatine power with 0.017 M NaCl solution. The human blood was reasonably simulated by 0.08 M NaCl solution. Both simulants were accurate and robust enough to represent the expected properties of the human wrist for BIM, providing effective and low-cost ingredients of tissue-mimicking materials. Additionally, the whole phantom-pumping system is easy to operate with controllable changes in blood simulant volume.

- **A promising electrode configuration for more accurate arterial diameter estimation**

An important contribution of this thesis was the investigation of various electrode configurations from both simulation and phantom experimental perspectives, which improved the accuracy of quantification in the arterial diameter-dependent impedance variance and thereby provided more robust arterial diameter values for the development of cuffless BPM in the future.

Three different CC electrode spacings and three different PU electrode spacings were separately carried out by FEA and phantom experiments. The FEA provided a straightforward approach to observe the uniformity of current density and E-field throughout the wrist model. The phantom experiment was performed to verify the simulated outcomes. Both simulated and experimental results demonstrated the current density in the middle region between CC electrodes was approximately uniform by increasing L_{CC}. Additionally, PU electrode spacings showed a nearly proportional relationship between basal resistance and L_{PU}. Even though larger L_{PU} was found to be more sensitive to changes caused by arterial blood volume change and hence indicative of obtaining more pronounced pulse

waves in the actual measurement with human body, it did not lead to a more accurate estimation of arterial diameters. Conversely, shorter L_{PU} induced lower percent errors of estimated diameters because shorter L_{PU} comprised of a more uniform E-field region.

More importantly, the band electrode configuration showed more accurate estimation than the conventional 4-spot electrode approach in both simulation and phantom experiments due to a larger extent of parallel E-field distribution within the wrist model. The band electrode method has not been applied previously in the literature for pulse sensing on the wrist. Furthermore, the proposed band electrode configuration should also be easy to implement in actual BIM with human subjects in the future. For example, it could be a wristband made of conductive textile electrodes with flexibility and wearability for long-term monitoring by avoiding the use of gels.

- **The band electrode configuration for overall pulse sensing**

Previous studies lacked investigation of another adjacent pulsatile blood (i.e., ulnar artery) under BIM. It is rare to find a previous study that investigated two synchronously pulsatile arteries in the wrist/forearm model from either computational simulation or phantom experiment perspectives. This thesis particularly modelled two pulsatile arteries in the simulation and constricted both arteries in the phantom experiments, providing an insight into the contribution of multi-arteries to impedance signals.

Both simulation and phantom experimental results demonstrated the significant effects of the contralateral artery on the overall current distribution, weakening the capability of the conventional 4-spot electrode configuration to accurately represent the electrical responses of tissues and cross-sectional area change of the blood from the mathematical perspective. In the tissue phantom experiments, both separately pulsatile artery and synchronously pulsatile arteries were performed. The summation of the individual resistance changes caused by a single pulsatile artery was approximately equal to the measured resistance change caused by two synchronously pulsatile arteries, confirming the measured impedance signal at the wrist contains the pulsatile information from both arteries for both 4-spot electrode and band electrode configurations. Remarkably, the band electrode configuration showed high sensitivity to any pulsatile blood throughout the wrist and therefore could be applied for overall blood volume change estimation.

7.2 Future directions

This work accomplished promising accuracies for estimated arterial diameters. However, perceiving the distinction between simulation/phantom and the actual anatomy of the human wrist, several potential limitations need to be investigated and, if found to be significant, addressed in the future.

From a modelling perspective, the applied mathematical modelling relied on the uniformity of the E-field inside the measured body segment. However, the real properties of human tissues are not homogenous, and the anatomy is much more complex (e.g., smaller arteries and arterioles). Human tissues as dielectric materials also exhibit distinct frequency-dependent permittivity. Future modelling could take the permittivity into account to reveal more dielectric responses in the frequency range. Additionally, beyond the RC circuit modelled in this work, more sophisticated equivalent circuits for human tissue can be applied and further explored, such as modelling tissue as a constant phase element (CPE) [43, 44]. Within the scope of this thesis, the electrical contribution due to arterial diameter change was almost completely reflected in the resistance changes rather than the reactance changes. The observed results clearly indicated the dominant contribution of resistance changes was due to blood volume change, which would not be different even if a CPE is considered. However, a CPE should be investigated as a means to model more complex geometry and tissue properties.

From a computational simulation perspective, the 3D wrist model could be developed further. This simulation only represented the pulsatile blood as several instances of arterial diameters. Future research is expected to model blood flow dynamics and simultaneously observe impedance changes, assigning the velocity-dependent blood conductivity change to represent the contribution of red blood cell orientation. Moreover, the geometry can be refined to be more realistic, separating the bone domain into individual radius and ulna, and gradually changing the thickness of tissue layers from distal to proximal.

Different from the present simulation and phantom situations, knowledge of absolute arterial diameters required an initial calibration in the actual measurement, requiring another technique to determine the basal diameter, such as ultrasound. Several previous studies have

already investigated and provided promising ultrasound-based techniques and systems for accessorial arterial diameter measurement [45, 46].

This thesis was carried out in well-controllable conditions from simulation and phantom experiment perspectives. The observed outcomes are desired to be further validated by clinical investigation with human subjects. The motivation of this research is to improve the performance of current cuffless BPM (e.g., PWPM) by adding accurate arterial diameter information. Future work is expected to verify the ability of the proposed electrode configuration for PTT/PAT/PWV determination and combine the estimated arterial diameter into existing mathematical models for more accurate BP estimation.

7.3 Closure

The BPM is an efficient clinical method to monitor cardiovascular function and a strong predictor of death and cardiovascular diseases. In recent years, PWPM-based systems have been investigated and developed for more portable cuffless BPM, which are based on the strong relationship between PTT/PAT/PWV and the changes in BP. However, the blood volume/ cross-sectional area changes, as another related indicator, were usually ignored in previously published studies. BIM is a low-cost and portable technique for ambulatory hemodynamic monitoring. Therefore, this research was carried out to accurately estimate the arterial diameter (change) from impedance variance on the wrist.

Different from previous arterial diameter estimation approaches, this thesis focused on the effects of various electrode configurations on current density and E-field distribution within the wrist. Both computational simulation and tissue phantom experiments were investigated in this work, demonstrating the promising band electrode configuration with a longer L_{CC} and a shorter L_{PU} in the middle region could achieve a more uniform E-field distribution such that the cross-sectional area change was estimated more accurately. This thesis describes a novel electrode configuration on the wrist to provide more accurate arterial diameter information for more accurate BP estimation in envisaged future studies with human participants.

CHAPTER 8. REFERENCE LIST

[1] C. M. M. Lawes, S. V. Hoorn, M. R. Law, P. Elliott, S. MacMahon, and A. Rodgers, 'Blood pressure and the global burden of disease 2000. Part II: Estimates of attributable burden', *Heart Dis.*, p. 8, 2006.

[2] M. A. Weber *et al.*, 'Clinical Practice Guidelines for the Management of Hypertension in the Community: A Statement by the American Society of Hypertension and the International Society of Hypertension', *J. Clin. Hypertens.*, vol. 16, no. 1, pp. 14–26, Jan. 2014, doi: 10.1111/jch.12237.

[3] '2017 ACC/AHA/AAPA/ABC/ACPM/AGS/APhA/ASH/ASPC/NMA/PCNA Guideline for the Prevention, Detection, Evaluation, and Management of High Blood Pressure in Adults: Executive Summary: A Report of the American College of Cardiology/American Heart Association Task Force on Clinical Practice Guidelines', p. 56.

[4] P. A. James *et al.*, '2014 Evidence-Based Guideline for the Management of High Blood Pressure in Adults: Report From the Panel Members Appointed to the Eighth Joint National Committee (JNC 8)', *JAMA*, vol. 311, no. 5, p. 507, Feb. 2014, doi: 10.1001/jama.2013.284427.

[5] J. Booth, 'A Short History of Blood Pressure Measurement', *Proc. R. Soc. Med.*, vol. 70, no. 11, pp. 793–799, Nov. 1977, doi: 10.1177/003591577707001112.

[6] B. H. McGhee and M. E. J. Bridges, 'Monitoring Arterial Blood Pressure: What You May Not Know', p. 15.

[7] B. Gupta, 'Invasive blood pressure monitoring', p. 6.

[8] E. P. Mccutcheon, R. F. Rushmer, O. Jacobson, and H. Sandier, 'Korotkoff Sounds: An Experimental Critique', *Circ. Res.*, vol. 20, no. 2, pp. 149–161, Feb. 1967, doi: 10.1161/01.RES.20.2.149.

[9] Lippincott Williams & Wilkins, Ed., *Best practices: evidence-based nursing procedures*, 2nd ed. Philadelphia: Lippincott Williams & Wilkins, 2007.

[10] M. Sharma *et al.*, ‘Cuff-Less and Continuous Blood Pressure Monitoring: A Methodological Review’, *Technologies*, vol. 5, no. 2, p. 21, May 2017, doi: 10.3390/technologies5020021.

[11] B. S. Alpert, D. Quinn, and D. Gallick, ‘Oscillometric blood pressure: a review for clinicians’, *J. Am. Soc. Hypertens.*, vol. 8, no. 12, pp. 930–938, Dec. 2014, doi: 10.1016/j.jash.2014.08.014.

[12] C. C. Y. Poon and Y. T. Zhang, ‘Cuff-less and Noninvasive Measurements of Arterial Blood Pressure by Pulse Transit Time’, in *2005 IEEE Engineering in Medicine and Biology 27th Annual Conference*, Shanghai, China, 2005, pp. 5877–5880. doi: 10.1109/IEMBS.2005.1615827.

[13] A. Chandrasekhar, C.-S. Kim, M. Naji, K. Natarajan, J.-O. Hahn, and R. Mukkamala, ‘Smartphone-based blood pressure monitoring via the oscillometric finger-pressing method’, *Sci. Transl. Med.*, vol. 10, no. 431, p. eaap8674, Mar. 2018, doi: 10.1126/scitranslmed.aap8674.

[14] ‘HeartGuide | Wearable Blood Pressure Monitor | Omron’, *Healthcare Wellness & Healthcare Products*. https://omronhealthcare.com/products/heartguide-wearable-blood-pressure-monitor-bp8000m/ (accessed Aug. 15, 2019).

[15] M. Forouzanfar, S. Ahmad, I. Batkin, H. R. Dajani, V. Z. Groza, and M. Bolic, ‘Coefficient-Free Blood Pressure Estimation Based on Pulse Transit Time–Cuff Pressure Dependence’, *IEEE Trans. Biomed. Eng.*, vol. 60, no. 7, pp. 1814–1824, Jul. 2013, doi: 10.1109/TBME.2013.2243148.

[16] ‘Finapres - Continuous non-invasive hemodynamics’. https://www.finapres.com/ (accessed Jun. 04, 2022).

[17] B. Imholz, ‘Fifteen years experience with finger arterial pressure monitoring: assessment of the technology’, *Cardiovasc. Res.*, vol. 38, no. 3, pp. 605–616, Jun. 1998, doi: 10.1016/S0008-6363(98)00067-4.

[18] N. L. Pace and T. D. East, ‘Simultaneous Comparison of Intraarterial, Oscillometric, and Finapres Monitoring During Anesthesia’:, *Anesth. Analg.*, vol. 73, no. 2, p. 213???220, Aug. 1991, doi: 10.1213/00000539-199108000-00017.

[19] D. N. Stokes, T. Clutton-Brock, C. Patil, J. M. Thompson, and P. Hutton, ‘Comparison of Invasive and Non-invasive Measurement of Continuous Arterial Pressure Using the Finapres’, *Br. J. Anaesth.*, vol. 67, no. 1, pp. 26–35, Jul. 1991, doi: 10.1093/bja/67.1.26.

[20] D. J. Carlson, G. Dieberg, J. R. Mcfarlane, and N. A. Smart, ‘Blood pressure measurements in research: suitability of auscultatory, beat-to-beat, and ambulatory blood pressure measurements’, *Blood Press. Monit.*, vol. 24, no. 1, pp. 18–23, Feb. 2019, doi: 10.1097/MBP.0000000000000355.

[21] M. Kawahara, ‘Evaluation of tie Accuracy of Non*invasive Automatic Blood Pressure Monitors’, *Anesth Prog*, p. 4, 1990.

[22] R. D. M. Jones, A. G. Brown, C. J. Roulson, I. D. Smith, and S. C. Chan, ‘The upgraded Finapres 2300e.: A clinical evaluation of a continuous noninvasive blood pressure monitor’, *Anaesthesia*, vol. 47, no. 8, pp. 701–705, Aug. 1992, doi: 10.1111/j.1365-2044.1992.tb02396.x.

[23] H. Gesche, D. Grosskurth, G. Küchler, and A. Patzak, ‘Continuous blood pressure measurement by using the pulse transit time: comparison to a cuff-based method’, *Eur. J. Appl. Physiol.*, vol. 112, no. 1, pp. 309–315, Jan. 2012, doi: 10.1007/s00421-011-1983-3.

[24] D. McAuley, B. Silke, and S. Farrell, ‘Reliability of blood pressure determination with the Finapres with altered physiological states or pharmacodynamic conditions’, *Clin. Auton. Res.*, vol. 7, no. 4, pp. 179–184, Aug. 1997, doi: 10.1007/BF02267979.

[25] A. Elvan-Tapnar *et al.*, ‘Validation and use of the FinometerTM for blood pressure measurement in normal, hypertensive and pre-eclamptic pregnancy’, *J. Hypertens.*, vol. 21, no. 11, pp. 2053–2060, Nov. 2003, doi: 10.1097/00004872-200311000-00014.

[26] O. Kemmotsu, M. Ueda, H. Otsuka, T. Yamamura, D. C. Winter, and J. S. Eckerle, ‘Arterial Tonometry for Noninvasive, Continuous Blood Pressure Monitoring during Anesthesia’:, *Anesthesiology*, vol. 75, no. 2, pp. 333–340, Aug. 1991, doi: 10.1097/00000542-199108000-00023.

[27] R. Mukkamala *et al.*, ‘Toward Ubiquitous Blood Pressure Monitoring via Pulse Transit Time: Theory and Practice’, *IEEE Trans. Biomed. Eng.*, vol. 62, no. 8, pp. 1879–1901, Aug. 2015, doi: 10.1109/TBME.2015.2441951.

[28] K. Belani *et al.*, ‘A New Noninvasive Method to Measure Blood Pressure: Results of a Multicenter Trial’, *Anesthesiology*, vol. 91, no. 3, p. 686, Sep. 1999, doi: 10.1097/00000542-199909000-00021.

[29] G. K. Archibald, V. Heights, T. G. Curran, H. Danielson, S. Paul, and R. C. Thede, ‘54 Method of Positioning a Sensor for Determining Blood Pressure of an Artery’, p. 26, 1998.

[30] ‘ANSI/AAMI/ISO 81060-2:2013, Non-invasive sphygmomanometers — Part 2: Clinical investigation of automated measurement type’, p. 55, 2013.

[31] E. O’brien, N. Atkins, F. Mee, and K. O’malley, ‘Evaluation of Blood Pressure Measuring Devices’, *Clin. Exp. Hypertens.*, vol. 15, no. 6, pp. 1087–1097, Jan. 1993, doi: 10.3109/10641969309037096.

[32] E. O’Brien *et al.*, ‘European Society of Hypertension International Protocol revision 2010 for the validation of blood pressure measuring devices in adults’:, *Blood Press. Monit.*, vol. 15, no. 1, pp. 23–38, Feb. 2010, doi: 10.1097/MBP.0b013e3283360e98.

[33] ‘IEEE Standard for Wearable Cuffless Blood Pressure Measuring Devices’, IEEE, 2014. doi: 10.1109/IEEESTD.2014.6882122.

[34] G. S. Stergiou, B. S. Alpert, S. Mieke, J. Wang, and E. O’Brien, ‘Validation protocols for blood pressure measuring devices in the 21st century’, *J. Clin. Hypertens.*, vol. 20, no. 7, pp. 1096–1099, Jul. 2018, doi: 10.1111/jch.13294.

[35] A. A. Leung *et al.*, ‘Hypertension Canada’s 2016 Canadian Hypertension Education Program Guidelines for Blood Pressure Measurement, Diagnosis, Assessment of Risk, Prevention, and Treatment of Hypertension’, *Can. J. Cardiol.*, vol. 32, no. 5, pp. 569–588, May 2016, doi: 10.1016/j.cjca.2016.02.066.

[36] D. S. Picone *et al.*, ‘Accuracy of Cuff-Measured Blood Pressure’, *J. Am. Coll. Cardiol.*, vol. 70, no. 5, pp. 572–586, Aug. 2017, doi: 10.1016/j.jacc.2017.05.064.

[37] ‘Blood Pressure Monitors Archives’, *Medaval*. https://medaval.ie/device-category/blood-pressure-monitors/ (accessed Sep. 19, 2019).

[38] R. McManus, P. Lacy, C. Clark, N. Chapman, and P. Lewis, ‘Reporting of blood pressure monitor validation studies’:, *Blood Press. Monit.*, vol. 23, no. 4, pp. 214–215, Aug. 2018, doi: 10.1097/MBP.0000000000000334.

[39] J. E. Sharman and T. H. Marwick, ‘Accuracy of blood pressure monitoring devices: a critical need for improvement that could resolve discrepancy in hypertension guidelines’, *J. Hum. Hypertens.*, vol. 33, no. 2, pp. 89–93, Feb. 2019, doi: 10.1038/s41371-018-0122-6.

[40] J. E. Sharman *et al.*, ‘Lancet commission on hypertension group position statement on the global improvement of accuracy standards for devices that measure blood pressure’:, *J. Hypertens.*, p. 1, Sep. 2019, doi: 10.1097/HJH.0000000000002246.

[41] G. Weltman, G. Sullivan, and D. Bredon, ‘THE CONTINUOUS MEASUREMENT OF ARTERIAL PULSE WAVE VELOCITY*t’, p. 2, 1964.

[42] D. Špulák, ‘Parameters for Mean Blood Pressure Estimation Based on Electrocardiography and Photoplethysmography’, p. 4, 2011.

[43] A. Milan *et al.*, ‘Current assessment of pulse wave velocity: comprehensive review of validation studies’, *J. Hypertens.*, vol. 37, no. 8, pp. 1547–1557, Aug. 2019, doi: 10.1097/HJH.0000000000002081.

[44] J. C. Bramwell and A. V. Hill, ‘The velocity of pulse wave in man’, *Proc. R. Soc. Lond. Ser. B Contain. Pap. Biol. Character*, vol. 93, no. 652, pp. 298–306, Apr. 1922, doi: 10.1098/rspb.1922.0022.

[45] J.W. Remington, ‘The physiology of the aorta and major arteries’, *Handb. Physiol.*, vol. 2, pp. 799–838, Jan. 1963.

[46] K. Hayashi, ‘Mechanical Properties of Soft Tissues and Arterial Walls’, in *Biomechanics of Soft Tissue in Cardiovascular Systems*, G. A. Holzapfel and R. W. Ogden, Eds. Vienna: Springer Vienna, 2003, pp. 15–64. doi: 10.1007/978-3-7091-2736-0_2.

[47] D. J. Hughes, C. F. Babbs, L. A. Geddes, and J. D. Bourland, ‘Measurements of Young’s Modulus of Elasticity of the Canine Aorta with Ultrasound’, p. 15, 1979.

[48] B. Gribbin, A. Steptoe, and P. Sleight, ‘Pulse Wave Velocity as a Measure of Blood Pressure Change’, *Psychophysiology*, vol. 13, no. 1, pp. 86–90, Jan. 1976, doi: 10.1111/j.1469-8986.1976.tb03344.x.

[49] L. A. Geddes, M. H. Voelz, C. F. Babbs, J. D. Bourland, and W. A. Tacker, ‘Pulse Transit Time as an Indicator of Arterial Blood Pressure’, *Psychophysiology*, vol. 18, no. 1, pp. 71–74, Jan. 1981, doi: 10.1111/j.1469-8986.1981.tb01545.x.

[50] T. Ma and Y. T. Zhang, ‘A Correlation Study on the Variabilities in Pulse Transit Time, Blood Pressure, and Heart Rate Recorded Simultaneously from Healthy Subjects’, in *2005 IEEE Engineering in Medicine and Biology 27th Annual Conference*, Shanghai, China, 2005, pp. 996–999. doi: 10.1109/IEMBS.2005.1616585.

[51] R. P. Smith, J. Argod, J.-L. Pepin, and P. A. Levy, ‘Pulse transit time: an appraisal of potential clinical applications’, *Thorax*, vol. 54, no. 5, pp. 452–457, May 1999, doi: 10.1136/thx.54.5.452.

[52] T. Wibmer *et al.*, ‘Pulse Transit Time and Blood Pressure During Cardiopulmonary Exercise Tests’, vol. 63, p. 10, 2014.

[53] R. Padwal, ‘Cuffless Blood Pressure Measurement: How Did Accuracy Become an Afterthought?’, *Am. J. Hypertens.*, vol. 32, no. 9, pp. 807–809, Aug. 2019, doi: 10.1093/ajh/hpz070.

[54] J. E. Aldrich, ‘Basic physics of ultrasound imaging’:, *Crit. Care Med.*, vol. 35, no. Suppl, pp. S131–S137, May 2007, doi: 10.1097/01.CCM.0000260624.99430.22.

[55] R. S. C. Cobbold, *Foundations of biomedical ultrasound*. Oxford ; New York: Oxford University Press, 2007.

[56] J. O. Arndt, J. Klauske, and F. Mersch, ‘The diameter of the intact carotid artery in man and its change with pulse pressure’, *Pflügers Archiv*, vol. 301, no. 3, pp. 230–240, 1968, doi: 10.1007/BF00363770.

[57] M. Cinthio, T. Jansson, Å. R. Ahlgren, K. Lindström, and H. W. Persson, ‘A Method for Arterial Diameter Change Measurements Using Ultrasonic B-Mode Data’, *Ultrasound Med. Biol.*, vol. 36, no. 9, pp. 1504–1512, Sep. 2010, doi: 10.1016/j.ultrasmedbio.2010.05.022.

[58] F. Beux *et al.*, ‘Automatic evaluation of arterial diameter variation from vascular echographic images’, *Ultrasound Med. Biol.*, vol. 27, no. 12, pp. 1621–1629, Dec. 2001, doi: 10.1016/S0301-5629(01)00450-1.

[59] S. Graf *et al.*, ‘Experimental and clinical validation of arterial diameter waveform and intimal media thickness obtained from B-mode ultrasound image processing’, *Ultrasound Med. Biol.*, vol. 25, no. 9, pp. 1353–1363, Nov. 1999, doi: 10.1016/S0301-5629(99)00089-7.

[60] R. W. Stadler, W. C. Karl, and R. S. Lees, ‘New methods for arterial diameter measurement from B-mode images’, *Ultrasound Med. Biol.*, vol. 22, no. 1, pp. 25–34, Jan. 1996, doi: 10.1016/0301-5629(95)02017-9.

[61] V. Gemignani, F. Faita, L. Ghiadoni, E. Poggianti, and M. Demi, ‘A System for Real-Time Measurement of the Brachial Artery Diameter in B-Mode Ultrasound Images’, *IEEE Trans. Med. Imaging*, vol. 26, no. 3, pp. 393–404, Mar. 2007, doi: 10.1109/TMI.2006.891477.

[62] A. A. R. Kamal, J. B. Harness, G. Irving, and A. J. Mearns, ‘Skin photoplethysmography — a review’, *Comput. Methods Programs Biomed.*, vol. 28, no. 4, pp. 257–269, Apr. 1989, doi: 10.1016/0169-2607(89)90159-4.

[63] J. Weinman, A. Hayat, and G. Raviv, ‘Reflection photoplethysmography of arterial-blood-volume pulses’, *Med. Biol. Eng. Comput.*, vol. 15, no. 1, pp. 22–31, Jan. 1977, doi: 10.1007/BF02441571.

[64] J. Allen, ‘Photoplethysmography and its application in clinical physiological measurement’, *Physiol. Meas.*, vol. 28, no. 3, pp. R1–R39, Mar. 2007, doi: 10.1088/0967-3334/28/3/R01.

[65] A. B. Hertzman, ‘Photoelectric Plethysmography of the Nasal Septum in Man’, *Exp. Biol. Med.*, vol. 37, no. 2, pp. 290–292, Nov. 1937, doi: 10.3181/00379727-37-9543P.

[66] A. B. Hertzman, ‘Photoelectric Plethysmography of the Fingers and Toes in Man’, *Exp. Biol. Med.*, vol. 37, no. 3, pp. 529–534, Dec. 1937, doi: 10.3181/00379727-37-9630.

[67] A. B. Hertzman, W. C. Randall, and K. E. Jochim, ‘THE ESTIMATION OF THE CUTANEOUS BLOOD FLOW WITH THE PHOTOELECTRIC PLETHYSMOGRAPH’, *Am. J. Physiol.-Leg. Content*, vol. 145, no. 5, pp. 716–726, Mar. 1946, doi: 10.1152/ajplegacy.1946.145.5.716.

[68] D. Biswas, N. Simoes-Capela, C. Van Hoof, and N. Van Helleputte, ‘Heart Rate Estimation From Wrist-Worn Photoplethysmography: A Review’, *IEEE Sens. J.*, vol. 19, no. 16, pp. 6560–6570, Aug. 2019, doi: 10.1109/JSEN.2019.2914166.

[69] M. Ghamari, ‘A review on wearable photoplethysmography sensors and their potential future applications in health care’, *Int. J. Biosens. Bioelectron.*, vol. 4, no. 4, 2018, doi: 10.15406/ijbsbe.2018.04.00125.

[70] C. El-Hajj and P. A. Kyriacou, ‘A review of machine learning techniques in photoplethysmography for the non-invasive cuff-less measurement of blood pressure’, *Biomed. Signal Process. Control*, vol. 58, p. 101870, Apr. 2020, doi: 10.1016/j.bspc.2020.101870.

[71] P. C.-P. Chao, C.-C. Wu, D. H. Nguyen, B.-S. Nguyen, P.-C. Huang, and V.-H. Le, ‘The Machine Learnings Leading the Cuffless PPG Blood Pressure Sensors Into the Next Stage’, *IEEE Sens. J.*, vol. 21, no. 11, pp. 12498–12510, Jun. 2021, doi: 10.1109/JSEN.2021.3073850.

[72] M. Hosanee *et al.*, ‘Cuffless Single-Site Photoplethysmography for Blood Pressure Monitoring’, *J. Clin. Med.*, vol. 9, no. 3, p. 723, Mar. 2020, doi: 10.3390/jcm9030723.

[73] D. Ramsingh, B. Alexander, and M. Cannesson, ‘Clinical review: Does it matter which hemodynamic monitoring system is used?’, *Crit. Care*, vol. 17, no. 2, p. 208, 2012, doi: 10.1186/cc11814.

[74] J. Truijen, J. J. van Lieshout, W. A. Wesselink, and B. E. Westerhof, ‘Noninvasive continuous hemodynamic monitoring’, *J. Clin. Monit. Comput.*, vol. 26, no. 4, pp. 267–278, Aug. 2012, doi: 10.1007/s10877-012-9375-8.

[75] T. W. L. Scheeren and M. A. E. Ramsay, ‘New Developments in Hemodynamic Monitoring’, *J. Cardiothorac. Vasc. Anesth.*, vol. 33, pp. S67–S72, Aug. 2019, doi: 10.1053/j.jvca.2019.03.043.

[76] M. L. Mateu Campos *et al.*, ‘Techniques available for hemodynamic monitoring. Advantages and limitations’, *Med. Intensiva Engl. Ed.*, vol. 36, no. 6, pp. 434–444, Aug. 2012, doi: 10.1016/j.medine.2012.09.004.

[77] M. R. Pinsky and D. Payen, ‘Functional hemodynamic monitoring’, *Crit. Care*, vol. 9, no. 6, p. 566, 2005, doi: 10.1186/cc3927.

[78] L. Briesenick, F. Michard, and B. Saugel, ‘Mobile Devices for Hemodynamic Monitoring’, in *Annual Update in Intensive Care and Emergency Medicine 2020*, J.-L. Vincent, Ed. Cham: Springer International Publishing, 2020, pp. 655–665. doi: 10.1007/978-3-030-37323-8_50.

[79] G. Anand, Y. Yu, A. Lowe, and A. Kalra, ‘Bioimpedance analysis as a tool for hemodynamic monitoring: overview, methods and challenges’, *Physiol. Meas.*, vol. 42, no. 3, p. 03TR01, Mar. 2021, doi: 10.1088/1361-6579/abe80e.

[80] M. Min, P. Annus, H. Koiv, A. Krivosei, T. Uuetoa, and J. Lamp, ‘Bioimpedance sensing - a viable alternative for tonometry in non-invasive assessment of central aortic pressure’, in *2017 IEEE International Symposium on Medical Measurements and Applications (MeMeA)*, Rochester, MN, USA, May 2017, pp. 373–378. doi: 10.1109/MeMeA.2017.7985905.

[81] K. Sel, D. Osman, and R. Jafari, ‘Non-Invasive Cardiac and Respiratory Activity Assessment from Various Human Body Locations Using Bioimpedance’, *IEEE Open J. Eng. Med. Biol.*, pp. 1–1, 2021, doi: 10.1109/OJEMB.2021.3085482.

[82] M.-C. Cho, J.-Y. Kim, and S. Cho, ‘A bio-impedance measurement system for portable monitoring of heart rate and pulse wave velocity using small body area’, in *2009 IEEE International Symposium on Circuits and Systems*, Taipei, Taiwan, May 2009, pp. 3106–3109. doi: 10.1109/ISCAS.2009.5118460.

[83] F. M. Liebman and S. Bagno, ‘The behavior of the red blood cells in flowing blood which accounts for conductivity changes’, *Biomed. Sci. Instrum.*, vol. 4, pp. 25–35, 1968.

[84] R. L. Gaw, B. H. Cornish, and B. J. Thomas, ‘The Electrical Impedance of Pulsatile Blood Flowing Through Rigid Tubes: A Theoretical Investigation’, *IEEE Trans. Biomed. Eng.*, vol. 55, no. 2, pp. 721–727, Feb. 2008, doi: 10.1109/TBME.2007.903531.

[85] A. Mugeb and A. Larvushkin, ‘Model-based Assessment of Brachial Artery Diameter From Electrical Impedance Measurement’, in *2021 Ural Symposium on Biomedical Engineering, Radioelectronics and Information Technology (USBEREIT)*, Yekaterinburg, Russia, May 2021, pp. 0098–0101. doi: 10.1109/USBEREIT51232.2021.9455041.

[86] M. Al-harosh, M. Yangirov, D. Kolesnikov, and S. Shchukin, ‘Bio-Impedance Sensor for Real-Time Artery Diameter Waveform Assessment’, *Sensors*, vol. 21, no. 24, p. 8438, Dec. 2021, doi: 10.3390/s21248438.

[87] M. Sugawara, K. Niki, H. Furuhata, S. Ohnishi, and S. Suzuki, ‘Relationship between the pressure and diameter of the carotid artery in humans’, *Heart Vessels*, vol. 15, no. 1, pp. 49–51, Jan. 2000, doi: 10.1007/PL00007261.

[88] T. Huynh, R. Jafari, and W.-Y. Chung, ‘An Accurate Bioimpedance Measurement System for Blood Pressure Monitoring’, *Sensors*, vol. 18, no. 7, p. 2095, Jun. 2018, doi: 10.3390/s18072095.

[89] T.-W. Wang, W.-X. Chen, H.-W. Chu, and S.-F. Lin, ‘Single-Channel Bioimpedance Measurement for Wearable Continuous Blood Pressure Monitoring’, *IEEE Trans. Instrum. Meas.*, vol. 70, pp. 1–9, 2021, doi: 10.1109/TIM.2020.3035578.

[90] M. Metshein, H. Kõiv, P. Annus, and M. Min, ‘Electrode Optimization for Bioimpedance Based Central Aortic Blood Pressure Estimation’, in *World Congress on Medical Physics and Biomedical Engineering 2018*, vol. 68/2, L. Lhotska, L. Sukupova, I. Lacković, and G. S. Ibbott, Eds. Singapore: Springer Singapore, 2019, pp. 497–501. doi: 10.1007/978-981-10-9038-7_92.

[91] B. Ibrahim, D. Hall, and R. Jafari, ‘Pulse Wave Modeling using Bio-Impedance Simulation Platform based on a 3D Time-Varying Circuit Model’, *IEEE Trans. Biomed. Circuits Syst.*, pp. 1–1, 2021, doi: 10.1109/TBCAS.2021.3059211.

[92] K. Pesti, M. Metshein, P. Annus, H. Koiv, and M. Min, ‘Electrode Placement Strategies for the Measurement of Radial Artery Bioimpedance: Simulations and Experiments’, *IEEE Trans. Instrum. Meas.*, vol. 70, pp. 1–10, 2021, doi: 10.1109/TIM.2020.3011784.

[93] G. Anand and A. Lowe, ‘Investigating Electrical Impedance Spectroscopy for Estimating Blood Flow-Induced Variations in Human Forearm’, *Sensors*, vol. 20, no. 18, p. 5333, Sep. 2020, doi: 10.3390/s20185333.

[94] Y. Yu, G. Anand, A. Lowe, H. Zhang, and A. Kalra, ‘Towards Estimating Arterial Diameter Using Bioimpedance Spectroscopy: A Computational Simulation and Tissue Phantom Analysis’, *Sensors*, vol. 22, no. 13, p. 4736, Jun. 2022, doi: 10.3390/s22134736.

[95] R. A. Payne, C. N. Symeonides, D. J. Webb, and S. R. J. Maxwell, ‘Pulse transit time measured from the ECG: an unreliable marker of beat-to-beat blood pressure’, *J. Appl. Physiol.*, vol. 100, no. 1, pp. 136–141, Jan. 2006, doi: 10.1152/japplphysiol.00657.2005.

[96] K. W. Chan, K. Hung, and Y. T. Zhang, ‘Noninvasive and cuffless measurements of blood pressure for telemedicine’, in *2001 Conference Proceedings of the 23rd Annual International Conference of the IEEE Engineering in Medicine and Biology Society*, Istanbul, Turkey, 2001, vol. 4, pp. 3592–3593. doi: 10.1109/IEMBS.2001.1019611.

[97] Y. Chen, C. Wen, G. Tao, M. Bi, and G. Li, 'Continuous and Noninvasive Blood Pressure Measurement: A Novel Modeling Methodology of the Relationship Between Blood Pressure and Pulse Wave Velocity', *Ann. Biomed. Eng.*, vol. 37, no. 11, pp. 2222–2233, Nov. 2009, doi: 10.1007/s10439-009-9759-1.

[98] Y. Choi, Q. Zhang, and S. Ko, 'Noninvasive cuffless blood pressure estimation using pulse transit time and Hilbert–Huang transform', *Comput. Electr. Eng.*, vol. 39, no. 1, pp. 103–111, Jan. 2013, doi: 10.1016/j.compeleceng.2012.09.005.

[99] D. Griggs *et al.*, 'Design and development of continuous cuff-less blood pressure monitoring devices', in *2016 IEEE SENSORS*, Orlando, FL, USA, Oct. 2016, pp. 1–3. doi: 10.1109/ICSENS.2016.7808908.

[100] H. T. Ma, 'A Blood Pressure Monitoring Method for Stroke Management', *BioMed Res. Int.*, vol. 2014, pp. 1–7, 2014, doi: 10.1155/2014/571623.

[101] E. K. Park *et al.*, 'Continuous measurement of systolic blood pressure using the PTT and other parameters', in *2005 IEEE Engineering in Medicine and Biology 27th Annual Conference*, Shanghai, China, 2005, pp. 3555–3558. doi: 10.1109/IEMBS.2005.1617247.

[102] P. Fung, G. Dumont, C. Ries, C. Mott, and M. Ansermino, 'Continuous noninvasive blood pressure measurement by pulse transit time', in *The 26th Annual International Conference of the IEEE Engineering in Medicine and Biology Society*, San Francisco, CA, USA, 2004, vol. 3, pp. 738–741. doi: 10.1109/IEMBS.2004.1403264.

[103] J. Proença, J. Muehlsteff, X. Aubert, and P. Carvalho, 'Is pulse transit time a good indicator of blood pressure changes during short physical exercise in a young population?', in *2010 Annual International Conference of the IEEE Engineering in Medicine and Biology*, Buenos Aires, Aug. 2010, pp. 598–601. doi: 10.1109/IEMBS.2010.5626627.

[104] D. Špulák, 'Parameters for Mean Blood Pressure Estimation Based on Electrocardiography and Photoplethysmography', p. 4.

[105] X. Teng and Y. Zhang, ‘Theoretical Study on the Effect of Sensor Contact Force on Pulse Transit Time’, *IEEE Trans. Biomed. Eng.*, vol. 54, no. 8, pp. 1490–1498, Aug. 2007, doi: 10.1109/TBME.2007.900815.

[106] W. Chen, T. Kobayashi, S. Ichikawa, Y. Takeuchi and T. Togawa, ‘Continuous estimation of systolic blood pressure using the pulse arrival time and intermittent calibration’, *Biol. Eng.*, vol. 38, p. 8, 2000.

[107] C. P. Chua and C. Heneghan, ‘Continuous Blood Pressure Monitoring using ECG and Finger Photoplethysmogram’, in *2006 International Conference of the IEEE Engineering in Medicine and Biology Society*, New York, NY, Aug. 2006, pp. 5117–5120. doi: 10.1109/IEMBS.2006.259612.

[108] X. Ding, Y. Zhang, and H. K. Tsang, ‘Impact of heart disease and calibration interval on accuracy of pulse transit time–based blood pressure estimation’, *Physiol. Meas.*, vol. 37, no. 2, pp. 227–237, Feb. 2016, doi: 10.1088/0967-3334/37/2/227.

[109] X.-R. Ding, Y.-T. Zhang, J. Liu, W.-X. Dai, and H. K. Tsang, ‘Continuous Cuffless Blood Pressure Estimation Using Pulse Transit Time and Photoplethysmogram Intensity Ratio’, *IEEE Trans. Biomed. Eng.*, vol. 63, no. 5, pp. 964–972, May 2016, doi: 10.1109/TBME.2015.2480679.

[110] S. O. Heard, A. Lisbon, I. Toth, and R. Ramasubramanian, ‘An evaluation of a new continuous blood pressure monitoring system in critically ill patients’, *J. Clin. Anesth.*, vol. 12, no. 7, pp. 509–518, Nov. 2000, doi: 10.1016/S0952-8180(00)00201-4.

[111] A. Jadooei, O. Zaderykhin, and V. I. Shulgin, ‘Adaptive algorithm for continuous monitoring of blood pressure using a pulse transit time’, in *2013 IEEE XXXIII International Scientific Conference Electronics and Nanotechnology (ELNANO)*, Kiev, Apr. 2013, pp. 297–301. doi: 10.1109/ELNANO.2013.6552042.

[112] M. Masè, W. Mattei, R. Cucino, L. Faes, and G. Nollo, ‘Feasibility of cuff-free measurement of systolic and diastolic arterial blood pressure’, *J. Electrocardiol.*, vol. 44, no. 2, pp. 201–207, Mar. 2011, doi: 10.1016/j.jelectrocard.2010.11.019.

[113] P. S. Pandian *et al.*, ‘Smart Vest: Wearable multi-parameter remote physiological monitoring system’, *Med. Eng. Phys.*, vol. 30, no. 4, pp. 466–477, May 2008, doi: 10.1016/j.medengphy.2007.05.014.

[114] C. C. Y. Poon, Y.-T. Zhang, G. Wong, and W. S. Poon, ‘The beat-to-beat relationship between pulse transit time and systolic blood pressure’, in *2008 International Conference on Technology and Applications in Biomedicine*, Shenzhen, China, May 2008, pp. 342–343. doi: 10.1109/ITAB.2008.4570616.

[115] M. Y.-M. Wong, C. C.-Y. Poon, and Y.-T. Zhang, ‘An Evaluation of the Cuffless Blood Pressure Estimation Based on Pulse Transit Time Technique: a Half Year Study on Normotensive Subjects’, *Cardiovasc. Eng.*, vol. 9, no. 1, pp. 32–38, Mar. 2009, doi: 10.1007/s10558-009-9070-7.

[116] Y.-L. Zheng, ‘An Armband Wearable Device for Overnight and Cuff-less Blood Pressure Measurement’, *IEEE Trans. Biomed. Eng.*, p. 11, 2013.

[117] Y. Dong, J. Kang, Y. Yu, K. Zhang, Z. Li, and Y. Zhai, ‘A Novel Model for Continuous Cuff-less Blood Pressure Estimation’, in *2018 11th International Symposium on Communication Systems, Networks & Digital Signal Processing (CSNDSP)*, Budapest, Jul. 2018, pp. 1–6. doi: 10.1109/CSNDSP.2018.8471889.

[118] J. Kim, J. Park, K. Kim, Y. Chee, Y. Lim, and K. Park, ‘Development of A Nonintrusive Blood Pressure Estimation System for Computer Users’, *Telemed. E-Health*, vol. 13, no. 1, pp. 57–64, Feb. 2007, doi: 10.1089/tmj.2006.0034.

[119] Q. Zhang, X. Zeng, W. Hu, and D. Zhou, ‘A Machine Learning-Empowered System for Long-Term Motion-Tolerant Wearable Monitoring of Blood Pressure and Heart Rate With Ear-ECG/PPG’, *IEEE Access*, vol. 5, pp. 10547–10561, 2017, doi: 10.1109/ACCESS.2017.2707472.

[120] J. Espina, T. Falck, J. Muehlsteff, Yilin Jin, M. A. Adan, and X. Aubert, ‘Wearable body sensor network towards continuous cuff-less blood pressure monitoring’, in *2008 5th International Summer School and Symposium on Medical Devices and Biosensors*, Hong Kong, China, 2008, pp. 28–32. doi: 10.1109/ISSMDBS.2008.4575008.

[121] Health Care Technology and Innovation Centre, IIT Madras Research Park 2 Easwari Engineering College, Anna University, S. Ilango, and P. Sridhar, 'A Non-Invasive Blood Pressure Measurement using Android Smart Phones', *IOSR J. Dent. Med. Sci.*, vol. 13, no. 1, pp. 28–31, 2014, doi: 10.9790/0853-13142831.

[122] H. Lin, W. Xu, N. Guan, D. Ji, Y. Wei, and W. Yi, 'Noninvasive and Continuous Blood Pressure Monitoring Using Wearable Body Sensor Networks', *IEEE Intell. Syst.*, vol. 30, no. 6, pp. 38–48, Nov. 2015, doi: 10.1109/MIS.2015.72.

[123] 'ASUS VivoWatch BP (HC-A04) | VivoWatch', *ASUS Global*. https://www.asus.com/VivoWatch/ASUS-VivoWatch-BP-HC-A04/ (accessed Aug. 19, 2019).

[124] A. Chandrasekhar, M. Yavarimanesh, K. Natarajan, J.-O. Hahn, and R. Mukkamala, 'PPG Sensor Contact Pressure Should Be Taken Into Account for Cuff-Less Blood Pressure Measurement', *IEEE Trans. Biomed. Eng.*, vol. 67, no. 11, pp. 3134–3140, Nov. 2020, doi: 10.1109/TBME.2020.2976989.

[125] 'Visi mobile system'. https://www.soterawireless.com/ (accessed Apr. 02, 2022).

[126] B. Soller, D. McCombie, and B. Kanter, 'GE DINAMAPTM CARESCAPETM V100', p. 8, 2015.

[127] W. Wang, P. Mohseni, K. Kilgore, and L. Najafizadeh, 'PulseLab: An Integrated and Expandable Toolbox for Pulse Wave Velocity-based Blood Pressure Estimation', in *2021 43rd Annual International Conference of the IEEE Engineering in Medicine & Biology Society (EMBC)*, Mexico, Nov. 2021, pp. 5654–5657. doi: 10.1109/EMBC46164.2021.9630916.

[128] 'PulseLab MATLAB Toolbox'. https://sites.google.com/view/pulselab/home (accessed Apr. 03, 2022).

[129] C.-S. Kim, A. M. Carek, R. Mukkamala, O. T. Inan, and J.-O. Hahn, 'Ballistocardiogram as Proximal Timing Reference for Pulse Transit Time Measurement: Potential for Cuffless Blood Pressure Monitoring', *IEEE Trans. Biomed. Eng.*, vol. 62, no. 11, pp. 2657–2664, Nov. 2015, doi: 10.1109/TBME.2015.2440291.

[130] S. L.-O. Martin *et al.*, 'Weighing Scale-Based Pulse Transit Time is a Superior Marker of Blood Pressure than Conventional Pulse Arrival Time', *Sci. Rep.*, vol. 6, no. 1, Dec. 2016, doi: 10.1038/srep39273.

[131] P. Yousefian *et al.*, 'The Potential of Wearable Limb Ballistocardiogram in Blood Pressure Monitoring via Pulse Transit Time', *Sci. Rep.*, vol. 9, no. 1, p. 10666, Dec. 2019, doi: 10.1038/s41598-019-46936-9.

[132] P. Yousefian *et al.*, 'Pulse Transit Time-Pulse Wave Analysis Fusion Based on Wearable Wrist Ballistocardiogram for Cuff-Less Blood Pressure Trend Tracking', *IEEE Access*, vol. 8, pp. 138077–138087, 2020, doi: 10.1109/ACCESS.2020.3012384.

[133] A. E. Dastjerdi, M. Kachuee, and M. Shabany, 'Non-invasive blood pressure estimation using phonocardiogram', in *2017 IEEE International Symposium on Circuits and Systems (ISCAS)*, Baltimore, MD, USA, May 2017, pp. 1–4. doi: 10.1109/ISCAS.2017.8050240.

[134] D. Rai, H. K. Thakkar, S. S. Rajput, J. Santamaria, C. Bhatt, and F. Roca, 'A Comprehensive Review on Seismocardiogram: Current Advancements on Acquisition, Annotation, and Applications', *Mathematics*, vol. 9, no. 18, p. 2243, Sep. 2021, doi: 10.3390/math9182243.

[135] A. M. Carek, J. Conant, A. Joshi, H. Kang, and O. T. Inan, 'SeismoWatch: Wearable Cuffless Blood Pressure Monitoring Using Pulse Transit Time', *Proc. ACM Interact. Mob. Wearable Ubiquitous Technol.*, vol. 1, no. 3, pp. 1–16, Sep. 2017, doi: 10.1145/3130905.

[136] M. M. H. Shandhi, B. Semiz, S. Hersek, N. Goller, F. Ayazi, and O. T. Inan, 'Performance Analysis of Gyroscope and Accelerometer Sensors for Seismocardiography-Based Wearable Pre-Ejection Period Estimation', *IEEE J. Biomed. Health Inform.*, vol. 23, no. 6, pp. 2365–2374, Nov. 2019, doi: 10.1109/JBHI.2019.2895775.

[137] V. G. Ganti, A. M. Carek, B. N. Nevius, J. A. Heller, M. Etemadi, and O. T. Inan, 'Wearable Cuff-Less Blood Pressure Estimation at Home via Pulse Transit Time',

IEEE J. Biomed. Health Inform., vol. 25, no. 6, pp. 1926–1937, Jun. 2021, doi: 10.1109/JBHI.2020.3021532.

[138] Y. Chen, C. Wen, H. Tang, and L. X. Teng, 'The relationship between different pulse wave velocity and systolic/diastolic pressure', in *2008 3rd IEEE Conference on Industrial Electronics and Applications*, Singapore, Jun. 2008, pp. 1185–1190. doi: 10.1109/ICIEA.2008.4582705.

[139] H. Liu, K. Ivanov, Y. Wang, and L. Wang, 'Toward a Smartphone Application for Estimation of Pulse Transit Time', *Sensors*, vol. 15, no. 10, pp. 27303–27321, Oct. 2015, doi: 10.3390/s151027303.

[140] A. Rasool, M. Rafiq, A. Nasir, and F. M. Kashif, 'Continuous and Noninvasive Blood Pressure Estimation by Two-Sensor Measurement of Pulse Transit Time', in *2018 14th International Conference on Emerging Technologies (ICET)*, Islamabad, Nov. 2018, pp. 1–5. doi: 10.1109/ICET.2018.8603612.

[141] F. Tabei, J. M. Gresham, B. Askarian, K. Jung, and J. W. Chong, 'Cuff-Less Blood Pressure Monitoring System Using Smartphones', *IEEE Access*, vol. 8, pp. 11534–11545, 2020, doi: 10.1109/ACCESS.2020.2965082.

[142] 'Biobeat watch', *Biobeat*. https://www.bio-beat.com/products (accessed Apr. 02, 2022).

[143] D. Nachman *et al.*, 'Comparing blood pressure measurements between a photoplethysmography-based and a standard cuff-based manometry device', *Sci. Rep.*, vol. 10, no. 1, p. 16116, Dec. 2020, doi: 10.1038/s41598-020-73172-3.

[144] A. Eisenkraft and D. Nachman, 'Human study of the Biobeat device allowing for non-invasive wireless continuous measurement of blood pressure Comparing Biobeat measurements to the International Protocol (Revision 2010) requirements', 2018, doi: 10.13140/RG.2.2.16570.03527.

[145] C. Qiu *et al.*, 'Wearable Blood Pressure Monitoring Based on Bio-Impedance and Photoplethysmography Sensors on the Arm', p. 3, 2018.

[146] S. Bang, C. Lee, J. Park, M.-C. Cho, Y.-G. Yoon, and S. Cho, 'A pulse transit time measurement method based on electrocardiography and bioimpedance', in *2009*

IEEE Biomedical Circuits and Systems Conference, Beijing, China, Nov. 2009, pp. 153–156. doi: 10.1109/BIOCAS.2009.5372060.

[147] W. Lee and S. Cho, 'Integrated All Electrical Pulse Wave Velocity and Respiration Sensors Using Bio-Impedance', *IEEE J. Solid-State Circuits*, vol. 50, no. 3, pp. 776–785, Mar. 2015, doi: 10.1109/JSSC.2014.2380781.

[148] S.-H. Liu, G.-H. Cai, D.-C. Cheng, and Y.-F. Huang, 'Using impedance-plethysmography technique for cuffless blood pressure measurement', in *2017 IEEE International Conference on Systems, Man, and Cybernetics (SMC)*, Banff, AB, Oct. 2017, pp. 395–399. doi: 10.1109/SMC.2017.8122636.

[149] G. Chen, C. Au, and J. Chen, 'Textile Triboelectric Nanogenerators for Wearable Pulse Wave Monitoring', *Trends Biotechnol.*, vol. 39, no. 10, pp. 1078–1092, Oct. 2021, doi: 10.1016/j.tibtech.2020.12.011.

[150] S. Harimurti, H. Zakaria, and T. L. Erawati Rajab, 'Wearable and Flexible Devices for Cuff-less Blood Pressure Estimation and Monitoring: A Review', in *2021 International Symposium on Electronics and Smart Devices (ISESD)*, Bandung, Indonesia, Jun. 2021, pp. 1–6. doi: 10.1109/ISESD53023.2021.9501582.

[151] P. M. Nabeel, V. R. Kiran, J. Joseph, V. V. Abhidev, and M. Sivaprakasam, 'Local Pulse Wave Velocity: Theory, Methods, Advancements, and Clinical Applications', *IEEE Rev. Biomed. Eng.*, vol. 13, pp. 74–112, 2020, doi: 10.1109/RBME.2019.2931587.

[152] P.-Y. Huang, W.-C. Lin, B. Y.-C. Chiu, H.-H. Chang, and K.-P. Lin, 'Regression analysis of radial artery pulse palpation as a potential tool for traditional Chinese medicine training education', *Complement. Ther. Med.*, vol. 21, no. 6, pp. 649–659, Dec. 2013, doi: 10.1016/j.ctim.2013.08.011.

[153] S. Tanaka, Shumei Gao, M. Nogawa, and K.-I. Yamakoshi, 'Noninvasive measurement of instantaneous, radial artery blood pressure', *IEEE Eng. Med. Biol. Mag.*, vol. 24, no. 4, pp. 32–37, Jul. 2005, doi: 10.1109/MEMB.2005.1463393.

[154] T. H. Huynh, R. Jafari, and W.-Y. Chung, 'Noninvasive Cuffless Blood Pressure Estimation Using Pulse Transit Time and Impedance Plethysmography', *IEEE*

Trans. Biomed. Eng., vol. 66, no. 4, pp. 967–976, Apr. 2019, doi: 10.1109/TBME.2018.2865751.

[155] V. P. Rachim and W.-Y. Chung, 'Multimodal Wrist Biosensor for Wearable Cuff-less Blood Pressure Monitoring System', *Sci. Rep.*, vol. 9, no. 1, p. 7947, Dec. 2019, doi: 10.1038/s41598-019-44348-3.

[156] Y.-P. Hsu and D. J. Young, 'Skin-Coupled Personal Wearable Ambulatory Pulse Wave Velocity Monitoring System Using Microelectromechanical Sensors', *IEEE Sens. J.*, vol. 14, no. 10, pp. 3490–3497, Oct. 2014, doi: 10.1109/JSEN.2014.2345779.

[157] A. Attarpour, A. Mahnam, A. Aminitabar, and H. Samani, 'Cuff-less continuous measurement of blood pressure using wrist and fingertip photo-plethysmograms: Evaluation and feature analysis', *Biomed. Signal Process. Control*, vol. 49, pp. 212–220, Mar. 2019, doi: 10.1016/j.bspc.2018.12.006.

[158] B. Ibrahim, A. Akbari, and R. Jafari, 'A novel method for pulse transit time estimation using wrist bio-impedance sensing based on a regression model', in *2017 IEEE Biomedical Circuits and Systems Conference (BioCAS)*, Torino, Oct. 2017, pp. 1–4. doi: 10.1109/BIOCAS.2017.8325054.

[159] B. Ibrahim and R. Jafari, 'Continuous Blood Pressure Monitoring using Wrist-worn Bio-impedance Sensors with Wet Electrodes', p. 4, 2018.

[160] N. Pm, J. Joseph, S. Karthik, M. Sivaprakasam, and M. Chenniappan, 'Bi-Modal Arterial Compliance Probe for Calibration-Free Cuffless Blood Pressure Estimation', *IEEE Trans. Biomed. Eng.*, pp. 1–1, 2018, doi: 10.1109/TBME.2018.2866332.

[161] T. H. Huynh, R. Jafari, and W.-Y. Chung, 'Noninvasive Cuffless Blood Pressure Estimation Using Pulse Transit Time and Impedance Plethysmography', *IEEE Trans. Biomed. Eng.*, pp. 1–1, 2018, doi: 10.1109/TBME.2018.2865751.

[162] V. P. Rachim, T. H. Huynh, and W.-Y. Chung, 'Wrist Photo-Plethysmography and Bio-Impedance Sensor for Cuff-Less Blood Pressure Monitoring', p. 4, 2018.

[163] M. Metshein, P. Annus, R. Land, M. Min, and A. Aabloo, ‘Availability and variations of cardiac activity in the case of measuring the bioimpedance of wrist’, in *2018 IEEE International Instrumentation and Measurement Technology Conference (I2MTC)*, Houston, TX, USA, May 2018, pp. 1–5. doi: 10.1109/I2MTC.2018.8409684.

[164] B. Ibrahim and R. Jafari, ‘Cuffless Blood Pressure Monitoring from an Array of Wrist Bio-Impedance Sensors Using Subject-Specific Regression Models: Proof of Concept’, *IEEE Trans. Biomed. Circuits Syst.*, vol. 13, no. 6, pp. 1723–1735, Dec. 2019, doi: 10.1109/TBCAS.2019.2946661.

[165] W. Lee and S. Cho, ‘An Integrated Pulse Wave Velocity Sensor using Bio-impedance and Noise-shaped Body Channel Communication’, p. 3, 2013.

[166] S.-H. Liu, D.-C. Cheng, and C.-H. Su, ‘A Cuffless Blood Pressure Measurement Based on the Impedance Plethysmography Technique’, *Sensors*, vol. 17, no. 5, p. 1176, May 2017, doi: 10.3390/s17051176.

[167] J.-J. Huang, Y.-M. Huang, and A. R. See, ‘Studying Peripheral Vascular Pulse Wave Velocity Using Bioimpedance Plethysmography and Regression Analysis’, p. 8, 2017.

[168] T. Huynh, R. Jafari, and W.-Y. Chung, ‘An Accurate Bioimpedance Measurement System for Blood Pressure Monitoring’, *Sensors*, vol. 18, no. 7, p. 2095, Jun. 2018, doi: 10.3390/s18072095.

[169] K. B. Abdessalem and R. B. Salah, ‘Diagnosis of arterial thrombosis and stenosis in blood vessel Using bioimpedance analysis’, vol. 02, no. 07, p. 6, 2015.

[170] Y. H. Shash, M. A. A. Eldosoky, and M. T. Elwakad, ‘The effect of vascular diseases on bioimpedance measurements: mathematical modeling’, *Biomed. Res. Ther.*, vol. 5, no. 6, Jun. 2018, doi: 10.15419/bmrat.v5i6.453.

[171] R. Mohamed, M. El Dosoky, and M. El-Wakad, ‘The effect of heart pulsatile on the measurement of artery bioimpedance’, *J. Electr. Bioimpedance*, vol. 8, no. 1, p. 101, Dec. 2017, doi: 10.5617/jeb.4677.

[172] G. Anand, A. Lowe, and A. M. Al-Jumaily, ‘Simulation of impedance measurements at human forearm within 1 kHz to 2 MHz’, *J. Electr. Bioimpedance*, vol. 7, no. 1, p. 20, May 2016, doi: 10.5617/jeb.2657.

[173] G. Anand, A. Lowe, and A. Al-Jumaily, ‘Tissue phantoms to mimic the dielectric properties of human forearm section for multi-frequency bioimpedance analysis at low frequencies’, *Mater. Sci. Eng. C*, vol. 96, pp. 496–508, Mar. 2019, doi: 10.1016/j.msec.2018.11.080.

[174] O. I. Shuvo and M. N. Islam, ‘Sensitivity Analysis of the Tetrapolar Electrical Impedance Measurement Systems Using COMSOL Multiphysics for the non-uniform and Inhomogeneous Medium’, *Dhaka Univ. J. Sci.*, vol. 64, no. 1, pp. 7–13, Jun. 2016, doi: 10.3329/dujs.v64i1.28517.

[175] K. Pesti, H. Koiv, and M. Min, ‘Simulation of the Sensitivity Distribution of Four-Electrode Impedance Sensing on Radial Artery’, in *2019 IEEE Sensors Applications Symposium (SAS)*, Sophia Antipolis, France, Mar. 2019, pp. 1–6. doi: 10.1109/SAS.2019.8705976.

[176] F. N. van de Vosse and N. Stergiopulos, ‘Pulse Wave Propagation in the Arterial Tree’, *Annu. Rev. Fluid Mech.*, vol. 43, no. 1, pp. 467–499, Jan. 2011, doi: 10.1146/annurev-fluid-122109-160730.

[177] Z. Marcinkevics, M. Greve, J. I. Aivars, R. Erts, and A. H. Zehtabi, ‘Relationship between arterial pressure and pulse wave velocity using photoplethysmography during the post-exercise recovery period’, p. 10, 2009.

[178] F. Heydari, M. P. Ebrahim, J.-M. Redoute, K. Joe, K. Walker, and M. Rasit Yuce, ‘A Chest-Based Continuous Cuffless Blood Pressure Method: Estimation and Evaluation Using Multiple Body Sensors’, *Inf. Fusion*, p. S1566253519301939, Jul. 2019, doi: 10.1016/j.inffus.2019.07.001.

[179] C. Douniama, C. Sauter, and R. Couronne, ‘Blood Pressure Tracking Capabilities of Pulse Transit Times in Different Arterial Segments: A Clinical Evaluation’, p. 4, 2009.

[180] M. Butlin, F. Shirbani, E. Barin, I. Tan, B. Spronck, and A. P. Avolio, ‘Cuffless Estimation of Blood Pressure: Importance of Variability in Blood Pressure Dependence of Arterial Stiffness Across Individuals and Measurement Sites’, *IEEE Trans. Biomed. Eng.*, vol. 65, no. 11, pp. 2377–2383, Nov. 2018, doi: 10.1109/TBME.2018.2823333.

[181] A. E. Dastjerdi, M. Kachuee, and M. Shabany, ‘Nonlinear Cuff-less Blood Pressure Estimation of Healthy Subjects Using Pulse Transit Time and Arrival Time’, *IEEE Trans. Instrum. Meas.*, vol. 66, no. 12, pp. 3299–3308, Dec. 2017, doi: 10.1109/TIM.2017.2745081.

[182] Y. Xu, W. Zhang, D. Wang, and P. Ping, ‘A calibration method for cuffless continue blood pressure measurement using Gaussian normalized pulse transit time’, in *2018 IEEE International Instrumentation and Measurement Technology Conference (I2MTC)*, Houston, TX, USA, May 2018, pp. 1–5. doi: 10.1109/I2MTC.2018.8409817.

[183] Xiao-Rong Ding and Yuan-Ting Zhang, ‘Photoplethysmogram intensity ratio: A potential indicator for improving the accuracy of PTT-based cuffless blood pressure estimation’, in *2015 37th Annual International Conference of the IEEE Engineering in Medicine and Biology Society (EMBC)*, Milan, Aug. 2015, pp. 398–401. doi: 10.1109/EMBC.2015.7318383.

[184] I. Sharifi, S. Goudarzi, and M. B. Khodabakhshi, ‘A novel dynamical approach in continuous cuffless blood pressure estimation based on ECG and PPG signals’, *Artif. Intell. Med.*, vol. 97, pp. 143–151, Jun. 2019, doi: 10.1016/j.artmed.2018.12.005.

[185] J. Seo, S. J. Pietrangelo, H.-S. Lee, and C. G. Sodini, ‘Noninvasive arterial blood pressure waveform monitoring using two- element ultrasound system’, *IEEE Trans. Ultrason. Ferroelectr. Freq. Control*, vol. 62, no. 4, pp. 776–784, Apr. 2015, doi: 10.1109/TUFFC.2014.006904.

[186] V. P. Rachim, S. Kang, J.-H. Baek, and S.-M. Park, ‘Unobtrusive, Cuffless Blood Pressure Monitoring Using a Soft Polymer Sensor Array With Flexible Hybrid

Electronics', *IEEE Sens. J.*, vol. 21, no. 8, pp. 10132–10142, Apr. 2021, doi: 10.1109/JSEN.2021.3059864.

[187] P. Krisai, A. S. Vischer, L. Kilian, A. Meienberg, M. Mayr, and T. Burkard, 'Accuracy of 24-hour ambulatory blood pressure monitoring by a novel cuffless device in clinical practice', *Heart*, p. heartjnl-2018-313592, Sep. 2018, doi: 10.1136/heartjnl-2018-313592.

[188] H. W. Lui and K. L. Chow, 'A Novel Calibration Procedure of Pulse Transit Time Based Blood Pressure Measurement with Heart Rate and Respiratory Rate', p. 5, 2018.

[189] 'Machine learning', *Wikipedia*. Aug. 17, 2019. Accessed: Aug. 21, 2019. [Online]. Available: https://en.wikipedia.org/w/index.php?title=Machine_learning&oldid=911275251

[190] A. L. Samuel, 'Some studies in machine learning using the game of checkers', p. 13, 1959.

[191] 'A Cuffless BP measurement using ECG and PPG sensors', vol. 2, no. 7, p. 4, 2018.

[192] J. Y. Kim, B. H. Cho, S. M. Im, M. J. Jeon, I. Y. Kim, and S. I. Kim, 'Comparative study on artificial neural network with multiple regressions for continuous estimation of blood pressure', in *2005 IEEE Engineering in Medicine and Biology 27th Annual Conference*, Shanghai, China, 2005, pp. 6942–6945. doi: 10.1109/IEMBS.2005.1616102.

[193] Y. Kurylyak, F. Lamonaca, and D. Grimaldi, 'A Neural Network-based method for continuous blood pressure estimation from a PPG signal', in *2013 IEEE International Instrumentation and Measurement Technology Conference (I2MTC)*, Minneapolis, MN, USA, May 2013, pp. 280–283. doi: 10.1109/I2MTC.2013.6555424.

[194] M. Liu, L.-M. Po, and H. Fu, 'Cuffless Blood Pressure Estimation Based on Photoplethysmography Signal and Its Second Derivative', *Int. J. Comput. Theory Eng.*, vol. 9, no. 3, pp. 202–206, 2017, doi: 10.7763/IJCTE.2017.V9.1138.

[195] S. Chen, Z. Ji, H. Wu, and Y. Xu, ‘A Non-Invasive Continuous Blood Pressure Estimation Approach Based on Machine Learning’, *Sensors*, vol. 19, no. 11, p. 2585, Jun. 2019, doi: 10.3390/s19112585.

[196] S. R. Mansouri, A. Lowe, H. G. Hosseini, and M. M. Baig, ‘Blood Pressure Estimation from Electrocardiogram and Photoplethysmography Signals Using Continuous Wavelet Transform and Convolutional Neural Network’, p. 9, 2019.

[197] M. Kachuee, M. M. Kiani, H. Mohammadzade, and M. Shabany, ‘Cuffless Blood Pressure Estimation Algorithms for Continuous Health-Care Monitoring’, *IEEE Trans. Biomed. Eng.*, vol. 64, no. 4, pp. 859–869, Apr. 2017, doi: 10.1109/TBME.2016.2580904.

[198] S. Maqsood *et al.*, ‘A survey: From shallow to deep machine learning approaches for blood pressure estimation using biosensors’, *Expert Syst. Appl.*, vol. 197, p. 116788, Jul. 2022, doi: 10.1016/j.eswa.2022.116788.

[199] A. Polinski, M. Pietrewicz, T. Kocejko, A. Bujnowski, J. Ruminski, and J. Wtorek, ‘A Meta-Analysis of Pulse Arrival Time Based Blood Pressure Estimation’, p. 4, 2018.

[200] ‘PhysioNet Databases’. https://physionet.org/about/database/ (accessed Jun. 06, 2022).

[201] A. A. Anisimov and T. V. Sergeev, ‘Influence of Heart Rate Variability on Algorithm of Blood Pressure Estimation by Pulse Wave Propagation Time’, in *2018 Third International Conference on Human Factors in Complex Technical Systems and Environments (ERGO)s and Environments (ERGO)*, Saint Petersburg, Russia, Jul. 2018, pp. 166–169. doi: 10.1109/ERGO.2018.8443894.

[202] J. Feng, Z. Huang, C. Zhou, and X. Ye, ‘Study of continuous blood pressure estimation based on pulse transit time, heart rate and photoplethysmography-derived hemodynamic covariates’, *Australas. Phys. Eng. Sci. Med.*, vol. 41, no. 2, pp. 403–413, Jun. 2018, doi: 10.1007/s13246-018-0637-8.

[203] S. C. Millasseau, R. P. Kelly, J. M. Ritter, and P. J. Chowienczyk, ‘Determination of age-related increases in large artery stiffness by digital pulse contour analysis’, *Clin. Sci.*, vol. 103, no. 4, pp. 371–377, Oct. 2002, doi: 10.1042/cs1030371.

[204] S. A. Esper and M. R. Pinsky, ‘Arterial waveform analysis’, *Best Pract. Res. Clin. Anaesthesiol.*, vol. 28, no. 4, pp. 363–380, Dec. 2014, doi: 10.1016/j.bpa.2014.08.002.

[205] S. N. Zaidi and S. M. Collins, ‘Orthostatic stress and area under the curve of photoplethysmography waveform’, *Biomed. Phys. Eng. Express*, vol. 2, no. 4, p. 045006, Jul. 2016, doi: 10.1088/2057-1976/2/4/045006.

[206] M. Voelz, ‘Measurement of the blood-pressure constantk, over a pressure range in the canine radial artery’, *Med. Biol. Eng. Comput.*, vol. 19, no. 5, pp. 535–537, Sep. 1981, doi: 10.1007/BF02442765.

[207] A. C. Dornhorst, P. Howard, and G. L. Leathart, ‘Respiratory Variations in Blood Pressure’, *Circulation*, vol. 6, no. 4, pp. 553–558, Oct. 1952, doi: 10.1161/01.CIR.6.4.553.

[208] M. Pagani *et al.*, ‘Low and High Frequency Components of Blood Pressure Variability’, *Ann. N. Y. Acad. Sci.*, vol. 783, no. 1 Neuroprotecti, pp. 10–23, Aug. 1996, doi: 10.1111/j.1749-6632.1996.tb26704.x.

[209] L. H. Peterson, ‘Regulation of Blood Vessels’, *Circulation*, vol. 21, no. 5, pp. 749–759, May 1960, doi: 10.1161/01.CIR.21.5.749.

[210] A. E. W. Johnson *et al.*, ‘MIMIC-III, a freely accessible critical care database’, *Sci. Data*, vol. 3, no. 1, p. 160035, Dec. 2016, doi: 10.1038/sdata.2016.35.

[211] G. S. Stergiou *et al.*, ‘A Universal Standard for the Validation of Blood Pressure Measuring Devices’, p. 7, 2018.

[212] C. M. Lawes, S. V. Hoorn, M. R. Law, P. Elliott, S. MacMahon, and A. Rodgers, ‘Blood pressure and the global burden of disease 2000. Part 1: Estimates of blood pressure levels’:, *J. Hypertens.*, vol. 24, no. 3, pp. 413–422, Mar. 2006, doi: 10.1097/01.hjh.0000199801.72563.6f.

[213] B. Ibrahim and R. Jafari, ‘Cuffless blood pressure monitoring from a wristband with calibration-free algorithms for sensing location based on bio-impedance sensor array and autoencoder’, *Sci. Rep.*, vol. 12, no. 1, p. 319, Dec. 2022, doi: 10.1038/s41598-021-03612-1.

[214] A. Vybornova, E. Polychronopoulou, A. Wurzner-Ghajarzadeh, S. Fallet, J. Sola, and G. Wuerzner, ‘Blood pressure from the optical Aktiia Bracelet: a 1-month validation study using an extended ISO81060-2 protocol adapted for a cuffless wrist device’, *Blood Press. Monit.*, vol. 26, no. 4, pp. 305–311, Aug. 2021, doi: 10.1097/MBP.0000000000000531.

[215] J. Sola, A. Vybornova, S. Fallet, E. Polychronopoulou, A. Wurzner-Ghajarzadeh, and G. Wuerzner, ‘Validation of the optical Aktiia bracelet in different body positions for the persistent monitoring of blood pressure’, *Sci. Rep.*, vol. 11, no. 1, p. 20644, Dec. 2021, doi: 10.1038/s41598-021-99294-w.

[216] ‘Aktiia - BP band’. https://aktiia.com/uk/ (accessed Apr. 05, 2022).

[217] T. B. Plante *et al.*, ‘Validation of the Instant Blood Pressure Smartphone App’, *JAMA Intern. Med.*, vol. 176, no. 5, p. 700, May 2016, doi: 10.1001/jamainternmed.2016.0157.

[218] N. van Helmond, S. S. Martin, and T. B. Plante, ‘Is cuffless blood pressure measurement already here?’, *J. Hypertens.*, vol. 38, no. 4, pp. 774–775, Apr. 2020, doi: 10.1097/HJH.0000000000002344.

[219] J. B. Cohen *et al.*, ‘History and Justification of a National Blood Pressure Measurement Validated Device Listing’, *Hypertension*, vol. 73, no. 2, pp. 258–264, Feb. 2019, doi: 10.1161/HYPERTENSIONAHA.118.11990.

[220] E. O’Brien, E. Dolan, and G. S. Stergiou, ‘Achieving reliable blood pressure measurements in clinical practice: It’s time to meet the challenge’, *J. Clin. Hypertens.*, vol. 20, no. 7, pp. 1084–1088, Jul. 2018, doi: 10.1111/jch.13323.

[221] B. S. Alpert, ‘Can “FDA-cleared” blood pressure devices be trusted? A call to action:’, *Blood Press. Monit.*, vol. 22, no. 4, pp. 179–181, Aug. 2017, doi: 10.1097/MBP.0000000000000279.

[222] T. Tamura, ‘Cuffless Blood Pressure Monitors: Principles, Standards and Approval for Medical Use’, *IEICE Trans. Commun.*, vol. E104.B, no. 6, pp. 580–586, Jun. 2021, doi: 10.1587/transcom.2020HMI0002.

[223] E. O’Brien, B. S. Alpert, and G. S. Stergiou, ‘Accurate blood pressure measuring devices: Influencing users in the 21st century’, *J. Clin. Hypertens.*, vol. 20, no. 7, pp. 1138–1141, Jul. 2018, doi: 10.1111/jch.13278.

[224] E. O’Brien, G. S. Stergiou, and M. J. Turner, ‘The quest for accuracy of blood pressure measuring devices’, *J. Clin. Hypertens.*, vol. 20, no. 7, pp. 1092–1095, Jul. 2018, doi: 10.1111/jch.13279.

[225] C. Gabriel, S. Gabriel, and E. Corthout, ‘The dielectric properties of biological tissues: I. Literature survey’, *Phys. Med. Biol.*, vol. 41, no. 11, pp. 2231–2249, Nov. 1996, doi: 10.1088/0031-9155/41/11/001.

[226] S. Gabriel, R. W. Lau, and C. Gabriel, ‘The dielectric properties of biological tissues: II. Measurements in the frequency range 10 Hz to 20 GHz’, *Phys. Med. Biol.*, vol. 41, no. 11, pp. 2251–2269, Nov. 1996, doi: 10.1088/0031-9155/41/11/002.

[227] S. Gabriel, R. W. Lau, and C. Gabriel, ‘The dielectric properties of biological tissues: III. Parametric models for the dielectric spectrum of tissues’, *Phys. Med. Biol.*, vol. 41, no. 11, pp. 2271–2293, Nov. 1996, doi: 10.1088/0031-9155/41/11/003.

[228] J. Nyboer, M. M. Kreider, and L. Hannapel, ‘Electrical Impedance Plethysmography: A Physical and Physiologic Approach to Peripheral Vascular Study’, *Circulation*, vol. 2, no. 6, pp. 811–821, Dec. 1950, doi: 10.1161/01.CIR.2.6.811.

[229] R. J. Maughan, J. S. Watson, and J. Weir, ‘The relative proportions of fat, muscle and bone in the normal human forearm as determined by computed tomography’, *Clin. Sci.*, vol. 66, no. 6, pp. 683–689, Jun. 1984, doi: 10.1042/cs0660683.

[230] J. U. Kim, Y. J. Lee, J. Lee, and J. Y. Kim, ‘Differences in the Properties of the Radial Artery between *Cun* , *Guan* , *Chi* , and Nearby Segments Using Ultrasonographic Imaging: A Pilot Study on Arterial Depth, Diameter, and Blood

Flow', *Evid. Based Complement. Alternat. Med.*, vol. 2015, pp. 1–7, 2015, doi: 10.1155/2015/381634.

[231] S. Grampp, S. Majumdar, M. Jergas, P. Lang, A. Gies, and HarryK. Genant, 'MRI of bone marrow in the distal radius: in vivo precision of effective transverse relaxation times', *Eur. Radiol.*, vol. 5, no. 1, Feb. 1995, doi: 10.1007/BF00178080.

[232] G. A. Toomayan, F. Robertson, N. M. Major, and B. E. Brigman, 'Upper extremity compartmental anatomy: clinical relevance to radiologists', *Skeletal Radiol.*, vol. 35, no. 4, pp. 195–201, Apr. 2006, doi: 10.1007/s00256-005-0063-3.

[233] L. Weinberg, M. Spanger, C. Tan, and M. Nikfarjam, 'Postoperative wristwatch-induced compressive neuropathy of the hand: a case report', *J. Med. Case Reports*, vol. 9, no. 1, p. 141, Dec. 2015, doi: 10.1186/s13256-015-0625-5.

[234] B.-S. Yoo *et al.*, 'Anatomical consideration of the radial artery for transradial coronary procedures: arterial diameter, branching anomaly and vessel tortuosity', *Int. J. Cardiol.*, vol. 101, no. 3, pp. 421–427, Jun. 2005, doi: 10.1016/j.ijcard.2004.03.061.

[235] C. Giannattasio *et al.*, 'Effects of Heart Rate Changes on Arterial Distensibility in Humans', *Hypertension*, vol. 42, no. 3, pp. 253–256, Sep. 2003, doi: 10.1161/01.HYP.0000085199.33254.15.

[236] J.-W. Lee *et al.*, 'Reference diameter and characteristics of the distal radial artery based on ultrasonographic assessment', *Korean J. Intern. Med.*, vol. 37, no. 1, pp. 109–118, Jan. 2022, doi: 10.3904/kjim.2020.685.

[237] T. Ashraf, Z. Panhwar, S. Habib, M. A. Memon, F. Shamsi, and J. Arif, 'Size of radial and ulnar artery in local population', vol. 60, no. 10, p. 3, 2010.

[238] S. Beniwal, K. Bhargava, and S. K. Kausik, 'Size of distal radial and distal ulnar arteries in adults of southern Rajasthan and their implications for percutaneous coronary interventions', *Indian Heart J.*, vol. 66, no. 5, pp. 506–509, Sep. 2014, doi: 10.1016/j.ihj.2014.08.010.

[239] S. Dharma, S. Kedev, T. Patel, S. V. Rao, O. F. Bertrand, and I. C. Gilchrist, 'Radial artery diameter does not correlate with body mass index: A duplex ultrasound

analysis of 1706 patients undergoing trans-radial catheterization at three experienced radial centers', *Int. J. Cardiol.*, vol. 228, pp. 169–172, Feb. 2017, doi: 10.1016/j.ijcard.2016.11.145.

[240] B. B. Karki, M. D. Bhattarai, M. R. Bajracharya, S. Karki, and A. R. Devkota, 'Correlation of neck and wrist circumference with waist circumference', *J. Adv. Intern. Med.*, vol. 3, no. 2, pp. 47–51, Dec. 2015, doi: 10.3126/jaim.v3i2.14063.

[241] 'IEC 60601', *Wikipedia*. Jun. 10, 2022. Accessed: Jun. 16, 2022. [Online]. Available: https://en.wikipedia.org/w/index.php?title=IEC_60601&oldid=1092467861

[242] H. Kim, E. Kim, C. Choi, and W.-H. Yeo, 'Advances in Soft and Dry Electrodes for Wearable Health Monitoring Devices', *Micromachines*, vol. 13, no. 4, p. 629, Apr. 2022, doi: 10.3390/mi13040629.

[243] J. de Rigal, C. Escoffier, B. Querleux, B. Faivre, P. Agache, and J.-L. Lévêque, 'Assessment of Aging of the Human Skin by In Vivo Ultrasonic Imaging', *J. Invest. Dermatol.*, vol. 93, no. 5, pp. 621–625, Nov. 1989, doi: 10.1111/1523-1747.ep12319741.

[244] T. Baum *et al.*, 'Cortical and trabecular bone structure analysis at the distal radius—prediction of biomechanical strength by DXA and MRI', *J. Bone Miner. Metab.*, vol. 31, no. 2, pp. 212–221, Mar. 2013, doi: 10.1007/s00774-012-0407-8.

[245] H. V. Riekkinen, K. O. Karkola, and A. Kankainen, 'The radial artery is larger than the ulnar', *Ann. Thorac. Surg.*, vol. 75, no. 3, pp. 882–884, Mar. 2003, doi: 10.1016/S0003-4975(02)04557-5.

[246] Y. Yu, 'Development of skeletal muscle phantoms for mechanical properties and dielectric properties at low frequencies', Auckland University of Technology, 2018.

[247] Y. Yu, A. Lowe, G. Anand, and A. Kalra, 'Tissue phantom to mimic the dielectric properties of human muscle within 20 Hz and 100 kHz for biopotential sensing applications', in *2019 41st Annual International Conference of the IEEE Engineering in Medicine and Biology Society (EMBC)*, Berlin, Germany, Jul. 2019, pp. 6490–6493. doi: 10.1109/EMBC.2019.8856530.

[248] C. Gabriel, A. Peyman, and E. H. Grant, ‘Electrical conductivity of tissue at frequencies below 1 MHz’, *Phys. Med. Biol.*, vol. 54, no. 16, pp. 4863–4878, Aug. 2009, doi: 10.1088/0031-9155/54/16/002.

[249] A. Peyman, C. Gabriel, and E. H. Grant, ‘Complex permittivity of sodium chloride solutions at microwave frequencies’, *Bioelectromagnetics*, vol. 28, no. 4, pp. 264–274, May 2007, doi: 10.1002/bem.20271.

[250] C. S. Widodo, H. Sela, and D. R. Santosa, ‘The effect of NaCl concentration on the ionic NaCl solutions electrical impedance value using electrochemical impedance spectroscopy methods’, East Java, Indonesia, 2018, p. 050003. doi: 10.1063/1.5062753.

[251] Z. Moro, ‘Considerations on the accuracy of measurements of electrical conductivity of liquids’, p. 6, 2006.

[252] ‘MFIA 500 kHz / 5 MHz Impedance Analyzer | Zurich Instruments’, Dec. 20, 2019. https://www.zhinst.com/en/products/mfia-impedance-analyzer (accessed Jul. 14, 2022).

[253] C. Chassagne, E. Dubois, M. L. Jiménez, J. P. M. van der Ploeg, and J. van Turnhout, ‘Compensating for Electrode Polarization in Dielectric Spectroscopy Studies of Colloidal Suspensions: Theoretical Assessment of Existing Methods’, *Front. Chem.*, vol. 4, Jul. 2016, doi: 10.3389/fchem.2016.00030.

[254] K. Arquilla, A. Webb, and A. Anderson, ‘Textile Electrocardiogram (ECG) Electrodes for Wearable Health Monitoring’, *Sensors*, vol. 20, no. 4, p. 1013, Feb. 2020, doi: 10.3390/s20041013.

[255] A. B. Nigusse, B. Malengier, D. A. Mengistie, G. B. Tseghai, and L. Van Langenhove, ‘Development of Washable Silver Printed Textile Electrodes for Long-Term ECG Monitoring’, *Sensors*, vol. 20, no. 21, p. 6233, Oct. 2020, doi: 10.3390/s20216233.

[256] N. Keawploy, R. Venkatkarthick, P. Wangyao, X. Zhang, R. Liu, and J. Qin, ‘Eco-Friendly Conductive Cotton-Based Textile Electrodes Using Silver- and Carbon-

Coated Fabrics for Advanced Flexible Supercapacitors', *Energy Fuels*, vol. 34, no. 7, pp. 8977–8986, Jul. 2020, doi: 10.1021/acs.energyfuels.0c01419.

[257] L. Corchia, G. Monti, F. Raheli, G. Candelieri, and L. Tarricone, 'Dry Textile Electrodes for Wearable Bio-Impedance Analyzers', *IEEE Sens. J.*, vol. 20, no. 11, pp. 6139–6147, Jun. 2020, doi: 10.1109/JSEN.2020.2972603.

[258] E. Hernández-Balaguera, E. López-Dolado, and J. L. Polo, 'Obtaining electrical equivalent circuits of biological tissues using the current interruption method, circuit theory and fractional calculus', *RSC Adv.*, vol. 6, no. 27, pp. 22312–22319, 2016, doi: 10.1039/C5RA24535D.

[259] E. Hernández-Balaguera, H. Vara, and J. L. Polo, 'Identification of Capacitance Distribution in Neuronal Membranes from a Fractional-Order Electrical Circuit and Whole-Cell Patch-Clamped Cells', *J. Electrochem. Soc.*, vol. 165, no. 12, pp. G3104–G3111, 2018, doi: 10.1149/2.0161812jes.

APPENDIX

A. Dielectric properties of human tissues

Table 36. Dielectric properties of the fat, blood and muscle assigned in Chapter 4.

Dielectric properties		Bulk conductivity [S/m]			Relative permittivity		
Tissues		fat	blood	muscle	fat	blood	muscle
Frequency [kHz]	1	0.022404	0.70000	0.32115	24104.000	5258.600	434930.000
	10	0.023830	0.70004	0.34083	1085.300	5248.200	25909.000
	50	0.024246	0.70080	0.35182	172.420	5197.700	10094.000
	100	0.024414	0.70292	0.36185	92.885	5120.000	8089.200
	200	0.024585	0.71034	0.38408	56.015	4925.300	6377.700
	300	0.024690	0.72100	0.40693	44.075	4694.900	5226.900
	400	0.024769	0.73389	0.42782	38.134	4445.200	4339.300
	500	0.024833	0.74816	0.44590	34.559	4188.600	3647.300
	600	0.024890	0.76315	0.46125	32.158	3933.900	3105.500
	700	0.024941	0.77835	0.47421	30.425	3687.300	2678.000
	800	0.024989	0.79339	0.48519	29.109	3452.600	2336.900
	900	0.025035	0.80803	0.49458	28.069	3232.000	2061.500
	1000	0.025079	0.82211	0.50268	27.222	3026.300	1836.400
	1500	0.025290	0.88212	0.53071	24.520	2213.300	1154.400
	2000	0.025501	0.92605	0.54761	22.952	1680.700	825.980
	5000	0.026918	1.04000	0.59008	18.181	596.120	308.260
	10000	0.029152	1.09670	0.61683	13.767	280.030	170.730
	50000	0.034677	1.19260	0.67808	6.8758	94.205	77.063
	100000	0.036295	1.23300	0.70759	6.0741	76.818	65.972

Table 37. Dielectric properties of the assessorial tissues assigned in Chapter 5.

Tissues		Bulk conductivity [S/m]			Relative permittivity		
		Skin	Cortical bone	Cancellous bone	Skin	Cortical bone	Cancellous bone
Frequency [kHz]	1	0.00065738	0.020157	0.08153	32135	2702.4	12320
	10	0.0029317	0.02043	0.082623	29010	521.64	1657.8
	50	0.029369	0.020642	0.083422	21876	264.19	613.18
	100	0.065836	0.020791	0.083892	15357	227.64	471.71
	200	0.11502	0.021081	0.084622	8849.2	203.74	387.42
	300	0.14402	0.021407	0.085314	6012.6	191.44	350.43
	400	0.1635	0.021771	0.086015	4514.6	182.27	326.43
	500	0.17798	0.022165	0.086731	3610	174.5	308.16
	600	0.18951	0.022582	0.087459	3011	167.55	293.11
	700	0.19913	0.023014	0.088194	2586.9	161.18	280.15
	800	0.20744	0.023456	0.088932	2271.4	155.25	268.69
	900	0.21479	0.023904	0.089668	2027.4	149.71	258.37
	1000	0.2214	0.024353	0.090399	1832.8	144.51	248.97
	1500	0.24747	0.026544	0.093913	1247.4	122.62	211.61
	2000	0.26649	0.02854	0.097112	948.6	106.05	184.71
	5000	0.32493	0.036488	0.11062	397.84	58.885	108.88
	10000	0.366	0.042822	0.12282	221.81	36.772	70.779
	50000	0.46982	0.057124	0.15505	84.761	17.744	33.258
	100000	0.5232	0.064313	0.1725	65.969	15.283	27.629

B. Instrument accuracy of the multi-frequency impedance analyser

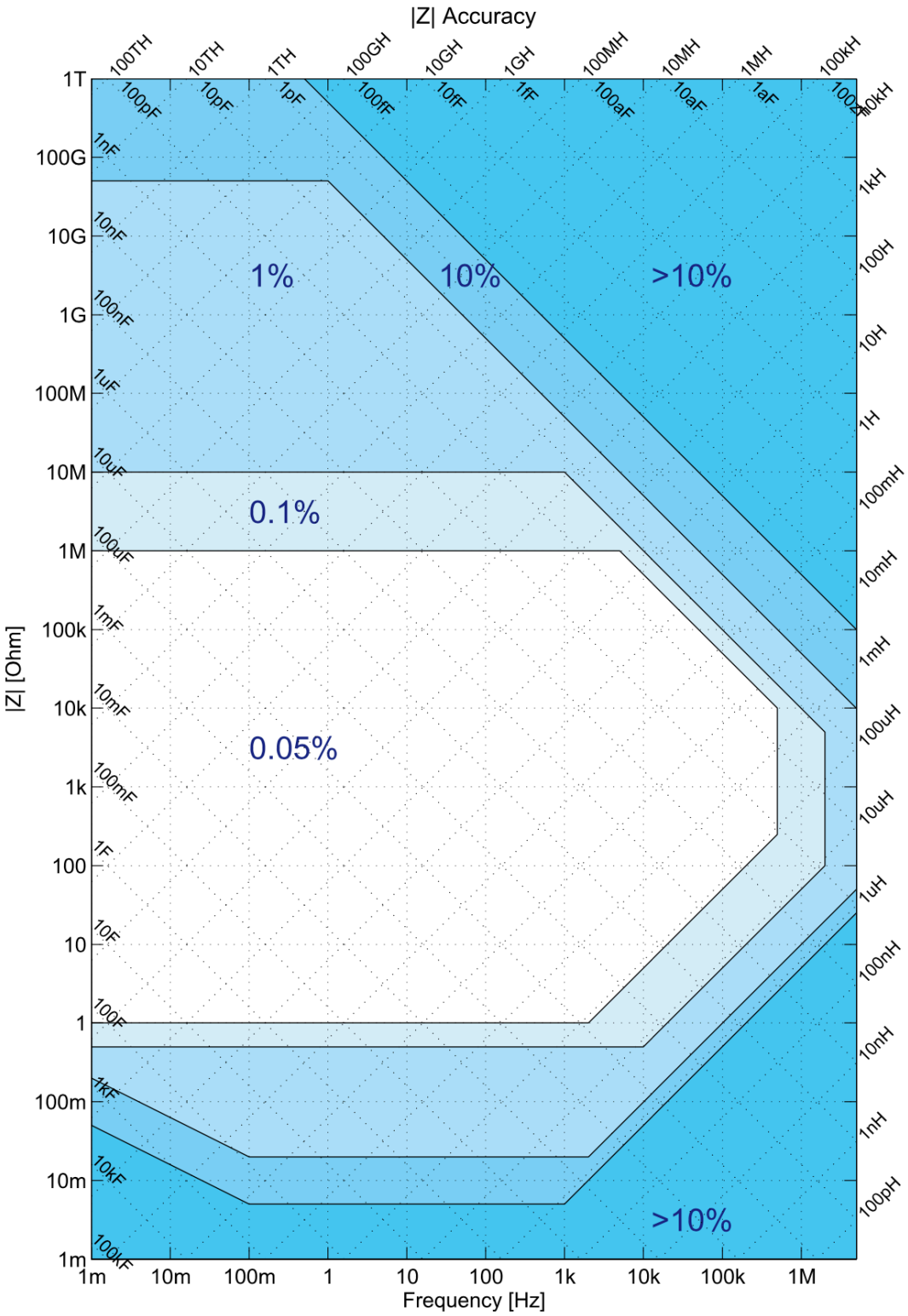

Figure 94. Instrument accuracy of the multi-frequency impedance analyser [252]